IntechOpen

Dendrimers

Fundamentals and Applications

Edited by Claudia Maria Simonescu

DENDRIMERS - FUNDAMENTALS AND APPLICATIONS

Edited by **Claudia Maria Simonescu**

Dendrimers - Fundamentals and Applications
http://dx.doi.org/10.5772/intechopen.68738
Edited by Claudia Maria Simonescu

Contributors

Yaping Dan, Haigang Wu, Hideo Takezoe, Osamu Haba, Igor M Neelov, Elena Popova, Dilorom Khamidova, Faizali Komilov, Baljinder Singh, Aanchal Ghai, Shalini Chopra, Ida Monika Franiak-Pietryga, Bradley Messmer, Barbara Ziemba, Dorota Skowrońska-Krawczyk, Vassilis Kostopoulos, Athanasios Kotrotsos, Claudia Maria Simonescu

Notice

First published in London, United Kingdom, 2018 by IntechOpen
eBook (PDF) Published by IntechOpen, 2019
IntechOpen is the global imprint of INTECHOPEN LIMITED, registered in England and Wales, registration number: 11086078, The Shard, 25th floor, 32 London Bridge Street
London, SE19SG – United Kingdom
Printed in Croatia

British Library Cataloguing-in-Publication Data
A catalogue record for this book is available from the British Library

Additional hard and PDF copies can be obtained from orders@intechopen.com

Dendrimers - Fundamentals and Applications
Edited by Claudia Maria Simonescu

p. cm.

Print ISBN 978-1-78923-058-1

Online ISBN 978-1-78923-059-8

eBook (PDF) ISBN 978-1-83881-351-2

Meet the editor

Prof. Claudia Maria Simonescu, PhD, is working as a full-time professor at the Department of Analytical Chemistry and Environmental Engineering, Faculty of Applied Chemistry and Materials Science, Politehnica University of Bucharest, Romania. She received her PhD degree in Chemistry and completed one postdoctoral research training in Industrial Biotechnology. Her research and teaching activities are in the fields of materials science and environmental engineering. The research activities resulted in the development of nine books, two laboratory works, and a chapter published at the *International Publishing House*. She is also an author of 70 ISI-ranked journals and 21 articles published in proceedings of international scientific conferences with 267 citations (Web of Science). Dr. Claudia Maria Simonescu is a member of international professional bodies and a member of editorial board of international scientific journals. She was also selected as a reviewer for 35 international journals and for research project competitions launched by the Executive Agency for Higher Education, Research, Development and Innovation Funding (UEFISCDI) from Romania, and as a reviewer for the National Commission for Scientific and Technological Research (CONICYT) of the Ministry of Chile and *National Fund for Scientific and Technological Development* (FONDECYT) regular competition.

Contents

Preface

Dendrimers are a new and important class of macromolecules increasingly used in recent years in the fields of medicine, biology, materials science, synthetic organic chemistry, biotechnology, environmental engineering, optics, electronics, catalysis, electrochemistry, photochemistry, and sensors and even for production of cosmetics and personal care products.

Dendrimers: Fundamentals and Applications aims to provide an interdisciplinary approach of this exciting and rapidly growing area of research. A general introduction to the subject of dendrimers, including definition, properties, and the main applications, is provided. Subsequent sections discuss topics including dendrimers as drug nanocarriers, computer simulation of interaction of lysine dendrimers with different peptides, radiolabeled dendrimers for molecular imaging of tumor angiogenesis, dendrimers as functional materials, dendrimers as dopant atom carriers, and dendrimers in self-healing technology.

Throughout the book, examples from the authors' work and other current researches are also mentioned. This book will appeal to a wide range of scientists, including nonspecialists who require an introduction to fundamentals of dendrimers and their application in the field of biology, medicine, liquid crystal devices, electronics, quantum devices, and self-healing technology.

Prof. Claudia Maria Simonescu, PhD
Analytical Chemistry and Environmental Engineering Department
Politehnica University of Bucharest
Faculty of Applied Chemistry and Materials Science
Bucharest, Romania

Chapter 1

Introductory Chapter: Dendrimers as Nanoengineered Materials and Their Applications

Claudia Maria Simonescu

Additional information is available at the end of the chapter

http://dx.doi.org/10.5772/intechopen.75844

1. Introduction

Over the last years, a great attention has been paid to develop and discover new materials with potential applications in our daily lives. From these new materials, dendrimers, as a new class of synthetic polymers discovered in the late 1970s by German scientist Fritz Vögtle, at the University of Bonn, and American chemist Donald Tomalia who was working at Dow Chemical Corporation have been readily engineered to be used in many industrial applications.

Dendrimers are defined as nano-scaled macromolecules having a particular architecture with three definite domains: (1) one central core represented by either a single atom or an atomic group with at least two similar chemical functions, (2) many branches bonded to the core composed by repeat units resulting a series of radially concentric layers named generations and (3) numerous terminal functional groups located at the edge of the molecule which determine the properties of dendrimers [1]. These structural characteristics imposed properties essential for their applicability such as: (i) controlled shape, (ii) accurate dimensions and an extraordinary diversity of peripheral functions (theoretically inexhaustible), (iii) ability to simultaneously create isotropic and anisotropic assemblies, (iv) almost perfect compatibility with other nanomolecules such as: DNA, metal nanocrystals or carbon nanotubes, (v) a remarkable self-assembly potential, (vi) the ability to combine both mineral and organic compounds simultaneously, (vii) the tendency to encapsulate or to be associated in unimolecular functional mechanisms. All these are in accordance with the high number of the researches reported in scientific literature and with the numerous applications of dendrimers. By using as keyword "dendrimers" one searching on ScienceDirect revealed a number of 18,549 results of which 550 are in the first 2 months of this year.

Regarding the applications of dendrimers, the most important are in: medicine [2], catalysis [3], nanoparticle synthesis [4], environmental protection and remediation [5], electrochemistry [6], photochemistry [7], electronics [8], sensors [9], batteries [10], optics [11], biology [12], cosmetics, and personal care product [13].

Substantial progress and many studies have been performed towards the employing of dendrimers for therapeutic and diagnostic purposes for cancer treatment. In this field, the dendrimers were involved as anti-neoplastics and contrast agents, in photodynamic therapy, photothermal therapy and neutron capture therapy [14]. Impressive results have been registered regarding uses of dendrimers for lung, breast, ovarian, pancreatic, cervical and brain cancer treatments.

An emerging field to apply dendrimers is genetics. Selective replacing of defective or deficient genes inside cells is expecting to take place by embedding genetic material into dendritic structures. This is called "gene therapy" and it was previously attempted using a genetically modified virus. In this therapy, the genetically modified virus has been attached to the cells and injects its DNA. The body recognized these "good" viruses as a disease and it attacks them. In case of dendrimers, this immune-system reaction does not occur and they can be applied successfully.

Dendrimers are also considered as excellent candidates for tissue engineering applications [15].

Recently, dendrimers have shown exciting applications in environmental remediation [15]. They are used as adsorbents for organic and inorganic compounds from water as well as materials for different treatment technologies. Many studies reported the application of dendrimers for removal and recovery of heavy metals, precious metals, dyes, and phenol from wastewater. The removal mechanisms and the factors affecting adsorption/removal parameters have been discussed and presented in these studies [5]. These applications are due to their tunable architectures and their selectivity [5, 15].

The cavity of dendrimers has been exploited as "nanoreactors" for accommodating of different guests from metallic nanoparticles to biomolecules [16]. By this encapsulation, it will be registered an improving properties of guests such as solubility and biocompatibility. One control of the size and the shape of nanoparticles can be also shown when the synthesis of nanoparticles has been performed in dendrimers.

Considering the key role of dendrimers in many processes and reactions, it is expected an increase of developments and researches/articles and books in this field.

Author details

Claudia Maria Simonescu

Address all correspondence to: claudiamaria.simonescu@chimie.upb.ro

Analytical Chemistry and Environmental Engineering Department, Politehnica University of Bucharest, Faculty of Applied Chemistry and Materials Science, Romania

References

[1] Caminade A-M, Laurent R, Majoral J-P. Characterization of dendrimers. Advanced Drug Delivery Reviews. 2005;**57**:2130-2146

[2] Tomalia D, Reyna L, Svenson S. Dendrimers as multi-purpose nanodevices for oncology drug delivery and diagnostic imaging. Biochemical Society Transactions. 2007;**35**(Pt 1):61-67

[3] Karakhanov EA et al. Palladium nanoparticles on dendrimer-containing supports as catalysts for hydrogenation of unsaturated hydrocarbons. Molecular Catalysis. 2017;**440**: 107-119

[4] Sun W et al. Dendrimer-based magnetic iron oxide nanoparticles: Their synthesis and biomedical applications. Drug Discovery Today. 2016;**21**(12):1873-1885

[5] Sajid M et al. Removal of heavy metals and organic pollutants from water using dendritic polymers based adsorbents: A critical review. Separation and Purification Technology. 2018;**191**:400-423

[6] Jin X, Zhou L, Zhu B, Jiang X, Zhu N. Silver-dendrimer nanocomposites as oligonucleotide labels for electrochemical stripping detection of DNA hybridization. Biosensors and Bioelectronics. 2018. DOI: 10.1016/j.bios.2018.02.033

[7] Militello MP et al. Novel PAMAM dendrimers with porphyrin core as potential photosensitizers for PDT applications. Journal of Photochemistry and Photobiology A: Chemistry. 2018;**353**:71-76

[8] Sun K et al. Near-infrared thermally activated delayed fluorescent dendrimers for the efficient non-doped solution-processed organic light-emitting diodes. Organic Electronics. 2017;**48**:389-396

[9] Wang H, Xu Q, Wang J, Du W, Liu F, Hu X. Dendrimer-like amino-functionalized hierarchical porous silica nanoparticle: A host material for 2,4-dichlorophenoxyacetic acid imprinting and sensing. Biosensors and Bioelectronics. 2018;**100**:105-114

[10] Bhattacharya P et al. Polyamidoamine dendrimer-based binders for high-loading lithium–sulfur battery cathodes. Nano Energy. 2016;**19**:176-186

[11] Shoaee S et al. Assessing the sensing limits of fluorescent dendrimer thin films for the detection of explosive vapors. Sensors and Actuators B. 2017;**239**:727-733

[12] Caminade A-M, Ouali A, Laurent R, Turrin C-O, Majoral J-P. Coordination chemistry with phosphorus dendrimers. Applications as catalysts, for materials, and in biology. Coordination Chemistry Reviews. 2016;**308**:478-497

[13] Caminade AM, Wei Y, Majoral JP. Dendrimers and macrocycles: Reciprocal influence on the properties. Comptes Rendus Chimie. 2009;**12**:105-120

[14] Wolinsky JB, Grinstaff MW. Therapeutic and diagnostic applications of dendrimers for cancer treatment. Advanced Drug Delivery Reviews. 2008;**60**:1037-1055

[15] Sajid M. Dendrimers based sorbents: Promising materials for analytical extractions. Trends in Analytical Chemistry. 2018;**98**:114-127

[16] Sadjadi S. Chapter 6: Dendrimers as Nanoreactors. In book: Organic Nanoreactors: From Molecular to Supramolecular Organic Compounds. In: Samahe S, editor. Kidlington, UK: Academic Press Elsevier; 2016:159-201. ISBN: 978-0-12-801713-5. DOI: 10.1016/B978-0-12-801713-5.00006-9

Section 1

Concepts in Dendrimer-based Nanomedicine

Chapter 2

Dendrimers as Drug Nanocarriers: The Future of Gene Therapy and Targeted Therapies in Cancer

Ida Franiak-Pietryga, Barbara Ziemba,
Bradley Messmer and Dorota Skowronska-Krawczyk

Additional information is available at the end of the chapter

http://dx.doi.org/10.5772/intechopen.75774

Abstract

Synthetic polymers, such as dendrimers, play a critical role in pharmaceutical discovery and development. Advances in the application of nanotechnology in medicine have given rise to multifunctional "smart" nanocarriers that can deliver one or more therapeutic agents safely and selectively to cancer cells, including intracellular gene-specific targeting. Dendrimers with their 3D nanopolymeric architectures are highly attractive class of drug and gene delivery vector. Advances in understanding and manipulating genes gave scientists a tool to make changes in people DNA to prevent or treat diseases. Over the past decade, gene therapy has been in use in clinical trials. The inactivation of the tumor suppressor genes is the main idea of the development of gene therapy in the cancer treatment. Broad spectrum of delivery concepts, including viral vectors, liposomes, cationic polymers and dendrimers, cell-penetrating peptides and gold and magnetic nanoparticles have been investigated. A well-designed vector is the most desirable approach to increase the safety of gene therapy, which is still in its infancy stages in cancer research. More experimental and clinical trials are focused on well-designed and effective doses of vectors that are essential for therapeutic efficacy of gene therapy for its potential in clinical use against a wide variety of cancers.

Keywords: nanocarriers, targeted therapy, gene therapy, cancer, drug delivery system, RNA therapeutics, dendriplex, non-viral vectors

1. Introduction

Cancer is one of the world's most stressful diseases with no apparent cure in sight for several tumor types and millions of new cases reported every year [1]. Cancer chemotherapy using conventional anticancer agents has been slowed down by several challenges such as severe toxicity, poor membrane permeability, rapid clearance, and narrow therapeutic index. In this regard, a wide range of nanoparticles such as liposomes, polymeric micelles, polymeric nanoparticles, dendrimers, silica nanoparticles, and carbon nanotubes with their structural, physicochemical, and functional diversity can be utilized to enhance drug loading and enable drug internalization in target cancer cells while limiting uptake in normal tissues and cells [2, 3]. The development of smart cancer treatment approaches revolves engineering such unique nanosystems carrying drug and gene payloads that can passively or/and actively target cancer cells [4]. Gene therapy and newer molecular target-based anticancer tactics involve the use of potent but highly labile agents such as monoclonal antibodies, aptamers, siRNA and miRNA that are readily degraded and/or have limited stability *in vivo* [5]. The big limitation of conventional anticancer agents is a poor therapeutic response and adverse side-effects involving healthy organs [6]. To overcome those limitations searching for new effective carrier vectors is very important. They might protect the payload from degradation during the transit, enhance targeting efficiency, optimize drug release profiles, and reduce the adverse toxic effect caused by the non-target organ accumulation of cytotoxic drugs [7–9].

2. Dendrimers

Dendrimers are globular macromolecules sized 1–100 nm with an architecture consisting of three distinct domains: a central core, a hyperbranched mantle, and a corona with peripheral reactive functional groups [10]. The high level of control over the synthesis of dendritic architecture makes dendrimers a nearly perfect (spherical) nanocarrier with predictable properties. Many different kinds of dendrimers, including polyamidoamine (PAMAM), poly(propylene imine) (PPI), poly(glycerol-co-succinic acid), poly-L-lysine (PLL), melamine, triazine, poly(glycerol), poly[2,2-bis(hydroxymethyl)propionic acid], poly(ethylene glycol) (PEG), and carbohydrate-based and citric acid-based ones, have been successfully developed for drug delivery [11–14]. The most widely investigated vectors for medical application are two dendrimers: PAMAM and PPI [15, 16]. Those two amine-terminated dendrimers display stimuli-responsive (pH-dependent) drug release behavior. The tertiary amine groups are deprotonated at high pH (alkaline), causing a collapse of the dendrimer on itself, which is named 'back folding' [17]. The utility of dendrimers can be appreciated by their ability to traverse several delivery barriers using two overarching principles, namely active and passive tumor targeting.

3. Cancer treatment and limitations of chemotherapy

Surgery and radiation are the main common treatment in solid tumors as soon as they are recommended to undertake considering the tumor infiltration. These kinds of treatments are

considered as local treatments [18]. As it is well recognized, surgery can be disfiguring and radiation can be damaging to local healthy tissues and organs. Chemotherapy is the third option in cancer treatment, which is called adjuvant therapy to surgery and radiotherapy. It is based on cytotoxic effect (cell-killing therapy). The most desirable effect of chemotherapy is to eliminate cancer completely, which is still in most cases the wishful thinking. If such a cure is not possible, the good result is to even stop the growing tumor [19]. Despite some excellent drugs are available, the efficacy of many existing chemotherapeutics is limited by their inability to reach their therapeutic site of action in sufficient amounts to be effective [20]. In most cases, patients are administered with an excess of medications that are distributed throughout the whole body, and thus, it is extremely difficult to avoid distribution into healthy organs and tissues and the depression of the immune system. It always gives the limitation of dosage that can be given and, in turn, prevents these drugs from achieving the potential cures [21]. Current anticancer drugs often have a poor therapeutic index and they cause a lot of side effects [22]. A major concern is when the medications affect non-cancer cells, causing the adverse reduction of red and white blood cells, and affecting the gastrointestinal tract triggering nausea and diarrhea [23]. To reduce, or even better to avoid such side effects, the drug delivery to the tumor is optimized by preparing carriers containing an active agent associated with a molecule capable to accurately target cancer cells such as antibody drug conjugates (ADC) or nanoparticles [24–26].

4. Dendrimers as drug delivery systems

Dendrimers have been engineered as nanodevices, either in nanocarrier drug approaches or as drugs *per se*. The biological effect of dendrimers is caused by terminal moieties and is responsible for the global efficiency. Dendrimers due to their proper, reproducible, and optimized design parameters overcoming the physicochemical limitations of classical drugs (for example, solubility, specificity, stability, biodistribution, and therapeutic efficiency) are successful. They are also able to omit biological problems to reach the right targets such as first-pass effect, immune clearance, cell penetration, and off-target interactions [27]. Polymers are commonly used materials for nanoparticles-based delivery [28], among them dendrimers are the ones more commonly used as a non-viral delivery system. The best drug carrier should meet several requirements such as drug retention, release the drug, unaffecting by the immune system, extending the time in blood circulation, and specific targeting to cells or organs [29]. When a drug carrier is applied to the patient and reaches the level of the blood, it starts an intricate trip before it is able to reach the destination of the target site. When they attach to the target cell membrane, they undergo the endocytosis process. There are several parameters of dendrimers that can facilitate the process. We have to emphasize also the impact of the body structure including size, shape, additional chemistry on the surface, and mechanical flexibility [30]. The nanoparticles, due to their size, have a huge impact on the circulation time if they are applied intravenously (IV), so they are safe for the smallest capillaries and they are not able to clog them [31]. Cellular uptake by phagocytosis and endocytosis is also particle size dependent [32, 33]. The unique uniformity of dendrimers gives them the ability to cross the membrane of cancer cells. The anticancer drug can be either non-covalently encapsulated in the core of the dendrimer or covalently conjugated to its surface, being possible to customize

the drug release profiles by controlled depolarization processes [34, 35]. When amphiphilic dendrimers with a hydrophobic core and hydrophilic branches encapsulate the anticancer drugs, it helps to utilize these dendrimers in local treatments such as intratumoral injections. Such a solution helps to solubilize the hydrophobic drugs and leaves the drug unaltered [36]. The attachment of anticancer drugs to the surface groups of the dendrimer by covalent chemical bonds offers also some other advantages compared to the non-covalent encapsulation. Besides the enhancement of solubilization of the drugs, it is possible to attach many different hydrophobic anticancer drugs, and the controlled release is being maintained [37, 38].

Dendrimers have already been used as passive anticancer nanocarriers [38–41]. There are preclinical promising results *in vitro* as well as *in vivo* with active targeting dendrimers [36]. For example, antibody-dendrimer conjugates showed better efficacy than free antibodies [42–45]. It has been also reported that dendrimers modified with folic acid on the surface generated better tumor accumulations that untargeted controls or free drug, producing a stronger reduction of the tumor mass [46, 47]. Moreover, sugar-modified PPI dendrimers tested by our research team at University of Lodz, Poland, are very attractive and specific for leukemia and lymphoma cells derived from lymphocytes B. Depending on the sugar on the surface and the number of molecules, we can observe the different extend of triggering apoptosis in those cells due to the diversity in affecting particular gene pathways [48–51]. Lysine dendrimers, PAMAM, PPI, and phosphorus have been reported to be able to modulate amyloid peptide aggregation in solution [52–54]. The deposition of amyloid fibrils is characteristic in neurological disorders as well as prion and Alzheimer's diseases. Some of the positively charged dendrimers could even inhibit the growth of amyloid fibrils or even disrupt existing mature of these fibrils. Others could decrease the number of toxic amyloid oligomers [55, 56]. The slow translation of preclinical studies to clinical trials may be due to the toxicity of dendrimers [46, 47], with the aim of the current research in the development of new biocompatible and less toxic alternatives [57, 58].

Once these molecular machines arrive at the target site inside the living organism, several barriers must be overcome. Nanocarriers are usually internalized by endocytic processes [59], the processes called vesicular internalization. The most widely studied endocytic pathways are clathrin-mediated endocytosis, caveolae-mediated endocytosis, and macropinocytosis, but other cellular pathways have been recently identified, including clathrin- and caveolae-independent endocytosis and phagocytosis [60]. Molecules, which are internalized by the cell membrane, are endocytosed by the early endosomes pathway. They may progress later to late endosomes and lysosomes. If the loading of dendrimer targets the nucleus, thus the nuclear membrane is another barrier that the dendrimer should come across [61].

We should be very careful designing the drug delivery system because unexpectedly our desired nanovector might have its own power. This is what our genetic research has shown—4th generation PPI glycodendrimers with maltotriose molecules directly trigger mechanism of apoptosis in mitochondria of lymphocytes B, particularly those transformed to the leukemic cells. That discovery was successfully patented (US 9,877,85) and applied as a potential drug for lymphoproliferative disorders coming from B cells, such as chronic lymphocytic leukemia (CLL) or B-lymphoma. The power of these glycodendrimers relied on the ability to affect several genetic pathways simultaneously, and as opposed to the commonly used drugs or the new ones already proved by FDA, they affect the cell genome very quickly and efficiently according to the natural death process initiation (**Figure 1**).

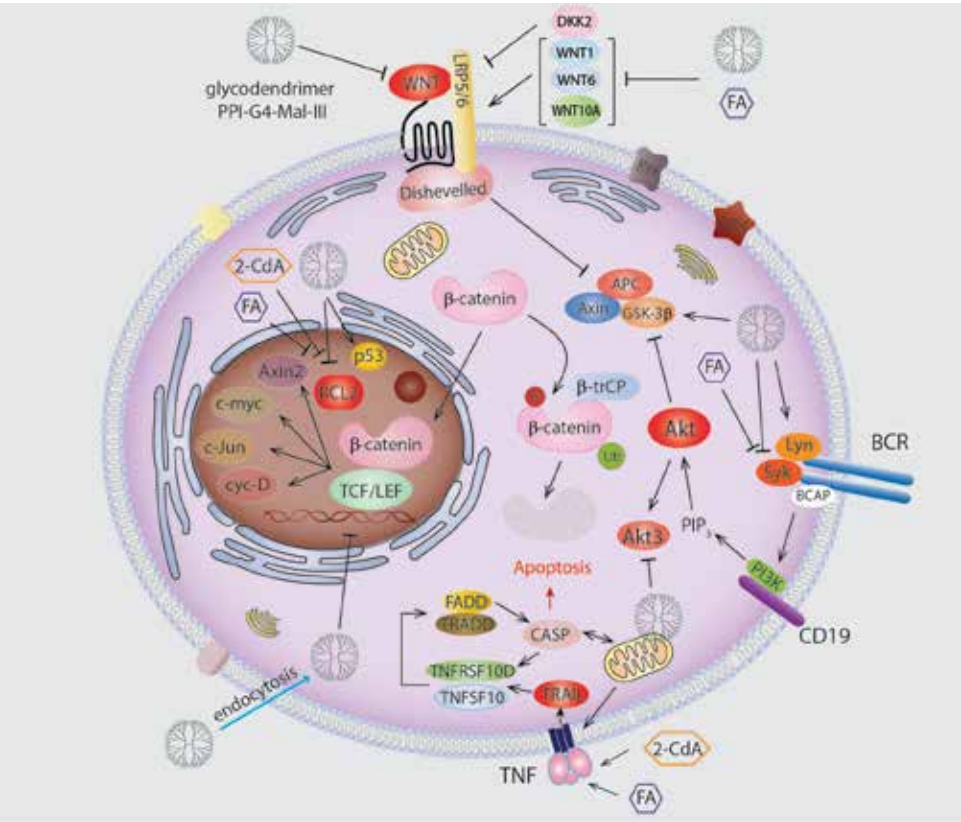

Figure 1. Mechanism of action—PPI-G4-OS-Mal3 dendrimers in B-lymphocyte (the illustration prepared by B. Ziemba).

5. Delivery of RNA therapeutics

During the past decades, RNA-based drugs have arisen as good candidates to cure the diseases at the gene and RNA levels. Since 1990, it has been known that nucleic acids can be used to modify protein production in vivo [62]. However, therapeutic RNA delivery has been limited for a long time by many different factors [63]. It is known that naked, single-stranded RNA is easily degraded by nucleases. It can also activate an immune system and is too large to be able to passively cross the cell membrane. Moreover, the negative charge of RNA causes the problem to enter the cell. Therefore, an additional solution should be provided to facilitate cellular entry and escape from endosomes [63, 64]. Typically, cationic polymers (e.g. dendrimers) are used to electrostatically condense the negatively charged RNA into nanoparticles [65]. Very important for effective nucleic acid delivery are modifications made to RNA itself [66], to make it more resistant to degradation and render them unrecognizable by the immune system [67]. RNAs can be modified by means of chemical alterations to the ribose sugar [67, 68], the phosphate linkage, and the individual bases [69–72]. One of such modified RNA is locked nucleic acid (LNA) modification. LNA's ribose moiety is modified with an extra bridge between the 2′ oxygen and 4′ carbon. The bridge "locks" the ribose in the 3′-*endo*(North) conformation. LNA nucleotides can be mixed with DNA or RNA residues in the oligonucleotide whenever

preferred and hybridize with DNA or RNA according to Watson-Crick base-pairing rules. Due to the high stability of LNA-RNA it started to be used in a biotechnology field in a pharmaceutical business [73]. The multi-valent folate (FA)-conjugated 3WJ RNP constructed to harbor anti-miR-21 LNA sequences (FA-3WJ-LNA-miR21). Specifically targeted anti-miR-21 LNA was delivered to glioblastoma cells. It caused the knock down of miR-21 expression in *in vitro* and *in vivo* models with favorable biodistribution. The results are indicative of the clinical benefit of FA-3WJ RNP-based gene therapy for the successful targeted therapy of developing and even recurring glioblastoma [74]. In the other study, (LNA)-anti-miR was reported as a blockage factor of miR-182-5p in human breast cancer cell line (MCF-7). MTT (3-[4,5 dimethylthiazol-2-yl]-2,5-diphenyl tetrazolium bromide) assay and annexin/propidium iodide staining at different time points after LNA-anti-miR-182-5p transfection were accomplished. The results showed that miR-182-5p inhibition induces apoptosis and thus reduces the viability of MCF-7 cells. These results can be used in translational medicine for future investigation in breast cancer and approach treatment based on antisense therapy.

siRNA is not the only RNA drug to be examined for protein knockdown at the clinical stage (NCT01676259) [75, 76]. Antisense oligonucleotides (ASO) were the first RNA drugs successfully reported in clinical trials. They are able to block protein translation through Watson-Crick base pairing with the target mRNA, similar way to siRNA mechanism, and they can also be modified to improve their stability [77–79]. Despite that the ASOs inhibit protein production through the sterically blocking ribosome attachment or eliciting RNase-H activation, they are also able to promote the exon skipping, which may lead to a deletion of faulty sequences within proteins and thus it can make a protein upregulation, that can be used in diseases where certain genes are repressed [80].

An emerging, but less clinically improved, is microRNA (miRNA) platform for protein knockdown. Endogenous miRNAs are non-coding RNAs that are regulatory factors for a variety of cellular pathways and are often downregulated in diseases [81]. Exogenous mRNAs, or miRNA mimics, delivered therapeutically could make a knockdown of several proteins simultaneously, which might be very useful in cancer, where having a single disease-relevant target is rare [82]. The first miRNA mimic therapy to enter clinical trials was MRX-34—a liposomal-encapsulated miRNA mimic from Mirna Therapeutics meant to treat variety of cancers [83]. Despite the big number of carriers, mRNA molecules are significantly larger than (600–10,000 kDa) than the previously discussed siRNAs (~14 kDa) and ASOs (4–10 kDa), which poses an additional challenge for delivery of mRNA therapeutics [84]. Therapeutic applications based on mRNA are currently being explored as vaccinations against cancer, infectious diseases, and gene editing. Cancer mRNA vaccines have experienced accelerated development in cancer immunotherapy. The majority of approaches tested in clinical trials employ adoptive transfer of DCs transfected with mRNA coding for tumor-specific antigens (TSAs) and immunomodulation of T cells with mRNAs expressing chimeric antigen receptors (CARs) or TSAs [85–87].

The most recent and the most sophisticated gene delivery is CRISPR-Cas system that also relies on Watson-Crick base-pairing between a single guide RNA (sgRNA) and a corresponding DNA target site followed by a distinct protospacer-adjacent motif (PAM), which is a 3–5 nucleotide DNA sequence required for binding Cas9 and cleavage of the target sequence.

It leads to the double-stranded break (DSB) into a DNA molecule [88]. DSBs can be repaired by cells using non-homologous end joining (NHEJ) and homology-directed repair (HDR). NHEJ results in insertions and deletions causing permanent gene knockout [89]. CRISPR-Cas components based on nanoparticle mRNA delivery are therapeutically attractive due to the temporary ability of mRNA expression. There is also no risk of genomic integration and mRNA cytoplasmic activity, mitigating the need to overcome the nuclear barrier in comparison with pDNA [90]. The major challenges for RNA-based drugs and CRISPR-Cas therapies will be shaping the scope of upcoming clinical trials.

6. Clinical studies of dendrimers for targeted cancer therapy

To design the most effective and variety therapies for different kinds of cancer, an effective vector protecting siRNA that is non-toxic and can be targeted at selected cells is necessary [91, 92]. Several classes of dendrimers seem to be good candidates for carriers of oligonucleotides. Cationic carbosilane dendrimers (CBD) characterized by Si—O or Si—C bond and terminated with ammonium or amine groups, form also complexes with siRNAs.

There are many reports presenting promising results in the topic of nucleic acids delivery using complexes called 'dendriplexes' [93–95]. Among variety of proposed candidates, PAMAM dendrimers are the most explored dendrimers type, followed by poly(propylene imine) (PPI) dendrimers, poly(L-lysine) (PLL) dendrimers, and some others [96].

PAMAM dendrimers, hydrophilic, biocompatible, and non-immunogenic particles, are build of ethylenediamine core (most commonly) and methyl acrylate and ethylenediamine branches [97, 98]. They have been successfully used as nucleic acid delivery systems in many *in vitro* and *in vivo* researches of which we present selected examples [107–119].

The transfection efficiency of PAMAM dendrimers largely depends on their generation, which determines the structure of the PAMAM molecule: higher generations are more compact and spherical than the low ones and provide a surface with a high density of primary amines therefore form more stable dendriplexes with higher efficiency [99, 100]. However, dendrimers with high generations results in higher toxicity due to a large number of terminal cationic groups which can interact with negatively charged cell components, e.g. cell membranes causing their disruption [101, 102]. This disadvantage can be diminishing by surface modification with different targeting or shielding moieties providing with not only low toxicity but also enhance the cell uptake and specific accumulation of nucleic acid molecules inside cells [103–106]. For example, novel targeted nanoparticle system consisting of FLT3 ligand-conjugated PAMAM G7 encapsulating a pivotal tumor suppressor and negative regulator of *FLT3* miRNA—miR-150, was developed by Jiang et al. [107] to treat *FLT3*-overexpressing acute myeloid leukemia (AML), a leukemia associated with unfavorable prognosis. The system demonstrated high efficacy significantly inhibiting progression of FLT3-overexpressing AML *in vivo* with no obvious side effects on normal hematopoiesis. In other research, Liu et al. demonstrated that triethanolamine (TEA)-core PAMAM dendrimer is able to deliver Hsp27 siRNA effectively to a castrate-resistant prostate cancer model *in vitro* [108] and *in vivo* [109] and produce potent gene silencing of the heat-shock protein 27 (HSP27), leading

to a notable anticancer effect. To further improve the delivery system, the arginine-terminated PAMAM-G4 dendrimers were developed with the aim of combining and harnessing the unique siRNA delivery properties of the TEA-core PAMAM dendrimer and the cell-penetrating advantages of the arginine-rich motif. The modification led to improved cell uptake of siRNA by comparison with non-modified bearing PAMAM-G4 and to yield potent gene silencing in human hematopoietic CD34+ stem cells [110] and anticancer effects with no discernible toxicity in both *in vitro* and *in vivo* models [110, 111]. Another example of a delivery system where the modification aiming at increasing the efficiency yield is FA-decorated PAMAM G4 (G4-FA) used as a vector for local delivery of siRNA against vascular endothelial growth factor A (siVEGFA) in a xenograft HN12 tumor mouse model of head and neck squamous cell carcinomas. The G4-FA/siVEGFA complex exhibited high tumor uptake, sustained retention properties and pronounced tumor suppression in even single- or two-dose regimen studies [112]. Thioaptamer (TA)-modified PAMAM dendrimers, on the other hand, are proposed as effective miRNA deliver system to breast cancer cells constituting a prototype that it could be safely used in pre-clinical and clinical research [113].

A frequent way of using dendriplexes in anticancer therapy is to provide them in conjunction with approved anticancer agents [114–116]. Researchers from Virginia Commonwealth University used nanoplexes of PAMAM dendrimer with polyethylene glycol and lactobionic acid complexed with AEG-1 siRNA against hepatocellular carcinoma (HCC), a fatal cancer with no effective therapy. Applied in the combination with all-trans retinoic acid (ATRA), the complex developed a profound and synergistic inhibition in tumor growth in human HCC xenografts model suggesting, that combinatorial approach might be an effective way to combat resistant types of cancer [117]. Liu et al. used PAPMAM dendrimers as a nanoparticle delivery platform for a MDR1 gene targeting siRNA to reverse multidrug resistance (MDR) in human breast cancer MCF-7/ADR cells. This PAMAM-siMDR1 complex decorated additionally with phospholipid demonstrated high gene silencing efficiency and enhanced cellular uptake of siMDR1 resulting in rising of cellular accumulation of doxorubicin (DOX), inhibition of the tumor cell migration, and due to synergistic work with paclitaxel (PTX), increase of cell apoptosis, and cell phase regulation [118]. More complex system designed in order to achieve effective treatment to MDR breast cancer is PAMAM functionalized graphene oxide (GO-PAMAM) which can load DOX and MMP-9 shRNA plasmid at the same time [119].

It is still a challenging task to deliver the anticancer drugs to brain tumors and overcome the restriction of blood-brain barrier (BBB). He et al. [12] have proposed recently an interesting approach. G4.0 PAMAM dendrimers have been conjugated with two targeted ligands—transferrin and wheat germ agglutinin. Such conjugates were used for crossing the BBB and incorporation drugs to brain tumor cells. That dual-targeting drug carrier system allowed to deliver successfully DOX inside the brain tumor and provided a potential therapy for brain cancer [12].

Dendrimers have been investigated for ophthalmic drug delivery since it offers a number of advantages as a carrier system. They may improve effective delivery of therapeutic agents to intraocular tissues, such as the retina or choroid, using non-invasive delivery methods. Eye cancers are not among the most common but also in this area, scientists have started to look for inspiration in nanoparticles [120]. Kang et al. made a successful single injection of subconjunctival

G3.5 PAMAM dendrimer to transgenic murine retinoblastoma with no associated toxicity. The higher dose of nanoparticle even could reach and decrease the tumor burden in the untreated, contralateral eye [121].

Poly(propylene imine) (PPI) dendrimers are constructed from a 1,4-diaminobutane core and propylene imine branches [122]. Positively charged surface of PPI dendrimers provides an interaction with nucleic acids, enabling the dendritic scaffold to be used as a vector for gene transfection [123].

As in the case of the PAMAM dendrimers, the surface of PPI dendrimers can be freely modified to reduce their toxicity and increase their uptake by target cells. A small library of alkanoate-modified PPI G5 dendrimers was developed and tested for their ability to transfect DNA to neuroblastoma Neuro-2a cells. It was shown that a balanced hydrophobic surface modification results in improved transfection, low cytotoxicity, and hemotoxicity [124]. Much larger modifications of PPI dendrimers in order to increase their efficiency as gene carriers have been made by a team of researchers from The State University of New Jersey [123–126]. In 2009, Taratula et al. modified PPI G5-siRNA complex with dithiol-containing cross-linker molecules followed by PEG coating. To direct the complex specifically to the human ovarian and lungs cancer cells, an analog of luteinizing hormone-releasing hormone (LHRH) peptide was conjugated to the end of PEG. The modification and targeting approach confers the complex stability in plasma and intracellular bioavailability, promoted its tumor-specific uptake and accumulation in the cells, and efficient gene silencing. Moreover, in vivo study confirmed high specificity of the proposed targeting delivery approach [125]. A year later, the same team developed a novel way to compact and deliver nucleic acids with lower, third-generation PPI dendrimers by using gold nanoparticles (AuNP) as a "labile catalytic" packaging agents. The AuNP helped dendrimers to compact siRNA but were not included in the final complex. The efficiency of mRNA silencing by this approach was even higher than that with PPI G5 dendrimers [126]. To further improve the efficiency of investigated delivery systems, the authors developed siRNA vectors based on PPI G5 dendrimers and superparamagnetic iron oxide nanoparticles, together with incorporation of PEG coating and LHRH conjugation. This novel multifunctional siRNA delivery system improved selective internalization into cancer cells and increased the efficiency of targeted gene silencing *in vitro* and sufficiently enhanced *in vivo* activity of anticancer drug—cisplatin [127]. In further studies the team designed a drug delivery system (DDS) containing a PPI dendrimer as a carrier and a LHRH peptide as a tumor-targeting moiety, siRNA targeted to CD44 mRNA and anticancer drug—PTX. The proposed DDS was tested in vitro and in vivo using metastatic ovarian cancer cells. The treatment resulted in suppression of CD44 mRNA and protein expression, induction of cell death and tumor melting, and moreover, it was free from adverse side effects [128]. The potential of PPI dendrimers as a core of delivery complexes was also investigated in the combination therapy against multidrug-resistant breast cancer cells (MCF-7/ADR). Copolymer consisting of PPI dendrimer, Pluronic P123 and anti-CD44 monoclonal antibody (anti-CD44-P123-PPI) loaded with pDNA-iMDR1-shRNA against MDR1 protein demonstrated high efficiency of transfection contributing to increased sensitivity of cancer cells to the DOX. The results demonstrated that the administration of anti-CD44-P123-PPI/pDNA-iMDR1-shRNA nanocomplexes combined with DOX inhibit tumor growth more efficiently than DOX alone [129]. Poly(propylene imine) (PPI) dendrimers with surface modification with maltose have been

tested as drug carriers for nucleoside analog (NA) 5′-triphosphates. The study showed the interactions between PPI dendrimers of 3rd (G3) or 4th (G4) generation and cytidine-5′-triphosphate (CTP) measured by Isothermal Titration Calorimetry method. CTP was used as a good representative molecule of pyrimidine nucleoside analog (NA)—cytarabine (ara-CTP) commonly used in leukemia treatment. Dendriplexes made of PPI dendrimers and NAs may help to improve NA limitations such as low solubility and stability or resistance in leukemia cells. The study depicted that dendrimer generation is responsible for the efficiency of complex formation. Also a type of surface modification of dendrimer with maltose residues and a type of solvent used to prepare dendriplexes were evaluated. The results of PPI dendrimers creating complexes with CTP were highly efficient that makes them promising candidates for a drug delivery system [130]. As soon as we know that cationic nature of PPI dendrimers makes it possible to form complexes with nucleotide Ara-C triphosphate forms (Ara-CTP), the authors went further to test the concept of applying PPI glycodendrimers as a drug delivery system. They wanted to facilitate the delivery of cytarabine to cancer cells to overcome metabolic limitations of the drug. As a leukemic cell lines models they used 1301 and HL-60 as well as peripheral blood mononuclear cells. The enhanced activity of Ara-C triphosphate forming (Ara-CTP) complexes with PPI-M dendrimers had been shown. An enhanced uptake and cytotoxicity of Ara-CTP-dendriplexes toward 1301 cells with blocked human equilibrative nucleoside transporter, hENT1, suggested that it might be a multipurpose candidate for resistant acute lymphoblastic leukemia chemotherapy with lower expression of hENT1 [131]. It has been also reported that PPI-Ma-DS did not impact THP-1 cells (monocytic cell line model of innate immunity effectors) viability and growth even at high concentrations (up to 100 μM). They also did not induce expression of genes for important signaling pathways: Jak/STAT, Keap1/Nrf2 and ER stress. The high concentrations of 4th generation PPI-Mal-DS (25–100 μM) induced nuclear translocation of p65 NF-κB protein and its DNA-binding activity. It leads to NF-κB-dependent increased expression of mRNA for NF-κB targets: *IGFBP3*, *TNFAIP3*, and *TNF*. The 3rd generation of PPI-Mal-DS dendrimers did not exert the same effect. There was observed no increase in pro-inflammatory cytokine secretion which is a very promising result [132]. PPI-5G dendrimers, similar to PAMAM, also possessed the ability to deliver anticancer drugs to brain tumors. Gajbhije and Jain reported polysorbate-80-conjugated PPI dendrimers for targeted delivery of docetaxel (DTX) to the brain tumor [133]. This complex reduced the tumor volume more than 50% after 1 week of treatment. It is because this formulation owing the higher BBB permeability of polysorbate-80-anchored dendrimers [134]. The other report showed that PPI-5G dendrimers conjugated with thiamine exhibited improved delivery of PTX across the BBB and the preferential brain uptake of PTX by the nanoconjugates might be attributed to the association with the thiamine transporters or increased passive diffusion secondary to an improved concentration gradient of the dendrimers located at the BBB interface [135].

Poly(L-lysine) (PLL) dendrimers, amino acid-based macromolecules characterized by high biocompatibility and low toxicity, have also been developed as non-viral vectors for gene delivery [136–139]. In example, in 2002 it was reported that dendritic PLL G5 and G6 transfected DNA into several different cell lines with high efficiency and without any cytotoxic effects [139]. The results of more recent studies confirm previous reports. Newly synthesized

siRNA carriers containing amphiphilic PLL dendrons exhibited not only the siRNA binding properties but also the ability to inhibit the proliferation of glioblastoma cells while being non-toxic for cell types that share the anatomical space with tumor cells during the course of the disease [140]. Research on the use of PLL dendritic structures as gene carriers in combination with traditional anticancer drugs also yields promising results. PLL G3 dendrimers with a silsesquioxane cubic core were conjugated with a c(RGDfK) peptide through PEG spacer for codelivery of DOX and siRNA to glioblastoma U87 cells. The complex showed high transfection efficiency and gene silencing and was more toxic to U87 cells than free DOX [141].

7. Concluding remarks

Although conventional chemotherapy has been the cornerstone in the fight against cancer, is far from being totally satisfactory due to the problems related with their formulation, pharmacokinetics, and the last but not least, severe side effects of such a therapy. Last past decades the huge progress has been made in the understanding of the disease, its molecular background and development of newer targeted therapies. Unfortunately, an effective treatment of several forms of cancer still remains a major challenge. Recent advances in drugs based on dendrimer and gene delivery using dendrimers as a vector has appeared as a great option to overcome the limitations of conventional chemotherapy. Currently, more than 50% of the cancers are not curable and drug nanocarriers might help to decrease this percentage. Nanomedicine represents one of the fastest growing research areas and is regarded as one of the most promising tools for cancer treatment. Several solutions based on nanoparticles have been developed and many are used in clinical cancer care. Liposomes and polymer conjugates were the first nanocarriers to be approved by FDA; however, only five liposomal drugs, two polymer-protein conjugates, and two dendrimers are in the market up to date. Abraxane®, an albumin-bound paclitaxel nanoparticle, has been approved by FDA in 2005 for the treatment of metastatic breast cancer. In 2012 the same drug has been approved for the first-line treatment of advanced non-small lung cancer and in 2013 for the metastatic pancreatic cancer. There was an absence of evidence and guidance, regulatory decisions on nanomedicine therapeutics. The FDA collaborates with the Nanotechnology Characterization Laboratory (NCL) to facilitate the regulatory review and in-depth characterization of nanodrugs in medicine. The European Technology Platform on Nanomedicine (ETPN) set up a European Nano-Characterization Laboratory (EU-NCL) as the part of the Horizon2020 project. The regulatory problems seem to be finally overcome since FDA published the Guidance for Industry ('Drug Products, Including Biological Products, that Contain Nanomaterials') in December 2017 (https://www.fda.gov/Drugs/GuidanceComplianceRegulatoryInformation/Guidances/default.htm). Looking into the future, the use of cancer theragnostics, combining anticancer targeted therapy and diagnosis by multifunctional nanoparticles, that combine the therapeutic and imaging agent, might be a revolution in the cancer treatment because they allow to diagnose, visualize, and kill the cancer cells simultaneously and both treatment and diagnostic in the real time. This is a future of medicine, right now it still seems to be a science-fiction movie, but proudly we are coming closer every year to such an amazing progress in diagnostic and treatment thanks to the broad usage of nanoparticles and nanotechnology.

Acknowledgements

The authors wish to acknowledge the founding support from GeneaMed LTD, Poland and Fulbright Commission support to IFP during the scholarship 'Fulbright Senior Award 2016-2017' at the University of California San Diego.

Author details

Ida Franiak-Pietryga[1,2,3]*, Barbara Ziemba[2,3], Bradley Messmer[4] and Dorota Skowronska-Krawczyk[1]

*Address all correspondence to: ida.fp@interia.pl

1 Ophthalmology Department, University of California San Diego, San Diego CA, Lodz, Poland

2 Department of Clinical and Laboratory Genetics, Medical University of Lodz, Lodz, Poland

3 GeneaMed LTD, Lodz, Poland

4 Abreos Biosciences, San Diego, CA, USA

References

[1] Ferlay J et al. Cancer incidence and mortality worldwide: Sources, methods and major patterns in GLOBOCAN 2012. International Journal of Cancer. 2015;**136**(5):E359-E386

[2] Sahoo S, Labhasetwar V. Nanotech approaches to drug delivery and imaging. Drug Discovery Today. 2003;**8**:1112-1120

[3] Abeylath SC, Ganta S, Iyer AK, Amiji M. Combinatorial-designed multifunctional polymeric nanosystems for tumor-targeted therapeutic delivery. Accounts of Chemical Research. 2011;**44**(10):1009-1017

[4] Iyer AK, Duan Z, Amiji MM. Nanodelivery systems for nucleic acid therapeutics in drug resistant tumors. Molecular Pharmaceutics. 2014;**11**(8):2511-2526

[5] Dande P et al. Improving RNA interference in mammalian cells by 4′-thio-modified small interfering RNA (siRNA): Effect on siRNA activity and nuclease stability when used in combination with 2′-O-alkyl modifications. Journal of Medicinal Chemistry. 2006;**49**(5):1624-1634

[6] Ferraresi V et al. Toxicity and activity of docetaxel in anthracycline-pretreated breast cancer patients: A phase II study. American Journal of Clinical Oncology. 2000;**23**(2):132-139

[7] Liu Y, Miyoshi H, Nakamura M. Nanomedicine for drug delivery and imaging: A promising avenue for cancer therapy and diagnosis using targeted functional nanoparticles. International Journal of Cancer. 2007;**120**(12):2527-2537

[8] Pauwels EKJ, Erba P. Towards the use of nanoparticles in cancer therapy and imaging. Drug News & Perspectives. 2007;**20**(4):213-220

[9] Thakur S, Tekade RK, Kesharwani P, Jain NK. The effect of polyethylene glycol spacer chain length on the tumor-targeting potential of folate-modified PPI dendrimers. Journal of Nanoparticle Research. 2013;**15**(5):1625

[10] Tomalia DA. Birth of a new macromolecular architecture: Dendrimers as quantized building blocks for nanoscale synthetic polymer chemistry. Progress in Polymer Science (Oxford). 2005;**30**(3-4):294-324

[11] Bhadra D, Bhadra S, Jain S, Jain NK. A PEGylated dendritic nanoparticulate carrier of fluorouracil. International Journal of Pharmaceutics. 2003;**257**(1-2):111-124

[12] He H et al. PEGylated poly(amidoamine) dendrimer-based dual-targeting carrier for treating brain tumors. Biomaterials. 2011;**32**(2):478-487

[13] Crampton HL, Simanek EE. Dendrimers as drug delivery vehicles: Non-covalent interactions of bioactive compounds with dendrimers. Polymer International. 2007;**56**(4):489-496

[14] Tomalia DA, Reyna LA, Svenson S. Dendrimers as multi-purpose nanodevices for oncology drug delivery and diagnostic imaging. Biochemical Society Transactions. 2007;**35**(1):61-67

[15] Kannan RM, Nance E, Kannan S, Tomalia DA. Emerging concepts in dendrimer-based nanomedicine: From design principles to clinical applications. Journal of Internal Medicine. 2014;**276**(6):579-617

[16] Kesharwani P, Jain K, Jain NK. Dendrimer as nanocarrier for drug delivery. Progress in Polymer Science. 2014;**39**(2):268-307

[17] Kesharwani P, Tekade RK, Jain NK. Formulation development and in vitro-in vivo assessment of the fourth-generation PPI dendrimer as a cancer-targeting vector. Nanomedicine. 2014;**9**(15):2291-2308

[18] Brizel DM et al. Hyperfractionated irradiation with or without concurrent chemotherapy for locally advanced head and neck cancer. The New England Journal of Medicine. 1998;**338**(25):1798-1804

[19] DeVita VT, Lawrence TS, Rosenberg SA. De Vita, Hellman, and Rosenberg's Cancer: Principles & practice of Oncology: Thenth Edition. Wolters Kluwer Health Adis (ESP); Jan 7, 2015:2280. ISBN (print): 9781451192940; ISBN (electronic): 9781469894553

[20] Chaplin DJ, Hill SA, Bell KM, Tozer GM. Modification of tumor blood flow: Current status and future directions. Seminars in Radiation Oncology. 1998;**8**(3):151-163

[21] Needham D, Dewhirst MW. The development and testing of a new temperature-sensitive drug delivery system for the treatment of solid tumors. Advanced Drug Delivery Reviews. 2001;**53**(3):285-305

[22] Hoelder S, Clarke PA, Workman P. Discovery of small molecule cancer drugs: Successes, challenges and opportunities. Molecular Oncology. 2012;**6**(2):155-176

[23] Aslam MS, Naveed S, Ahmed A, Abbas Z, Gull I, Athar MA. Side effects of chemotherapy in cancer patients and evaluation of patients opinion about starvation based differential chemotherapy. Journal of Cancer Therapy. 2014;**5**(July):817-822

[24] Wang Z, Guravaiah N, Ning C, He Y, Yao L, Wang J. Antibody drug conjugates: The forefront of targeted chemotherapy for cancer treatment. Journal of Drug Design and Research. 2015;**2**:2-9

[25] Sievers EL, Senter PD. Antibody-drug conjugates in cancer therapy. Annual Review of Medicine. 2013;**64**(1):15-29

[26] Wicki A, Witzigmann D, Balasubramanian V, Huwyler J. Nanomedicine in cancer therapy: Challenges, opportunities, and clinical applications. Journal of Controlled Release. 2015;**200**:138-157

[27] Mignani S et al. Anticancer copper(II) phosphorus dendrimers are potent proapoptotic Bax activators. European Journal of Medicinal Chemistry. 2017;**132**:142-156

[28] Anderson DG, Lynn DM, Langer R. Semi-automated synthesis and screening of a large library of degradable cationic polymers for gene delivery. Angewandte Chemie International Edition. 2003;**42**(27):3153-3158

[29] Needham D, Dewhirst MW. The development and testing of a new temperature-sensitive drug delivery system for the treatment of solid tumors. Advanced Drug Delivery Reviews. 2001 Dec 31;**53**(3):285-305

[30] Yoo JW, Doshi N, Mitragotri S. Adaptive micro and nanoparticles: Temporal control over carrier properties to facilitate drug delivery. Advanced Drug Delivery Reviews. 2011; **63**(14-15):1247-1256

[31] Moghimi SM, Hunter AC, Murray JC. Long-circulating and target-specific nanoparticles: Theory to practice. Pharmacological Reviews. 2001;**53**(2):283-318

[32] Rejman J, Oberle V, Zuhorn IS, Hoekstra D. Size-dependent internalization of particles via the pathways of clathrin- and caveolae-mediated endocytosis. The Biochemical Journal. 2004;**377**(1):159-169

[33] Wu LP, Ficker M, Christensen JB, Trohopoulos PN, Moghimi SM. Dendrimers in medicine: Therapeutic concepts and pharmaceutical challenges. Bioconjugate Chemistry. 2015; **26**(7):1198-1211

[34] Tong R, Cheng J. Anticancer polymeric nanomedicines. Polymer Reviews. 2007;**47**(3): 345-381

[35] Pérez-Herrero E, Fernández-Medarde A. Advanced targeted therapies in cancer: Drug nanocarriers, the future of chemotherapy. European Journal of Pharmaceutics and Biopharmaceutics. 2015;**93**:52-79

[36] Wolinsky JB, Grinstaff MW. Therapeutic and diagnostic applications of dendrimers for cancer treatment. Advanced Drug Delivery Reviews. 2008;**60**(9):1037-1055

[37] Li MH et al. Dendrimer-based multivalent methotrexates as dual acting nanoconjugates for cancer cell targeting. European Journal of Medicinal Chemistry. 2012;**47**(1):560-572

[38] Khandare JJ et al. Dendrimer versus linear conjugate: Influence of polymeric architecture on the delivery and anticancer effect of paclitaxel. Bioconjugate Chemistry. 2006;**17**(6): 1464-1472

[39] Dhanikula RS, Hildgen P. Influence of molecular architecture of polyether-co-polyester dendrimers on the encapsulation and release of methotrexate. Biomaterials. 2007;**28**(20): 3140-3152

[40] Wang L et al. Encapsulation of curcumin within poly(amidoamine) dendrimers for delivery to cancer cells. Journal of Materials Science. Materials in Medicine. 2013;**24**(9):2137-2144

[41] Ly TU, Tran NQ, Hoang TKD, Phan KN, Truong HN, Nguyen CK. Pegylated dendrimer and its effect in fluorouracil loading and release for enhancing antitumor activity. Journal of Biomedical Nanotechnology. 2013;**9**(2):213-220

[42] Shukla R et al. HER2 specific tumor targeting with dendrimer conjugated anti-HER2 mAb. Bioconjugate Chemistry. 2006;**17**(5):1109-1115

[43] Patri AK, Myc A, Beals J, Thomas TP, Bander NH, Baker JR. Synthesis and in vitro testing of J591 antibody-dendrimer conjugates for targeted prostate cancer therapy. Bioconjugate Chemistry. 2004;**15**(6):1174-1181

[44] Thomas TP et al. In vitro targeting of synthesized antibody-conjucated dendrimer nanoparticles. Biomacromolecules. 2004;**5**(6):2269-2274

[45] Wu G. Targeted delivery of methotrexate to epidermal growth factor receptor-positive brain tumors by means of cetuximab (IMC-C225) dendrimer bioconjugates. Molecular Cancer Therapeutics. 2006;**5**(1):52-59

[46] Malik N et al. Dendrimers: Relationship between structure and biocompatibility in vitro, and preliminary studies on the biodistribution of125I-labelled polyamidoamine dendrimers in vivo. Journal of Controlled Release. 2000;**65**(1-2):133-148

[47] Duncan R, Izzo L. Dendrimer biocompatibility and toxicity. Advanced Drug Delivery Reviews. 2005;**57**(15):2215-2237

[48] Franiak-Pietryga I et al. Dendrimer-based nanoparticles for potential personalized therapy in chronic lymphocytic leukemia: Targeting the BCR-signaling pathway. International Journal of Biological Macromolecules. 2016;**88**:156-161

[49] Franiak-Pietryga I et al. Blockage of Wnt/β-catenin signaling by nanoparticles reduces survival and proliferation of CLL cells in vitro—Preliminary study. Macromolecular Bioscience. 2017;**17**(11):1-9. DOI: 10.1002/mabi.201700130

[50] Franiak-Pietryga I et al. The influence of maltotriose-modified poly(propylene imine) dendrimers on the chronic lymphocytic leukemia cells in vitro: Dense shell G4 PPI. Molecular Pharmaceutics. 2013;**10**(6):2490-2501

[51] Franiak-Pietryga I et al. PPI-G4 glycodendrimers upregulate TRAIL-induced apoptosis in chronic lymphocytic leukemia cells. Macromolecular Bioscience. 2017;**17**(5):1-8. DOI: 10.1002/mabi.201600169

[52] Klajnert B et al. EPR study of the interactions between dendrimers and peptides involved in Alzheimer's and prion diseases. Macromolecular Bioscience. 2007;**7**(8):1065-1074

[53] Klajnert B, Cladera J, Bryszewska M. Molecular interactions of dendrimers with amyloid peptides: pH dependence. Biomacromolecules. 2006;**7**(7):2186-2191

[54] Mignani S et al. Can dendrimer based nanoparticles fight neurodegenerative diseases? Current situation versus other established approaches. Progress in Polymer Science. 2017;**64**:23-51

[55] Wasiak T et al. Phosphorus dendrimers affect Alzheimer's (AB 1-28) peptide and MAP-tau protein aggregation. Molecular Pharmaceutics. 2012;**9**(3):458-469

[56] Neelov IM et al. Molecular properties of lysine dendrimers and their interactions with Aβ-peptides and neuronal cells. Current Medicinal Chemistry. 2013;**20**(1):134-143

[57] Van Der Poll DG et al. Design, synthesis, and biological evaluation of a robust, biodegradable dendrimer. Bioconjugate Chemistry. 2010;**21**(4):764-773

[58] Lim J et al. The role of the size and number of polyethylene glycol chains in the biodistribution and tumor localization of triazine dendrimers. Molecular Pharmaceutics. 2008;**5**(4):540-547

[59] Canton I, Battaglia G. Endocytosis at the nanoscale. Chemical Society Reviews. 2012;**41**(7): 2718

[60] Doherty GJ, McMahon HT. Mechanisms of endocytosis. Annual Review of Biochemistry. 2009;**78**(1):857-902

[61] Tayo L. Stimuli-responsive nanocarriers for intracellular delivery. Biophysical Reviews. 2017;**9**(6):931-940

[62] Wolff J et al. Direct gene transfer into mouse muscle in vivo. Science (80-). 1990;**247**:1465-1468

[63] Kaczmarek JC, Kowalski PS, Anderson DG. Advanced in the delivery of RNA therapeutics: From concept to clinical reality. Genome Medicine. 2017;**9**:60

[64] Sahay G, Alakhova DY, Kabanov AV. Endocytosis of nanomedicines. Journal of Controlled Release. 2010;**145**(3):182-195

[65] Pack DW, Hoffman AS, Pun S, Stayton PS. Design and development of polymers for gene delivery. Nature Reviews Drug Discovery. 2005;**4**(7):581-593

[66] Soutschek J et al. Therapeutic silencing of an endogenous gene by systemic administration of modified siRNAs. Nature. 2004;**432**(7014):173-178

[67] Morrissey DV et al. Potent and persistent in vivo anti-HBV activity of chemically modified siRNAs. Nature Biotechnology. 2005;**23**(8):1002-1007

[68] Wittrup A, Lieberman J. Knocking down disease: A progress report on siRNA therapeutics. Nature Reviews Genetics. 2015;**16**(9):543-552

[69] Bramsen JB et al. A large-scale chemical modification screen identifies design rules to generate siRNAs with high activity, high stability and low toxicity. Nucleic Acids Research. 2009;**37**(9):2867-2881

[70] Chiu Y-L. siRNA function in RNAi: A chemical modification analysis. RNA. 2003;**9**(9): 1034-1048

[71] Prakash TP et al. Positional effect of chemical modifications on short interference RNA activity in mammalian cells. Journal of Medicinal Chemistry. 2005;**48**(13):4247-4253

[72] Li B, Luo X, Dong Y. Effects of chemically modified messenger RNA on protein expression. Bioconjugate Chemistry. 2016;**27**(3):849-853

[73] Owczarzy R, You Y, Groth CL, Tataurov AV. Stability and mismatch discrimination of locked nucleic acid-DNA duplexes. Biochemistry. 2011;**50**(43):9352-9367

[74] Lee TJ et al. RNA nanoparticle-based targeted therapy for glioblastoma through inhibition of oncogenic miR-21. Molecular Therapy. 2017;**25**(7):1544-1555

[75] "ClinicalTrials.gov. NCT01676259: A phase II study of siG12D LODER in combination with chemotherapy in patients with unresectable locally advanced pancreatic cancer." [Online]. Available: https://clinicaltrials.gov/ct2/show/NCT01676259 [Accessed: 06-Mar-2017]

[76] Golan T et al. RNAi therapy targeting KRAS in combination with chemotherapy for locally advanced pancreatic cancer patients. Oncotarget. 2015;**6**(27):24560-24570

[77] Liang XH, Shen W, Sun H, Migawa MT, Vickers TA, Crooke ST. Translation efficiency of mRNAs is increased by antisense oligonucleotides targeting upstream open reading frames. Nature Biotechnology. 2016;**34**(8):875-880

[78] Askari FK, McDonnell WM. Antisense-oligonucleotide therapy. The New England Journal of Medicine. 1996;**334**(5):316-318

[79] Agrawal S. Importance of nucleotide sequence and chemical modifications of antisense oligonucleotides. Biochimica et Biophysica Acta - Gene Structure and Expression. 1999; **1489**(1):53-67

[80] Crooke ST, Wang S, Vickers TA, Shen W, Liang XH. Cellular uptake and trafficking of antisense oligonucleotides. Nature Biotechnology. 2017;**35**(3):230-237

[81] Christopher A, Kaur R, Kaur G, Kaur A, Gupta V, Bansal P. MicroRNA therapeutics: Discovering novel targets and developing specific therapy. Perspectives in Clinical Res earch. 2016;**7**(2):68

[82] Pereira DM, Rodrigues PM, Borralho PM, Rodrigues CMP. Delivering the promise of miRNA cancer therapeutics. Drug Discovery Today. 2013;**18**(5-6):282-289

[83] Beg MS et al. Abstract CT327: Multicenter phase I study of MRX34, a first-in-class microRNA miR-34 mimic liposomal injection. Cancer Research. 2014;**74**(19 Supplement):CT327-CT327

[84] Dowdy SF. Overcoming cellular barriers for RNA therapeutics. Nature Biotechnology. 2017;**35**(3):222-229

[85] Sullenger B, Nair S. From the RNA world to the clinic. Science (80-). 2016;**352**:1417-1420

[86] Oberli MA et al. Lipid nanoparticle assisted mRNA delivery for potent cancer immunotherapy. Nano Letters. 2017;**17**(3):1326-1335

[87] Kranz LM et al. Systemic RNA delivery to dendritic cells exploits antiviral defence for cancer immunotherapy. Nature. 2016;**534**(7607):396-401

[88] Doudna JA, Charpentier E. The new frontier of genome engineering with CRISPR-Cas9. Science. 2014;**346**(6213):1258096

[89] Rouet P, Smih F, Jasin M. Introduction of double-strand breaks into the genome of mouse cells by expression of a rare-cutting endonuclease. Molecular and Cellular Biology. 1994; **14**(12):8096-8106

[90] Yin H et al. Therapeutic genome editing by combined viral and non-viral delivery of CRISPR system components in vivo. Nature Biotechnology. 2016;**34**(3):328-333

[91] Ambesajir A, Kaushik A, Kaushik JJ, Petros ST. RNA interference: A futuristic tool and its therapeutic applications. Saudi Journal of Biological Sciences. 2012;**19**(4):395-403

[92] Angart P, Vocelle D, Chan C, Patrick Walton S. Design of siRNA therapeutics from the molecular scale. Pharmaceuticals. 2013;**6**(4):440-468

[93] Shcharbin D et al. How to study dendrimers and dendriplexes III. Biodistribution, pharmacokinetics and toxicity in vivo. Journal of Controlled Release. May 2014;**181**:40-52

[94] Shcharbin D, Pedziwiatr E, Blasiak J, Bryszewska M. How to study dendriplexes II: Transfection and cytotoxicity. Journal of Controlled Release. Jan. 2010;**141**(2):110-127

[95] Shcharbin D, Pedziwiatr E, Bryszewska M. How to study dendriplexes I: Characterization. Journal of Controlled Release. May 2009;**135**(3):186-197

[96] Wu J, Huang W, He Z. Dendrimers as carriers for siRNA delivery and gene silencing: A review. Scientific World Journal. Oct. 2013;**2013**:630654

[97] Lalwani S, Chouai A, Perez LM, Santiago V, Shaunak S, Simanek EE. Mimicking PAMAM dendrimers with amphoteric, hybrid triazine dendrimers: A comparison of dispersity and stability. Macromolecules. Sep. 2009;**42**(17):6723-6732

[98] Esfand R, Tomalia DA. Poly(amidoamine) (PAMAM) dendrimers: From biomimicry to drug delivery and biomedical applications. Drug Discovery Today. Apr. 2001;**6**(8): 427-436

[99] Kukowska-Latallo JF, Bielinska AU, Johnson J, Spindler R, Tomalia DA, Baker JR. Efficient transfer of genetic material into mammalian cells using starburst polyamidoamine dendrimers. Proceedings of the National Academy of Sciences of the United States of America. May 1996;**93**(10):4897-4902

[100] Jensen LB et al. Elucidating the molecular mechanism of PAMAM–siRNA dendriplex self-assembly: Effect of dendrimer charge density. International Journal of Pharmaceutics. Sep. 2011;**416**(2):410-418

[101] Mecke A et al. Direct observation of lipid bilayer disruption by poly(amidoamine) dendrimers. Chemistry and Physics of Lipids. 2004;**132**(1):3-14

[102] Fischer D, Li Y, Ahlemeyer B, Krieglstein J, Kissel T. In vitro cytotoxicity testing of polycations: Influence of polymer structure on cell viability and hemolysis. Biomaterials. 2003;**24**(7):1121-1131

[103] Palmerston Mendes L, Pan J, Torchilin V. Dendrimers as nanocarriers for nucleic acid and drug delivery in cancer therapy. Molecules. 2017;**22**(9):1401

[104] Reyes-Reveles J et al. mPEG-PAMAM-G4 nucleic acid nanocomplexes: Enhanced stability, RNase protection, and activity of splice switching oligomer and poly I:C RNA. Biomacromolecules. 2013;**14**(11):4108-4115

[105] Finlay J, Roberts CM, Lowe G, Loeza J, Rossi JJ, Glackin CA. RNA-based TWIST1 inhibition via dendrimer complex to reduce breast cancer cell metastasis. BioMed Research International. 2015;**2015**:1-12

[106] Roberts CM et al. Nanoparticle delivery of siRNA against TWIST to reduce drug resistance and tumor growth in ovarian cancer models. Nanomedicine: Nanotechnology, B iology, and Medicine. 2017;**13**(3):965-976

[107] Jiang X et al. Eradication of acute myeloid leukemia with FLT3 ligand-targeted miR-150 nanoparticles. Cancer Research. 2016;**76**(15):4470-4480

[108] Liu X et al. PAMAM dendrimers mediate siRNA delivery to target Hsp27 and produce potent antiproliferative effects on prostate cancer cells. ChemMedChem. 2009;**4**(8): 1302-1310

[109] Liu X et al. Efficient delivery of sticky siRNA and potent gene silencing in a prostate cancer model using a generation 5 triethanolamine-core PAMAM dendrimer. Molecular Pharmaceutics. 2012;**9**(3):470-481

[110] Liu X et al. Promoting siRNA delivery via enhanced cellular uptake using an arginine-decorated amphiphilic dendrimer. Nanoscale. 2015;**7**(9):3867-3875

[111] Liu C, Liu X, Rocchi P, Qu F, Iovanna JL, Peng L. Arginine-terminated generation 4 PAMAM dendrimer as an effective nanovector for functional siRNA delivery in vitro and in vivo. Bioconjugate Chemistry. 2014;**25**(3):521-532

[112] Xu L, Yeudall WA, Yang H. Folic acid-decorated polyamidoamine dendrimer exhibits high tumor uptake and sustained highly localized retention in solid tumors: Its utility for local siRNA delivery. Acta Biomaterialia. 2017;**57**:251-261

[113] Fan W et al. Thioaptamer-conjugated CD44-targeted delivery system for the treatment of breast cancer in vitro and in vivo. Journal of Drug Targeting. 2016;**24**(4):359-371

[114] Kang L, Gao Z, Huang W, Jin M, Wang Q. Nanocarrier-mediated co-delivery of chemotherapeutic drugs and gene agents for cancer treatment. Acta Pharmaceutica Sinica B. 2015;**5**(3):169-175

[115] Ren Y et al. Sequential co-delivery of miR-21 inhibitor followed by burst release doxorubicin using NIR-responsive hollow gold nanoparticle to enhance anticancer efficacy. Journal of Controlled Release. 2016;**228**:74-86

[116] Zheng W et al. Multifunctional polyamidoamine-modified selenium nanoparticles dual-delivering siRNA and cisplatin to A549/DDP cells for reversal multidrug resistance. Acta Biomaterialia. 2015;**11**:368-380

[117] Rajasekaran D et al. Combination of nanoparticle-delivered siRNA for astrocyte elevated gene-1 (AEG-1) and all- trans retinoic acid (ATRA): An effective therapeutic strategy for hepatocellular carcinoma (HCC). Bioconjugate Chemistry. 2015;**26**(8):1651-1661

[118] Liu J et al. In vitro studies of phospholipid-modified PAMAM-siMDR1 complexes for the reversal of multidrug resistance in human breast cancer cells. International Journal of Pharmaceutics. 2017;**530**(1-2):291-299

[119] Gu Y et al. A polyamidoamine dendrimer functionalized graphene oxide for DOX and MMP-9 shRNA plasmid co-delivery. Materials Science and Engineering C 2017;**70**(Pt 1): 572-585

[120] Zarbin MA, Leary JF, Montemagno C, Ritch R, Humayun MS. Nanomedicine in ophthalmology. Clinicalgate. In: Retina. 5th ed. Vol. 1. 2012. pp. 689-715

[121] Kang SJ, Durairaj C, Kompella UB, O'Brien JM, Grossniklaus HE. Subconjunctival nanoparticle carboplatin in the treatment of murine retinoblastoma. Archives of Ophthalmology. 2009;**127**(8):1043-1047

[122] de Brabander-van den Berg EMM, Meijer EW. Poly(propylene imine) dendrimers: Large-scale synthesis by hetereogeneously catalyzed hydrogenations. Angewandte Chemie International Edition. 1993;**32**(9):1308-1311

[123] Pedziwiatr-Werbicka E, Ferenc M, Zaborski M, Gabara B, Klajnert B, Bryszewska M. Characterization of complexes formed by polypropylene imine dendrimers and anti-HIV oligonucleotides. Colloids and Surfaces. B, Biointerfaces. 2011;**83**(2):360-366

[124] Hashemi M et al. Preparation of effective and safe gene carriers by grafting alkyl chains to generation 5 polypropyleneimine. AAPS PharmSciTech. 2015;**16**(5):1002-1012

[125] Taratula O et al. Surface-engineered targeted PPI dendrimer for efficient intracellular and intratumoral siRNA delivery. Journal of Controlled Release. 2009;**140**(3):284-293

[126] Chen AM et al. Labile catalytic packaging of DNA/siRNA: Control of gold nanoparticles 'out' of DNA/siRNA complexes. ACS Nano. 2010;**4**(7):3679-3688

[127] Taratula O, Garbuzenko O, Savla R, Wang YA, He H, Minko T. Multifunctional nanomedicine platform for cancer specific delivery of siRNA by superparamagnetic iron oxide nanoparticles-dendrimer complexes. Current Drug Delivery. 2011;**8**(1):59-69

[128] Shah V, Taratula O, Garbuzenko OB, Taratula OR, Rodriguez-Rodriguez L, Minko T. Targeted nanomedicine for suppression of CD44 and simultaneous cell death induction in ovarian cancer: An optimal delivery of siRNA and anticancer drug. Clinical Cancer Research. 2013;**19**(22):6193-6204

[129] Gu J, Fang X, Hao J, Sha X. Reversal of P-glycoprotein-mediated multidrug resistance by CD44 antibody-targeted nanocomplexes for short hairpin RNA-encoding plasmid DNA delivery. Biomaterials. 2015;**45**:99-114

[130] Szulc A et al. Maltose modified poly(propylene imine) dendrimers as potential carriers of nucleoside analog 5′-triphosphates. International Journal of Pharmaceutics. 2015; **495**(2):940-947

[131] Szulc A, Pulaski L, Appelhans D, Voit B, Klajnert-Maculewicz B. Sugar-modified poly (propylene imine) dendrimers as drug delivery agents for cytarabine to overcome drug resistance. International Journal of Pharmaceutics. 2016;**513**(1-2):572-583

[132] Jatczak-Pawlik I et al. Sugar-modified poly(propylene imine) dendrimers stimulate the NF-κB pathway in a myeloid cell line. Pharmaceutical Research. 2017;**34**(1):136-147

[133] Gajbhiye V, Jain NK. The treatment of glioblastoma xenografts by surfactant conjugated dendritic nanoconjugates. Biomaterials. 2011;**32**(26):6213-6225

[134] Fang J-Y, Al-Suwayeh SA. Nanoparticles as delivery carriers for anticancer prodrugs. Expert Opinion on Drug Delivery. 2012;**9**(6):657-669

[135] Barenholz Y. Doxil®—The first FDA-approved nano-drug: Lessons learned. Journal of Controlled Release. 2012;**160**(2):117-134

[136] Okuda T, Kawakami S, Maeie T, Niidome T, Yamashita F, Hashida M. Biodistribution characteristics of amino acid dendrimers and their PEGylated derivatives after intravenous administration. Journal of Controlled Release. 2006;**114**(1):69-77

[137] Kawano T, Okuda T, Aoyagi H, Niidome T. Long circulation of intravenously administered plasmid DNA delivered with dendritic poly(L-lysine) in the blood flow. Journal of Controlled Release. 2004;**99**(2):329-337

[138] Yamagata M, Kawano T, Shiba K, Mori T, Katayama Y, Niidome T. Structural advantage of dendritic poly(L-lysine) for gene delivery into cells. Bioorganic & Medicinal Chemistry. 2007;**15**(1):526-532

[139] Ohsaki M, Okuda T, Wada A, Hirayama T, Niidome T, Aoyagi H. In vitro gene transfection using dendritic poly(L-lysine). Bioconjugate Chemistry;**13**(3):510-517

[140] Janiszewska J, Posadas I, Játiva P, Bugaj-Zarebska M, Urbanczyk-Lipkowska Z, Ceña V. Second generation amphiphilic poly-lysine dendrons inhibit glioblastoma cell proliferation without toxicity for neurons or astrocytes. PLoS One. 2016;**11**(11):e0165704

[141] Kaneshiro TL, Lu Z-R. Targeted intracellular codelivery of chemotherapeutics and nucleic acid with a well-defined dendrimer-based nanoglobular carrier. Biomaterials. 2009; **30**(29):5660-5666

Chapter 3

Lysine Dendrimers and Their Complexes with Therapeutic and Amyloid Peptides: Computer Simulation

Elena Popova, Dilorom Khamidova, Igor Neelov and Faizali Komilov

Additional information is available at the end of the chapter

http://dx.doi.org/10.5772/intechopen.71052

Abstract

Lysine dendrimers consist of natural lysine amino acid residues. Due to this reason, they are usually not as toxic as other dendrimers. Lysine dendrimers are often used in drug and gene delivery. These dendrimers penetrate blood-brain barrier and thus could be used for the delivery of drugs and other substances, for example, bioactive peptides to brain or elimination of disease-related peptides out of the brain. To do it, dendrimers should form complex with these peptides. In the present chapter, we describe computer simulation of the interaction of lysine dendrimer of the second generation with three different peptides and check does it form complexes with them. Two of these peptides (Semax and Epithalon) are nootropic peptides and third is the fragment of amyloid peptide, which forms amyloid fibrils and plaques in Alzheimer's disease. Our simulation demonstrates that the lysine dendrimers form complexes with these therapeutics peptides. Thus, we demonstrated that lysine dendrimer is a good candidate for the delivery of therapeutic peptides. We also have shown that lysine dendrimer destroys existing stacks of amyloid peptides and forms a stable complex with them. Thus, it looks that it could be used in future for the treatment of Alzheimer's diseases.

Keywords: lysine dendrimer, peptide delivery system, molecular dynamics, Semax, Epithalon

1. Introduction

Only a few of the peptide drugs reach their targets. Most of them accumulate in nontargeted organs and produce different side-effects. Drug delivery systems help to overcome these

problems and increase safety and efficacy of therapeutic peptides [1]. Traditional drug delivery systems include tablets, injections, suspensions, ointments, creams, liquids, and aerosols. Polymers are also used for this goal and protect drugs from biological degradation during delivery [2].

Dendrimers were synthesized in seventieth to eightieth of the last century [3]. They have regular branched (star-like) structure. Dendrimers have well-defined size and constant spherical shape. Many dendrimers have a large number of charged terminal groups available for functionalization [4, 5]. Dendrimers could be used for drug and gene delivery, as a branched core for multiple antigen peptides (MAPs) as well as antibacterial and antiviral agents. Also, they were proposed as potent anti-amyloid agents for the treatment of different neurodegenerative diseases (Alzheimer's, Parkinson's, etc.).

In the present chapter, we describe our results of simulation of the interaction of the second generation lysine dendrimer (**Figure 1**) with three types of peptides: Semax, Epithalon, and the fragment of amyloid peptide.

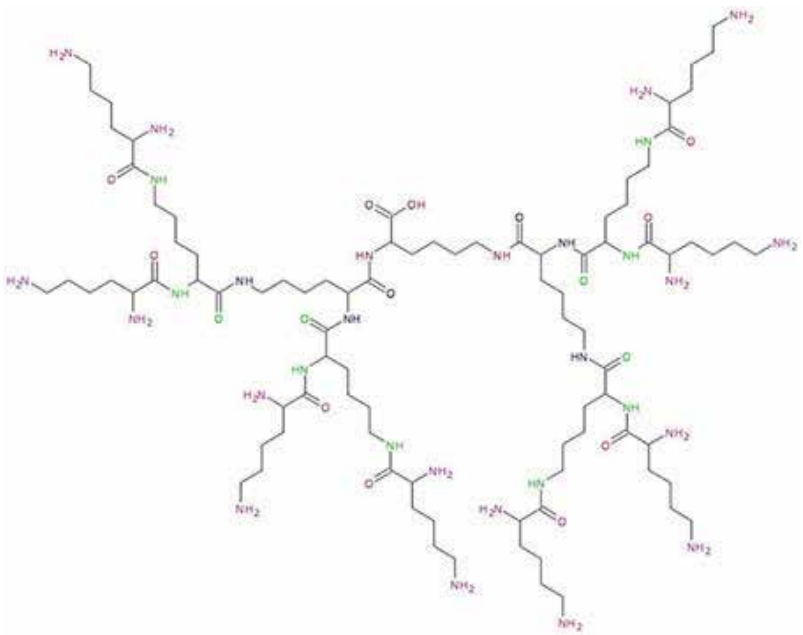

Figure 1. Structure of lysine dendrimer of the second generation.

2. Molecular dynamics simulation

Molecular dynamics simulation (MDS) is widely used for modeling of different polymer and biopolymer systems. In this approach, all atoms or groups of atoms in molecules in a system are represented by spherical beads. Chemical bonds between atoms are represented by

springs or rigid bonds. The dynamics of such mechanical model of real molecular systems is described by classical Newton equations of motion and the system of these equations for all beads in the system is solved numerically.

$$F_i = m_i \frac{d^2 r_i(t)}{dt^2} \tag{1}$$

where $r_i(t) = (x_i(t), y_i(t), z_i(t))$—the position vector of the ith particle (or its coordinates $x_i(t)$, $y_i(t)$, $z_i(t)$), F_i—the force acting on the ith particle at time t, and m_i—mass of the particle.

This method was applied for the first time for the study of simple 2D model of hard disks, which represents two-dimensional analog of a monoatomic gases [6]. Later, it was extended for simulation of liquids [7, 8] and coarse-grained model of linear polymer chains [9] and n-alkanes [10]. During the last 30 years, MDS was applied for the study of many molecular systems of different structure and composition. The potential energy in MDS usually includes the energy of valence bonds, the energy of valence angles, and dihedral angles as well as van der Waals energy and electrostatic energies. In the present study, the variant of molecular dynamics simulation approach realized in the framework of GROMACS 4.5.6 software package [11] and one of the most modern force fields (AMBER_99SB-ildn) was used for the representation of potential energy [12] of our system. The force field has the following form:

$$\begin{aligned} U(r_1, \ldots, r_N) = {} & \sum \frac{a_i}{2}(l_i - l_{i0})^2 + \sum \frac{b_i}{2}(\theta_i - \theta_{i0})^2 + \sum \frac{c_i}{2}[1 + \cos(n\omega_i - \gamma_i)] \\ & + \sum 4\varepsilon_{ij}\left[\left(\frac{\sigma_{ij}}{r_{il}}\right)^{12} - \left(\frac{\sigma_{ij}}{r_{il}}\right)^{6}\right] + \sum k \frac{q_i q_j}{r_{ij}} \end{aligned} \tag{2}$$

where l_i—valence bond lengths, θ_i—valence angles values, l_{i0} and θ_{i0}—equilibrium values of them, and a_i and b_i—force constants, correspondingly, $\varepsilon_{ij}$and σ_{ij}—values of Van der Waals parameters of Lenard-Jones 6–12 potential, q_i—partial charges, c_i, γ_i, and n—numerical coefficients in dihedral potential while summation is done through all i-beads or pairs of ith and jth beads in the system consisting of N beads.

The more detailed description of MDS method used in the present work including simulation of linear and branched polyelectrolytes as well as dendrimers has been described in [13–33]. All simulations were performed at normal conditions (temperature 300 K and pressure 1 atm).

The size of dendrimer and complexes at time t was evaluated by the mean square radius of gyration $R_g(t)$ which is defined from:

$$R_g^2(t) = \frac{1}{M} \times \left[\sum_{i=1}^{N} m_i \times |r_i(t) - R|^2\right], \tag{3}$$

where R—the center of mass of subsystem, r_i and m_i—coordinates and masses of i-atom correspondingly, N—the total number of atoms in subsystem, and M—the total mass of dendrimer. This function was calculated using *g_gyrate* function of GROMACS software.

Radial distribution of density $p(r)$ of atoms in dendrimer and complexes as well as distribution of ion pairs were calculated using g_rdf function of the GROMACS package.

To calculate the coefficient of translational mobility of dendrimer and complexes, the time dependence of the mean square displacements of the centers of inertia (MSD) of corresponding subsystem was calculated. MSD was calculated using g_msd function of GROMACS.

$$\left\langle \sum_i \Delta r^2(t + k\Delta t) \right\rangle = \left\langle (r(t + k\Delta t) - r(t))^2 \right\rangle = 6Dt \tag{4}$$

3. Semax peptide

Therapeutic Semax peptide with primary sequence Met-Glu-His-Phe-Pro-Gly-Pro [34] was selected in present chapter as the first peptide for study. Semax is one of the few synthetic regulatory peptides that, after all the fundamental research, have found its application in therapy as a nootropic and neuroprotective agent [35]. However, its penetration into the brain and mechanisms of action remain insufficiently studied. In addition, the peptide is rapidly destroyed by blood enzymes [36].

To check if lysine dendrimer forms a complex with Semax peptides, we prepared system containing lysine dendrimer of the second generation, 16 Semax peptides, and counterions in water and studied the time evolution of this system.

Snapshots of this system are shown in **Figure 2** at different time moments during MD simulation (water molecules are not shown for clarity). It is easy to see that at the beginning of the time trajectory (**Figure 2a**), all peptide molecules are located far from the dendrimer. After 20 ns (**Figure 2b**), some peptide molecules already sit on the surface of the dendrimer, and at the end of the simulation (**Figure 2c**), most of the peptide molecules are adsorbed on its surface.

The time dependence of gyration radius $R_g(t)$ (**Figure 3a**) shows that at the beginning of simulation, the size of subsystem consisting of lysine dendrimer and Semax peptides is big because peptides are located far from dendrimer. During first 30–40 ns, the value of $R_g(t)$ decreases

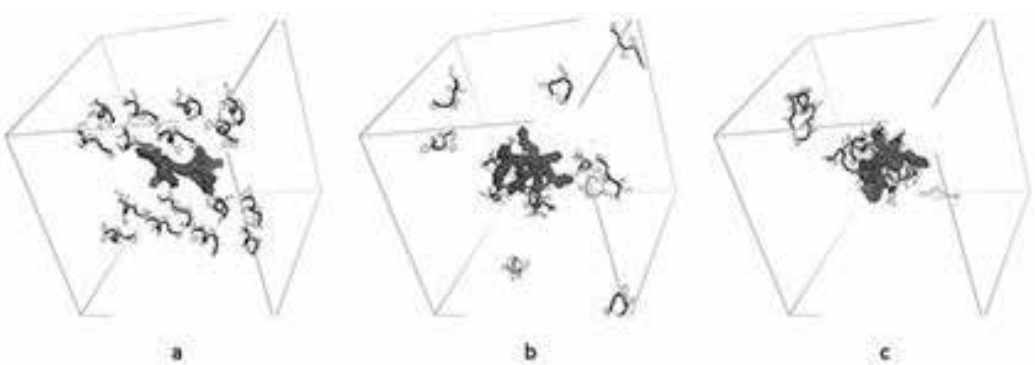

Figure 2. Snapshots of the dendrimer and Semax peptides at different time moments: $t = 0$ (a), $t = 20$ ns (b), $t = 160$ ns (c).

because peptides begin to adsorb on dendrimer surface. Stable dendrimer-peptides complex forms within 30–40 ns and after this time the size of complex fluctuates but its average value does not change with time.

Another quantity that can characterize complex formation is the hydrogen bond number (N) between dendrimer and peptides (see **Figure 3b**). In the beginning of simulation, there are no contacts between dendrimer and peptides and hydrogen bond number between them equals zero. The increase of this function with time during first 30–40 ns demonstrates that the number of contacts between dendrimer and peptides increases due to complex formation and after this time it fluctuates but its average value almost does not change with time. Thus, from **Figure 3b**, we can conclude that the system reaches equilibrium (plateau) state after 30–40 ns. This result correlates well with results for the gyration radius in **Figure 3a**.

We also calculated different equilibrium characteristics (see **Table 1** and **Figure 4**) of complex averaged through equilibrium part of our simulation ($t > 40$ ns). In particular, we calculated the mean square radius of gyration R_g of our dendrimer and complex (consisting of G2 and 16 Semax peptides) and obtained that the value of R_g of the complex is nearly twice larger than the size of dendrimer itself (see **Table 1**). It is quite natural because the molecular weight of the complexes also increases nearly twice in comparison with the molecular weight of the dendrimer. The shape of dendrimer and complex can be characterized by main components of the tensor of inertia R_g^{11}, R_g^{22}, R_g^{33}, (see **Table 1**). It can be roughly estimated by ratio R_g^{33}/R_g^{11} of largest and smallest eigenvalues of inertia tensor of the corresponding subsystem. The ratio is equal to 1.68 for dendrimer and 1.45 for dendrimer with peptides. Thus, we obtained that complex has more spherical shape than dendrimer.

The radial density distribution functions are shown in **Figure 4a**. It demonstrates that atoms of dendrimer (curve 2, **Figure 4a**) are located mainly in the center (i.e. at small distances r from the center of mass), whereas peptides (curve 1, **Figure 4**) are mainly on the surface of the

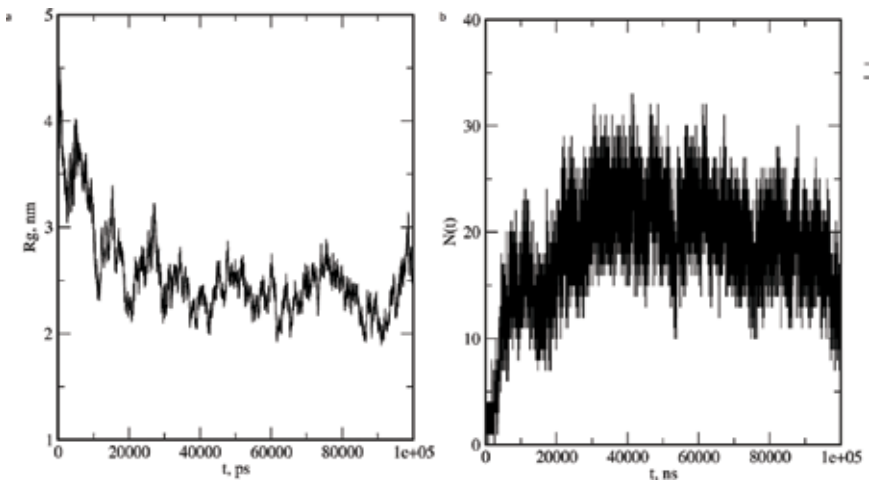

Figure 3. Time dependence of gyration radius of subsystem consisting of dendrimer and peptides (a) and time dependence of number of hydrogen bonds (N) between dendrimer and peptides during the complex formation (b).

System	R_g^{11} (nm)	R_g^{22} (nm)	R_g^{33} (nm)	R_g (nm)
Dendrimer (G2)	0.64	0.97	1.08	1.12
G2 + 16 Semax	1.36	1.88	1.97	2.30

Table 1. Eigenvalues R_g^{11}, R_g^{22}, R_g^{33} of tensor of inertia in dendrimer and Semax peptide complex.

complex. At the same time, some fraction of peptides could slightly penetrate into dendrimer but not to its inner part.

The average number of hydrogen bonds between peptides and dendrimers in the equilibrium state (which was determined from second part (t > 40 ns) of **Figure 3b**) shows how tightly peptides are connected with dendrimer. From our calculations, it follows that average hydrogen bonds number in equilibrium state for the complex is close to 19. It means that each peptide is connected in average by one hydrogen bond with dendrimer. We could also check how the number of hydrogen bonds in the equilibrium state fluctuates. It is easy to see from **Figure 3b** that fluctuations in hydrogen bond number between dendrimer and peptides in the complex are in the range of 8–30. It means that the average number of hydrogen bonds with dendrimer per peptide fluctuates between 0 and 2.

Another equilibrium characteristic of interaction between dendrimer and peptides in the complex is the distribution of ion pair numbers between their oppositely charged groups. **Figure 4b** shows the dependence of ion pair number on the distance between dendrimer charges and peptides charges (curve 1) in the complex as well as between dendrimer charges and counterions (curve 2). It is seen, that there is a sharp peak, corresponding to the direct contact

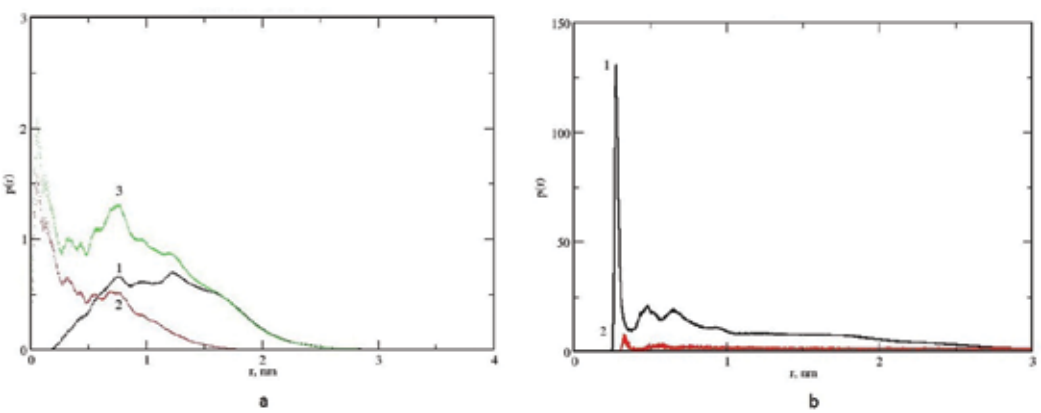

Figure 4. Radial distribution functions $p(r)$: density distribution of the atoms in the complex: 1—peptide atoms, 2—dendrimer atoms, 3—all atoms of the complex (a) and distribution function of ion pair numbers between opposite charges: 1—between NH_3^+ groups of the dendrimer and COO^- groups of peptides; 2—between NH_3^+ groups of the dendrimer and Cl^- ions (b).

between positively charged groups (NH_3^+) of dendrimer and negatively charged groups (COO^-) of the glutamic acid in peptides (curve 1) and peak between dendrimer charges and counterions is less pronounced (curve 2). It means that dendrimer and peptides are strongly connected by this ion pairs with each other, whereas dendrimer charges and counterions contacts are not so strong.

To determine diffusion coefficient of the dendrimer-peptide complex, we calculated its mean square displacement (MSD) as a function of time. It was obtained, that the time dependence of MSD function is close to linear in double logarithm coordinates (not shown). It means that the translational motion of complex is the diffusion-like motion. The diffusion coefficient of the complex was determined from the slope of the time dependence of MSD and it is equal to $(0.12 \pm 0.03) \times 10^5$ sm^2/s.

The results of simulation of the system consisting of lysine dendrimer of the second generation and 16 Semax peptides confirm that lysine dendrimer quickly forms complex with these peptides and thus lysine dendrimers could be a good candidate for using as a vehicle for delivery of Semax peptides.

4. Epithalon peptides

Therapeutic peptide Epithalon was selected in present chapter as the second model peptide. Biologically active regulatory peptides are promising and effective medicines in a wide range of diseases treatment. Such peptides are effective at low concentrations, selective, multifunctional, and completely biodegradable and do not produce side-effects [37]. Epithalon is a regulatory tetrapeptide with amino acid sequence of alanine-glutamate-asparagine-glycine (AENG). It is synthesized as analogs of the epithalamine peptide preparation and isolated from the epiphysis of the animal brain [38].

One of the most important properties of this peptide is its ability to activate the telomerase enzyme in patients' body and to prolong human cells life. The most well-known pharmacological properties of Epithalon are the following:

1. Regulation of neuroendocrine system.
2. Increased sensitivity of hypothalamus to endogenous hormonal effects.
3. Normalization of gonadotropin hormones, uric acid, and cholesterol level.
4. Strengthening of the immune system.
5. Inhibition of spontaneous and induced carcinogenesis.
6. Improves rheological properties of blood and reduces formation of blood clots.

To check if lysine dendrimer could form the complex with Epithalon peptides, we prepared system consisting of lysine dendrimer of second generation, 16 Epithalon peptides, counterions, and water and studied time evolution of this system.

Snapshots of a system consisting of dendrimers, peptides, and ions during simulation are shown in **Figure 5** (water molecules are not shown for clarity). It is easy to see that at the beginning of process (**Figure 5a**) peptide molecules located far from dendrimer. After 20 ns (**Figure 5b**), some part of the peptide molecules are already sitting on the surface of the dendrimer, and in the end (**Figure 5c**) most of the peptide molecules adsorbed on its surface. This behavior is very similar to that for the system consisting of dendrimer and Semax peptides discussed above.

The time dependence of radius of gyration $R_g(t)$ describes the process of transition of the system to equilibrium state with the formation of a complex between dendrimer and Epithalon peptides (see **Figure 6a**). From **Figure 6a**, one can see that at the beginning of simulation the size of subsystem consisting of dendrimer and peptides is big because peptides are far from dendrimer. During first 20–30 ns, the value of $R_g(t)$ decreases because peptides begin to adsorb on dendrimer surface and after this time the average value of R_g practically does not change with time. It means that stable dendrimer-peptides complex forms within 20–30 ns.

Another quantity that can characterize complex formation is the hydrogen bond number $N(t)$ between dendrimer and peptides (see **Figure 6b**). In the beginning of simulation, there are no contacts between dendrimer and peptides and the number of hydrogen bonds between them equals zero. The increase of this function with time during first 20–30 ns demonstrates that the number of contacts between dendrimer and peptides increases due to complex formation. From **Figure 6b**, we can conclude that the complex goes into an equilibrium (plateau) state after 30–40 ns. This result correlates well with the results for the gyration radius $R_g(t)$ in **Figure 6a**.

After equilibration and complex formation, all characteristics of complex fluctuate but their average values practically do not change with time. We calculated different equilibrium characteristics of complex averaged through these equilibrium part of our simulation ($t > 30$ ns).

It was obtained that in equilibrium state the size R_g of the complex (G2 and 16 Epithalon peptides) is near 2.18 times larger than the size of dendrimer itself. The shape of the complex can

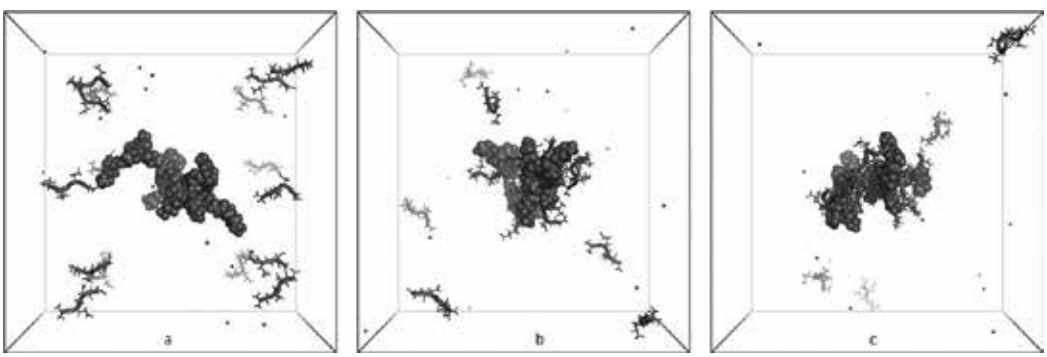

Figure 5. Time evolution of dendrimer and Epithalon peptides during complex formation: $t = 0$ (a), $t = 20$ ns (b), $t = 160$ ns (c).

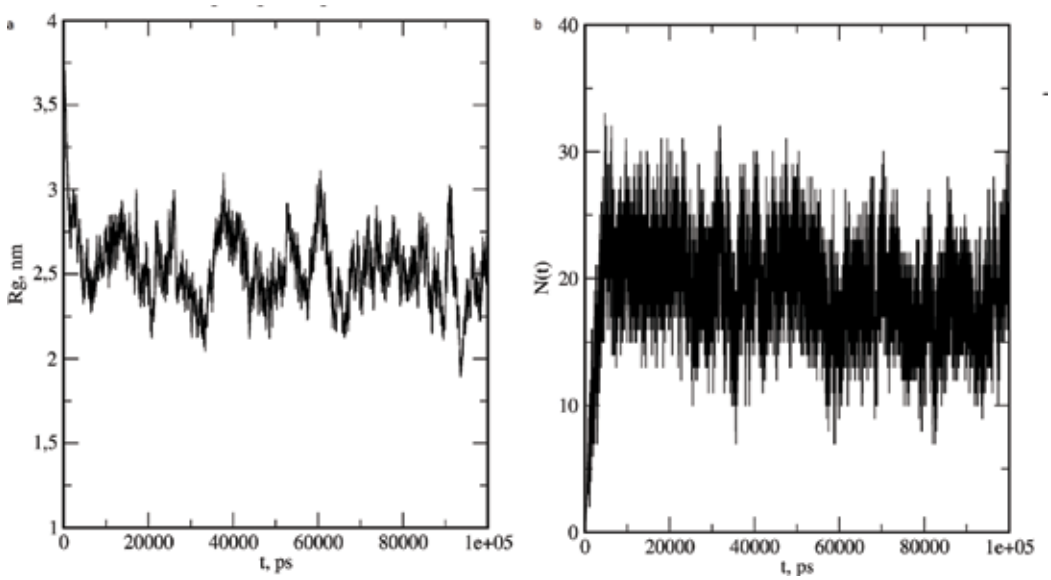

Figure 6. Time dependence of gyration radius $R_g(t)$ of subsystem consisting of the dendrimer and Epithalon peptides (a) and time dependence of number of hydrogen bonds (N) between dendrimer and Epithalon peptides during the complex formation (b).

System	R_g^{11} (nm)	R_g^{22} (nm)	R_g^{33} (nm)	R_g (nm)
Dendrimer (*G*2)	0,64	0,97	1,08	1,12
*G*2 + 16 Epithalon	1.76	2.08	2.26	2.44

Table 2. Eigenvalues R_g^{11}, R_g^{22}, R_g^{33} of tensor of inertia in dendrimer and Epithalon peptide complex.

be characterized by main components of the tensor of inertia R_g^{11}, R_g^{22}, R_g^{33} (see **Table 2**). In the simplest case, anisotropy can be characterized by R_g^{33}/R_g^{11}. For dendrimer, this ratio is equal to 1.69 and for the complex—1.28. Thus, the anisotropy of dendrimer with adsorbed Epithalon peptides is less than anisotropy of dendrimer itself as it was shown earlier for the complex of dendrimer with Semax peptides.

The equilibrium ($t > 30$ ns) radial density distribution functions $p(r)$ are shown in **Figure 7a**. It demonstrates that atoms of dendrimer (curve 2, **Figure 7a**) located in the center of the complex (i.e. at small distances r from the center of mass) and Epithalon peptides (curve 1, **Figure 7a**) located mainly on the surface of the complex. At the same time, some fraction of peptides could slightly penetrate into dendrimer but not to its inner part.

The average number of hydrogen bonds between dendrimer and Epithalon peptides in the equilibrium state (which was determined by averaging through $t > 30$ ns of **Figure 6b**) shows how tightly peptides are associated with dendrimer. From our calculations, it follows

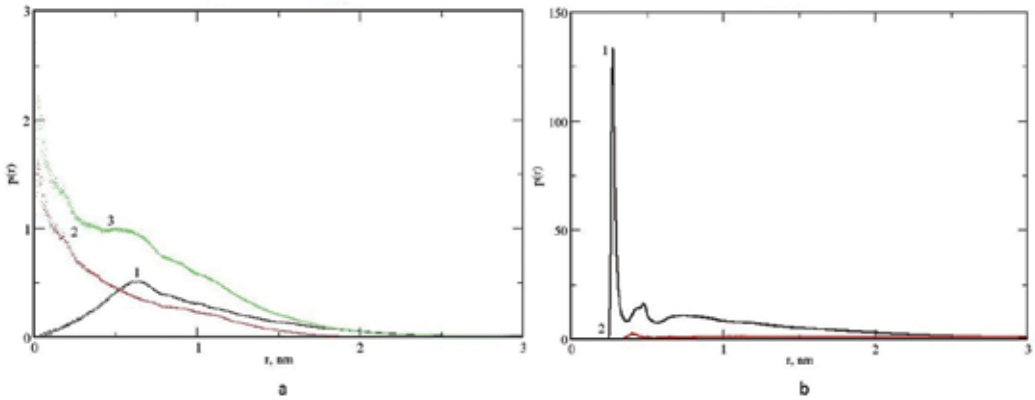

Figure 7. Radial distribution functions $p(r)$: density distribution of atoms in complex: 1—peptide atoms; 2—dendrimer atoms; 3—all atoms of the complex (a) and distribution function of ion pair numbers between opposite charges: 1—between NH_3^+ groups of the dendrimer and COO^- groups of peptides; 2—between NH_3^+ groups of the dendrimer and counterions (b).

that average hydrogen bond number in equilibrium state for the complex is close to 20. It means that each peptide is connected in average by one hydrogen bond with dendrimer. We also could check how the number of hydrogen bonds in the equilibrium state fluctuates. Fluctuations in hydrogen bonds number between dendrimer and peptides in the complex (see **Figure 6b**) are in the range of 9–28. It means that the average number of hydrogen bonds with dendrimer per peptide fluctuate between 0 and 2.

Figure 7b shows the dependence of ion pair numbers on the distance between dendrimer charges and Epithalon peptides charges in the complex as well as between dendrimer charges and counterions. It is seen that there is a sharp peak, corresponding to the direct contact between positively charged groups (NH_3^+) of dendrimer and negatively charged groups (COO^-) of peptides (curve 1) and significantly less sharp peak (curve 2) between dendrimer charges and counterions. It means that dendrimer and peptides are strongly connected at these points with each other, whereas dendrimer charges and counterions contacts are not so strong.

To determine diffusion coefficient of the dendrimer-peptide complex, we calculated its mean square displacement (MSD) as a function of time. It was obtained, that the time dependence of MSD function is close to linear in double logarithm coordinates (not shown). It means that the translational motion of complex is the diffusion-like motion. The diffusion coefficient of the complex was determined from the slope of the time dependence of MSD and is equal to $(0.21 \pm 0.03) \times 10^5$ sm^2/s.

The results of simulation of the system consisting of lysine dendrimer and Epithalon peptides confirm that the dendrimer could form complex with these peptides and thus lysine dendrimers could be a good candidate for using as a vehicle for delivery of Epithalon peptides.

http://dx.doi.org/10.5772/intechopen.71052

5. Amyloid fibrils

Fragment of amyloid peptide (LVFFAE) was selected in present chapter as a third model peptide. Many peptides and proteins have the ability to self-assembly into amyloid fibrils. Polypeptides that can form amyloid fibrils include molecules associated with neurodegenerative diseases [39, 40]. For example, in Alzheimer's disease, it is a β-amyloid peptide, in Parkinson's disease, it is a-synuclein protein, and in type 2 diabetes mellitus, it is an islet-amyloid peptide (IAPP, or amylin). The most studied are amyloid peptides that are also called amyloid-β peptides or Aβ-peptides.

It is known that synthetic protonated dendrimers (for example, polyamidoamine (PAMAM) dendrimers) can prevent aggregation of amyloid peptides [41]. It was also shown that they can destroy already existing amyloid fibrils in solution. Recently, it was experimentally shown that lysine dendrimers can also destroy amyloid fibrils [14].

To confirm the possibility of amyloid stack destruction by lysine dendrimer, we prepared system consisting of lysine dendrimer of second generation and 16 short amyloid peptides (LVFFAE) in water with counterions and studied the time evolution of this system.

From snapshots in **Figure 8**, one can see that at the beginning of the process (**Figure 8a**) all peptide molecules of the stack are located rather far from the dendrimer. After 20 ns (**Figure 8b**), a few of peptide molecules are already detached from the stack and adsorbed on the surface of dendrimer, and in the end of calculations after 160 ns (**Figure 8c**), most of the peptide molecules in the system adsorbed on its surface.

The first part (t < 20–30 ns) of the time dependence of gyration radius $R_g(t)$ describes the process of destruction of the amyloid stack by G2 dendrimer and dendrimer-peptides complex formation (**Figure 9a**). From **Figure 9a**, one can see that second generation dendrimer forms complex with 16 peptides within 20–30 ns. After that, the complex size $R_g(t)$ fluctuates slightly, but its average value R_g practically does not change systematically with time. Therefore, we can assume that after 20–30 ns the system is in equilibrium state. It correlates with snapshots that are shown in **Figure 8**. From **Figure 9b**, it can be concluded that the system reaches equilibrium (plateau) state after 20–30 ns.

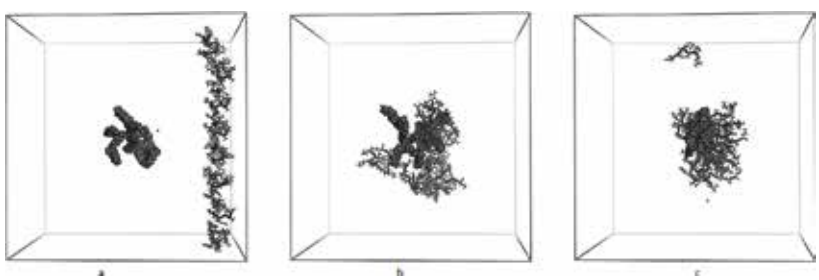

Figure 8. Snapshots of the LVFFAE stack and dendrimer at different time: t = 0 (a), t = 20 ns (b), t = 160 ns (c).

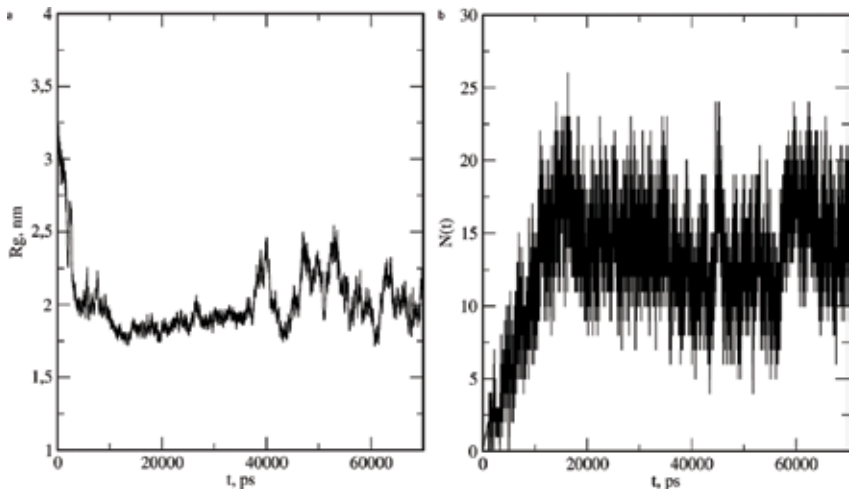

Figure 9. Time dependence of gyration radius of subsystem consisting of the dendrimer and peptides (a) and time dependence of hydrogen bonds number (*N*) between dendrimer and peptides during the complex formation (b).

The distance between neighboring peptides in amyloid stack (**Figure 10a**, curve 1) is an important characteristic of stability of the stack. The distance between dendrimer and peptides (**Figure 10a**, curve 2) allows estimating the rate of dendrimer-peptides complex formation after stack was destructed by dendrimer. At the beginning of simulation, the distances between the neighboring peptides of the stack are small. During first 20–30 ns, this distance is increase. It means that the destruction of amyloid stack occurs and peptides become separated from each other.

At the same time, the distance between dendrimer and peptides (**Figure 10a**, curve 2) in the beginning of the simulation (at $t = 0$) is large because peptides are located far from the

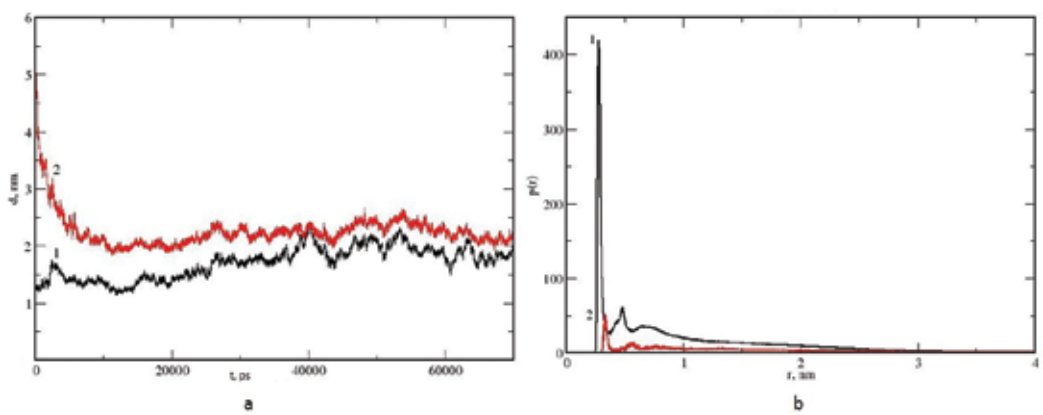

Figure 10. Changes in distances d between amyloid peptides (1) and between dendrimer and peptides (2) (a) and distribution function of ion pair numbers: 1—between NH_3^+ groups of the dendrimer and COO^- groups of peptides; 2—between NH_3^+ groups of the dendrimer and counterions (b).

dendrimer. During first 20–30 ns, the peptides become attracted by dendrimer and distance between them and dendrimer decreases. It means that the dendrimer of the second generation could destroy the stack of amyloid peptides and adsorb the peptides.

After complex formation (t > 20–30 ns), all characteristics of complex fluctuate but their average values do not change with time. We calculated different equilibrium characteristics of complex averaged through equilibrium part of our simulation (t > 30 ns).

In equilibrium state, the mean square radius of gyration R_g of the complex is 1.7 times larger than the size of the dendrimer G2 itself (see **Table 3**). The ratio R_g^{33}/R_g^{11} (which allows to roughly estimating anisotropy of molecule) is equal to 1.68 for dendrimer and 1.45 for the complex of dendrimer with peptides. Thus, the anisotropy of dendrimer with adsorbed amyloid peptides is again less than anisotropy of dendrimer itself as it was for previous two complexes of lysine dendrimer with model peptides Semax and Epithalon.

Radial distribution $p(r)$ density (not shown) obtained for this complex is similar to that for complexes of the dendrimer with two peptides (Semax and Epithalon) studied above. It demonstrates that dendrimer atoms are located mainly in the center of the complex and amyloid peptides are mainly on the surface of the complex. At the same time, some fraction of amyloid peptides could slightly penetrate into the outer part of the dendrimer.

The average number of hydrogen bonds N between dendrimer and LVFFAE peptides in our complex (determined from second part (t > 30 ns) of $N(t)$ from **Figure 9b**) is close to 15. It means that in average each amyloid peptide is connected by one hydrogen bond with dendrimer in the complex. Fluctuations in hydrogen bond number are in the range of 5–27, and it means that a number of hydrogen bonds per peptide can fluctuate between 0 and 2.

Figure 10b shows the dependence of number of ion pairs between dendrimer and peptide charges on the distance between them in the complex. One can see that there is a sharp peak, corresponding to the direct contact between positively charged groups (NH_3^+) of dendrimer and negatively charged groups (COO^-) in peptides (curve 1) and significantly less sharp peak between dendrimer charges and counterions (curve 2). It means that dendrimer and LVFFAE peptides are strongly connected at these points with each other, whereas dendrimer charges and counterions contacts are not so strong.

To determine diffusion coefficient of dendrimer-peptide complex, we calculated its mean square displacement (MSD) as a function of time. It was obtained that the time dependence of MSD function is close to linear in double logarithm coordinates (not shown). It means that the translational motion of complex is the diffusion-like motion. The coefficient of translational

System	R_g^{11} (nm)	R_g^{22} (nm)	R_g^{33} (nm)	R_g (nm)
Dendrimer (*G*2)	0,64	0,97	1,08	1,12
*G*2 + 16 LVFFAE	1,26	1,78	1,83	1,98

Table 3. Eigenvalues R_g^{11}, R_g^{22}, R_g^{33} of tensor of inertia in dendrimer and LVFFAE fibril complex.

diffusion of the complex was determined from the slope of the time dependence of MSD and is equal to $(0.13 \pm 0.04) \times 10^5$ sm^2/s.

The results of simulation of the system consisting of lysine dendrimer of second generation and fragments of amyloid peptides confirm that this lysine dendrimer could form the complex with amyloid peptides. Thus, lysine dendrimers could be a good candidate for using as anti-amyloid agent.

6. Conclusion

In the present chapter, we have shown that lysine dendrimer of the second generation could form stable complexes with therapeutic Semax and Epithalon peptides. We also have shown that this dendrimer could destroy the stable stacks of amyloid peptides and form stable complex with them. Thus, our simulations confirm that lysine dendrimers could be a good candidate for vehicles for the delivery of different nootropic peptides to brain and for the destruction of fibril consisting of disease-related peptides and elimination of them from the brain.

Acknowledgements

Computing resources for this study on supercomputers “Lomonosov” were provided by Supercomputer Centre of Moscow State University [42]. This work was supported by the grant of the Government of Russian Federation 074-U01 and by RFBR grant 16–03-00775.

Author details

Elena Popova[1,2], Dilorom Khamidova[3], Igor Neelov[2,4]* and Faizali Komilov[3]

*Address all correspondence to: i.neelov@mail.ru

1 Institute of Hygiene, Occupational Pathology and Human Ecology, St. Petersburg, Russia

2 ITMO University, St. Petersburg, Russia

3 Tajik National University, Dushanbe, Tajikistan

4 Institute of Macromolecular Compounds, St. Petersburg, Russia

References

[1] Caminade A-M, Turrin C-O, Laurent R, Ouali A, Delavaus-Nicot B. Dendrimers: Towards Catalitic, Material and Biomedical Uses. West Sussex, UK: A John Wiley & Sons, Ltd.; 2011. 515 p

[2] Bajpai AK, Bajpai J, Saini RK, Agrawal P, Tiwari A. Smart Biomaterial Devices. Polymers in Biomedical Sciences. Boca Raton: Taylor & Francis Group, LLC; 2017. 219 p

[3] Buhleier E, Wehner W, Vögtle F. "Cascade"- and "nonskid-chain-like" synthesis of molecular cavity topologies. Synthesis. 1978;**9**:155-158

[4] Kumar S, Pandita D. Dendrimers in drug delivery and targeting: Drug-dendrimer interactions and toxicity issues. Journal of Pharmacy and Bioalled Sciences. 2014;**6**(3):139-150

[5] Boas U, Sontjens SHM, Jensen KJ. New dendrimer-peptide host-guest complexes: Towards dendrimers as peptide carriers. Chembiochem. 2002;**3**(5):433-439

[6] Alder BJ, Wainwright TE. Molecular dynamics by electronic computers. In: Prigogine I, editor. International Symposium on Transport Processes in Statistical Mechanics. New York: Wiley Interscience; 1957. p. 97-131

[7] Verlet L. Computer "experiments" on classical fluids. I. Thermodynamical properties of Lennard-Jones molecules. Physics Review. 1967;**159**:98-103

[8] Rahman A, Stillinger FH. Molecular dynamics study of temperature effects on water structure and kinetics. The Journal of Chemical Physics. 1972;**57**:1281-1292

[9] Balabaev NK, Grivtsov AG, Shnol EE. Numerical Modeling of Motion of Molecules. Motion of Isolated Polymer Chain, preprint, Institute of Applied Mathematics. Moscow. 1972;**4**:38

[10] Ryckaert JP, Ciccotti G, Berendsen HJC. Numerical integration of Cartesian equations of motion of systems with constants-molecular dynamics of n-alkanes. Journal of Computational Physics. 1977;**23**:327-341

[11] Hess B, Kutzner C, Spoel D, Lindahl E. Gromacs 4: Algorithms for highly efficient, load-balanced, and scalable molecular simulation. Journal of Chemical Theory and Computation. 2008;**4**:435-447

[12] Hornak V, Abel R, Okur A, Strockbine D, Roitberg A, Simmerling C. Comparison of multiple amber force fields and development of improved protein backbone parameters. Proteins: Structure, Functions and Genetics. 2006;**65**:712-725

[13] Neelov I, Falkovich S, Markelov D, Paci E, Darinskii A, Tenhu H. Molecular Dynamics of Lysine Dendrimers. Computer Simulation and NMR. In: Dendrimers in Biomedical Applications. London: Royal Society of Chemistry; 2013. p. 99-114

[14] Neelov IM, Janaszewska A, Klajnert B, Bryszewska M, Makova N, Hicks D, Pearson H, Vlasov GP, Ilyash MY, Vasilev DS, Dubrovskaya NM, Tumanova NL, Zhuravin IA, Turner AJ, Nalieva NN. Molecular properties of lysine dendrimers and their interactions with Ab-peptides and neuronal cells. Current Medical Chemistry. 2013;**20**:134-143

[15] Markelov DA, Falkovich SG, Neelov IM, Ilyash MY, Matveev VV, Lahderanta E, Ingman P, Darinskii AA. Molecular dynamics simulation of spin-lattice NMR relaxation in poly-L-lysine dendrimers. Manifestation of the semiflexibility effect. Physical Chemistry and Chemical Physics. 2015;**17**:3214-3226

[16] Ennari J, Elomaa M, Neelov I, Sundholm F. Modelling of water free and water containing solid polyelectrolites. Polymer. 2000;**41**:985-990

[17] Ennari J, Neelov I, Sundholm F. Comparison of cell multipole and ewald summation methods for solid polyelectrolyte. Polymer. 2000;**41**:2149-2155

[18] Ennari J, Neelov I, Sundholm F. Molecular dynamics simulation of the peo sulfonic acid anion in water. Computational and Theoretical Polymer Science. 2000;**10**:403-410

[19] Ennari J, Neelov I, Sundholm F. Molecular dynamics simulation of the structure of PEO based solid polymer electrolytes. Polymer. 2000;**41**:4057-4063

[20] Ennari J, Neelov I, Sundholm F. Estimation of the ion conductivity of a PEO-based polyelectrolyte system by molecular modeling. Polymer. 2001;**42**(19):8043-8050

[21] Neelov I, Sundholm F. Modelling of gas transport properties of polymer electrolytes containing various amounts of water. Polymer. 2004;**45**:4171-4179

[22] Darinskii A, Gotlib Y, Lukyanov M, Neelov I. Computer simulation of the molecular motion in LC and oriented polymers. Progress in Colloid and Polymer Science. 1993;**91**:13-15

[23] Darinskii AA, Gotlib YY, Lyulin AV, Neelov IM. Computer modeling of polymer chain local dynamics in a field of a liquid crystal type. Vysokomolec. Soed. Ser. A. 1991;**33**:1211-1220

[24] Darinskii A, Lyulin A, Neelov I. Computer simulations of molecular motion in liquid crystals by the method of Brownian dynamics. Macromolecular Theory & Simulations. 1993;**2**:523-530

[25] Neelov IM, Adolf DB, Lyulin AV, Davies GR. Brownian dynamics simulation of linear polymers under elongational flow: Bead–rod model with hydrodynamic interactions. The Journal of Chemical Physics. 2002;**117**:4030-4041

[26] Neelov IM, Adolf DB. Brownian dynamics simulation of hyperbranched polymers under elongational flow. The Journal of Physical Chemistry. B. 2004;**108**:7627-7636

[27] Neelov IM, Adolf DB. Brownian dynamics simulations of dendrimers under elongational flow: Bead-rod model with hydrodynamic interactions. Macromolecules. 2003;**36**:6914-6924

[28] Sheridan PF, Adolf DB, Lyulin AV, Neelov I, Davies GR. Computer simulations of hyperbranched polymers: The influence of the Wiener index on the intrinsic viscosity and radius of gyration. The Journal of Chemical Physics. 2002;**117**:7802-7812

[29] Mazo MA, Shamaev MY, Balabaev NK, et al. Conformational mobility of carbosilane dendrimer: Molecular dynamics simulation. Physical Chemistry and Chemical Physics. 2004;**6**:1285-1289

[30] Okrugin B, Neelov I, Borisov O, Leermakers F. Structure of asymmetrical peptide dendrimers: Insights given by self-consistent field theory. Polymer. 2017;**125**:292-302

[31] Shavykin OV, Neelov IM, Darinskii AA. Is the manifestation of the local dynamics in the spin–lattice NMR relaxation in dendrimers sensitive to excluded volume interactions? Physical Chemistry Chemical Physics. 2016;**18**:24307-24317

[32] Falkovich S, Markelov D, Neelov I, Darinskii A. Are structural properties of dendrimers sensitive to the symmetry of branching? Computer simulation of lysine dendrimers. Journal of Chemical Physics. 2013;**139**:064903

[33] Neelov IM, Markelov DA, Falkovich SG, Ilyash MY, Okrugin BM, Darinskii AA. Mathematical modeling of lysine dendrimers. Temperature dependencies. Vysokomolec. Soed. Ser. A, 2013;**55**:963-970

[34] Shypshyna MS, Veselovsky NS, Myasoedov NF, Shram SI, Fedulova SA. Effect of peptide Semax on synaptic activity and short-term plasticity of glutamatergic synapses of co-cultured dorsal root ganglion and dorsal horn neurons. Fiziologicheskiĭ Zhurnal. 2015;**61**:48-55

[35] Shevchenko KV, Nagaev IY, Alfeeva LY, Andreeva LA, Kamenskii AA, Levitskaya NG, Shevchenko VP, Grivennikova IA, Myasoedov NF. Kinetics of semax penetration into the brain and blood of rats after its intranasal administration. Russian Journal of Bioorganic Chemistry. 2006;**32**(1):57-62

[36] Ashmarin IP, Samonina GE, Lyapina LA, Kamenskii AA, Levitskaya NG, Grivennikov IA, Dolotov OV, Andreeva LA, Myasoedov NF. Natural and hybrid ("chimeric") stable regulatory glyproline peptides. Pathophysiology. 2005;**11**:179-185

[37] Kozina LS, Arutjunyan AV, Stvolinskii SL, Havinson VH. Evaluation of the biological activity of regulatory peptides in model in-vitro experiments. Successes of Gerontology. 2008;**21**:68-73

[38] Havinson VH, Bondarev IE, Butjugov AA. Epithalon enduces telomerase activity and telomeres elongation in human somatic cells. Bulletin of Experimental Biology and Medicine. 2003;**135**(6):692-695

[39] Petkova AT, Yau WM, Tycko R. Experimental constraints on quaternary structure in Alzheimer's β-amyloid fibrils. Biochemistry. 2006;**45**:498-512

[40] Paravastu AK, Leapman RD, Yau WM, Tycko R. Molecular structural basis for polymorphism in Alzheimer's β-amyloid fibrils. Proceedings of the National Academy of Sciences of the United States of America. 2008;**105**:18349-18354

[41] Klajnert B, Cladera J, Bryszewska M. Molecular interaction of dendrimers with amyloid peptides: pH dependences. Biomacromolecules. 2006;**7**:2186-2191

[42] Sadovnichy V, Tikhonravov A, Voevodin V, Opanasenko V, editors. Contemporary high performance computing: From petascale toward exascale. Boca Raton, United States: Wiley and Sons; 2013. p. 283-307

Chapter 4

Radiolabeled Dendrimers as Potential PET Agents for Molecular Imaging of Tumor Angiogenesis

Anchal Ghai, Natasha Singh, Shalini Chopra and Baljinder Singh

Additional information is available at the end of the chapter

http://dx.doi.org/10.5772/intechopen.71189

Abstract

Introduction: Angiogenesis is a normal physiological process that plays an imperative role during tumor development. We believe that the development of a non-invasive imaging technique targeting angiogenesis can provide a better understanding of this important process. Positron emission tomography (PET) – a highly sensitive imaging technique can offer accurate degree of disease quantification. The phenomenon of enhanced permeability and retention effect (EPR effect) is now becoming the gold standard in cancer targeting drug designing. Dendrimers have the ability to exhibit EPR effect for targeted therapeutic/drug delivery approach. Therefore, molecular imaging of tumor angiogenesis using radio-labeled dendrimers is expected to broaden the possibilities for drug development.

Body: In the present chapter, the significance of performing conjugation chemistry of bifunctional chelators quality control parameters of the radiolabeled dendrimer conjugates *in vitro* stability, animal biodistribution, radiation dosimetry and molecular imaging of animal tumor model after injecting radiotracer have also been discussed in detail.

Conclusion: Conjugation of the radio-metal complexes to larger molecules like dendrimers has created a new domain of research in the field of biomedical applications. Therefore, it has been proposed to develop new effective targeting moieties suitable for radiolabeling with PET tracers so as to perform molecular imaging studies.

Keywords: dendrimers, radiolabeling, PET imaging, tumor angiogenesis

1. Introduction

The present chapter highlights the importance of dendrimer based radio imaging of angiogenesis as a novel approach for molecular imaging of carcinogenesis because of their topology,

functionality and dimensions. The high loading capacity of dendrimers enables them to deliver chemotherapeutic agents as well. The dendrimer-drug complexes designed for either targeted or non-targeted drug delivery successfully penetrate through the leaky vasculature of tumor and accumulate in the cancer tissue. However, the added advantage of using dendrimer-drug complexes specifically designed for targeted delivery is that they bind to specific receptors over-expressed on the surface of cancer cells, thereby, increasing their residence time over the cell surface. Thus, the development of dendrimer complexes that incorporate the targeting ligands, anticancer drugs and positron emission tomography (PET)/β emitting radionuclides may provide the way for combinational anticancer therapies along with the *in vivo* imaging of the targeted tumor.

2. Tumor angiogenesis

Angiogenesis is an essential physiological process that involves formation of new blood vessels from the pre-existing ones and is one of the fundamental processes required for normal growth and development [1]. It has been recognized long ago that most solid tumors are perfused by large number of blood vessels [2]. The ability of a tumor to stimulate the formation of new blood vessels enables expansion of tumors, local invasion and dissemination. Thus, angiogenesis is also considered as one of the key requirements during tumor development as it provides oxygen and nutrients to the otherwise dormant tumors and without which the tumor cannot grow beyond 2.0–3.0 mm in diameter [3, 4]. Tumor comprises of cells that proliferate aberrantly and have lost the ability to regulate growth. Thus, tumor cells like normal cells require adequate supply of oxygen and nutrients and also needs an effective mean to remove wastes in order for metabolic processes to occur [5]. In order to fulfill these requirements, tumor cells can establish their own blood supply and this ability of tumors to promote the formation of new capillaries from the pre-existing ones is called the angiogenic switch. Tumor induced blood vessels are abnormal and leaky in nature. Since, the leaky vasculature of tumor blood vessels provides an efficient route of exit for tumor cells to leave the primary site and enter the main circulation, angiogenesis, thus has been considered as the critical component of metastasis [6].

3. Imaging of tumor angiogenesis

Angiogenesis is considered as an important therapeutic target in both cardiovascular and malignant diseases [7]. In cardiovascular diseases, the therapeutic goal is to perfuse the ischemic tissue and to promote recovery from ischemic injury by inducing angiogenesis [8, 9]. On the other hand, in tumor angiogenesis, the angiogenic therapeutic approach is based on inhibiting angiogenesis, which is responsible for tumor growth and metastasis [10]. This fact has led to an increased search for new anti-angiogenic molecules and to design targeted anti-angiogenic strategies for cancer treatment and the prevention of cancer recurrence or metastasis [11, 12]. Further, with the increasing use of anti-angiogenic drugs in the field of oncology,

the importance of imaging the angiogenic process has also increased. Various candidates for diagnosing angiogenesis include vascular endothelial growth factor (VEGF), circulating endothelial progenitor cells and biopsy specimens.

Though, biopsy specimens are extremely rich in information but they suffer a limitation from sampling bias and inherent invasiveness. The traditional gold standard measure of angiogenesis is the histological estimate of microvascular density (MVD) which quantifies the average number of micro vessels within a selected microscopic field. However, this method is invasive and will vary according to the location from which the biopsy is taken and may cause under or overestimation of the degree of angiogenesis.

Thus, the development of non-invasive imaging technique, specifically targeting angiogenesis among other biological processes would provide a better understanding of this important process and would also enable the evaluation of anti-angiogenic effect of new drugs administered as adjuvant therapy to reduce tumor growth.

4. Imaging techniques

Certain imaging modalities like computed tomography (CT) angiography, high resolution magnetic resonance angiography and contrast enhanced ultrasound are available for structural visualization of microvasculature. Multi detector (MDCT) angiography has better spatial and temporal resolution and is considered as the most useful modality in evaluating vascular structures [13]. The spatial resolution of MDCT is about 1.0 mm and the size of a human capillary is about 7.0–10.0 μm. Thus, MDCT can still not adequately visualize microvasculature [14]. Several molecules like growth factor receptors, tyrosine kinase receptors and G-protein coupled receptors can be used as specific targets for angiogenesis imaging [7].

Radionuclide based imaging techniques like single photon emission computed tomography (SPECT) and PET can offer accurate degree of disease quantification (progression/regression) in view of the high sensitivity of these imaging modalities [15]. In PET imaging, the annihilation of an electron-positron pair gives rise to two 511 KeV gamma ray photons being emitted at 180°. These high energy photons are then detected by a detector ring which is made up of crystals like bismuth germanium oxide (BGO), gadolinium oxyorthosilicate (GSO) or lutetium oxyorthosilicate (LSO).

Undoubtedly, the success of such this modality lies with the development of specific molecular imaging probes for the accurate diagnosis of angiogenesis and for identifying the responders/non-responders at an early stage after the initiation of treatment [7]. Over the last decade, PET imaging has emerged as a very powerful imaging technique for use in the direct imaging of angiogenesis in animal (eventually human) models, an early diagnosis, complete staging and early treatment response assessment [16]. The ability of PET imaging to detect picomolar concentration of tracer accumulation makes it several times more sensitive technique than the SPECT imaging [17]. PET imaging not only enables *in vivo* visualization of physiological processes at molecular level but also helps in its quantification. PET may be considered as a

functional or a targeted imaging modality. The staging can be done more accurately using PET when compared to any other conventional diagnostic means and thus it might be used independently as the first diagnostic choice [18].

5. Role of dendrimers in angiogenesis imaging

Most of the low molecular weight anticancer drugs have a characteristic to move in and out of blood vessels freely, unless the drug is linked with a tumor specific molecular ligand like anti-VEGF antibodies or receptor-specific ligands having high binding constant [19]. However, despite their high selectivity, the slow clearance rate of antibodies limits their clinical application. Recent studies have revealed that tumor cells have diverse epitopes because of great magnitude of mutation frequency even among the same cancer patient. Thus, the specific antibodies and ligands show inefficient binding with each of the diverse epitopic targets [20, 21]. In order to overcome this problem, the phenomenon of enhanced permeability and retention effect (EPR effect) is now becoming the gold standard in cancer targeting drug designing. The EPR effect is based on macromolecular, polymeric and micellar particles including nanoparticles [22]. The leaky blood vessels of tumors enables the molecules of size greater than 40 kDa to escape out of the tumor blood vessels and accumulate into the tumor tissues whereas this EPR effect is not present in normal tissues [23]. Thus, this unique phenomenon of EPR effect is being exploited increasingly for anticancer drug development.

The concept of nanomedicine has been used extensively to develop biocompatible products for targeted drug delivery and sustained drug release at the targeted sites [24]. Nanomedicine is an emerging field that deals with interactions between molecules, cells and engineered substances like molecular fragments, atoms and molecules They have a high available surface area per unit of volume and they can be engineered to have different sizes, shapes and chemical compositions, hollow or solid structures [25]. Nanodelivery systems are believed to allow for more specific targeting. Nanotechnology products like fullerenes or dendrimers, macromolecular, micellar and polymeric particles have the ability to exhibit EPR effect for targeted therapeutic/drug delivery approach [22, 24].

Dendrimers are highly branched; 3-dimensional polymeric structures which are usually classified by the number of repeated branching cycles formed during synthesis and are reported to have an emerging role in a variety of biomedical applications [26]. They can be used as biomimetic catalysts, drug carriers, gene delivery and can also be used in boron neutron capture therapy [27–30]. The dendrimers are considered potentially advantageous due to their numerous surface functional groups, relatively low immunogenicity and also their size, which is very close to various important biological polymers. Lower generation dendrimers are asymmetric in nature and are considered as more open structures when compared to dendrimers of higher generation. With the increasing generation, dendrimers acquire a globular structure [31] and forms a closed membrane like structure due to the dense packing of branches.

Dendrimers are monodisperse molecules and their solubility is influenced by the nature of functional groups present on the surface of dendrimers, that is, dendrimers with hydrophilic

terminal groups are soluble in polar solvents whereas dendrimers possessing hydrophobic end groups are soluble in non-polar solvents [32]. The need to study the biological properties of dendrimers is very important because of their increasing use in biomedical applications. The molecular dimensions of dendrimers are comparable to medium sized proteins [33].

Though, dendrimers have been extensively used as magnetic resonance imaging (MRI) contrast agents and drug delivery carriers, however, the complex of radionuclides with polyamidoamine (PAMAM) dendrimers in order to perform molecular imaging of tumor angiogenesis is a new field. In the past, dendrimers have been extensively studied as prospective carriers for drug delivery, gene delivery and moieties for modifying the drug solubility and absorption [34, 35]. The geometry of the molecule and the charges present on the surface of dendrimers influence the microvascular extravasation of polymers across the endothelial barrier.

EPR effect has been widely used for passive targeting of macromolecular anticancer agents to angiogenic solid tumors. Dendrimers with hydrophilic surfaces and molecular weights above 25–30 kDa are usually retained in the circulation for longer periods and provide an enhanced opportunity for passive targeting via EPR effect.

Many studies describing the process of dendrimer-chelator conjugation and subsequent complexation with metal ions and the potential use of dendrimers as probes in MRI and fluorescent imaging have been cited previously [36, 37]. However, studies with regard to radiolabeling of these dendrimer-chelator conjugates as PET imaging probes are very few.

6. Radionuclides used for molecular imaging of dendrimers

More than 80.0% of the radiopharmaceuticals used in nuclear medicine imaging are technetium −99 m (^{99m}Tc) based tracers. However, a dramatic shift toward the development of PET-based novel tracers using fluorine-18 (^{18}F), carbon-11 (^{11}C), gallium-68 (^{68}Ga) and copper 64 (^{64}Cu) positron emitters have been witnessed over the last few years. Majority of these radiopharmaceuticals are administered intravenously. Radiopharmaceuticals can be divided into diagnostics and therapeutics depending on their medical applications. Diagnostic radiopharmaceuticals are predominantly metal complexes with an organic chelator for metal-essential agents or a chelator-biomolecule conjugate for target-specific radiopharmaceuticals. In general, a target-specific radiopharmaceutical can be divided into four parts: targeting biomolecule (BM), pharmacokinetic modifying (PKM) linker, bifunctional coupling or chelating agent (BFC) and radionuclide.

7. Bifunctional chelating agents (BFC)

Chelators used for labeling with PET radionuclides are usually dominated by polydentate chelators like 1,4,7-triazacyclononane-triacetic acid (NOTA), 1,4,7,10-tetraazacyclododecane-tetraacetic acid (DOTA), diethylenetriaminepentaacetic acid (DTPA), DTPA-monoamide and 4-(4,7-bis(2-(tert-butoxy)-2-oxoethyl)-1,4,7-triazacyclononan-1-yl)-5-(tert-butoxy)-

5-oxopentanoic acid (NODA-GA $(tBu)_3$) etc. These chelators are also called as "bifunctional chelating agents" as they possess a metal binding moiety as well as a chemically reactive functional group. The radionuclide of interest can bind to the metal binding moiety and the chemically reactive functional group provides the requisite chemistry for covalent attachment to the targeting vector/carrier of interest like proteins [38], peptides [39] or nanoparticles. BFC is covalently attached to the targeting molecule and strongly coordinates the radio-metal. The design of BFC depends upon number of fundamental criteria. Foremost seems the metal complex stability followed by other coordination chemistry criteria such as charge, chelator cavity size compatibility with the ionic radius of the radionuclide, chelate denticity and availability of donor binding groups of appropriate chemical character. Two additional properties are also critical to consider: the rate at which the metal complex forms and the rate of dissociation. All of these criteria are interrelated. Cavity size must accommodate the ionic radius of the radionuclide such that all of required donor groups can be properly aligned for optimal binding to the metal ion in such a way to adequately encapsulate the ion thereby providing high stability and limiting dissociation. The suitable radio-metals are diverse in their properties and coordination chemistry, so, unfortunately there is no bifunctional chelating agent suitable for all radionuclides. The selection of BFC depends upon the oxidation state of the radio-metal that makes it imperative to understand the coordination chemistry of chelators with any given radionuclide to be labeled. Any BFC that forms a thermodynamically stable radio-metal chelate with high kinetic inertness is considered as an ideal BFC.

8. Chelating groups/techniques

There are several conjugation groups that can be used for the attachment of a BFC to the biomolecule like anhydride, isothiocyanate, bromoacetamide, iodoacetamide, N-hydroxysuccinimide (NHS) ester and maleimide. All of these conjugation groups are electrophiles, which require a nucleophile functionality in the biomolecule but in some cases, the biomolecule of interest contains groups like carboxylic acid only which are electrophilic in nature. In these cases, a nucleophile like ethylenediamine, is used to convert the electrophilic group into a nucleophilic group. These reactive groups, can serve as "linkers" for conjugation of a BFC. Selection of conjugation group depends largely on the "linker" in biomolecules. Very often the "linker" is a primary amine or a thiol group. The functional groups reactive toward primary amines include DTPA dianhydride, NHS-activated esters and isothiocyanates while maleimide is very reactive to thiols.

DTPA anhydride – DTPA dianhydride is commercially available and reacts readily with primary amines to form the DTPA-biomolecule conjugate in both aqueous and non-aqueous media [40, 41]. For small biomolecules, the cross-linking may result in the improved receptor binding kinetics and proves to be beneficial because simultaneous binding of two biomolecules on adjacent receptor sites will result in a slow dissociation of the receptor ligand. Asymmetric anhydrides of DTPA and DOTA have also been used to prepare their bio conjugates [42–44].

http://dx.doi.org/10.5772/intechopen.71189

NHS ester – The NHS esters have intermediate reactivity toward amines and are highly selective for aliphatic amines at an optimum pH of 8.0–9.0 in aqueous systems. Molecules containing a carboxylic group can be converted into its NHS ester, making NHS-activated ester groups among the most powerful and the most commonly used conjugation groups for large (antibodies) and small biomolecules [45, 46].

Isothiocyanates – Isothiocyanates are also reactive to amine groups, and form thiourea bonds with primary amines from proteins or small biomolecules. They show intermediate reactivity toward amines at pH 9.0–9.5 in aqueous solutions and are more stable in water than NHS esters.

Aromatic isothiocyanates are often used to conjugate biomolecules onto DTPA and DOTA analogs [45, 46].

Maleimide – Maleimide reacts with a thiol group at a pH of 7.0 and leads to the formation of a thioether bond [47]. Maleimides can hydrolyze at higher pH (>8.0) to form non-reactive maleimic acids. The only limitation of using maleimide as a conjugation group is that not many biomolecules contain thiol groups thereby limiting the use of maleimide as a chelator.

Radiolabeling of DTPA and DOTA-biomolecule conjugates – DTPA analogs have a major advantage of being used as BFCs as they can be radiolabeled with high labeling efficiency even under mild conditions, but the kinetic instability of these metal chelates results in dissociation of the radio-metal from the chelate.

DOTA analogs can be used as BFCs because if the kinetic inertness of their radio-metal chelates. However, the radiolabeling of DOTA chelates depends upon various factors like chelate concentration, pH, reaction temperature and incubation time, buffer concentration and presence of metal ions such as Zn (II) and Fe (III) [48–51]. In spite of the high solution stability of their radio-metal chelates, slow radiolabeling kinetics remains a major obstacle for the wide use of DOTA analogs as BFCs in target-specific radiopharmaceuticals. Coordination chemistry plays an imperative role in designing BFCs, radiolabeling, solution stability, modification of pharmacokinetics and formulation development.

9. Characterization and purification techniques

Certain mass spectroscopic techniques are utilized to determine the yields of bio-conjugation reactions. Liquid chromatography-mass spectrometry (LC–MS) technique is used for the characterization of dendrimers with mass below 3000 Da. Electrospray ionization-mass spectrometry (ESI-MS) is used for dendrimers which are able to form stable multiple charged species. Matrix assisted laser desorption ionization: time of flight mass spectrometry technique (MALDI-tof) is used to characterize the chelate dendrimer conjugates with high molecular weight. These mass spectrometric techniques are used to analyze and compare the mass spectra of unmodified dendrimers and dendrimer-chelate conjugates in order to confirm the degree of conjugation. The average number of chelate molecules conjugated at the surface of dendrimer molecule is calculated using the formula:

$$\text{Number of DOTA molecules conjugated} = \left[(\text{Increase in molecular weight relative to unmodified dendrimer}) \div (\text{Molecular weight of BFC})\right]. \quad (1)$$

Conjugation of BFCs with dendrimer can also be confirmed by Fourier transform-infrared spectroscopy (FT-IR). Chromatography techniques like size exclusion chromatography (SEC) helps in the purification and separation of dendrimer-chelate conjugates from free BFC's according to their sizes.

10. Dendrimer-chelate cytotoxicity

"Cationic" dendrimers (e.g., amine terminated PAMAM dendrimers) are generally hemolytic and cytotoxic [52]. The toxicity of dendrimers depends upon the generation number and increases with the increasing number of surface groups. Anionic dendrimers that bear carboxylate surface groups are not cytotoxic even at a broad concentration range [53]. Amine terminated PAMAM dendrimers are believed to have been showing more cytotoxicity because of the interaction between positively charged dendrimers and the negatively charged cell membranes [54]. Thus, the cytotoxicity of these cationic dendrimers can be decreased by either shielding or decreasing the positive charge on their surface. Thus, the positively charged groups are usually capped with neutral molecules [55, 56]. Similarly, the surface amino groups/carboxylate groups of dendrimers are modified with BFCs resulting in a significant decrease in the number of positive charges on their surface. The toxicity of dendrimers on cells is concentration, time and generation dependent. Previous studies have demonstrated that the dendrimers with surface modifications are less toxic and more biocompatible when compared with the unmodified dendrimers [52, 54].

11. Radiolabeling of dendrimer-chelate conjugates

The radiolabeling of the purified and characterized dendrimer-chelate conjugates depends upon various factors and needs to be standardized. The ability of these bifunctional chelators to coordinate with a variety of metals makes them more sensitive to metallic impurities and contaminants *en route* the reaction process. Also, considerable attention has to be given for optimizing the reaction conditions so as to achieve best results for all conjugation and radiolabeling experiments [57]. Factors like buffer pH, buffer volume, concentration of conjugate and incubation time has to be optimized in order to achieve best radiolabeling efficiency. The lead for setting up the range of test conditions for optimizing the radiolabeling of dendrimers with different radio-metals was taken from the previous studies [58].

12. ^{68}Ga containing dendrimers for PET imaging

More than 80.0% of the radiopharmaceuticals used in nuclear medicine imaging are ^{99m}Tc based tracers. Among, several PET radionuclides, there has been a renewed interest in ^{68}Ga for many

http://dx.doi.org/10.5772/intechopen.71189

reasons. ^{68}Ga is well suited for use as a radiolabel for PET because of its comparatively shorter half-life of 68 min. The emission of two divergent photons per decay allows the construction of three-dimensional images. Also, the advances in generator technology for ^{68}Ga production, favorable chemistry of ^{68}Ga for radio-complexation have paved the way for emerging applications of ^{68}Ga radiopharmaceuticals [59]. The most stable oxidation state of gallium in aqueous solution is +3 and its coordination number is 6. The coordination chemistry of Ga^{3+} is very similar to high spin Fe^{3+} ion. Both the ions have oxidation state of +3 and have almost same ionic radii (62 pm for Ga^{3+} and 65 pm for Fe^{3+}). Ga(III) can undergo ligand exchange with protein transferrin when injected into the biological system. Transferrin contains two iron binding sites with high affinity for this metal ion. At physiological conditions, the human transferrin has a high binding affinity for Ga^{3+} given by log KST = 20.3 [60]. Thus, radiolabeling of ^{68}Ga is best achieved by using bifunctional chelators which can strongly chelate the gallium ion and are covalently bound to targeting vectors [61, 62]. The most widely used bifunctional chelator for ^{68}Ga radionuclide labeling is DOTA [63]. Ga(DOTA) complex is stable enough to be used in clinical practice. These macrocyclic chelators display high conformational and size selectivity toward metal ions. This category of chelators can encapsulate the metal ions with high efficiency keeping it away from the competing species like blood transferrin [64].

The pH of buffer plays an important role in radiolabeling procedures especially with ^{68}Ga. In aqueous solution, free hydrated gallium, that is, $[Ga(H_2O)_6]^{3+}$ is stable under acidic conditions (pH < 3). At slightly higher pH, the aqueous solution chemistry is determined by the hydrolysis of the aqua ion leading to the formation of insoluble trihydroxide, that is, $Ga(OH)_3$. At physiological pH, the solubility of gallium is high due to the exclusive formation of $[Ga(OH)^{4-}]$ ions [61]. Formation of $Ga(OH)_3$ due to the hydrolysis can be avoided by using stabilizing weak ligands like acetate, citrate or HEPES as conjugating as well as radiolabeling buffers. For use as a radiopharmaceutical, a gallium compound must be either thermodynamically stable toward hydrolysis at physiological pH or be kinetically stable in the time frame of an imaging procedure. The reaction kinetics for the incorporation of Ga^{3+} is inversely related to pH [65]. The complexation of Ga^{3+} by DOTA shows slow kinetics because of its cavity size and eight donor atoms. Therefore, the radiolabeling procedures were carried at an elevated temperature of 90–100°C.

13. Quality control

ITLC – The radiolabeling efficiency is estimated chromatographically using ITLC-silica gel strips as the stationary phase and solvents such as ammonium acetate: methanol as mobile phase. The radiolabeled preparation is spotted at the origin of ITLC strips, dried and introduced into the solvent chamber containing mobile solvent. The mobile solvent is allowed to reach the top of the ITLC strip; the strip is removed, dried in air, cut into two halves and measured for its radioactivity in order to calculate its radiolabeling efficiency. The retention factor (R_f) can also be calculated, the strips are marked from origin and divided into 10 equal sections each of 1.0 cm. The strips are cut, put into the test tubes and counts can be recorded in sodium iodide (NaI) well counter. The observed counts from each segment can be plotted as a linear graph and the R_f value for radiolabeled dendrimers can be evaluated.

***In vitro* stability assay** – The *in vitro* stability of the radiolabeled formulation can be determined by radio-chromatography using ITLC. The radiolabeling efficiency of the formulation is calculated at various time intervals. This assay depicts the pattern of degradation of radiolabeled formulation as a function of time.

***In vitro* serum stability assay** – The stability of radiolabeled dendrimers in systemic circulation is usually evaluated by performing serum stability assay. The radiolabeled formulation is measured for any degree of degradation, if any due to enzymatic or other factors present in the blood/serum.

Lipophilicity assay – Affinity of radiolabeled formulation toward the organic phase (octanol) and aqueous phase, phosphate buffered saline (PBS) can be determined by calculating the organic/aqueous partition coefficient. Log P value is considered as the measure of lipophilicity and can be calculated by using the formula:

$$\text{Log P} = \log \left[\text{Counts in organic phase (octanol)}/\text{Counts in aqueous phase (PBS)}\right] \quad (2)$$

14. Biodistribution and dosimetry studies

It is important to perform biodistribution and dosimetry studies with any new radiopharmaceutical to study the dose absorbed by various "critical organs" and also to study the pharmacokinetics of these newer tracers [66]. The documentation of pharmacokinetics and dosimetry data and submission of the same to the 'regulatory authorities' provide a robust evidence for seeking permission to carry out first 'human studies' and thus, has a translational relevance. Whenever new or experimental radiopharmaceuticals are administered to patients, it becomes mandatory to get information on the patient's radiation exposure by performing a dosimetry study. The procedure used to assess the organ's absorbed doses has been summarized in MIRD pamphlet number 21 [67] and includes two major steps. Firstly, the quantification of the time integrated activity for each tissue localizing the radiopharmaceutical and secondly, determination of the S values, that is, the absorbed dose to target tissues per decay, in each source tissue were carried out. The S values for a radionuclide as required for the internal dosimetry must be based upon the internationally accepted reference anatomic phantoms as defined by the International Commission on Radiological Protection [68]. Further, the effective dose can be calculated by using the tissue weighing factors and the absorbed dose values to the organs. The critical organs of interest in humans for the use of a new radiopharmaceutical clinically are generally evaluated in preclinical studies in rodents and other mammalian species. However, estimates derived from the animal studies are usually considered sufficient for the purpose of grant of regulatory permissions for human trials [69].

15. Molecular imaging with radiolabeled dendrimers

Dendrimers can be used to target the tumor vasculature by modifying their surface through covalent conjugation. Such a modification increases the targeting potential of

dendrimers toward cancer cells [70]. A combination of imaging modalities and several biocompatible and biodegradable dendrimers over the decade has been used to develop bio-imaging probes that have prolonged plasma half-lives, enhanced stability, reduced toxicity and improved target specificity. However, the application of dendrimers in nuclear medicine and radiochemistry is still at its infancy. With the escalating knowledge of science and research in the field of oncology, the development of new drug delivery systems has attained great heights. It is believed that rapid technological and scientific progresses in the development of bio-imaging dendrimers and their role as drug delivery agents will provide new research opportunities for use of dendrimers in the preclinical and clinical development of new therapies. Due to the 3-dimensional structure and presence of numerous functional groups on the surface, dendrimers have generated huge interest and attention as drug delivery systems. They provide a platform for attaching drugs or genes and further releasing them through several mechanisms which include either *in vivo* degradation of drug dendrimer covalent bonding due to the presence of certain enzymes or drug release due to changes in physical environment such as pH and temperature.

16. Conclusion

The high loading capacity of dendrimers enables them to deliver chemotherapeutic agents as well. The dendrimer-drug complexes designed for either targeted or non-targeted drug delivery successfully penetrate through the leaky vasculature of tumor and accumulate in the cancer tissue. However, the added advantage of using dendrimer-drug complexes specifically designed for targeted delivery is that they bind to specific receptors overexpressed on the surface of cancer cells, thereby, increasing their residence time over the cell surface. Thus, the development of dendrimer complexes that incorporates the targeting ligands, anticancer drugs and PET/β emitting radionuclides may provide the way for combinational anticancer therapies along with the *in vivo* imaging of the targeted tumor.

Author details

Anchal Ghai[1], Natasha Singh[2], Shalini Chopra[3] and Baljinder Singh[3]*

*Address all correspondence to: drbsingh5144@yahoo.com

1 Mallinckrodt Institute of Radiology, Optical Imaging Lab, Washington University School of Medicine, Saint Louis, Missouri, USA

2 BIDMC Genomics, Proteomics, Bioinformatics and Systems Biology Center, Beth Israel Deaconess Medical Center, Boston, MA, USA

3 Department of Nuclear Medicine & PET, PGIMER, Chandigarh, India

References

[1] Greenblatt M, Shubi P. Tumor angiogenesis: Transfilter diffusion studies in the hamster by the transparent chamber technique. Journal of the National Cancer Institute. 1968;**41**:111-124

[2] Baeriswyl V, Christofori G. The angiogenic switch in carcinogenesis. Seminars in Cancer Biology. 2009;**19**:329-337

[3] Folkman J. Angiogenesis in cancer, vascular, rheumatoid and other disease. Nature Medicine. 1995;**1**:27-31

[4] Hanahan D, Weinberg RA. The hallmarks of cancer. Cell. 2000;**100**:57-70

[5] Hicklin DJ, Ellis LM. Role of the vascular endothelial growth factor pathway in tumor growth and angiogenesis. Journal of Clinical Oncology. 2005;**23**:1011-1027

[6] Dvorak HF, Brown LF, Detmar M, Dvorak AM. Vascular permeability factor/vascular endothelial growth factor, microvascular hyperpermeability, and angiogenesis. The American Journal of Pathology. 1995;**146**:1029-1039

[7] Lee HY, Jeong JM. Multimodality imaging of angiogenesis. The Open Nuclear Medicine Journal. 2010;**2**:166-170

[8] Stegmann TJ. New approaches to coronary heart disease: Induction of neovascularization by growth factors. BioDrugs. 1999;**11**:301-308

[9] Deveza L, Choi J, Yang F. Therapeutic angiogenesis for treating cardiovascular diseases. Theranostics. 2012;**2**:801-814

[10] Brown JM, Giaccia AJ. The unique physiology of solid tumors: Opportunities (and problems) for cancer therapy. Cancer Research. 1998;**58**:1408-1416

[11] Kerbel R, Folkman J. Clinical translation of angiogenesis inhibitors. Nature Reviews. Cancer. 2002;**2**:727-739

[12] Cai W, Chen X. Anti-angiogenic cancer therapy based on integrin alphavbeta3 antagonism. Anti-Cancer Agents in Medicinal Chemistry. 2006;**6**:407-428

[13] Ippolito D, Sironi S, Pozzi M, et al. Hepatocellular carcinoma in cirrhotic liver disease: Functional computed tomography with perfusion imaging in the assessment of tumor vascularization. Academic Radiology. 2008;**15**:919-927

[14] Engelke C, Schaefer-Prokop C, Schirg E, Freihorst J, Grubnic S, Prokop M. High-resolution CT and CT angiography of peripheral pulmonary vascular disorders. Radiographics. 2002;**22**:739-764

[15] Miller JC, Pien HH, Sahani D, Sorensen AG, Thrall JH. Imaging angiogenesis: Applications and potential for drug development. Journal of the National Cancer Institute. 2005;**97**:172-187

[16] Townsend DW. Physical principles and technology of clinical PET imaging. Annals of the Academy of Medicine, Singapore. 2004;**33**:133-145

[17] Rahmim A, Zaidi H. PET versus SPECT: Strengths, limitations & challenges. Nuclear Medicine Communications. 2008;**29**:193-207

[18] Hicks RJ. Should positron emission tomography/computed tomography be the first rather than the last test performed in the assessment of cancer? Cancer Imaging. 2012; **12**:315-323

[19] Maeda H, Bharate GY, Daruwalla J. Polymeric drugs for efficient tumor-targeted drug delivery based on EPR-effect. European Journal of Pharmaceutics and Biopharmaceutics. 2009;**71**:409-419

[20] Tobias S, Jones S, Laura D, Wood D, Parsons W. The consensus coding sequences of human breast and colorectal cancers. Science. 2006;**314**:268-274

[21] Wood LD, Parsons DW, Jones S, et al. The genomic landscapes of human breast and colorectal cancers. Science. 2007;**318**:1108-1113

[22] Enhanced KG. Permeability and retention (EPR) effect for anticancer nanomedicine drug targeting. Methods in Molecular Biology. 2010;**624**:25-37

[23] Fang J, Nakamura H, Maeda H. The EPR effect: Unique features of tumor blood vessels for drug delivery, factors involved, and limitations and augmentation of the effect. Advanced Drug Delivery Reviews. 2011;**63**:136-151

[24] Bharali DJ, Khalil M, Gurbuz M, Simone TM, Mousa SA. Nanoparticles and cancer therapy: A concise review with emphasis on dendrimers. International Journal of Nanomedicine. 2009;**4**:1-7

[25] Peer D, Karp JM, Hong S, Farokhzad OC, Margalit R, Langer R. Nanocarriers as an emerging platform for cancer therapy. Nature Nanotechnology. 2007;**2**:751-760

[26] Tomalia DA, Fréchet J. Discovery of dendrimers and dendritic polymers: A brief historical perspective. Journal of Polymer Science Part A: Polymer Chemistry. 2002;**40**:2719-2728

[27] Huck WTS, Prins LJ, Fokkens RH, Nibbering NMM, van Veggel FCJM, Reinhoudt DN. Convergent and divergent noncovalent synthesis of metallodendrimers. Journal of the American Chemical Society. 1998; **120**:6240-6246

[28] Peppas NA, Nagai T, Miyajima M. Prospects of using star polymers and dendrimers in drug delivery and other pharmaceutical application. Pharmaceutical Technology – Japan. 1994;**10**:611-617

[29] Bielinska AU, Kukowska-Latallo JF, Johnson J, Tomalia DA, Baker JR. Regulation of in vitro gene expression using antisense oligonucleotides or antisense expression plasmids transfected using starburst PAMAM dendrimers. Nucleic Acids Research. 1996; **24**:2176-2182

[30] Hawthorne MF. The role of chemistry in the development of boron neutron capture therapy of cancer. Angewandte Chemie International Edition. 1993;**32**:950-984

[31] Caminati G, Turro NJ, Tomalia DA. Photophysical investigation of starburst dendrimers and their interactions with anionic and cationic surfactants. Journal of the American Chemical Society. 1990;**112**:8515-8522

[32] Fréchet JMJ. Functional polymers and dendrimers: Reactivity, molecular architecture. Science. 1994;**263**:1710-1715

[33] Baig TNJ, Dwivedi V, Singh A, Srivastava A, Tripathi PK. A review about dendrimers: Synthesis, types, characterization and applications. International Journal of Advances in Pharmacy, Biology and Chemistry. 2015;**4**:2277-4688

[34] Dong ZQ, Katsumi H, Sakane T, Yamamoto A. Effects of polyamidoamine (PAMAM) dendrimers on the nasal absorption of poorly absorbable drugs in rats. International Journal of Pharmaceutics. 2010;**393**:244-252

[35] Borowska K, Laskowska B, Magon A, Mysliwiec B, Pyda M, Wolowiec S. PAMAM dendrimers as solubilizers and hosts for 8-methoxypsoralene enabling transdermal diffusion of the guest. International Journal of Pharmaceutics. 2010;**398**:185-189

[36] Talanov VS, Regino CAS, Kobayashi H, Bernardo M, Choyke PL, Brechbiel MW. Dendrimer-based nanoprobe for dual modality magnetic resonance and fluorescence imaging. Nano Letters. 2006;**6**:1459-1463

[37] Xu RZ, Wang YL, Wang XL, Jeong EK, Parker DL, Lu ZR. In vivo evaluation of a PAMAM-Cystamine-(Gd-DO3A) conjugate as a biodegradable macromolecular MRI contrast agent. Experimental Biology and Medicine. 2007;**232**:1081-1089

[38] Chinn P, Braslawsky G, White C, Hanna N. Antibody therapy of non-Hodgkin's B-cell lymphoma. Cancer Immunology, Immunotherapy. 2003;**52**:257-280

[39] Norenberg JP, Krenning BJ, Konings IRHM, et al. Bi-213-[DOTA(0),Tyr(3)]octreotide peptide receptor radionuclide therapy of pancreatic tumors in a preclinical animal model. Clinical Cancer Research. 2006;**12**:897-903

[40] Eisenwiener KP, Powell P, Macke HR. A convenient synthesis of novel bifunctional prochelators for coupling to bioactive peptides for radiometal labelling. Bioorganic & Medicinal Chemistry Letters. 2000;**10**:2133-2135

[41] Liu S, Edwards DS. Synthesis and characterization of two (111)In-labeled DTPA-peptide conjugates. Bioconjugate Chemistry. 2001;**12**:630-634

[42] Pippin CG, Parker TA, McMurry TJ, Brechbiel MW. Spectrophotometric method for the determination of a bifunctional DTPA ligand in DTPA-monoclonal antibody conjugates. Bioconjugate Chemistry. 1992;**3**:342-345

[43] Sherry AD, Brown RD, Geraldes CFG, Koenig SH, Kuan KT, Spiller M. Synthesis and characterization of the gadolinium (3+) complex of DOTA-propylamide – a model DOTA-protein conjugate. Inorganic Chemistry. 1989;**28**:620-622

[44] Sieving PF, Watson AD, Rocklage SM. Preparation and characterization of paramagnetic polychelates and their protein conjugates. Bioconjugate Chemistry. 1990;**1**:65-71

[45] Lewis MR, Raubitschek A, Shively JE. A facile, water-soluble method for modification of proteins with DOTA. Use of elevated temperature and optimized pH to achieve high specific activity and high chelate stability in radiolabeled immunoconjugates. Bioconjugate Chemistry. 1994;**5**:565-576

[46] Lewis MR, Shively JE. Maleimidocysteineamido-DOTA derivatives: New reagents for radiometal chelate conjugation to antibody sulfhydryl groups undergo pH-dependent cleavage reactions. Bioconjugate Chemistry. 1998;**9**:72-86

[47] McCall MJ, Diril H, Meares CF. Simplified method for conjugating macrocyclic bifunctional chelating agents to antibodies via 2-iminothiolane. Bioconjugate Chemistry. 1990;**1**: 222-226

[48] Stimmel JB, Stockstill ME, Kull Jr FC. Yttrium-90 chelation properties of tetraazatetraacetic acid macrocycles, diethylenetriaminepentaacetic acid analogues, and a novel terpyridine acyclic chelator. Bioconjugate Chemistry. 1995;**6**:219-225

[49] Liu S, Ellars CE, Edwards DS. Ascorbic acid: Useful as a buffer agent and radiolytic stabilizer for metalloradiopharmaceuticals. Bioconjugate Chemistry. 2003;**14**:1052-1056

[50] Liu S, Cheung E, Ziegler MC, Rajopadhye M, Edwards DS. (90)Y and (177)Lu labeling of a DOTA-conjugated vitronectin receptor antagonist useful for tumor therapy. Bioconjugate Chemistry. 2001;**12**:559-568

[51] Liu S, Edwards DS. Stabilization of (90)Y-labeled DOTA-biomolecule conjugates using gentisic acid and ascorbic acid. Bioconjugate Chemistry. 2001;**12**:554-558

[52] Roberts JC. Preliminary biological evaluation of polyamidoamine (PAMAM) starburst dendrimers. Journal of Biomedical Materials Research. 1996;**30**:53-65

[53] Wolinsky JB, Grinstaff MW. Therapeutic and diagnostic applications of dendrimers for cancer treatment. Advanced Drug Delivery Reviews. 2008;**60**:1037-1055

[54] Malik N, Wiwattanapatapee R, Klopsch R, et al. Dendrimers: Relationship between structure and biocompatibility in vitro, and preliminary studies on the biodistribution of 125I-labelled polyamidoamine dendrimers in vivo. Journal of Controlled Release. 2000;**65**:133-148

[55] Hong SBA, Mecke A, et al. Interaction of poly(Amidoamine) dednrimers with supported lipid bilayers and cells: Hole formation and the relation to transport. Bioconjugate Chemistry. 2004;**15**:774-782

[56] Diall MS, Christie S, Swaminathan P, Balogh L, Shi X, Goddard WA. Dendritic chelating agents 1 cu (II) binding to ethylene diamine core 147 poly(amidoamine) dendrimers in aqueous solutions. Langmuir. 2004;**20**:2640-2651

[57] Pellegrini PA, Howell NR, Shepherd RK, et al. Synthesis and Radiolabelling of DOTA-linked glutamine analogues with Ga-67,Ga-68 as markers for increased glutamine metabolism in tumour cells. Molecules. 2013;**18**:7160-7178

[58] Biricova V, Laznickova A, Laznicek M, Polasek M, Hermann P. Radiolabeling of PAMAM dendrimers conjugated to a pyridine-N-oxide DOTA analog with 111In: Optimization of reaction conditions and biodistribution. Journal of Pharmaceutical and Biomedical Analysis. 2011;**56**:505-512

[59] Ghai A, Singh B, Hazari PP, Schultz MK, Parmar A, Kumar P, et al. Radiolabeling optimization and characterization of [68Ga] labeled DOTA–polyamido-amine dendrimer conjugate -animal biodistribution and PET imaging results. Applied Radiation and Isotopes. 2015;**105**:40-46

[60] Harris WR. Thermodynamic binding constants of the zinc human-serum transferrin complex. Biochemistry. 1983;**22**:3920-3926

[61] Fani M, Andre JP, Maecke HR. Ga-68-PET: A powerful generator-based alternative to cyclotron-based PET radiopharmaceuticals. Contrast Media & Molecular Imaging. 2008;**3**:53-63

[62] de Sa A, Matias AA, Prata MIM, Geraldes CFGC, Ferreira PMT, Andre JP. Gallium labeled NOTA-based conjugates for peptide receptor-mediated medical imaging. Bioorganic & Medicinal Chemistry Letters. 2010;**20**:7345-7348

[63] Roivainen A, Tolvanen T, Salomaki S, et al. Ga-68-labeled oligonucleotides for in vivo imaging with PET. Journal of Nuclear Medicine. 2004;**45**:347-355

[64] Harris WR, Pecoraro VL. Thermodynamic binding constants for gallium transferrin. Biochemistry. 1983;**22**:292-299

[65] Bartholoma MD, Louie AS, Valliant JF, Zubieta J. Technetium and gallium derived radiopharmaceuticals: Comparing and contrasting the chemistry of two important radiometals for the molecular imaging era. Chemical Reviews. 2010;**110**:2903-2920

[66] IAEA. Role of internal dosimetry in nuclear medicine. Report of a Consultancy Meeting [WWWDocument] Available from: /http://nucleus.Iaea.Org/HHW/MedicalPhysics/NuclearMedicine/InternalDosimetry/consultantsreport/Report_of_CM_Internal_Dosimetry.pdfS. 2012

[67] Bolch WE, Eckerman KF, Sgouros G, Thomas SR. MIRD pamphlet No. 21: A generalized schema for radiopharmaceutical dosimetry-standardization of nomenclature. Journal of Nuclear Medicine. 2009;**50**:477-484

[68] Kaul A. Radiation dose to patients from radiopharmaceuticals: Addendum 3 to ICRP Publication 53. Ann ICRP. 2008; 38

[69] Kesner ALHW, Czernin J, Padgett H, Phelps ME, Silverman DH. Radiation dose estimates for [18F]5-fluorouracil derived from PET-based and tissue-based methods in rats. Molecular Imaging and Biology. 2008;**10**:341-348

[70] Banerjee D, Harfouche R, Sengupta S. Nanotechnology-mediated targeting of tumor angiogenesis. Vascular Cell. 2011;**3**:3

Section 2

Dendrimers as Functional Materials

Chapter 5

Azodendrimers as a Functional Material

Hideo Takezoe and Osamu Haba

Additional information is available at the end of the chapter

http://dx.doi.org/10.5772/intechopen.70715

Abstract

Dendrimers can behave as active functional materials, if they are substituted at their tail ends by azo groups. The dendrimers we developed spontaneously attach to interfaces or surfaces, providing us with a variety of functions. After describing the synthesis of dendrimers and azodendrimers, we first review functions for static uses; alignment surface for liquid crystals (LCs). Then, a major part of this review is devoted to the introduction for dynamic uses. Because of photo-induced *trans-cis* isomerization, the azodendrimers act as a command surface, which enables us to control LC orientation. Azodendrimer layers were formed at glass substrates, LC droplets in polymers, and surfaces of microparticles in LCs. Photo-controlled *trans*- and *cis*-forms, respectively, provide homeotropic and planar orientations of LCs. The photo-irradiation induces dewetting of dendrimer layers as well. Photo-induced orientation changes of LCs provide us with various applications and novel phenomena; photo-controlled macroscopic physical properties such as thermal transport, defect structure changes in LC colloids and LC systems with microinclusions, and even dynamics of inclusions in LCs.

Keywords: azo, surface, interface, liquid crystal, command surface, photo-induced phenomenon, dewetting, liquid crystal colloid, microparticle, defect structure

1. Introduction

Azo molecules show photo-induced conformational changes based on *trans-cis* photo-isomerization. The conformational changes lead to various functions such as a macroscopic deformation in polymers containing azo groups [1] and a command surface for liquid crystals (LCs) providing orientation changes [2, 3]. The readers may find a lot of review articles on this topic [4]. Dendrimers have a controlled structure with a central core and well-defined branched terminals and have been an expanding research area in recent three decades [5]. We can easily imagine that dendrimers with azo chromophores (azodendrimers) in the internal structure and on peripheries are quite intriguing research aspects in material

science and applications. Namely, photo-irradiation onto azodendrimers exerts not only the *trans-cis* conformational change of azo moiety but also the dendrimer structure, which brings about a variety of functions [6]; switching device or data storage using Langmuir-Blodgett films of azodendrimer molecules [7], active materials for electro-optic applications [8], LC photo-orientation [9], photo-controlled chirooptics [10], and enhanced optical nonlinearity [11]. We found some additional benefits by introducing azo linkages into our dendrimers. In this chapter, we review such functions offered by azobenzene-containing dendrimers (azodendrimers). After an introduction and syntheses of azodendrimers, we describe (1) spontaneous surface modification by dendrimers for LC displays, (2) application for controlling physical parameters, (3) photo-triggered dewetting surface and its control, (4) application to memory devices using a LC showing an anchoring transition, (5) command surfaces in restricted surfaces such as LC droplets, silica microparticle surfaces, and (6) controlling surface anchoring strength for LC orientation. Through these applications, we want to emphasize the important functions, which are provided not only by dendrimers themselves but also by introducing azo groups into dendrimers.

2. Motivation and synthesis

Dendrimers are a kind of polymeric materials consisting of regular multi-branched structure with a specific topology. Dendrimers are known to exhibit low viscosity and good solubility comparing with linear polymers with comparable molecular weights because of less tangled molecular structures. Their molecular structures consist of core units, branched repeating units, and terminal groups. The modifications of the terminals are quite easy because the terminal functional groups are not hindered unlike the functional groups bound to the crowding main chain of linear polymers.

Introducing mesogenic groups into the terminal groups of flexible dendrimers provides the dendrimers with liquid crystalline natures [12]. Then we can expect better compatibility of the dendrimer with LCs. Such liquid crystalline dendrimers can be prepared using commercial polypropyleneimine dendrimers (PPIDs), whose chemical structure is shown in **Figure 1(a)**, and mesogen-carrying acrylates through the double-Michael addition to produce tertiary amine linkages, as shown in **Figure 1(b)** [13]. For the latter, we can use numerous acrylates, which have been reported in many literatures, developed for the syntheses of side-chain liquid crystalline polymers. The reaction can be carried out by simply heating in THF solution at 40–50°C, but requires two or more weeks in order to prevent the reaction from stopping at the secondary amine stage, which is difficult to be removed from the final product. Once the complete Michael addition, which means the absence of the residual primary or secondary amines, can be achieved, the resulting liquid crystalline dendrimer can be purified by simple precipitation to poor solvents such as methanol or hexane, which is chosen based on the solubility of the mesogenic units.

We have introduced various mesogens including biphenyls, phenyl benzoates, cyclohexylbenzene, and azobenzenes, as shown in **Figure 2** [13, 14]. We refer the liquid crystalline dendrimers as D*G*-*n*X, where *G* is the generation of PPID, *n* is the number of carbon atoms of the alkylene spacer between PPID and the mesogenic unit, and X represents the mesogen. The

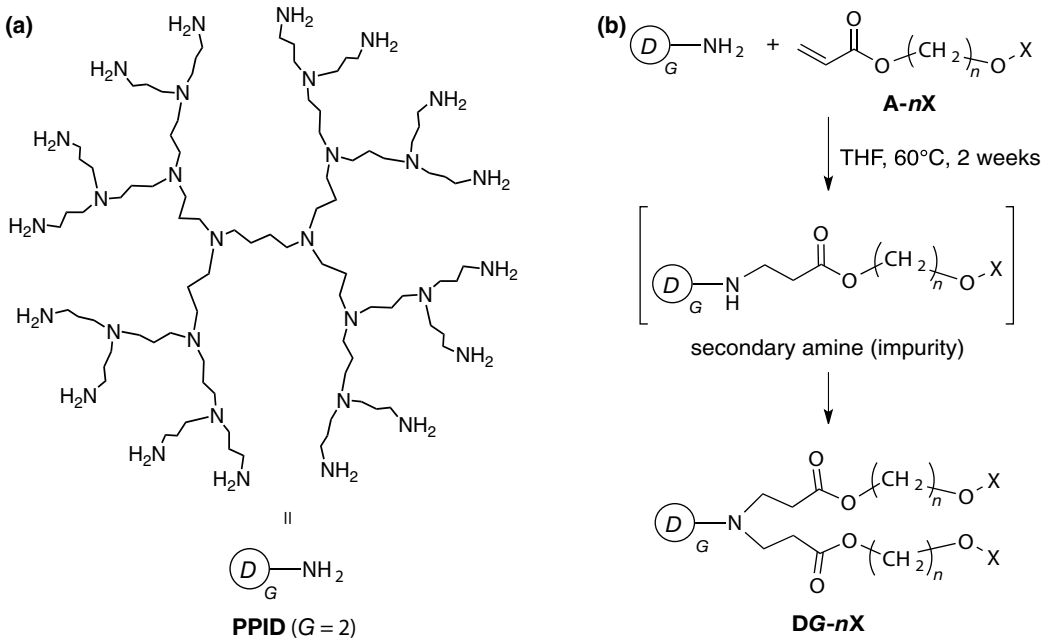

Figure 1. (a) Chemical structure of a polypropyleneimine dendrimers (PPID). *G* indicates the generation of PPID. (b) Preparation scheme of a liquid crystalline dendrimer from PPID and a mesogen-carrying acrylate. For X, see **Figure 2**.

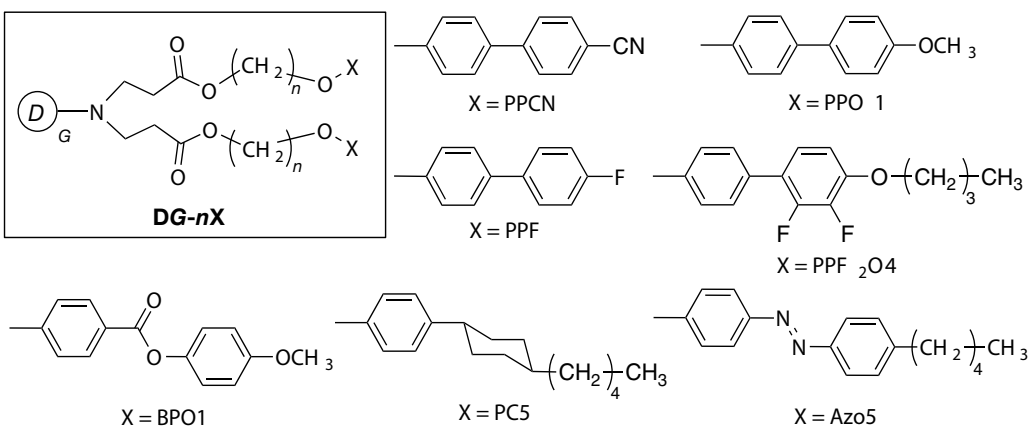

Figure 2. Chemical structures of mesogenic groups used for the preparation of liquid crystalline dendrimers synthesized. Please refer to **Table 1** for the phase sequences of each molecule.

obtained dendrimers exhibited thermotropic liquid crystalline nature. The phase transition temperatures are shown in **Table 1**. Regardless of the mesogen structure, the dendrimers tend to exhibit smectic (Sm) liquid crystalline phases. In the DG-10PPF$_2$O4 series, the larger generations of PPID made the smectic-isotropic transition temperature higher, but the generation

Dendrimer	Phase transition temperature[a]/°C	Homeotropic alignment[d]
D2-6PPCN	I 68 SmA −5 G	+
D2-6PPO1	I 96 SmA 90 SmE[b]	−
D2-6PPF	I 50 SmE[b]	−
D1-10PPF$_2$O4	I 72 SmA 56 SmE[b]	−
D2-10PPF$_2$O4	I 78 SmA 58 SmE[b]	+
D3-10PPF$_2$O4	I 86 SmA 51 SmE[b]	+
D4-10PPF$_2$O4	I 91 SmA 54 SmE[b]	+
D5-10PPF$_2$O4	I 97 SmA 54 SmE[b]	−
D2-6BPO1	I 67 SmA −3 G	−
D2-3PC5	I 74 SmA 16 SmB −14 G	+
D2-6PC5	I 69 SmA 17 SmB −21 G	+
D2-12PC5	I 80 SmA 73 SmB 5 G	−
D2-6Azo5	G − 5 SmB 34 SmA 85 I[c]	+

Signs: +, exhibited homeotropic orientation; −, exhibited random orientation.
[a]Recorded during the 2nd cooling scan with $\Delta T = -10$°C/min.
[b]Glass transition temperatures were not observed above −20°C.
[c]Recorded during the heating scan ($\Delta T = 10$°C/min).
[d]Tendency to show spontaneous homeotropic alignment between glass plates on slow cooling.

Table 1. The phase transition temperatures and the homeotropic alignment capability of the liquid crystalline dendrimers.

(*G*) did not affect the liquid crystalline phase. In the D2-*n*PC5 series, the longer alkylene spacers tend to stabilize the SmB phase rather than the SmA phase, which influences the spontaneous alignment of the dendrimers in cells, as will be mentioned below.

Some dendrimers exhibit spontaneous homeotropic orientation between two bare glass surfaces on slow cooling (typically $\Delta T = -1$°C/min). **Figure 3** shows the polarizing optical microscope images of D2-6PC5 under crossed polarizers during slow cooling from the isotropic melt. The focal conic texture disappeared and the area of a dark field gradually expanded. The typical cross isogyre was observed in the dark field by conoscopic observation under a polarizing optical microscope. From these results, we confirmed the homeotropic orientation of D2-6PC5 between bare glass surfaces.

These orientation behaviors are strongly influenced by the mesogenic phase structure. **Table 1** also lists the tendency to exhibit spontaneous homeotropic orientation together with the phase sequences. Among the D2-6X series, homeotropic orientation was observed for X = PPCN, PC5, and Azo5 as well as D2-10PPF$_2$O4. These dendrimers exhibited relatively wide temperature ranges of the SmA phase. On the other hand, the mesogens, PPO1 and PPF, showed a narrow SmA temperature range and no SmA phase, respectively. The similar tendency was more clearly observed in D2-*n*PC5 series. D2-12PC5, whose SmA range is only 7–8 K, did not

http://dx.doi.org/10.5772/intechopen.70715

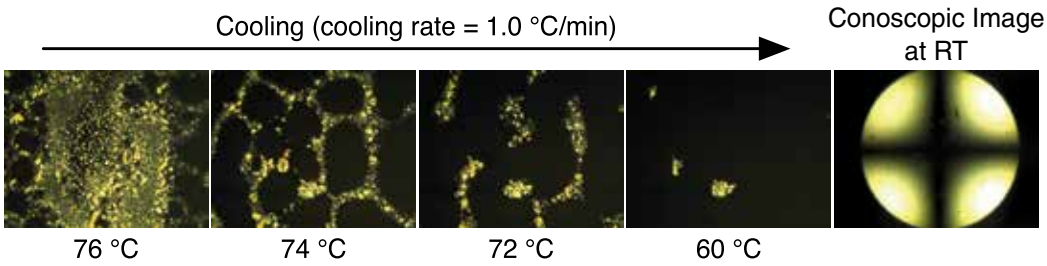

Figure 3. Photomicrographs of D2-6PC5 under crossed polarizers during slow cooling from the isotropic melt (from left to right, DT = −1°C/min). A conoscopic image at room temperature is also shown on the right.

exhibit the homeotropic orientation. In contrast, D2-*n*PC5's with $n = 3$ or 6 have a wide SmA range of around 50 K, and show good spontaneous homeotropic orientation. Therefore, the spontaneous homeotropic orientation seems to be realized in mesogens with the stable SmA phase, in which mesogens can easily move within the SmA layer structure rather than in the more highly ordered SmB or SmE phases. However, D2-6BPO1 did not show homeotropic orientation, although it exhibited the stable SmA phase. Thus, the orientation might require the alkyl termini longer than four carbons like PC5, Azo5, and PPF_2O4. The effect of the generation can be seen in D*G*-10PPF_2O4 ($G = 1$–5): the 1st and the 5th generation dendrimers did not align homeotropically. The former ($G = 1$) may not form well-ordered smectic structure. As for the latter ($G = 5$), the molecule is so large that the molecule becomes a spherical shape due to the steric repulsion between the terminal mesogens.

3. Application for liquid crystal alignment

The present dendrimers have an advantage for providing spontaneous LC alignment at surfaces and interfaces. In other words, no pretreatment of surfaces is necessary for obtaining good alignment. This advantage can be used for manufacturing LC displays. In this section, we introduce two applications of dendrimer molecules for LC alignment; LC displays and controlling physical parameters of LC cells.

The first issue to be discussed is how dendrimer molecules align at surfaces. Based on X-ray diffraction measurements, Li et al. [15] assigned a strong diffraction peak in a small angle region to $n = 2$ and concluded the periodicity corresponds to a stretched structure shown in **Figure 4(a)** [15]. However, other researchers assign this peak to $n = 1$ [16] and the periodicity is concluded to a half the stretched molecular length. Hence, the surface structure could be **Figure 4(b)** [17] or **Figure 4(c)** [18]. Additional important information for the surface structure is that the surface with azodendrimers is optical second-harmonic generation (SHG) active. **Figure 5** shows SHG intensity as a function of UV intensity [19]. The film is SHG active without UV irradiation. This is consistent with the models shown in **Figure 4(b)** and **(c)**. With increasing UV light intensity, SHG activity decreased. This is because the transformation to the *cis*-form destroys the polar orientation order. Further details are a future problem.

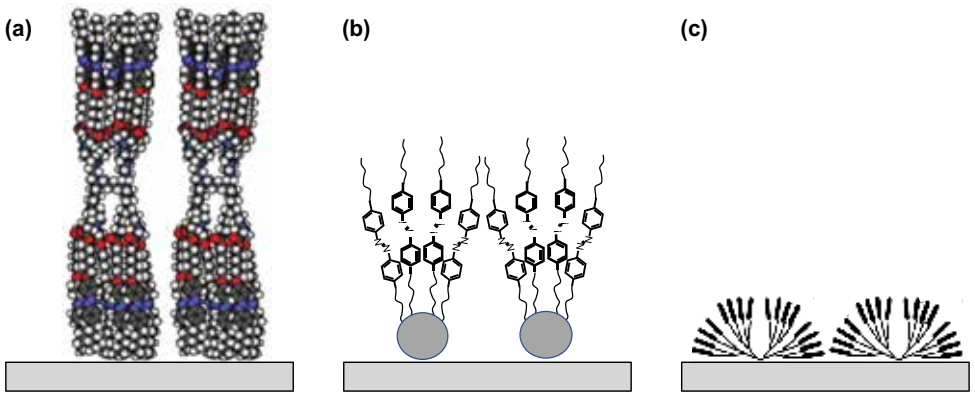

Figure 4. Model structures of dendrimer molecules adsorbed on a surface, (a) symmetric shape [15], (b) asymmetric shape [17], and (c) asymmetric fan shape [18]. Copyright 2012, American Chemical Society [15], Copyright 2015, National Academy of science [17], and Copyright 2014, Optical Society of America [18].

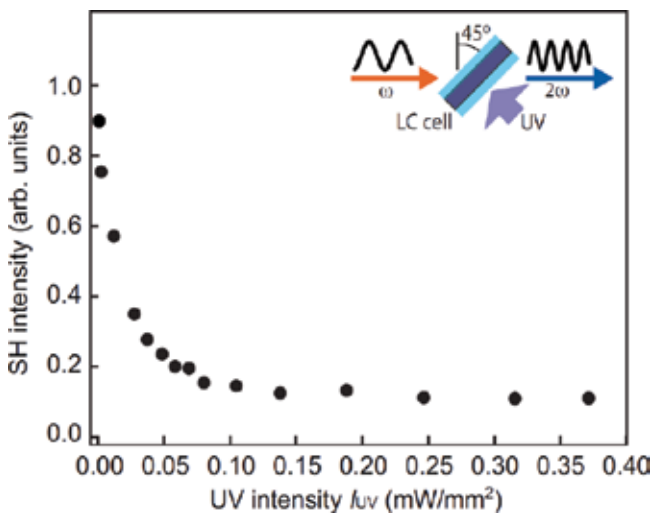

Figure 5. SHG intensity as a function of UV intensity [19]. Optical geometry is also shown in the figure. Copyright 2017, Royal Society of Chemistry.

3.1. Application for liquid crystal display

LC displays are essentially driven by an electric field. Hence, photo-induced switching is not relevant in LC displays. However, to introduce the capability of spontaneous alignment of LCs at surfaces/interfaces by the present dendrimers, we cannot avoid the description of the LC display application using dendrimers with and without azo linkages (see **Figure 2**).

The most important property is spontaneous adsorption of dendrimers onto substrate surfaces, resulting in spontaneous homeotropic alignment of LCs, which makes pre-surface treatment-free or polyimide-free LC displays possible [20]. The process of LC introduction into

an empty cell shown in **Figure 6(a)** and **(b)** are illustrations of the initial and final stages of the introduction of LCs containing dendrimers, respectively [21]. A corresponding texture is shown in **Figure 6(c)** [22]. In the injected area (right), homeotropic alignment is realized, but in the area far from the entrance (left), planar alignment is obtained because of the lack of surface coverage by dendrimers.

The application of dendrimers to a LC display was first reported in IDW (International Display Workshop) in 2011 [20]. Since the unperturbed state is homeotropic, application is principally possible for vertical alignment (VA) mode. The main advantage is of course polyimide-free spontaneous homeotropic (vertical) alignment just by dissolving dendrimers in LCs used. Momoi et al. [20, 21, 23] used a large glass substrate with dimensions 100 mm × 100 mm and large ITO interdigitated electrodes used for the in-plane switching (IPS) mode. The electrode with the gap of 10 μm covers a 10 mm × 10 mm area. **Figure 7** shows photographs of (a) off and (b) on states of a test cell of an LC mixture ZLI-4792 (Merck) containing 1% D2-6PC5 (see **Figure 2**) [20, 23]. The corresponding orientation change during the electro-optic switching between dark and bright is illustrated in **Figure 7(c)** and **(d)** [24]. A polarizing microscope image and a temporal electro-optic response behavior are shown in **Figure 8** [18].

An important question for practical applications is whether this method using dendrimers is applicable for all LCs and surfaces or not. Haba et al. [18] addressed this question. They used two dendrimers (D2-6PPCN and D2-6PC5) as shown in **Figure 2**, and two LCs; 4′-cyano-4-n-penthylbiphenyl (5CB) and a mixture ZLI-4792. Although 5CB could dissolve both dendrimers,

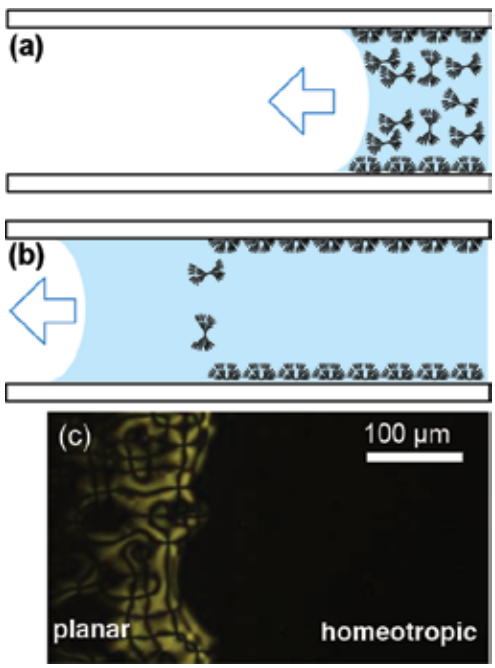

Figure 6. Cartoons showing the introduction of LC with dendrimers into a cell; (a) initial and (b) final stages. Actual photomicrograph image corresponding to (b) is also shown in (c).

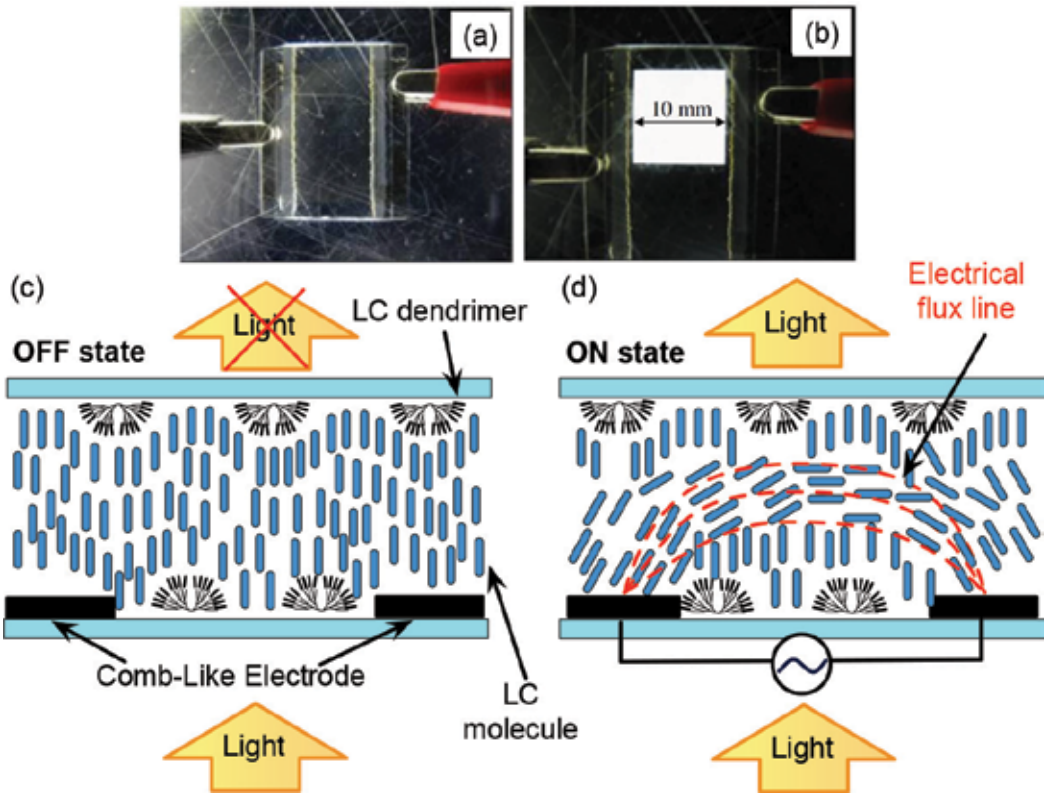

Figure 7. Electro-optic performance. Photographs of (a) off and (b) on states of a test cell [23]. The corresponding sectional images of the director orientations are also shown in (c) and (d), respectively. Copyright 2012, Society for Information Display.

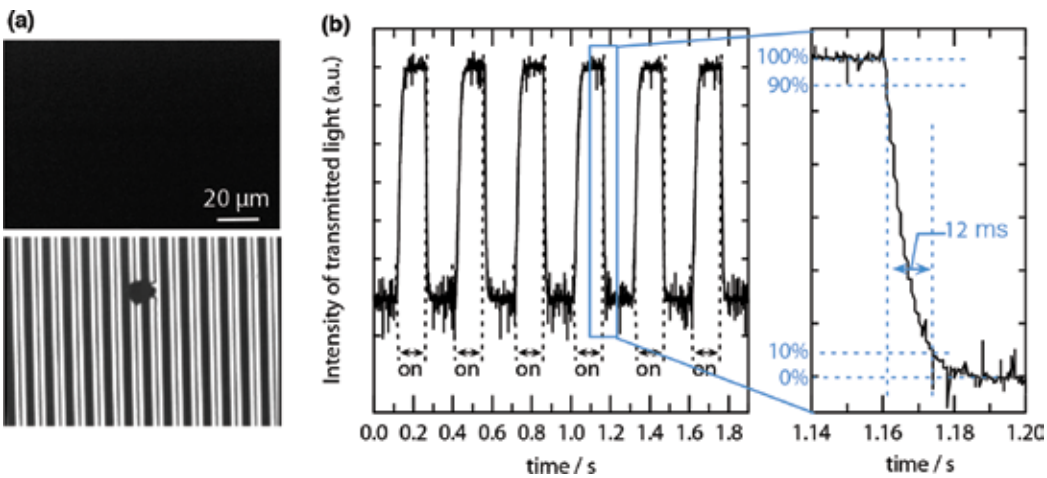

Figure 8. Electro-optic response [18]. (a) Polarizing optical microscope images in off (upper) and on (lower) states. (b) Temporal transmittance changes during sequential electric field application and termination. Copyright 2014, Optical Society of America.

D2-6PCN was not soluble in ZLI-4792. Both D2-6PPCN/5CB and D2-6PC5/ZLI-4792 gave good homeotropic alignment in the absence of an electric field. The surface free energy of substrates was found to be another important factor for good homeotropic alignment. Examination of contact angles for various surfaces showed that hydrophilic surfaces are important for good homeotropic alignment.

Another question is a possible use of azodendrimers for planar alignment, which is necessary for the twisted nematic (TN) and IPS modes. A new dendrimer was successfully developed for this purpose [25]. It is well known as a command surface [2] that surface azobenzene layer commands the orientation change from homeotropic-to-planar by photo-isomerization of the azobenzene. A cartoon of this phenomenon in the present azodendrimer case is illustrated in **Figure 9**. For the present purpose of IPS mode displays, however, there are two problems such as (1) prohibiting the relaxation to the *trans*-state and (2) realization of uniform planar orientation.

In order to prevent the relaxation and fix the planar orientation, we introduced a cinnamate group (**Figure 10(a)**), which is expected to dimerize and prevent the transformation of the *cis*-form to the *trans*-form. To examine the LC orientations upon photo-isomerization and relaxation, nematic LC mixture JC-5066XX (JNC, Japan) was doped with 1 wt% azodendrimer (D2-6AzoCin2). Solubility was poor and planar orientation was observed in most of the mixtures. Some of however, showed a good homeotropic orientation as shown in **Figure 10(b)**. Upon UV irradiation, the schlieren texture showing a planar orientation emerged, as shown in **Figure 10(c)**. More importantly, the planar texture remained after 72 days, as shown in **Figure 10(d)**. When we used D2-6Azo5 without a cinnamate group (**Figure 2**), however, stable planar orientation was not obtained after terminating UV irradiation. Thus, the cinnamate group in D2-6AzoCin2 is important for a stable and sustainable planar orientation [25]. We confirmed prolonged stability after 133 days using a different LC mixture (ZLI4792) [25].

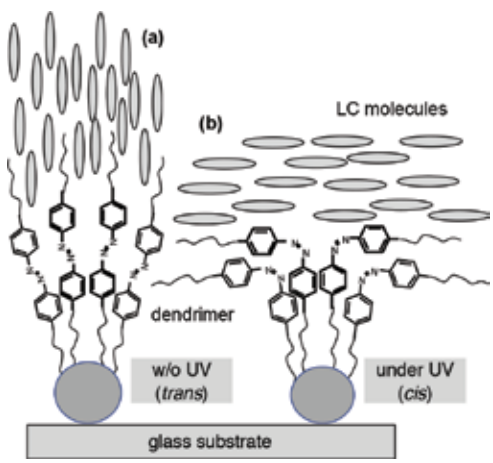

Figure 9. Cartoons showing a command surface effect. (a) Without UV light irradiation, dendrimers are in the *trans*-state, resulting in homeotropic orientation. (b) Unver UV light irradiation, dendrimers are in the *cis* state, resulting in planar orientation.

The second problem, uniform planar alignment, could be solved by using linearly polarized UV light irradiation [25]. Preferential orientation of LCs along the direction perpendicular to the polarization of UV light is well known [3]. The result is shown as photo-micrograph images under crossed polarizers subjected to a rotation of a microscope stage, as shown in **Figure 11**. At angles 0° (parallel to the linear polarization of UV light), complete dark views were obtained. At 45°, bright views due to the birefringence were obtained. Thus, a uniform planar alignment was successfully obtained. Electro-optic response was confirmed to occur. The detailed examination of the electro-optic response is a future problem.

3.2. Application for controlling physical parameters

As mentioned in Section 3.1, the present dendrimer molecules are useful for aligning LCs without pretreatment of surfaces. Initially, the surfaces force LCs to align homeotropically, as mentioned in Section 3.1. If we use azodendrimers, the surface acts as a command surface; UV and VIS light irradiation commands LC molecules to make planar and homeotropic orientations, respectively, due to *trans-cis* photo-isomerization (**Figure 9**). Since LCs have anisotropy,

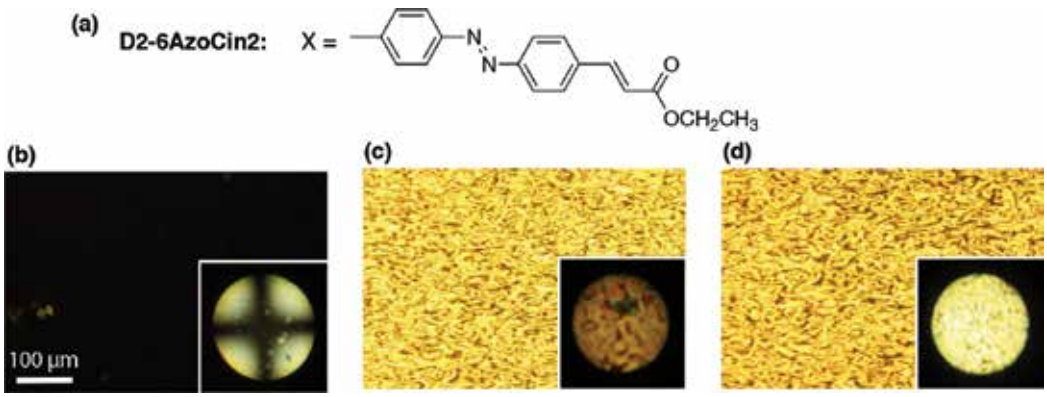

Figure 10. (a) Chemical structure of an azodendrimer with cinnamate tails. Please refer to **Figure 2** for X. Polarizing photomicrographs in (b) without UV light irradiation, (c) immediately after UV light irradiation, and (d) 72 days after terminating UV light. Photos taken by Mr. Shun Sato.

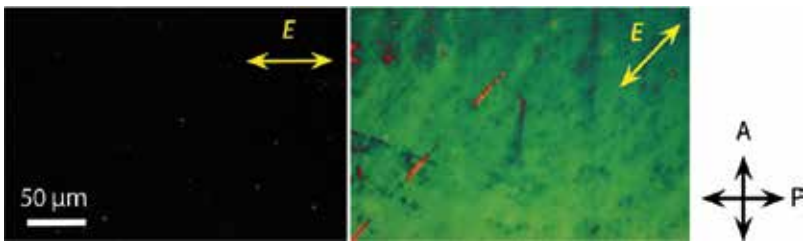

Figure 11. Polarizing photomicrographs of a cell after linearly polarized UV light irradiation. Two images are taken during the cell rotation under crossed polarizers. Photos taken by Mr. Shun Sato.

their physical parameters are also anisotropic. Namely, refractive index, dielectric constant, electric conductivity, etc. have different values depending on the direction with respect to the director. Actually, LC displays utilize the light transmittance change due to refractive index change caused by electric field-induced orientation change. We may find other applications by controlling the physical parameters using external stimuli. An electric field is one of important external stimuli, but is not always necessary. Instead, light irradiation is another useful external stimulus. Here we introduce a possible device using photo-controllable thermal diffusivity [26].

The sample used was 4′-n-pentyloxybiphenyl-4-carbonitrile (5OCB) containing a small amount (0.02 wt%) of azodendrimers. The thermal diffusivity was measured by a temperature wave method [27]. **Figure 12(a)** shows a temperature dependence of thermal diffusivity for a sample under UV (365 nm) light irradiation (cross), under VIS (420 nm) light irradiation (open circle), and without light irradiation (filled circle). It is natural to have a good agreement between the latter two data because of the same homeotropic alignment in both conditions. Photo-induced switching of the thermal diffusivity at 54°C is shown in **Figure 12(b)**. Upon UV and VIS light irradiation, the thermal diffusivity drastically changes almost by two times. The switching speed depends on light intensity. It was found that the switching rate linearly depends on UV and VIS light intensities. Under a moderate light intensity such as 5–10 mW/cm^2, the response time of a few tens of seconds was obtained.

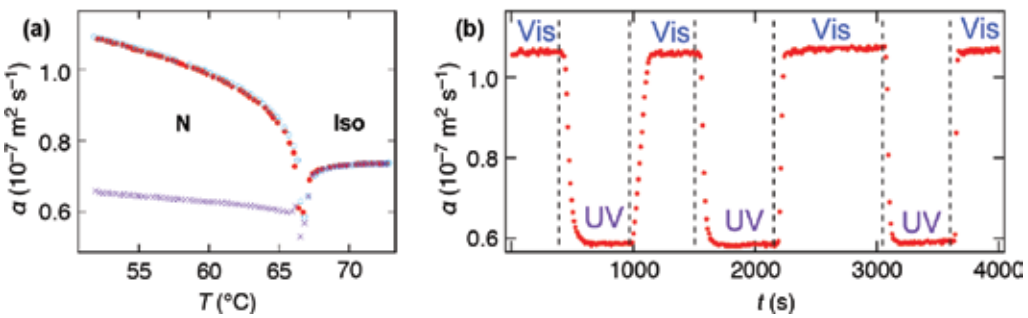

Figure 12. (a) Temperature dependence of thermal diffusivity under UV light irradiation (cross), under VIS light irradiation (open circle), and without light irradiation (filled circle). (b) Photo-induced temporal change of thermal diffusivity [26]. Copyright 2015, AIP Publishing.

4. Photo-triggered surface dewetting

One of the important applications of azo molecules is a surface relief grating formation, which is based on the phenomenon of photo-induced mass migration in azo-containing polymer films [28], low-molecular-mass azo compounds [29], and even in dendron-containing compounds [30]. According to Seki et al. [31], the mass migration in liquid crystalline azopolymers is highly sensitive to UV light compared with conventional amorphous polymer films. In this sense, the azodendrimer systems are a very attractive candidate for efficient mass migration upon UV light irradiation.

For experiments [15], quartz substrates were properly cleaned to be hydrophilic. Chloroform solution of azodendrimers was spin coated on such substrates. The samples were subjected to UV light irradiation.

Figure 13 shows atomic force microscopy (AFM) images of D2-6Azo5 after UV light irradiation under different conditions. The morphological change is remarkable, exhibiting the surface dewetting and providing a number of separated domains of a few micrometers [15]. Note that a linear polymer of almost identical molecular mass showed no change under the same experimental condition. Another important condition is the hydrophobicity of the substrate. No dewetting behavior was observed under the same experimental condition when hydrophobic surfaces were used. The morphological structure depends on many factors such as UV intensity, irradiation duration, film thickness, etc. The initial flat surface started to change above UV light intensity of 150 mJ cm^{-2}. First, holes grew, coalesced, and formed dome structures with increasing UV light intensity. Under UV light intensity of 400 mJ cm^{-2}, the dome height reached 770 nm, which was about eight times of the initial film thickness. The film thickness dependence of the morphology is shown in **Figure 13(a)**. With increasing the film thickness, the dome size increased and the dome density decreased. The films thicker than 100 nm did not show dewetting. Instead, some protrusions of several micrometers diameters were observed on the film surface. Patterned structure formation such as a surface relief grating is also possible using patterned UV light irradiation through photomasks. The result reflects the film thickness dependence. Namely, as shown in **Figure 13(b)**, hierarchical morphologies were observed in films thinner than 100 nm, but ordinary surface relief grating was formed in a film of 120 nm thick.

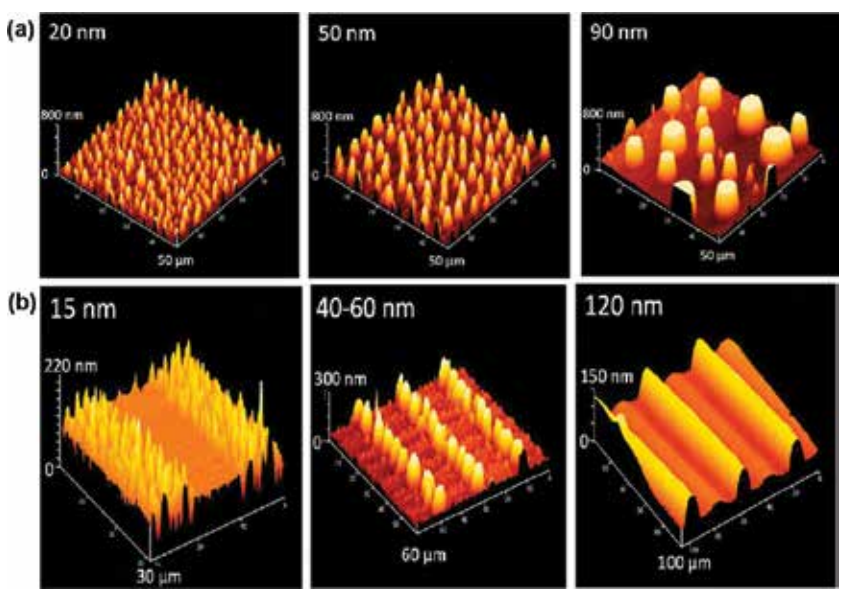

Figure 13. AFM images of azodendrimer surface layer with different thicknesses after UV light irradiation [15]. (a) Uniform and (b) patterned UV light irradiation. A sample with a 120 nm thick layer in (b) shows a simple conventional surface relief grating. Copyright 2012, American Chemical Society.

5. Memory device

LC devices are usually fabricated as sandwich cells with different surface orientations planar, homeotropic, and hybrid orientations obtained using two planar surfaces, two homeotropic surfaces, and (planar/homeotropic) surfaces, respectively. If we can manipulate the surface orientation locally, we can make memory devices. LC displays are one of the examples, where an electric field is applied using matrix-type electrodes to change the LC orientation locally. In this case, however, the perturbed LC orientation returns back to the original one after terminating the field, since the stable orientation is guaranteed by the surface anchoring condition. Using light irradiation is another useful technique for driving devices.

We proposed a novel bistable device using an anchoring transition and a command surface [32]. This device (**Figure 14(c)**) has advantages compared with devices, which use only anchoring transition (**Figure 14(a)**) [33] or command surface (**Figure 14(b)**) [2]. Here the anchoring

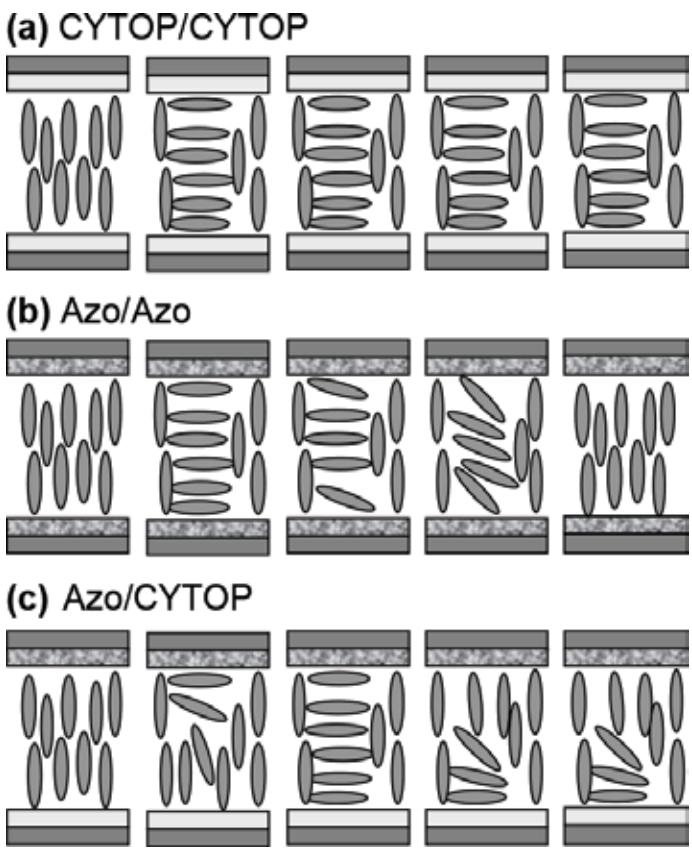

Figure 14. Cartoons showing orientation change upon UV light irradiation and termination (from left to right) in three cells with different surface layers; (a) CYTOP/CYTOP, (b) azodendrimer/azodendrimer, and (c) azodendrimer/CYTOP hybrid. Intense light irradiation is needed for an orientation change in (a). An induced planar orientation relaxes back to a homeotropic orientation in (b). A hybrid orientation is established and preserved in (c).

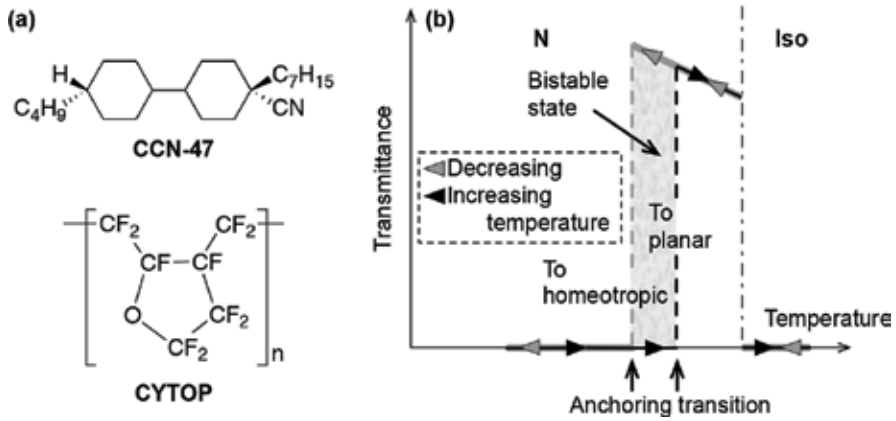

Figure 15. (a) Molecular structures of a LC compound (CCN-47) and a surface layer (CYTOP). The LC cell with the combination of CCN-47 and CYTOP exhibits a discontinuous anchoring transition. (b) Cartoon illustrating a discontinuous anchoring transition with a bistable temperature range (hatched area).

transition we used was a spontaneous discontinuous orientation transition between planar and homeotropic orientations. This phenomenon was clearly observed in a commercial compound 4′-butyl-4-heptyl-bicyclohexyl-4-carbonitrile (CCN-47, Merck) sandwiched by glass substrates with poly[perfluoro(4-vinyloxy-1-butene)] (CYTOP, Asahi Glass) (**Figure 15(a)**) on their surfaces [33]. As schematically shown in **Figure 15(b)**, the transmittance of the cell between crossed polarizers appears at the Isotropic (Iso)-nematic (N) transition, and suddenly drops to zero by decreasing temperature. This process is the manifestation of a discontinuous anchoring transition from planar to homeotropic alignment. On heating, the reverse change is observed at different temperatures. This means that there exists a temperature range (hatched area in **Figure 15(b)**) showing bistable states, where both planar and homeotropic orientations are stable. The existence of the bistable states provides us with a bistable memory device [34].

We constructed a hybrid cell consisting of CYTOP-coated and bare glass substrates (**Figure 14(c)**) and introduced a small amount (0.05 wt%) of azodendrimer molecules into the CCN-47 host [32]. In this cell, we confirmed stable performance as a memory device, as described in the following. First, the hybrid cell was cooled to room temperature. At this condition, the homeotropic orientation was realized. Then the cell was heated to a bistable temperature region, keeping the homeotropic orientation (dark view under crossed polarizers). UV light irradiation onto the cell induced the anchoring transition at the azodendrimer surface. The orientation change to a planar state propagated to the opposing surface, resulting in a bright spot. Since the anchoring transition is light-driven, the UV light intensity was very low (35 $\mu W/mm^2$), compared with laser (heat)-driven anchoring transitions (1 kW/mm^2) [34]. Hence, the present hybrid device is advantageous to the devices using only the anchoring transition (**Figure 14(a)**).

The advantage of the hybrid device over the device using only command surfaces (**Figure 14(b)**) is clear. If we use sandwich cells with azodendrimer-attached surfaces in both sides without using CYTOP, the azodendrimers play as a command surface, that is, a homeotropic-to-planar

orientation change occurs locally at the spot under UV irradiation. However, the life time of the *cis* (excited) state is finite, a few minutes to an hour depending on LCs (solvents) used. Hence, the planar orientation relaxes to the homeotropic orientation with time. On the contrary, the planar orientation at the CYTOP surface is very stable in the bistable temperature range. Hence after the relaxation to the *trans*-state at the dendrimer surface, a hybrid orientation, namely a homeotropic orientation at the dendrimer surface and a planar orientation at the CYTOP surface, is stabilized. The advantages of the present hybrid cell over cells with only CYTOP surfaces or only azodendrimer surfaces are clearly displayed in **Figure 14**. In this way, azodendrimer surfaces provide us with highly photo-sensitive surface for writing in devices keeping the memory capability using the anchoring transition phenomenon.

6. Photo-switching of liquid crystal orientation in different geometries

The azodendrimer command surface facing to LCs makes photo-switching of LC orientation possible, as mentioned above (see **Figure 9**). This phenomenon is well known on flat substrate surfaces, which are necessary to be coated with azo molecules before fabricating cells [2]. The present azodendrimers have a characteristic feature that the azodendrimer molecules are spontaneously adsorbed at interfaces. This means that we need no pretreatment of surfaces. Moreover, the molecules can be attached at interfaces, which we cannot intentionally treat beforehand, such as liquid/liquid interfaces. Only thing we have to do is just dissolving the azodendrimer molecules into LCs before preparing samples. Four examples are introduced in the following.

6.1. Defects in liquid crystal droplets

If LC molecules are mixed with other liquid materials such as water or glycerol and stirred, LC forms droplets with different sizes (**Figure 16(a)**). The formation of LC microdroplets with a

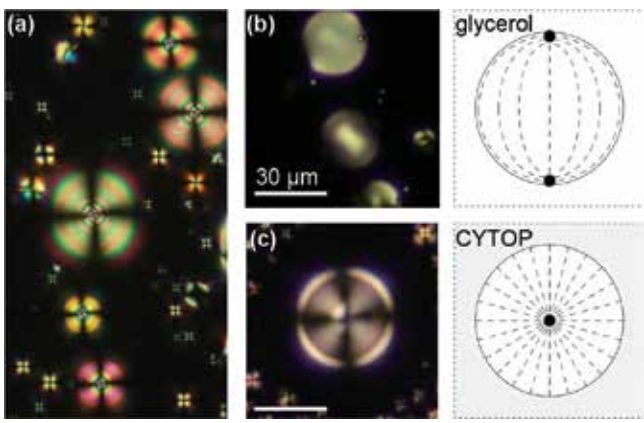

Figure 16. (a) Photomicrograph of LC droplets in water. Photomicrographs of a droplet of 5CB in (b) glycerol and (c) CYTOP [22]. If 5CB is doped with azodendrimers and is dispersed in glycerol, a radial orientation is realized like in (c). The structure changes from radial-to-bipolar by UV irradiation like in (b) [22]. Copyright 2013, John Wiley & Sons, Inc.

uniform size is one of topical fields, that is, microfluidics, which are interesting both from basic science and various applications [35].

The studies of LC microdroplets have been conducted since long time ago [36]. The LC orientations at interfaces are fixed when background liquid is chosen: LC molecules orient tangentially at glycerol interfaces. On the other hand, in aqueous solutions and hydrophobic polymer CYTOP, LC molecules align normal to the interface. Under crossed polarizers, LC droplets in glycerol and CYTOP show a bipolar image and a dark cross, respectively, being characteristic of tangential and radial molecular orientations, respectively, as shown in **Figure 16(b)** and **(c)** [22]. In previous studies, fixed surface conditions were used except for a work by Yamamoto et al. [37]. We introduced the azodendrimer molecules into host LCs, which provide normal orientation of LCs at droplet surfaces. In addition, planar orientation is induced by irradiating the droplet with ultraviolet (UV) light. We showed the orientation change of LCs upon UV and visible (VIS) light irradiation in three phases, nematic (N), cholesteric (Ch), and smectic A (SmA) [22], which will be described in the following. We used 5CB for the N phase. For a cholesteric material, a chiral dopant CB15 (Merck) was added to 5CB. For smectic A (SmS) materials, 4′-n-octyl-4-cyanobiphenyl (8CB) was also used. The dendrimer molecules added in LC hosts were 0.1–0.3 wt% of D2-6Azo5.

In the N phase, the textures are similar to **Figure 16(b)** and **(c)** under UV and VIS (or before UV irradiation), respectively [22]. In the Ch phase, concentric rings were observed when the sample was irradiated with UV light (**Figure 17(a)**), although they are vague because of a short helical pitch. If we use a Ch LC with a longer pitch, clear concentric rings with a periodic space are observed, as shown in **Figure 17(c)**. Under UV light, the surface orientation is planar (see

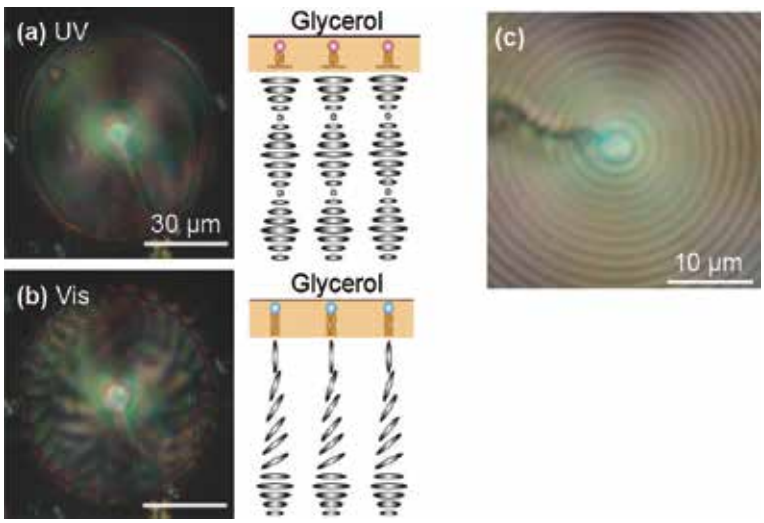

Figure 17. Photomicrographs of a droplet of a cholesteric LC-containing azodendrimers under (a) UV and (b) VIS light irradiation [22]. Schematic illustrations of molecular orientations corresponding to (a) and (b) are also shown on the right [22]. (c) Photomicrograph of a droplet of a cholesteric LC with a long helical pitch containing azodendrimers [22]. Concentric rings showing a helical structure with a helical axis along the radial direction are clearly seen. Copyright 2013, John Wiley & Sons, Inc.

Figure 17(a) right), so a helical structure with the helical axis along the radial direction is formed. Since the planar surface orientation overall the droplet surface inevitably induces defect(s), at least one defect line from the center of the droplet toward the surface emerges, as clearly seen in **Figure 17(c)**. The situation is more complicated under VIS light. The helical structure remains at least in the central region, which is identified by remaining concentric rings. The helical structure is disturbed from the surface region, where homeotropic orientation is achieved (see **Figure 17(b)** right). Many dark lines showing defects are observed in the texture (see **Figure 17(b)** left) [22].

In the SmA phase, the deformation is serious under UV light. Since the surface orientation is homeotropic under VIS light, an onion-like smectic layer structure is formed with the director being parallel to the radial direction (**Figure 18(b)**). A large extinction cross is a manifestation of the concentric SmA layer structure. Here the splay deformation of the director within each layer is allowed. The molecular orientation under UV light is complex, because the layer must be perpendicular to the surface. Since the reorientation occurs from the surface, curved smectic layers are formed in the outer region of the droplets, and are connected to concentric layer structure inside the droplets. As shown in **Figure 18(a)** right, many defect lines are formed along the radial direction, and are observed as a microscope image (**Figure 18(a)** left).

Droplet formations of LCs in other phases are interesting topics. Bent-shaped molecules exhibit various phases [38]. Particularly, many phases, in which reflection symmetry breaking occurs, such as the B2, B4, B7, DC (dark conglomerate), and N_{TB} (twist-bend nematic) phases would be interesting. How does chiral segregation occur in droplets, if it occurs? Bent-shaped molecules are also useful for the study of the blue phase (BP), since they stabilize the BP and expand the temperature range. The N phase of bent-shaped molecules also show peculiar

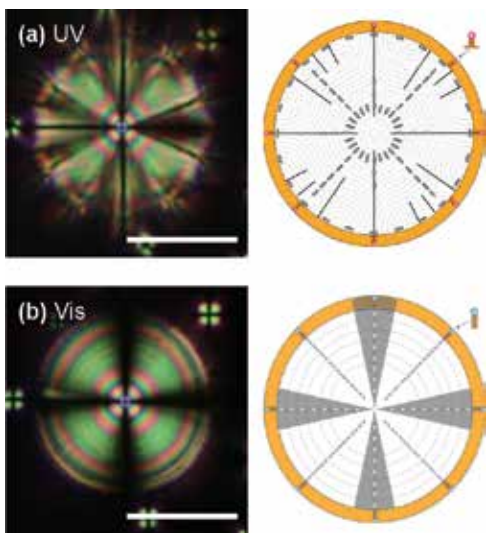

Figure 18. Photomicrographs of a droplet of a SmA LC-containing azodendrimers under (a) UV and (b) VIS light irradiation [22]. Schematic illustrations of molecular orientations corresponding to (a) and (b) are also shown on the right [22]. Copyright 2013, John Wiley & Sons, Inc.

features unlike the conventional N phase. Apart from the bent-shaped mesogens, the relationship between photo-induced reorientation phenomena as a function of elastic constants is another interesting topic. In homeotropic orientation, a splay deformation exists. In contrast, in tangential orientation, a bend deformation is the major component. UV-induced radial-to-bipolar reorientation is strongly suppressed in compounds with huge bend elastic constants compared with splay elastic constants. A compound reported in [39] is an example, in which bend elastic constant is a hundred times larger than splay elastic constants.

6.2. Defects in the vicinity of microspheres

Extensive studies have been made since late 1990s on the defect structures in the vicinity of microspheres [40] and the attractive forces between them [41]. The studies to control the microspheres and the defects around them by external stimuli have been widely made. The external fields used were an electric field [42], laser trapping [43], and thermal gradient [44]. As same as in LC/liquid interface mentioned above, however, the surface of microspheres is normally pretreated to have tangential or homeotropic orientation of LCs. Hence the surface orientation was fixed and no orientation changes have been studied except for the studies by Yamamoto et al. [37]. They observed photo-induced changes of topological defects around colloidal droplets dispersed in azobenzene-containing LCs. In our dendrimer case, photo-controllable interfaces can be provided just by introducing a small amount of azodendrimers into a LC host. The results are shown in [45].

The sample used was 5CB mixed with 0.1 wt% of azodendrimers (D2-6Az05) and a small amount (volume fraction of about 2×10^{-4}) of silica microparticles (about 3 μm in diameter). The sample was introduced into an empty cell of 25 μm thick with rubbing treated planar surfaces. **Figure 19** shows microscope images under crossed polarizers without (a)–(c) and with (d)–(f) a waveplate inserted along the direction diagonal to the crossed polarizers [45]. From the left to right, the temporal changes before ((a) and (d)), during ((b) and (e)), and after ((c) and (f)) UV irradiation are shown. These images are consistent to the defect structures, hedgehog, boojum, and Saturn ring, shown in Figure 19(g)–(i), respectively. Before UV irradiation (g), azodendrimers at surfaces are in a *trans*-state, providing a homeotropic orientation. During UV irradiation (h), *trans*-to-*cis* photo-isomerization leads to a planar (tangential) orientation. Once the azodendrimers at the surface relax to a *trans*-state, a homeotropic surface is realized. Then, the symmetric boojum structure never returns back to the asymmetric hedgehog structure, but to the symmetric Saturn ring structure. Hence, only the transformations between the boojum and the Saturn ring occur by the subsequent UV light on/off.

The response time upon light irradiation is dependent on the UV light intensity and is quite fast under high intensity UV irradiation, as shown in **Figure 20** [45]. The response is nearly exponential (**Figure 20(a)** inset). All processes complete within a one video frame (66 ms). Interestingly, the square of the switching rate is proportional to UV intensity (**Figure 20(b)**).

Let us consider the UV light intensity dependence of the response time assuming a two-level model (**Figure 21**). Here, k_{tc} and k_{ct} are the transition coefficients from *trans*-to-*cis* by UV light and from *cis*-to-*trans* by VIS light, respectively. k_r is a relaxation rate. The rate equation is given by.

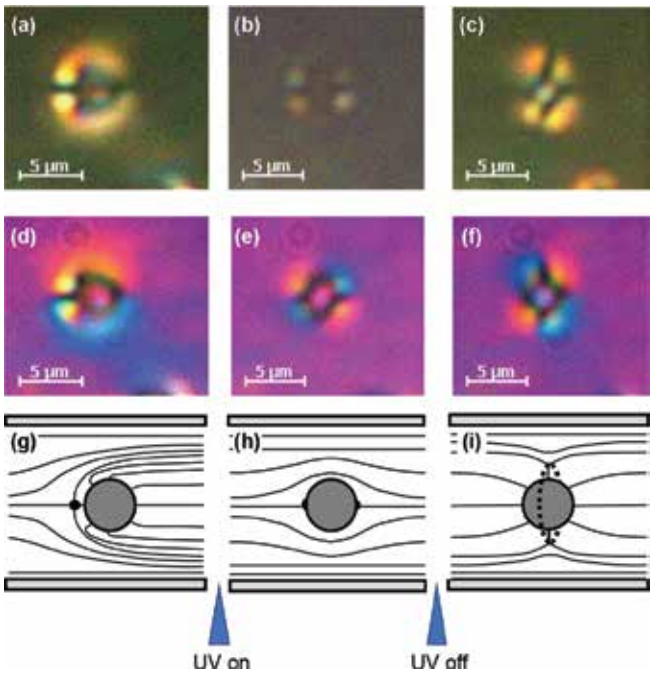

Figure 19. Photomicrographs showing defect structures around a microsphere under crossed polarizers (a)–(c), with a waveplate (d)–(f). A hedgehog defect (g) corresponding to (a) and (d) is observed before UV irradiation. A boojum defect (h) corresponding to (b) and (e) is observed during UV irradiation. A Saturn ring defect (i) corresponding to (c) and (f) is observed after turning off the UV irradiation [45]. Copyright 2014, Optical Society of America.

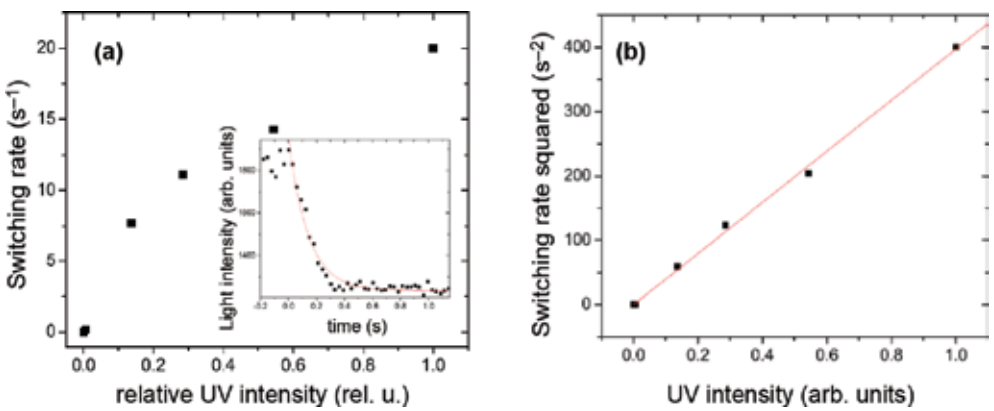

Figure 20. (a) Switching rate as a function of UV light intensity. Temporal change of transmittance is also shown in an inset. (b) Square of the switching rate as a function of UV light intensity [45]. Copyright 2014, Optical Society of America.

$$\dot{n_c} = k_{tc} I_{UV} n_t - k_{ct} I_{VIS} n_c - k_r n_c. \quad (1)$$

Here, n_t and n_c are numbers of *trans* and *cis* molecules, n is a total number of molecules ($n = n_t + n_c$), and $I_{UV/VIS}$ are UV/VIS light intensity. By neglecting the second (no VIS irradiation) and third (very long relaxation time) terms, we obtain.

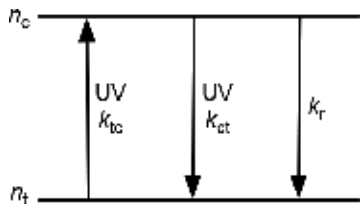

Figure 21. Two-level model for photoisomerization process.

$$n_c = n\left[1 - \exp\left(-\frac{t}{\tau}\right)\right]. \tag{2}$$

The exponential change shown in the inset of **Figure 20(a)** is reasonable. By using Eqs. (1) and (2) with $k_r = 0$, we obtain.

$$\frac{1}{\tau} = k_{tc} n I_{UV}. \tag{3}$$

The switching rate $(1/\tau)$ is proportional to the UV light intensity I_{UV}. Experimentally, however, $(1/\tau)^2$ is proportional to I_{UV}. The discrepancy may be attributed to the assumption $I_{VIS} = 0$ used. Actually, the experiments were made under VIS light from an optical microscope lump, which always induced the *cis*-to-*trans* transition.

6.3. Defects in the vicinity of microrods

The studies of microrods in LCs are much minor [46]. Here we first describe the defect structures around a microrod and their photo-induced changes [17]. Silica microrods used have their length of 10–20 μm and their diameter of 1.5 μm. **Figure 22** shows micrographs of a microrod in a homeotropically aligned LC cell and the director map around the rod. The background under crossed polarizers is dark because of the homeotropic alignment of LCs

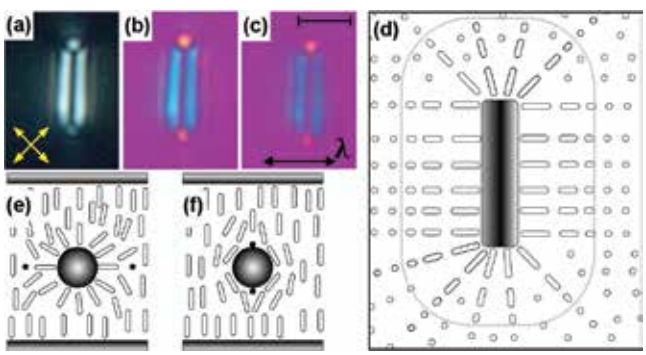

Figure 22. Photomicrographs of a nematic LC with a microrod in a homeotropic cell and corresponding director maps. Micrographs under (a) crossed polarizers, (b) and (c) with a waveplate. Before (a) and (b) and after (c) UV irradiation. Top view of the director orientations before UV irradiation is shown in (d). Side views before and after UV irradiation are shown in (e) and (f), respectively (SI in [17]).

(**Figure 22(a)**). The regions, where LC molecules orient along nearly 45° with respect to the polarizers, are brightest because of birefringence. The insertion of a waveplate gives a blue color at the sides of the rod and an orange color at the edges of the rod, being consistent with the director map shown in **Figure 22(d)**. **Figure 22(e)** is another view of the molecular orientation structure, where two defect lines perpendicular to the image plane (along the rod) are shown as dots.

Upon UV light irradiation, the blue color becomes lighter, but the blue and orange colors themselves do not change. This means that the LC molecules (director) do not orient along the long axis of the rod, but align tangentially perpendicular to the long axis, as shown in **Figure 22(f)**. In this situation, the slow and fast axes of the index ellipsoid do not change but the birefringence becomes smaller, being consistent with the microscope image (**Figure 22(c)**) and the molecular orientation structure (**Figure 22(f)**).

Next, let us describe the results in cells with planar surfaces [17]. Although the free energy does not depend on the orientation of a microrod sitting parallel to the surfaces in homeotropic cells, it does in planar cells, because the elastic energy of LCs and the energy of defects around the rod depend on how the rod orients with respect to the director. **Figure 23** shows the distribution of the rod orientation observed. Two distribution peaks can be seen at 0° and 60°. Full understanding of this distribution is not easy because of the difficulty particularly of the energy estimation of the defect structures.

Figure 24 shows the orientation field of the director around a microrod; (a) and (c) before UV irradiation and (b) and (d) under UV irradiation, where directors are perpendicular and parallel to the rod, respectively. The director orientations are visualized by green and yellow colors in the images seen with a waveplate, which are the same color as observed experimentally (see the actual microscope images at left top in each subfigure). Under UV irradiation (**Figure 24(b)** and **(d)**), the director changes the orientation to be parallel to the rod. In **Figure 24(b)**, where the microrod is almost parallel to the director, the director deformation is localized only at the edge of the rod, so that no color appears, as actually observed experimentally. If the rod

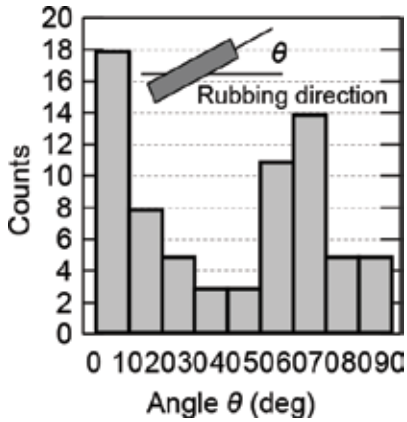

Figure 23. Angular distribution of rod orientation with respect to a rubbing direction (SI in [17]).

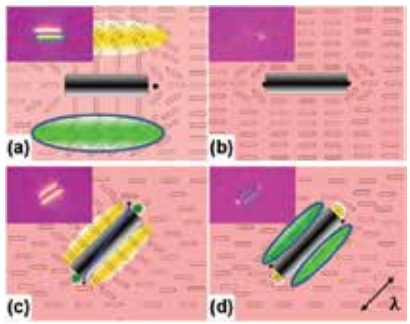

Figure 24. Photomicrographs (left up in each figure) of a nematic LC with a microrod in a planar cell and corresponding director [17]. Copyright 2015, National Academy of Science.

tilts from the director by 45° (**Figure 24(c)** and **(d)**), the director orientation in the vicinity of the rod changes from perpendicular to parallel with respect to the waveplate. Then, a color change from yellow to green occurs, as shown in **Figure 24(b)** and **(d)**. At the edges of the rod, an opposite color change occurs.

Such observations are possible when microrods are somehow fixed at surfaces. When rods are free from surfaces, additional dynamic motions are observed, which are the topics in the next section.

6.4. Dynamic motions of microrods

Figure 25 shows three different dynamic motions of microrods in LCs by UV irradiation [17]. When microrods are parallel to the director, we often observe a lateral motion of the microrods along the director as shown in **Figure 25(a)** and **(b)**. In the other case, the microrod motion appears as its length change (**Figure 25(c)** and **(d)**). This is the result of the rotation of the microrod about its short axis parallel to the surface. The most distinguished motion is

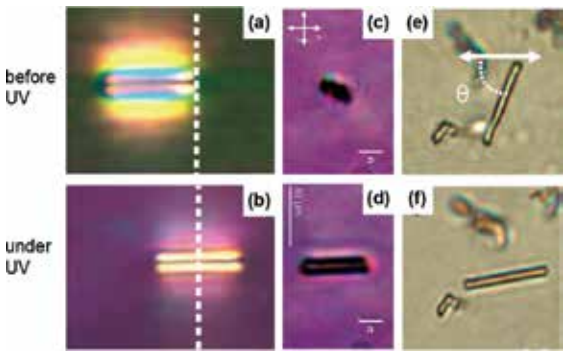

Figure 25. Photomicrographs showing dynamic motions of microrods: (a) and (b) before and during UV light irradiation, respectively, for a lateral motion along the director. (c) and (d) Before and during UV light irradiation, respectively, for a seesaw motion about an axis parallel to a cell surface. (e) and (f) Before and during UV light irradiation, respectively, for a seesaw motion about an axis normal to the cell surface [17]. Copyright 2015, National Academy of science.

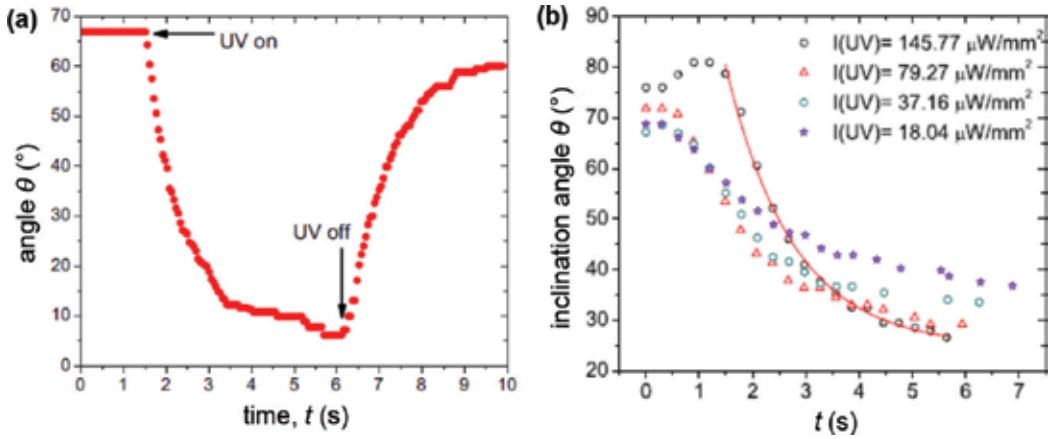

Figure 26. Rotation angle of the seesaw motion of microrods (a) after on and off of the UV light irradiation and (b) the irradiation power dependence [17]. Copyright 2015, National Academy of Science.

observed when rods orient to the direction with finite angles to the director, that is, microrod rotation about its short axis within a plane parallel to the surface (**Figure 25(e)** and **(f)**). The rod returns back to the original direction when UV light is turned off. Thus, the microrods make a seesaw motion by repeated UV light on/off.

The temporal rotation behavior is shown in **Figure 26(a)**, where the angle between the microrod long axis and the director is plotted as a function of time. The rod tends to rotate to the direction parallel to the director (0°) under UV irradiation. When the UV light is terminated, the rod tends to rotate back to the original direction. The rotation speed (response time) is faster and the rotation angle becomes larger with increasing UV light intensity, as shown in **Figure 26(b)**. The solid line in **Figure 26(b)** is the best theoretical fit. The switching angle and the switching rate (inverse switching time) are shown as a function of UV intensity in **Figure 27**. With increasing UV light intensity, the rotation angle becomes larger and the

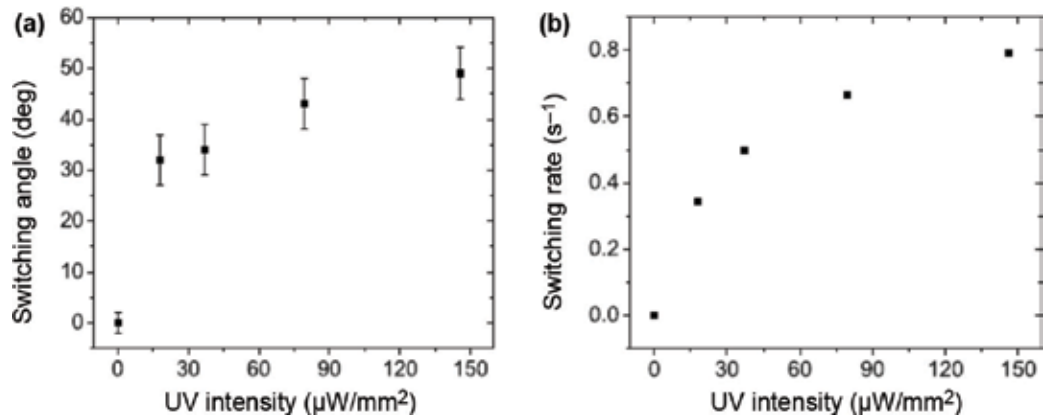

Figure 27. (a) UV intensity dependence of a saturated rotation angle of a microrod. (b) UV intensity dependence of a switching rate of a microrod [17]. Copyright 2015, National Academy of Science.

switching time becomes faster. As will be discussed in Section 7, the anchoring energy $W_a \sin^2\theta$ depends on n_t/n_c; the anchoring strength $W_a = +\infty$ when all azodendrimers are in the *trans*-form, $W_a = -\infty$ when all azodendrimers are in the *cis*-form, and $W_a = 0$ for $n_t = n_c$. At zero I_{UV}, $W_a = +\infty$. With increasing I_{UV}, W_a becomes negative, then the director rotation starts to occur. When the absolute value of W_a is small, the rotational torque is not efficiently transferred to the microrod. Hence the rotation speed is low. With increasing I_{UV}, $| W_a |$ becomes larger and the torque is efficiently transferred to the rod, resulting in faster rotation.

Important difference to the command surface is no use of polarized UV light. In the command surface, linearly polarized UV light irradiation forces the azo linkage to align perpendicular to the polarization direction [3]. On the contrary, linear polarization is not necessary in the present case. However, preferential bending direction in the *cis*-form is automatically chosen by the director field near the surfaces over which azodendrimers cover. Qualitative explanations for the translational and seesaw motions are illustrated in **Figure 28(a)** and **(b)**, respectively. For microrods to make a translational movement, the director field including defect structures must be asymmetric as shown in **Figure 28(a)**. In this case, it is expected that azo groups spontaneously bend (tilt) to a left-hand side upon UV irradiation. This motion forces LC molecules to rotate counterclockwise and clockwise at the upper and lower sides, respectively (1, 2, 3, and 4 in **Figure 28(a)**). The microrod is subjected to an external torque by this rotational motion, resulting in the translational motion to the right.

When the rod is tilted from the director field (**Figure 28(b)**), the director field is oppositely bends at both sides of the rod by UV light, so that the azo groups bend to opposite directions at both sides of the rod, resulting in clockwise rotation of LC molecules. The subsequent torque leads to the rotation of the rod toward the direction parallel to the director. When the UV light is terminated, the rod rotates back to the original orientation shown in **Figure 28(b)**.

Quantitative analysis of the switching behavior was made using a two-dimensional finite element method. With one-constant approximation of elastic constants K, azimuthal angle u of the director field is given by.

$$\Delta u(x, y, t) = \frac{\gamma}{K} \frac{\partial u(x, y, t)}{\partial t}, \tag{4}$$

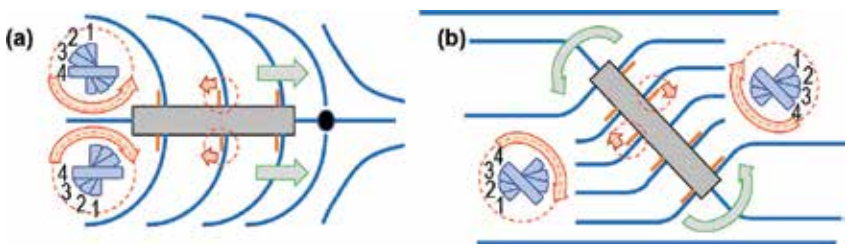

Figure 28. Cartoons showing the mechanisms of (a) the lateral motion and (b) the seesaw motion of microrods. Arrows indicate the bending direction in the *cis* state of azo groups [17]. The numbers from 1 to 4 in small blue rods show the rotation sequence of the directors in the vicinity of the microrods. Green arrows indicate the motion of the microrods by the torques exerted by the director rotations (red arrows) [17]. Copyright 2015, National Academy of Science.

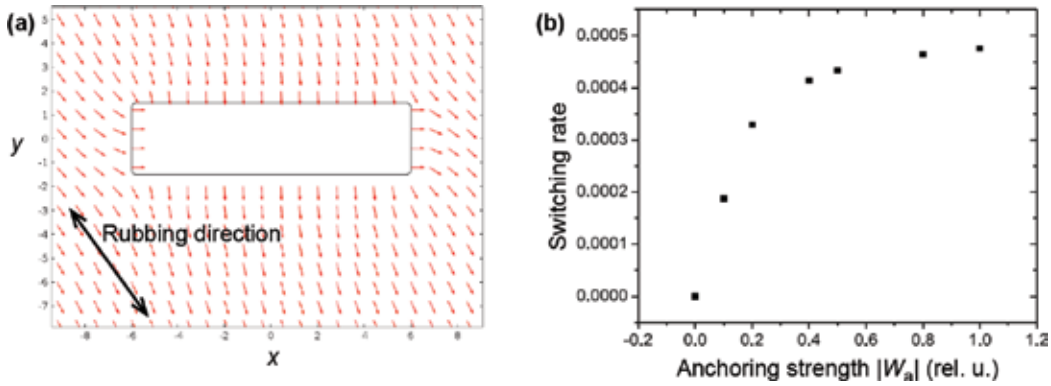

Figure 29. Simulation results of (a) a director map and (b) a switching rate as a function of anchoring strength. Since the anchoring strength is equivalent to the ratio of UV and VIS light intensities (see Section 7), (b) can be compared with **Figure 6–14(b)** under a constant VIS intensity with a sufficient agreement (SI in [17]).

where γ is a rotational viscosity coefficient. The switching behavior can be obtained by solving

$$\mathbf{n}\cdot\Delta u = \frac{W_a}{K}\sin\{2(u-u_0)\} \tag{5}$$

under an initial and boundary conditions. Here u_0 is the azimuthal angle of the director at the boundary. The results are shown in **Figure 29**; (a) the initial state of the director field and (b) switching rate (inverse switching speed) as a function of the absolute value of the anchoring strength. **Figure 29(b)** corresponds to **Figure 27(b)**, since the anchoring strength is directly related to the UV light intensity under a certain VIS light intensity (see Section 7).

7. Controlling surface anchoring strength

As mentioned in Section 6.4, the orientation change due to the command surface is considered to be the result of the change in the anchoring strength W_a depending on n_t and n_c ratio. Here we describe more quantitative discussion together with the experimental results of W_a as a function of the ratio of UV and VIS light intensities [19]. In the precedent section, we only paid attention to the UV light intensity I_{UV}, but neglected the effect of VIS intensity I_{VIS}. Careful experiment, however, indicates that the surface anchoring condition is governed both by I_{UV} and I_{VIS}, as shown in **Figure 30**; homeotropic alignment is realized when I_{VIS} is strong and I_{UV} is week, and planar alignment is realized in the opposite situation. The order parameter obtained by anisotropic infrared absorption of the C ≡ N peak shows the variation from positive to negative with increasing I_{UV} under a certain I_{VIS} light irradiation [19].

The anchoring strength W_a can be obtained by determining an extrapolation length ξ using the Freedericksz transition method in appropriate cell geometries.

$$\xi = K/W_a. \tag{6}$$

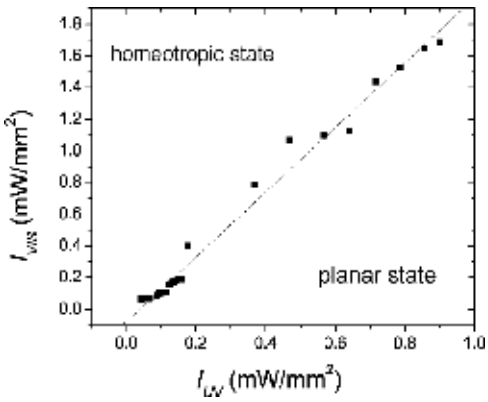

Figure 30. Homeotropic and planar states realized under different UV and VIS light intensities [19]. Copyright 2017, Royal Society of Chemistry.

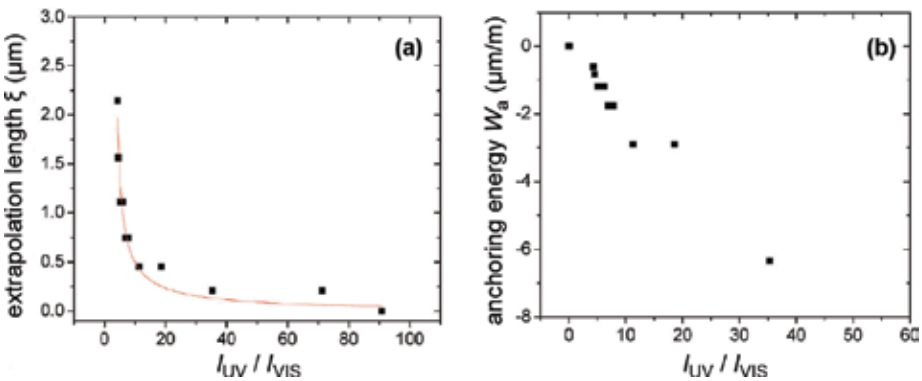

Figure 31. (a) Extrapolation length as a function of I_{UV}/I_{VIS}. (b) Anchoring energy as a function of I_{UV}/I_{VIS} [19]. Copyright 2017, Royal Society of Chemistry.

Here K is the elastic constant corresponding to the electric-induced director deformation. The obtained ξ and W_a are shown in **Figure 31**.

For the analysis of Eq. (1), we neglected the third term, that is, thermal relaxation from *cis*-to-*trans*, but properly took into account the second term, then we obtain the I_{UV}/I_{VIS}-dependent stationary values of *cis* and *trans* isomer populations, n_{c0} and n_{t0}, respectively:

$$n_{c0} = \frac{k_{tc} I_{UV}}{k_{tc} I_{UV} + k_{ct} I_{VIS}} n, \tag{7}$$

$$n_{t0} = \frac{k_{ct} I_{VIS}}{k_{tc} I_{UV} + k_{ct} I_{VIS}} n. \tag{8}$$

Considering that W_a is +∞ and –∞, when all azodendrimers are *trans* and *cis*, respectively, and assuming $W_a = 0$, when $n_t = n_c$, we can empirically write W_a as.

$$W_a = \kappa n \frac{n_t - n_c}{n_t n_c}, \tag{9}$$

where κ is a scaling factor. Using Eqs. (6)–(9), we obtain

$$W_a = \kappa \frac{(k_{ct} I_{VIS})^2 - (k_{tc} I_{UV})^2}{k_{ct} k_{tc} I_{VIS} I_{UV}} = \kappa \left(\frac{1}{\eta} - \eta \right) \tag{10}$$

and

$$\xi = \frac{K}{\kappa} \frac{\eta}{1 - \eta^2} \tag{11}$$

with $\eta = k_{tc} I_{UV} / k_{ct} I_{VIS}$. Since η is directly related to the experimental parameter I_{UV}/I_{VIS}, ξ vs. I_{UV}/I_{VIS} in **Figure 31** can be fitted by Eq. (11), as shown by a solid curve in **Figure 31(a)**. Thus, the director switching by photo-isomerization of azo molecules at surfaces is ascribed to the change of the anchoring strength at surfaces.

8. Summary

We introduced various functions given by azodendrimers. First, we summarized dendrimer molecules with mesogenic groups synthesized and their mesogenic phase sequences. Some of them have a strong tendency to align themselves to homeotropic orientation. As a function for static use, we described the use for LC display applications. Spontaneous homeotropic orientation is achieved just by doping LCs with a small amount of dendrimers without pre-surface treatment. This technique can be used not only for the VA mode but also for the IPS mode, if azo linkages are introduced to the dendrimers and photo treatment is applied using linear polarized light. We can find much more functions, if dendrimers are substituted at their tail ends by azo groups. The property of spontaneous adsorption of dendrimers onto a variety of surfaces and interfaces is very important, as exemplified in LC colloidal systems and LC systems with micro inclusions, which are the main topics of this review. Because of photo-induced *trans-cis* isomerization, the azodendrimers act as a command surface, which enables us to control LC orientation. Azodendrimers can be attached to form layers at a variety of surfaces and interfaces, that is, glass substrates, LC droplets in polymers, and surfaces of microparticles in LCs. Photo-controlled *trans*- and *cis*-forms, respectively, provide homeotropic and planar orientations of LCs. The photo-irradiation triggers azodendrimers transport (dewetting) and orientation changes, resulting in various changes; macroscopically physical properties such as thermal transport, microscopically orientational defect structure changes, and even dynamics of inclusions in LCs.

Acknowledgements

This chapter provides a review of our previous works related to physical and chemical measurements using azodendrimers. We acknowledge all coauthors particularly Prof. K. Yonetake, Prof. A. Eremin, and Dr. F. Araoka for their collaboration.

Author details

Hideo Takezoe[1] and Osamu Haba[2]*

*Address all correspondence to: haba@yz.yamagata-u.ac.jp

1 Toyota Physical and Chemical Research Institute, Nagakute, Aichi, Japan

2 Department of Organic Materials Science, Yamagata University, Yamagata, Japan

References

[1] (a) Yu Y, Nakano M, Ikeda T. Photomechanics: Directed bending of a polymer film by light. Nature. 2003;**425**:145-145. (b) Yu H, Ikeda T. Photocontrollable liquid-crystalline actuators. Advanced Materials. 2011;**23**:2149-2180

[2] Ichimura K, Suzuki Y, Seki T, Hosoki A, Aoki K. Reversible change in alignment mode of nematic liquid crystals regulated photochemically by command surfaces modified with an azobenzene monolayer. Langmuir. 1988;**4**:1214-1216

[3] Gibbons WM, Shannon PJ, Sun S-T, Swetlin BJ. Surface-mediated alignment of nematic liquid crystals with polarized laser light. Nature. 1991;**351**:49-50

[4] (a) Ichimura K. Photoalignment of liquid-crystal systems. Chemical Reviews. 2000;**100**: 1847-1873. (b) Natansohn A. Photoinduced motions in azo-containing polymers. Chemical Reviews. 2002;**102**:4139-4175. (c) Yu H. Recent advances in photoresponsive liquid-crystalline polymers containing azobenzene chromophores. Journal of Materials Chemistry C. 2014;**2**:3047-3054. (d) Seki T. Light-directed alignment, surface morphing and related processes: Recent trends. Journal of Materials Chemistry C. 2016;**4**:7895-7910

[5] Newkome GR, Moorefield C, Vögtle F. Dendritic Molecules: Concepts, syntheses, perspectives. VCH: Weinheim; 1996

[6] Archut A, Vogtle F, De Cola L, Azzellini GC, Balzani V, Ramanujam PS, Berg RH. Azobenzene-functionalized cascade molecules: Photoswitchable supramolecular systems. Chemistry—A European Journal. 1998;**4**:699-706

[7] Kim JM, Shin HK, Park E, Kim CK, Kwon S-S. The study on the optical characteristics of G4-48 azodendrimer by Langmuir-Blodgett method. Molecular Crystals and Liquid Crystals. 2010;**377**:197-200

[8] Gopalan P, Katz HE, McGee DJ, Erben C, Zielinski T, Bousquet D, Muller D, Grazul J, Olsson Y. Star-shaped azo-based dipolar chromophores: Design, synthesis, matrix compatibility, and electro-optic activity. Journal of the American Chemical Society. 2004;**126**:1741-1747

[9] Li X, Lu X, Lu Q, Yan D. Photoorientation of liquid crystalline azodendrimer by nanosecond pulsed laser for liquid crystal alignment. Macromolecules. 2007;**40**:3306-3312

[10] del J, Tejedor RM, Shinelatto LS, Sanchez C, Pinol M, Oriol L. Photocontrol of the Supramolecular chirality imposed by stereocenters in liquid crystalline azodendrimers. Chemistry of Materials. 2010;**22**:1714-1723

[11] (a) Lin W, Cui Y, Gao J, Yu J, Liang T, Qian G. Six-branched chromophores with isolation groups: Synthesis and enhanced optical nonlinearilty. Journal of Materials Chemistry. 2012;**22**:9202-9208. (b) Yu Y, Cui Y, Yang Y, Qian G. Design and preparation of hybrid films containing three-branched chromophores for nonlinear optical applications. RSC Advances. 2016;**6**:81969-81975

[12] (a) Kim Y-H. Lyotropic liquid crystalline hyperbranched aromatic polyamides. Journal of the American Chemical Society. 1992;**114**:4947-4948. (b) Percec V, Chu P, Ungar G, Zhou J. Rational design of the first nonspherical dendrimer which displays calamitic nematic and smectic thermotropic liquid. Journal of the American Chemical Society. 1995;**117**:11441-11454. (c) Lorenz K, Holter D, Stuhn B, Mulhaupt R, Frey H. A mesogen-functionized carbosilane dendrimer: A dendritic liquid crystalline polymer. Advanced Materials. 1996;**8**:414-416. (d) Ponomarenko SA, Boiko NI, Shibaev VP, Richardson RM, Whitehouse IJ, Rebrov EA, Muzafarov AM. Carbosilane liquid crystalline dendrimers: From molecular architecture to supramolecular nanostructures. Macromolecules. 2000;**33**:5549-5558

[13] Yonetake K, Masuko M, Morishita T, Suzuki K, Ueda M, Nagahata R. Poly(propyleneimine) dendrimers peripherally modified with mesogens. Macromolecules. 1999;**32**: 6578-6586

[14] (a) Haba O, Okuyama K, Osawa H, Yonetake K. Structures and properties of dendrimers having peripheral 2,3-difluorobiphenyl mesogenic units: Effects of dendrimer generation. Liquid Crystals. 2005;**32**:633-642. (b) Haba O, Hiratsuka D, Shiraiwa T, Koda T, Yonetake K, Momoi Y, Furuta K. Synthesis and characterization of polypropyleneimine dendrimers having peripheral mesogenic groups: Homeotropic orientation and mesogen structure. Molecular Crystals and Liquid Crystals. 2013;**574**:84-95

[15] Li W, Dohi T, Hara M, Nagano S, Haba O, Yonetake K, Seki T. Phototriggered mass migration consorted with surface dewetting in thin films of a liquid crystalline azobenzene-containing dendrimer. Macromolecules. 2012;**45**:6618-6627

[16] Private communications by S. Aya (Riken, Japan) and by C. Park (Univ. Colorado, USA)

[17] Eremin A, Hirankittiwong P, Chattham N, Nadashi H, Stannarius R, Limtrakul J, Haba O, Yonetake K, Takezoe H. Optically driven translational and rotational motions of microrod particles in a nematic liquid crystal. Proceedings of the National Academy of Sciences. 2015;**112**:1716-1720

[18] Haba O, Hiratsuka D, Shiraiwa T, Funakoshi N, Awano H, Koda T, Takahashi T, Yonetake K, Kwak M, Momoi Y, Kim N, Hong S, Kong D, Choi Y. Homeotropic orientation of nematic liquid crystals induced by dissolving polyprophyleneimine dendrimer having peripheral mesogens. Optical Materials Express. 2014;**4**:934-943

[19] Nadasi H, Stannarius R, Eremin A, Ito A, Ishikawa K, Haba O, Yonetake K, Takezoe H, Araoka F. Photomanipulation of the anchoring strength using a spontaneously adsorbed layer of azodendrimers. Physical Chemistry Chemical Physics. 2017;**19**:7597-7606

[20] Momoi Y, Furuta K, Kwak M, Koda T, Haba O, Yonetkae K. Surface analysis of polyimide-less LC alignment by dissolving dendrimer, abstract of IDW'11:1545-1548

[21] Sakuma T, Funakoshi N, Takahashi Y, Uchida M, Koda T, Haba O, Yonetake K, Kwak M, Momoi Y, Jeon J, An S, Xhoi D, Kang D, Choi Y, Jeon S. Polyimide-less alignment by dendrimers dissolved in liquid crystal, IDW/AD'12:1595-1598

[22] Lee G, Araoka F, Ishikawa K, Momoi Y, Haba O, Yonetake K, Takezoe H. Photo-induced ordering transition in microdroplets of liquid crystals with azodendrimer. Particle and Particle Systems Characterization. 2013;**30**:847-852

[23] Momoi Y, Kwak M, Choi D, Choi Y, Jeong K, Koda T, Haba O, Yonetake K. Polimide-free LCD by dissolving dendrimers. Journal of the Society for Information Display. 2012;**20**:486-492

[24] Haba O, Yonetake K. Application of dendrimers to liquid crystal displays. Journal of the Japan Society of Colour Material (in Japanese). 2013;**86**:433-438

[25] Haba O, Itabashi H, Sato S, Machida K, Koda T, Yonetake K, Kwak M, Momoi Y, Kim N, Hong S, Kang D, Choi Y. UV-induced stable planar alignment of nematic LCs using a polypropyleneimine dendrimer having a mesogen consisting of cinnamate and azobenzene moieties. Molecular Crystals and Liquid Crystals. 2015;**610**:201-209

[26] Ryu M, Takezoe H, Haba O, Yonetake K, Morikawa J. Photo-controllable thermal diffusivity and thermal conductivity driven by the orientation change of nematic liquid crystal with azodendrimers. Applied Physics Letters. 2015;**107**:221901-1-221901-4

[27] Morikawa J, Hashimoto T. Thermal diffusivity of aromatic polyimide thin films by temperature wave analysis. Journal of Applied Physics. 2009;**105**:113506-1-113506-9

[28] (a) Rochon P, Batalla E, Natansohn A. Optically induced surface gratings on azoaromatic polymer films. Applied Physics Letters. 1995;**66**:136-138. (b) Kim DY, Tripathy SK, Li L, Kumar J. Laser-induced holographic surface relief gratings on nonlinear optical polymer films. Applied Physics Letters. 1995;**66**:1166-1168

[29] (a) Nakano H, Takahashi T, Kadota T, Shirota Y. Formation of a surface relief grating using a novel azobenzene-based photochromic amorphous molecular material. Advanced Materials. 2002;**14**:1157-1160. (b) Ishow E, Lebon B, He Y, Wang X, Bouteiller L, Galmeche L, Nakatani K. Structural and photoisomerization cross studies of polar photochromic monomeric glasses forming surface relief gratings. Chemistry of Materials. 2006;**18**:1261-1267

[30] Galgano JJ, Karunatilaka C, Rethwisch DG, Tivanski AV. Atomic force microscopy study of photoreversible nanoscale surface relief grating patterns on side chain dendritic polyester thin films. Colloids and Surfaces A. 2010;**360**:167-174

[31] (a) Ubukata T Seki T, Ichimura K. Surface relief gratings in host-guest supramolecular materials. Advanced Materials. 2000;**12**:1675-1678. (b) Isayama J, Nagano S, Seki T. Phototriggered mass migrating motions in liquid crystalline azobenzene polymer films with systematically varied thermal properties. Macromolecules. 2010;**43**:4105-4112

[32] Ikeda T, Aya S, Araoka F, Ishikawa K, Haba O, Yonetake K, Momoi Y, Takezoe H. Novel bistable device using anchoring transition and command surface. Applied Physics Express. 2013;**6**:061701-1-061701-3

[33] Dhara S, Kim JK, Jeong SM, Kogo R, Araoka F, Ishikawa K, Takezoe H. Anchoring transition of transversely polar liquid-crystal molecules on perfluoropolymer surfaces. Physical Review E. 2009;**79**:060701(R)-1-060701(R)-4

[34] (a) Kim JK, Araoka F, Jeong SM, Dhara S, Ishikawa K, Takezoe H. Bistable device using anchoring transition of nematic liquid crystals. Applied Physics Letters. 2009;**95**:063505-1-063505-3. (b) Jampani VSR, Skarabot M, Takezoe H, Musevic I, Dhara S. Laser-driven microflow-induced bistable orientation of a nematic liquid crystal in perfluoropolymer-treated unrubbed cells. Optics Express. 2013;**21**:724-729

[35] (a) Shyang L, Cheng Y, Zhao Y. Emerging droplet microfluidics. Chemical Reviews. 2017;**117**:7964-8040. (b) Wang X, Bukusoglu E, Abbott NI. A practical guide to the preparation of liquid crystal-templated microparticles. Chemistry of Materials. 2017;**29**:53-61. (c) Sengpta A. Herminghaus S, Bahr C. Liquid crystal microfluidics: Surface, elastic and viscous interactions. Liquid Crystals Reviews. 2014;**2**:73-110

[36] (a) Press MJ, Arrott AS. Theory and experiments on configurations with cylindrical symmetry in liquid-crystal droplets. Physical Review Letters. 1974;**33**:403-406. (b) Stark H. Physics of colloidal dispersions in nematic liquid crystals. Physics Reports. 2001;**351**:387-474. (c) Blanc C, Coursault D, Lacaze E. Ordering nano- and microparticles assemblies with liquid crystals. Liquid Crystals Reviews. 2013;**1**:83-109. (d) Orlova T, Asshoff SJ, Yamaguchi T, Katsonis N, Brasselet E. Creation and manipulation of topological states in chiral nematic microspheres. Nature Communications. 2015;**6**:7603-1-7603-9

[37] (a) Yamamoto T, Tabe Y, Yokoyama H. Photochemical transformation of topological defects formed around colloidal droplets dispersed in azobenzene-containing liquid crystals. Colloids and Surfaces A: Physicochemical and Engineering Aspects. 2009;**334**:155-159. (b) Yamamoto T, Tabe Y, Yokoyama H. Photochemical manipulation of topological defects in liquid-crystal emulsions doped with azobenzene derivatives. Thin Solid Films. 2006;**509**:81-84

[38] Takezoe H, Eremin A. Bend-shaped Liquid Crystals–Structures and Physical Properties. CRC Press; Boca Raton. 2017

[39] (a) Aya S, Obara H, Pociecha D, Araoka F, Okano K, Ishikawa K, Gorecka E, Yamashita T, Takezoe H. Highly elastic liquid crystal with bend elastic constant of sub-nN mediated by the resident molecular assemblies. Advanced Materials. 2014;**26**:1918-1922. (b) Aya S, Ogino S, Hayashi Y, Okano K, Pociecha D, Le KV, Araoka F, Kawauchi S, Gorecka E,

Vaupotic N, Takezoe H, Ishikawa K. Structure-sensitive bend elastic constants between piconewton and sub-nanonewton in diphenylacetylene-core-based liquid crystals. Physical Review E. 2014;**90**:042506-1-042506-6

[40] (a) Kleman M, Lavrentovich OD. Topological point defects in nematic liquid crystals. Philosophical Magazine. 2006;**86**:4117-4137. (b) Lavrentovich OD. In: Arodz H, editor. Defects in liquid crystals: Surface and interfacial anchoring effects, in patterns of symmetry breaking. Netherland: Kluwer Academic Pub.; 2003

[41] (a) Poulin P, Cabuil V, Weitz DA. Direct measurement of colloidal forces in an anisotropic solvent. Physical Review Letters. 1997;**79**:4862-4865. (b) Poulin P, Stark H, Lubensky TC, Weitz DA. Novel colloidal interactions in anisotropicfluids. Science. 1997;**275**:1770-1773

[42] Pishnyak OP, Shiyanovskii SV, Lavrentovich OD. Aggregation of colloidal particles in a non-equilibrium backflow induced by electrically-driven reorientation of the nematic liquid crystal. Journal of Molecular Liquids. 2011;**164**:132-142

[43] Smalyukh II, Kaputa DS, Kachynski AV, Kuzmin AN, Prasad PN. Optical trapping of director structures and defects in liquid crystals using laser tweezers. Optics Express. 2007;**15**:4359-4371

[44] Skarabot M, Lokar Z, Musevic I. Transport of particles by a thermally induced gradient of the order parameter in nematic liquid crystals. Physical Review E. 2013;**87**:062501-1-062501-6

[45] Hirankittiwong P, Chattham N, Limtrakul J, Haba O, Yonetake K, Eremin A, Stannarius R, Takezoe H. Optical manipulation of the nematic director field around microspheres covered with an azo-dendrimer monolayer. Optics Express. 2014;**22**:20087-20093

[46] (a) Lapointe C, Hultgren A, Silevitch DM, Felton EJ, Reich DH, Leheny RL. Elastic torque and the levitation of metal wires by a nematic liquid crystal. Science. 2004;**303**:652-655. (b) Tkalec U, Skarabot M, Musevic I. Interactions of micro-rods in a thin layer of a nematic liquid crystal. Soft Matter. 2008;**4**:2402-2409. (c) Juhl AT, Yang D-K, Tondiglia VP, Natarajan LV, White TJ, Bunning TJ. Ordering of glass rods innematic and cholesteric liquid crystals. Optical Materials Express. 2011;**1**:1536-1547. (d) Gharbi MA, Cavallaro Jr, M, Wu G, Beller DA, Kamien RD, Yang S, Stebe KJ. Micro-bullet assembly: Interactions of oriented dipoles in confined nematic liquid crystal. Liquid Crystals. 2013;**40**:1619-1627. (e) Mundoor H, Senyuk B, Smalyukh II. Triclinic nematic colloidal crystals from competing elastic and electrostatic interactions. Science. 2016;**352**:69-73

Section 3

Dendrimers in Self-healing Technology

Chapter 6

Self-healing of Structural Composites Containing Dendrimers as Healing Agent

Vassilis Kostopoulos and Athanasios Kotrotsos

Additional information is available at the end of the chapter

http://dx.doi.org/10.5772/intechopen.70884

Abstract

Dendrimers exhibit healing functionalities on polymer level. In the present chapter, the effect of hydrogen-bonded supramolecular polymers (SP) into high performance aerospace carbon fiber reinforced plastics (CFRPs) is assessed. More precisely, the interlaminar fracture toughness of unidirectional (UD) SP-modified composites (containing SP interleaves) and their healing capability were measured under mode I and mode II fracture loading conditions. During testing, these modified samples exhibited extended bridging between the interlaminar crack flanks, which considerably enhanced their interlaminar fracture toughness. Furthermore, SP pre-impregnated fiber layers (prepregs) were fabricated to facilitate the introduction of the self-healing agent (SHA) into the composite laminated structure. SP prepregs were used to modify quasi-isotropic CFRPs in a symmetric fashion, and the damage tolerance of the modified composites was investigated. To that direction, the SP-modified laminates were tested under low velocity impact (LVI) conditions, and compression after impact (CAI) tests were conducted prior and after the activation of the healing. Finally, examination of the morphology of fracture surface led to qualitative conclusions regarding the involved failure and healing mechanisms.

Keywords: composites, self-healing, hydrogen bonds, supramolecular polymers fracture mechanics, damage tolerance

1. Introduction

1.1. Background

During the last decades, the use of composites in aeronautics, wind energy, automotive, and other mechanical engineering applications has been significantly increased. The need for new materials with enhanced mechanical properties, low density and corrosion resistance combined

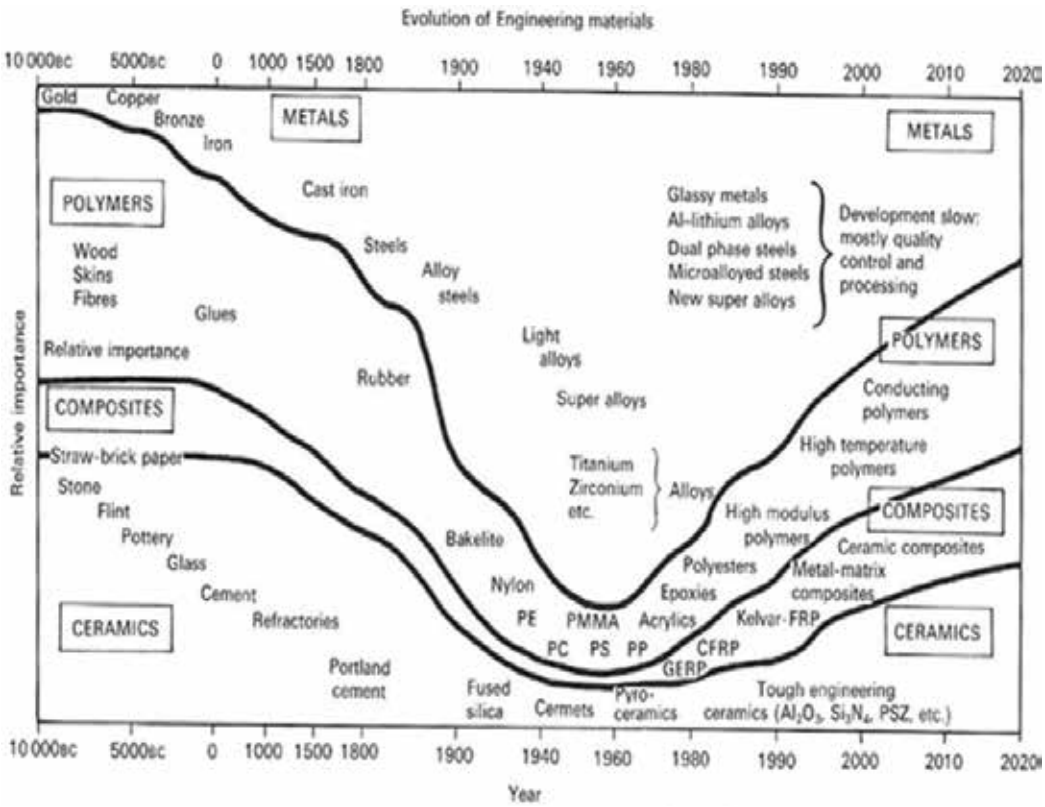

Figure 1. Schematic representation of the importance of four classes of materials (ceramics, composites, polymers, and metals) in mechanical and civil engineering as function of time [1].

with the necessity for greener operation of structures, was the main driver for intensive research and application of polymer-matrix-fiber-reinforced composites in many fields as structural materials. **Figure 1** shows the evolution in use of materials versus time. In this picture, the rapid increase in the use of polymers and composite materials, during the last decades is evident [1].

In addition, the use of composites and, especially, carbon/epoxy composites in aerospace applications has been considerably increased since 1960. Characteristic examples are Boeing 787 Dreamliner and Airbus 350-XWB in which their structural mass is made by 50 and 55% of composites, respectively. As it is expected, the extensive use of composites results to more fuel efficient and environmental friendly aircrafts. However, a primary limitation of composites is their poor interlaminar strength and fracture toughness that make them prone to delaminations [2, 3]. In [4], possible damage modes into a polymer composite are described in detail. Delamination is the result of out of plane LVI of a composite structure. Joining of the microcracks, developed into the polymer matrix under service loads, is another option for delaminations. It is obvious that delaminations can lead to significant suppression of the load-bearing capacity of the composite components and structures.

During the last decades, significant research effort has been invested to the improvement of interlaminar fracture performance of structural composites and especially of CFRPs. A variety

of methodologies have been proposed in the literature to prevent composites from delaminations. These include chemical modification of epoxy matrix systems (either by modifying the resin or the hardener), interleaving, hybridization, stitching, short-fibers, z-pinning, optimization of staking sequence, reactive rubbers and edge-cap reinforcement [5–14]. However, although the interlaminar fracture properties have been enhanced, delamination remains the main damage mode in the case of FRPs. Furthermore, conventional repair techniques [15, 16] of composites are time consuming, require extensive labor cost, and the repair defects face certain restrictions. These repair techniques involve patch repair (e.g., bonded external patch, bonded flush patch) or non-patch repair (e.g., resin injection, potting or filling and surface coating) [15, 16]. In the case of repair of primary structural components, the certification authorities required additional mechanical joining. **Figure 2(a)** illustrates a representative example of patch repair method in which the damage material is carefully removed by using a high-speed grinder [15]. After material removal, new composite plies are utilized to fill the created cavity. On the other hand, **Figure 2(b)** shows non-patch repair which includes resin injection through an access hole into the damage area. This method eliminates the removal of undamaged plies and results in higher recovery of the strength [16].

Thus, utilization of composites in human safety critical components has always to be accompanied with non-destructive testing techniques (NDTs) as damage monitoring tool. These techniques involve ultrasonics, surface waves, Acoustic emission, infrared thermography, and X-ray radiography [16]. It is also of note that conventional damage detection equipment is, in some cases, not able to detect tiny defects deep inside the material. However, these defects could rapidly propagate between two periodical inspections and lead the composite part to significant deterioration. This challenging situation acted as an inspiration for seeking of new repair methods; cheaper and applicable at the early stages of damage evolution. With an aim to address some principal weak points of conventional repair techniques, an emerging approach called "self-healing materials" [17, 18] has been proposed but not yet been applied to commercial composites. This smart technology aims to in-situ and autonomously repair damage and thus to lead to extension of the effective life-span of composite structures. Self-healing of

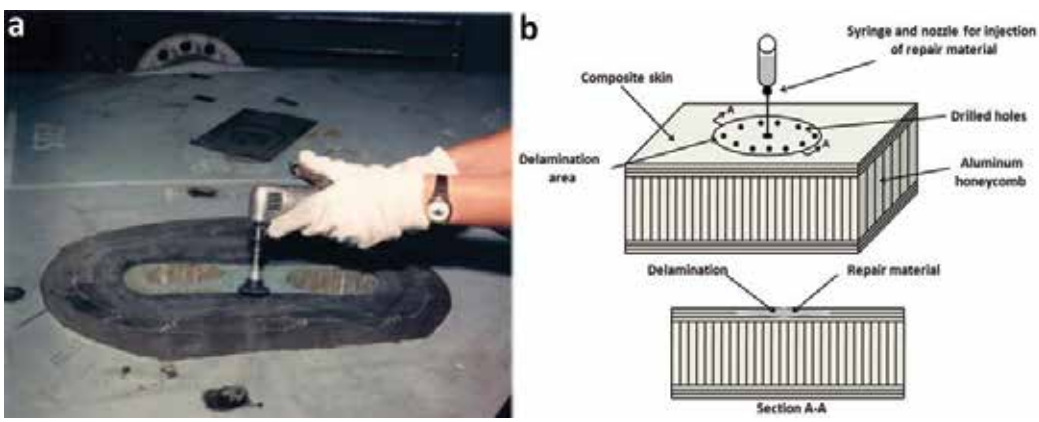

Figure 2. (a) Scarf cavity formation prior to patch repair [15]. (b) Depiction of the resin injection process into honeycomb panel skin's composite.

composites promises to mitigate the importance for detecting damage and to reduce the frequency of scheduled inspections.

Self-healing mechanisms incorporated into existing materials is an emerging alternative to conventional repair methods to remove cracks and restore performance. It is also considered as an intense research field over the last decades. A self-healing material [19] is a class of biomimetic materials that can autonomously repair damage and regain its initial properties after damage. Self-healing technologies could extend the service life and reliability of epoxy resins and their composites. Based on published research work, a typical way to classify self-healing systems is as: (a) autonomous (extrinsic) [20, 21] (capsule-based systems [20] or vascular-based systems [21]), where a container is prefilled with a liquid self-healing agent (SHA). (b) Non-autonomous [22, 23], where self-healing is created either by using a modifier with inherently reversible behavior [22] or by incorporating functional groups directly into a thermoset structure that can form reversible bonds (intrinsic [23]). While for non-autonomous self-healing, an external stimulus (heating) is required, autonomous self-healing operates at service temperature (not external stimulus is required).

A new technology that could be beneficial for self-healing in composites has been built on dendrimers (SP) [24]. Especially those based on reversible hydrogen bonding arrays show great promise as self-healing materials [25–27], since these materials can typically withstand multiple healing cycles without substantial loss of performance, because of the highly directional and fully reversible non-covalent interactions present into the polymer matrix. During the last decades, many types of dendrimers have been reported and are classified according to the type of the non-covalent bond involved. Dendrimers are classified into the following categories: SP based on hydrogen bonds [25–27], SP based on π-π stacking interaction [28], SP based on metal ligand interaction [29], and SP based on ionomer [30]. In the present chapter, the ureiodypyrimidone hydrogen bonding unit (UPy) as developed by Meijer and coworkers [27] has been employed because of its strong self-association, its synthetic accessibility, and the highly dynamic nature of low T_g-polymers comprising the UPy [31]. Most interestingly, UPy-polymers have recently been shown to give unprecedented toughening in polybutadiene-based interpenetrating networks [32].

In the present chapter, interleaves comprising self-healing materials based on hydrogen-bonded SP were successfully incorporated into high performance UD carbon/epoxy composites. The interlaminar fracture toughness of these modified composites and their healing capabilities were measured under mode I and II fracture loading conditions (Sections 3 and 4, respectively). During testing, these modified samples exhibited extended bridging phenomena, which considerably enhanced the interlaminar fracture toughness of the composites. Potential knock-down effect by the incorporation of the SP interleaf was quantified through three-point bending tests (3PB). Furthermore, SP carbon fiber prepregs were fabricated to simplify the incorporation process of SHA into the composite laminates. SP prepregs were further utilized to modify quasi-isotropic CFRPs. Potential knock-down effects and the induced healing capability of these modified composites were investigated under LVI and CAI tests. Finally, examination of the morphology of fracture surface led to qualitative conclusions regarding the involved failure and healing mechanisms.

2. Experimental

2.1. Materials and methods

2.1.1. Materials

The SP-modified composite laminates, which are used in the present chapter, were fabricated by UD carbon fiber/epoxy resin prepreg CE-1007 150-38. The prepreg tape material supplied by SGL Group, Germany having tensile strength of 2.4 GPa and axial Young modulus of 140 GPa. The SP was developed and supplied by Suprapolix, the Netherlands. The supplied material (batch identification code: SPSH01) is based on a low T_g (−66°C) polymer modified with UPy moieties.

2.1.2. Preparation of the SP interleaves and SP prepreg plies

The preparation process of the SP interleaves and prepregs are illustrated in **Figure 3**. The as-received polymer piece (**Figure 3(ai)**) was converted into a thin film by a two-step heating/pressuring treatment (**Figure 3(aii)**) using a hot press machine. On the other hand, the preparation process of the SP prepreg is illustrated in **Figure 3(b)**. Raw SP pieces (**Figure 3(bi)**) were placed on the top and bottom surfaces of dry UD carbon fabric. Then, the system was placed in between two Polytetrafluoroethylene (PTFE) films and converted into SP prepreg by a two-step heating/

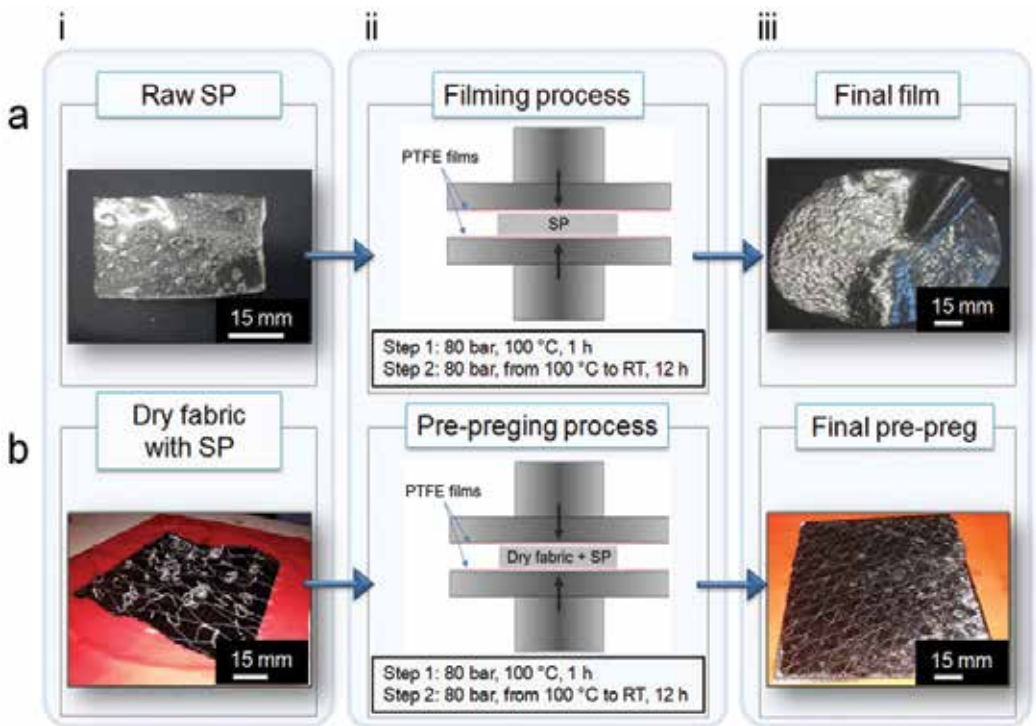

Figure 3. (a) Filming process of the SP and (b) preparation process of the SP-modified prepreg plies.

pressing treatment (**Figure 3(bii)**) using a hot press machine. Firstly, both systems were pressed under 80 bars at 100°C for 1 h. Then, heating was stopped and both the SP film and prepreg were left under 80 bars applied pressure overnight to cool down and reach their final form (**Figure 3** (**aiii**, **biii**)). The thickness of the film and prepreg was measured to be approximately 120 μm and 180 μm, respectively, with no significant thickness variations, using a digital caliper.

2.1.3. Mode I interlaminar fracture toughness testing

Quasi-static interlaminar fracture toughness tests described in Section 3 were performed at a 25 kN Instron Universal testing machine (Instron, High Wycombe, UK) at RT conditions. The mode I interlaminar fracture toughness was measured using the double cantilever beam (DCB) method according to the AITM 1.0005 standard issued by Airbus. DCB specimen dimensions and experimental setup are both illustrated in **Figure 5**. The 25-mm-long PTFE starter film that was placed at the central plane, at one edge of the samples to facilitate crack initiation is also shown. Two aluminum tabs were glued on the outer surfaces of the pre-cracked end of the specimens, for the application of the opening load. The specimens were loaded in tension at a cross-head velocity of 10 mm/min until the crack was propagated from starting point considered as zero to 75 mm. Five samples were tested each time for the calculation of G_{IC}. The mode I interlaminar fracture energy of the CFRPs was calculated using Eq. (1),

$$G_{IC} = \frac{A}{aw} \cdot 10^3 \left(\frac{kJ}{m^2} \right) \tag{1}$$

where, A is the required energy to achieve the total propagated crack length, a is the propagated crack length (final crack length minus initial crack length, a = 75 mm), and w is the specimen's width.

2.1.4. Mode II interlaminar fracture toughness testing

The mode II interlaminar fracture toughness tests described in Section 4 were measured using the three-point end-notched flexure (ENF) method according to the AITM 1.0006 standard issued by Airbus. Firstly, the DCB specimens were loaded under mode I in alignment with the AITM 1.0005 to create a natural sharp pre-crack. Then, the delaminated specimens were cut into ENF specimens as shown in **Figure 15**, according to AITM 1.0006. ENF specimen dimensions and experimental setup are both illustrated in **Figure 15**. The pre-cracked ENF specimens were subjected to flexural loading that generated a shear crack driving force at the crack tip region. The cross-head velocity was fixed at 1 mm/min. Five samples were tested for each fracture toughness assessment. The G_{IIC} was determined using Eq. (2),

$$G_{IIC} = \frac{9Pa^2d}{2w\left(\frac{1}{4}L^3 + 3\alpha^3\right)} \left(\frac{kJ}{m^2} \right) \tag{2}$$

where, d is the cross-head displacement at crack delamination onset, P is the critical load to start the crack, α is the initial crack length (from the support point to the end of the crack, α = 35 mm), w is the width of the specimen, and L is the span length (L = 100 mm). For accurate calculation of the G_{IIC}, the simple methodology described was applied.

2.1.5. Low velocity impact and post-impact testing

The core objective of the current characterization program, which is described in Section 5, is the determination of the low velocity impact resistance and the compression strength after impact of the proposed modified CFRP systems, since these characteristics dominate the damage tolerance of the composite material system. The LVI and CAI tests were performed at RT conditions according to AITM1-0010: 2015 standard of Airbus. A guided drop weight tester was utilized for this purpose. A drop tower equipped with a 16-mm diameter hemispherical aluminum impactor weighing 2.5 kg was employed. The selected impact energy was 25 J and was delivered by adjusting the initial height of the impactor. The impactor was manually left to fall from the pre-determined height and was arrested automatically after rebounding to avoid a second strike. The residual compressive strength of the damaged CFRP plates before and after the healing process was measured through CAI tests. For this purpose, an anti-buckling jig was employed to support the specimen edges and to inhibit Euler buckling. All tests were conducted at an Instron (250 kN) hydraulic machine. The specimens were loaded under displacement control of cross-head velocity of 0.5 mm/min.

2.1.6. Composites quality issues

C-scan inspection was performed on all the manufactured plates. A Physical Acoustics Corporation (PAC) UT C-Scan system was used with a 5 MHz transducer. C-scan images of plates intended for mode I, mode II, and LVI tests confirmed good qualities and showed absence of porosity and delaminations due to the manufacturing process.

2.1.7. Healing procedure and healing efficiency calculations

After first crack propagation under mode I or mode II or delamination damage due to LVI described below (Sections 3–5, respectively), the specimens were subjected to a simple healing cycle of heating under controlled through-the-thickness compression. The cycle comprised a 15 min dwell at 100°C under loading of 1 kN for mode I & II samples, while of 5 kN through the thickness compressive force was used for LVI samples, using a heat press machine. The applied temperature was chosen to be 23°C higher than the T_m value (approximately 77°C) of the SP material, for 15 min, in order to be sure that the SP will flow between the crack flanks and to achieve the healing effect. The healing temperatures were chosen based on previous in-house differential scanning calorimetry (DSC) measurements. The compressive loading value was chosen as the minimum necessary to ensure that the adjacent crack flanks were kept in close proximity during healing activation. The loading values were chosen as the minimum necessary to ensure that the adjacent crack flanks were kept in intimate contact during the healing procedure. Then, the samples were left to cool down at room temperature (RT). After the healing cycle, the samples were tested again using the same configurations. The calculations of the healing efficiency (HE) of every system were based on Eq. (3) for mode I and II tests and on Eq. (4) for LVI tests:

$$HE = \frac{M_{healed}}{M_{modified}} \cdot 100\ (\%) \tag{3}$$

$$HE = \frac{S_{healed}}{S_{damaged}} \cdot 100\ (\%) \tag{4}$$

where M or S (i.e., damage area) is the property under examination. M_{healed} and $M_{modified}$ are the values of the property after healing and before healing, respectively. S_{healed} and $S_{damaged}$ are the values of the property after healing and after LVI testing, respectively.

3. Mode I interlaminar fracture toughening and healing of carbon fiber/epoxy composites by hydrogen-bonded supramolecular polymer interlayers as SHA

3.1. Composites manufacturing

Two UD laminated plates made of 22 layers were manufactured for the needs of the current study; the reference plate and the modified one containing the SP interleafs at the mid-plane, both appropriate for mode I interlaminar fracture tests. **Figure 4** shows schematically the plate configuration. The dimensions of the plates were 300 mm × 150 mm × 3 mm. During the manufacturing process, two 13-μm-thick sheets of PTFE film were placed in the mid-thickness plane of both laminates as shown in **Figure 4**, to act as initial pre-crack according to the request of the interlaminar fracture test. In the case of the modified laminate, SP strips were carefully placed at the mid-plane as shown in **Figure 4**(**b**, **c**).

Following the lay-up, the laminates were vacuum bagged and cured in autoclave for 2 h at 130°C under 6 bars applied pressure, according to the prepreg manufacturer guidelines. The fiber volume fraction of all manufactured plates was calculated to be close to 60%. Moreover, the incorporation of the SP film in the mid-plane of the modified laminate did not appear to

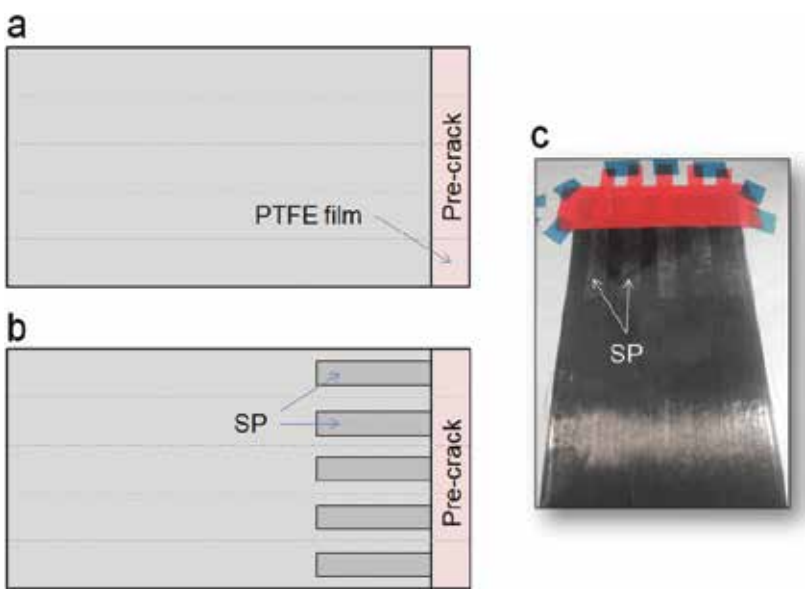

Figure 4. Schematic representation of (a) the reference plate and (b) the modified plate. (c) Photograph of the mid-plane placement of SP film, together with the PTFE initial crack formation.

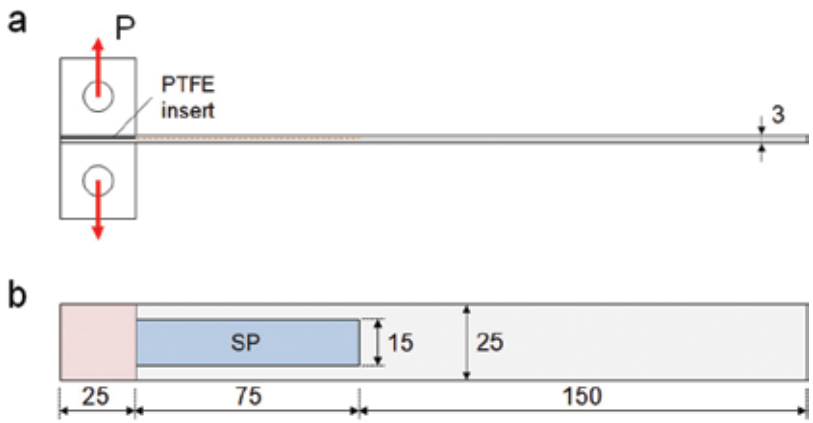

Figure 5. Schematic depiction of the modified DCB test specimen configuration. (a) Side view. (b) Top view. Dimensions in mm.

have a significant effect on the densities and the thicknesses of the samples. Five mode I samples were cut from both the reference and the modified plate. Two aluminum tabs were glued on the DCB specimen outer surfaces (**Figure 5**) using a two-component epoxy adhesive in order to apply the peel/opening forces.

3.2. Results and discussion

The study is deployed in two levels. The first level covers the assessment of the performance change due to the introduction of the SHA in the reference CFRP system. It is possible that the approach to introduce the healing functionality may jeopardize the load-bearing capacity of the composite. This change in performance is commonly referred to as the knock-down effect. The second level of this study deals with the healing functionality of the composite system and its performance. Essentially, once the SHA has been incorporated, the system is expected to have a healing functionality; meaning the capability to heal damage in the form of cracks (externally activated). The extent to which this functionality delivers its purposes is assessed in the second level of this work. Details on the procedure are given in the next paragraph.

3.2.1. Mode I fracture toughness: reference versus modified CFRP

The introduction of the SHA in the CFRP laminate is expected to have an impact on the material performance. In this paragraph, the impact of SHA on the mode I interlaminar fracture toughness is assessed according to specifications described in Section 2.1.3. To this purpose, load-displacement measurements were performed on the pre-cracked samples under mode I peel loading. The concluded load-displacement curves for the reference as well as for the SHA-modified samples are depicted in **Figure 6(a)**. For both composite DCB specimens, the applied load initially increased linearly prior the interlaminar pre-crack start to propagate, followed by a deviation from linearity and ended with a load drop as the crack starts to propagate. It is important to notice that the modified laminate that comprises the SP film as

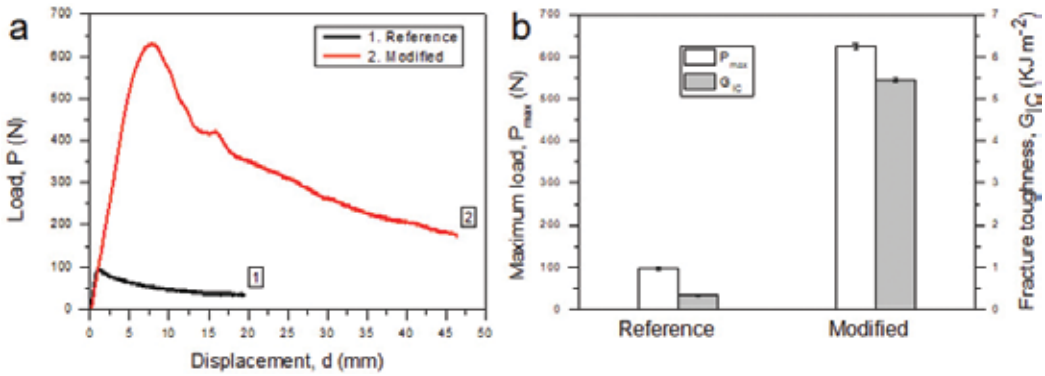

Figure 6. (a) Representative load (P) versus crack opening displacement (d) curves during the mode I interlaminar fracture toughness test of the reference and the modified CFRPs. (b) Comparison between the reference and the modified CFRP in terms of the P_{max} and the G_{IC} values, respectively.

interleaf in its mid-plane, displays a significantly higher P_{max} and calculated G_{IC}, when compared to the reference laminate without SP interleave (**Figure 6(b)**).

Figure 7 illustrates the bridging that occurs during crack propagation, resulting from the presence of the SP film in between the upper and lower crack surfaces of the sample. The crack appeared to propagate through the SP interleaf rather than along the SP/thermoset interface. Clearly, the presence of the SP interleaf reduces the crack opening displacement at a given applied load, due to the developed bridging within the crack flanks, and thus results in a lowering of the stress at the crack tip, and consequently in an increased mode I interlaminar

Figure 7. Illustration of the extended bridging phenomenon of the SP interleaf between the upper and the lower adjacent surfaces during mode I tests.

fracture toughness. Furthermore, the SP material displayed a high peel resistance. The results clearly show that the presence of the SP interleave in the plate resulted not only in a considerable increase of P_{max} (545%) but even more into a calculated G_{IC} that was increased with more than one order of magnitude (1550%).

Typical crack opening resistance curves (R-curves) under mode I loading conditions for the reference and the SP-modified composites are depicted in **Figure 8**. The G_{IC} value in composite laminates is of great importance, since it controls the initiation and the propagation of the delamination damage. As it is shown in **Figure 8**, the reinforcing effect of the SP film is apparent. The presence of the SP interleaf promotes the development of a bridging traction zone at the interlaminar region, which suppresses the crack tip opening stresses and as a result increases the resistance of the composite to both the initiation and the propagation of the delamination damage. The R-curve for the reference composite shows the plateau value already after reaching a crack length of 30 mm, resulting in a very limited damage process zone (lower than 5 mm). On the other hand, the R-curve for the SP-modified interleaf composite shows the plateau value only after reaching a crack length of 45 mm. This results in an extended damage process zone followed by a self-similar crack propagation pattern showing the typical delamination evolution mechanism up to a crack growth length of 80 mm and eventually resulting in a significant reduction of G_{IC} value at longer crack lengths.

The significant toughness increase observed for the modified interleaf is attributed to the enhanced SP material interface with the epoxy matrix, which is extremely strong thereby forming strong bonding between the SP polymer and the epoxy resulting in a transfer of the propagation of delamination to the SP material. This enhanced interface is visible in **Figure 9(b)**,

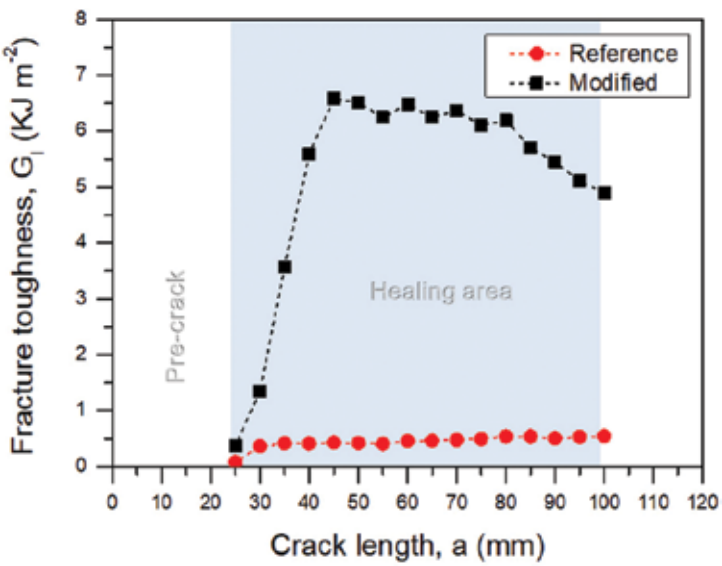

Figure 8. Representative R-curves of the reference and the modified CFRPs, showing the relation between G_I and crack length (a).

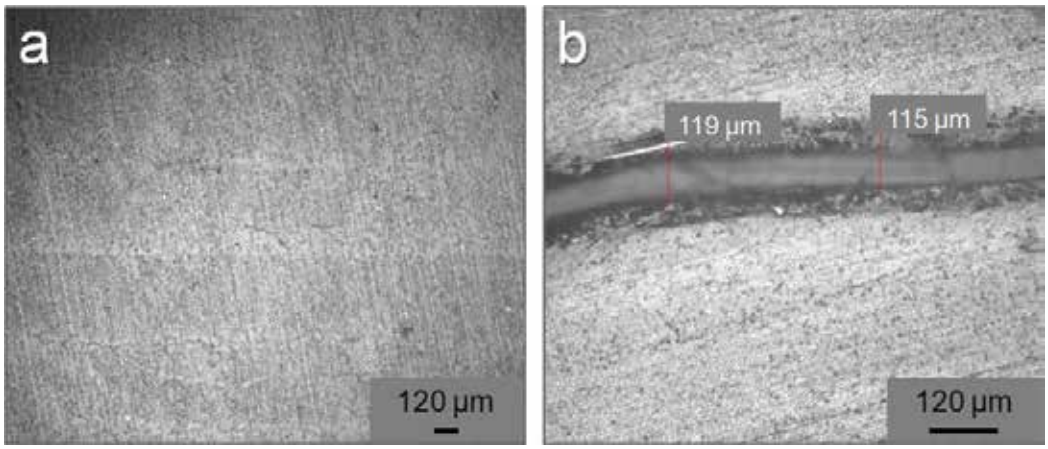

Figure 9. Cross section of the (a) reference and (b) SP interleaved-modified composite.

which shows infiltration by the SP material into the epoxy matrix as evidenced by the darkened region of the matrix next to SP interleaf.

In addition, there is also a clear difference between the failure types of the matrix. The reference material clearly shows brittle matrix failure with intact carbon fibers as observed with optical microscopy (**Figure 10(a)**). In contrast, the matrix of the SP-modified interleaf composite shows ductile failure, since both fracture surfaces are covered with the SP interleaf comprising partially pulled-out carbon fibers emanating from the edges of the SP film that the epoxy system exists (**Figure 10**(**b**, **c**)). This behavior reveals the strong bonding of the SP interleaf with both the matrix and the carbon fibers due to the infiltration. This strong bonding is foreseen to inhibit crack propagation because of the extra energy required for interfacial failure. In this turn, interfacial failure leads to frictional sliding and/or plastic deformation at the interface and finally to the propagation of delamination through the SP material as well as carbon fibers breakage or pull-out and crack bridging. Another characteristic of the SP was the formation of agglomerates on fractured surfaces locally, after the fracture of the SP interleaf (**Figure 10(d)**), probably originating from yielded SP bridges at the delamination interfaces.

3.2.2. Assessment of healing functionality of composites

The ability of these SP interleafs for self-healing of the cracked CFRP composites was investigated by subjecting the samples after the interlaminar crack propagation under mode I loading to a healing cycle of heating and compression of the laminates at 100°C for 15 min under a compressive load of 1 kN, as described in Section 2.1.7. Indeed, when the fractured samples had been removed from the loading frame after the mode I interlaminar fracture tests, and had been subjected to this healing cycle, a large recovery of the interlaminar fracture performance was observed. As can be seen in the resulting load-displacement curves for the SP-modified composites before and after the healing (**Figure 11(a)**), recovery of around 60% of P_{max} and G_{IC} values after the first healing cycle were monitored. In subsequent healing cycles on the same samples, a

http://dx.doi.org/10.5772/intechopen.70884

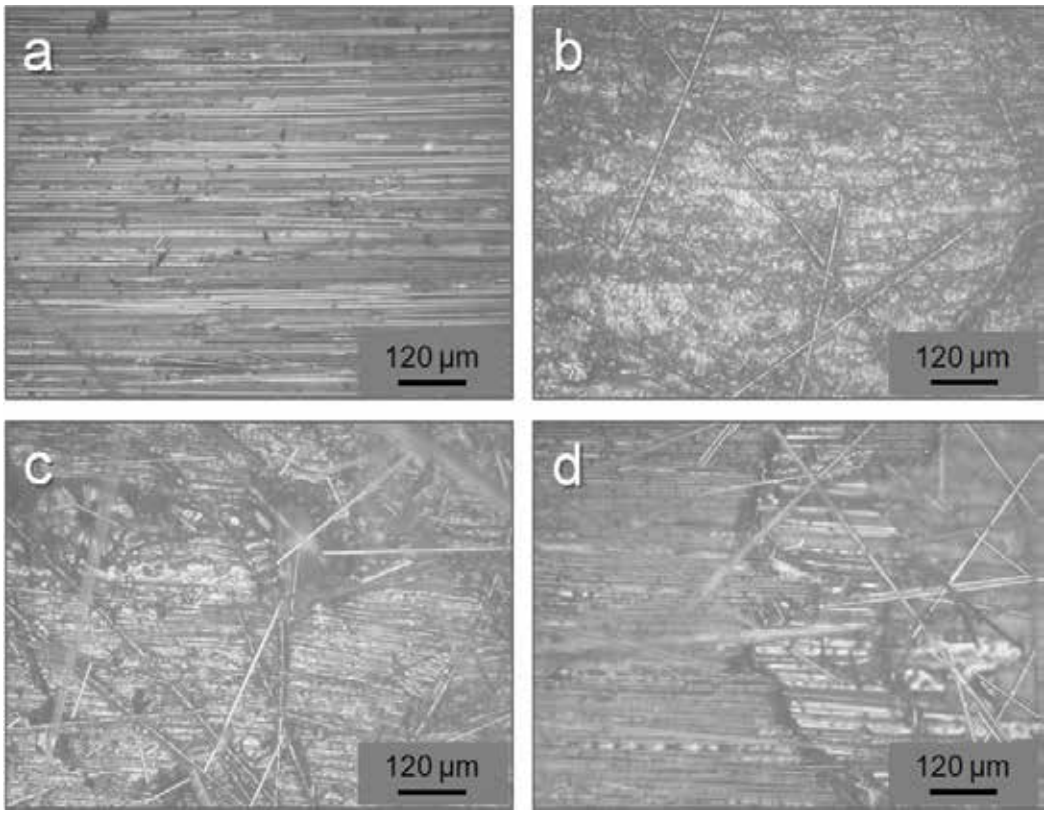

Figure 10. Fracture surfaces of the CFRPs. (a) Reference. (b) Bottom fracture plane of the SP interleaf-modified CFRP. (c) Top fracture plane of the SP interleaf-modified CFRP. (d) Illustration of the agglomerates on the top fracture plane of the modified CFRP. In the left side (of image (d)), the epoxy area is distinguished, while in the right side, the infiltrated area is distinguished by the SP material (photograph taken from the edge of the SP interleaf).

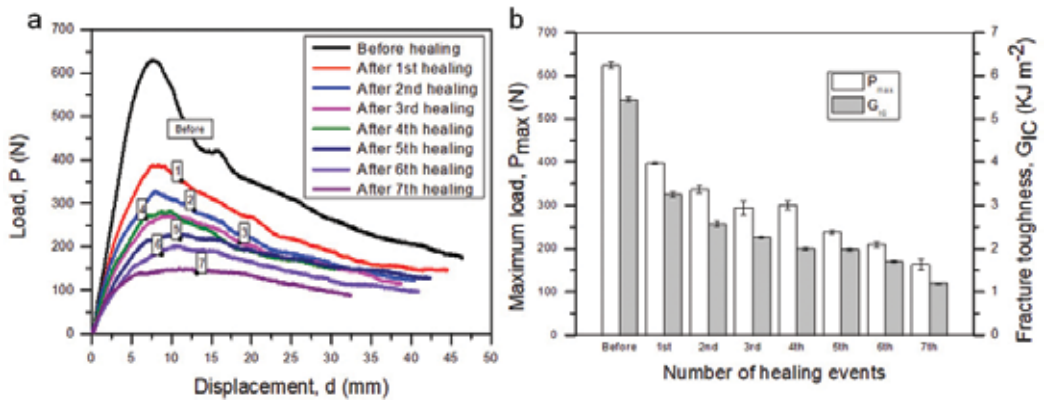

Figure 11. (a) Representative load (P) versus crack opening displacement (d) curves before and after the healing cycles during the mode I experiments. (b) Bar diagrams for the P_{max} and G_{IC} values, before and after the healing cycles in mode I experiments.

drop in HE was observed after each cycle until the recovery of P_{max} and G_{IC} values, after the seventh healing cycle, dropped at the level of 26 and 22%, respectively, when compared to the pristine samples (**Figure 11(b)**). Although, the bridging of crack flanks was still there during mode I interlaminar loading for the healed samples, its efficiency appeared to decrease with increasing number of healing cycles.

The ability of the healing interleaf to heal the cracks and to recover the fracture properties depends highly on the ability of the SP material's chains to reconnect themselves after mechanical rupture during the mode I experiments. It is important to notice that during manufacturing of the samples, there is a diffusion of SP polymer into the epoxy matrix and consequently, the intra SP propagation of the delamination under mode I loading. Due to the sufficiently low viscosity of the SP polymer at 100°C, it flows along the crack flanks and covers the debonded surfaces. The presence of the thermally reversible hydrogen bonds between the polymer chains, anchored strongly on the crack flanks, under mechanical loading, facilitates the extensive contact between the SP polymer chains and the final rebonding upon cooling. The observed reduction in the P_{max} and the G_{IC} values with increasing number of healing cycles, is attributed to the progressive deactivation of the thermally reversible hydrogen bonds versus exposure time at high temperature and an uneven distribution of the SP film over the debonded surfaces during the healing cycle at 100°C, which concludes to thickness variation of SP polymer and variation of the delamination propagation locally.

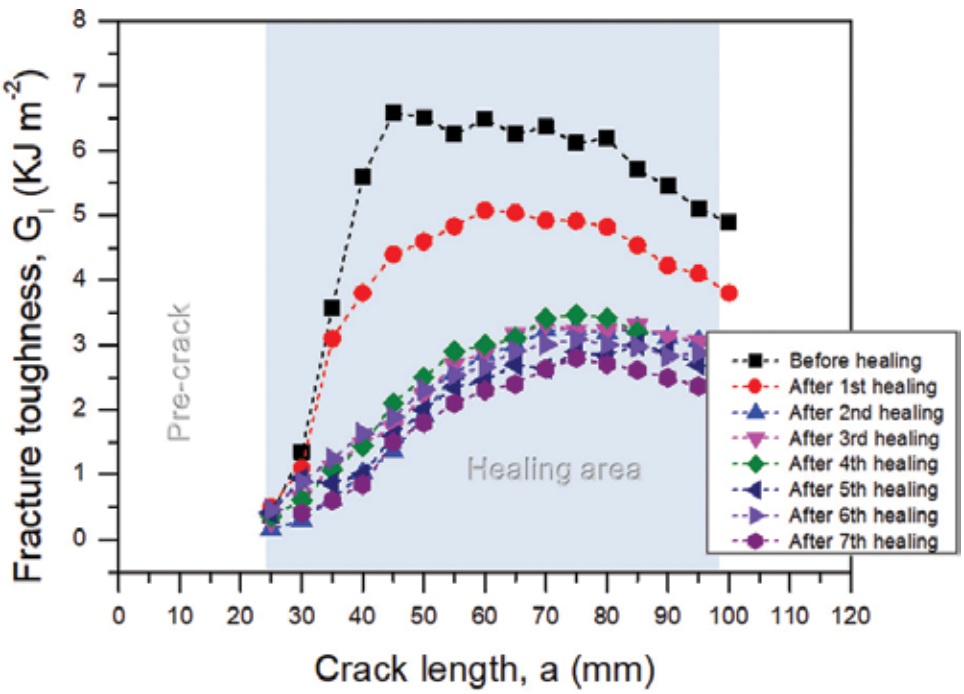

Figure 12. Representative R-curves of the modified composite before and after the healing cycles, showing the relation between G_I and crack length (a).

The typical R-curves under mode I loading conditions before and after the application of the healing cycles are depicted in **Figure 12**, and they are consistent with the load-displacement data. The general trend is that with increasing number of healing cycles, the G_{IC} values decrease and the plateau values of the G_{IC} reach at a slightly later stage than the corresponding plateau value of the pristine SP-modified interleaf composite, at 50 mm instead of 45 mm. In line with the pristine SP sample, the plateau value remains almost constant until a crack growth length of about 80 mm. It is necessary to stress that after the first rupture of the interleaf-modified composite, the only active material that works and keeps the upper and lower fractured surfaces together after healing activation, is the reversible polymer material and the epoxy matrix infiltrated by this. More information can be found in Ref. [33].

3.2.3. Knock-down effect on in-plane mechanical properties

The incorporation of the SP interleaf into composites laminate is expected to have an impact on in-plane properties of the composite. For this purpose, 3PB tests were conducted for the reference and the modified CFRPs, where a layer of SP polymer was placed at the middle surface of the composite. According to these experiments, it was shown that there was no knock-down effect on the flexural modulus (E_{flex}) of the composite as it was retained close to 55.5 GPa for both reference and modified CFRPs (due to the position chosen for the introduction of SP polymer). On the other hand, the flexural strength (σ_{max}) value was reduced by 22% (from approximately 638 to 493 MPa). Bar chart in **Figure 13** describes these results in detail. Based on this, a more detail investigation is needed for evaluating completely the effect of the introduction of SP polymers into the composite laminate.

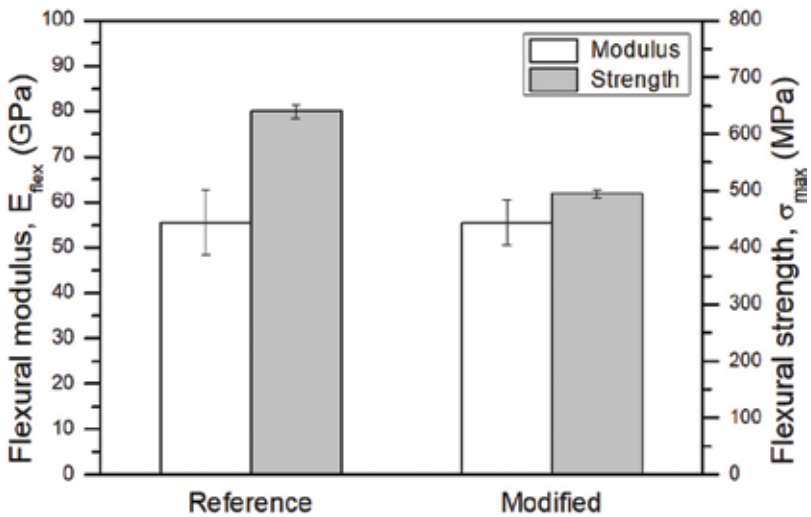

Figure 13. Knock-down effect of the SP interleaf on the E_{flex} and σ_{max} values of the CFRP.

4. Mode II interlaminar fracture toughening and healing of carbon fiber/epoxy composites by hydrogen-bonded supramolecular polymer interlayers as SHA

4.1. Composites manufacturing

Two UD laminated plates made of 22 prepreg layers were manufactured for the needs of the current study; the reference laminate and the modified laminate containing the SP interleaf on the mid-plane, both appropriate for deriving mode II interlaminar fracture specimens. **Figure 14** shows schematically the plate configuration with respect to the fracture pre-crack and the SHA location. During the manufacturing process, two 13-μm-thick sheets of PTFE film were placed in the mid-thickness plane of both laminates as shown in **Figure 14** to act as initial pre-crack according to the request of the interlaminar fracture test. In the case of the modified laminate, a SP strip was carefully placed on the mid-plane as shown in **Figure 14**(**b**, **c**). Following the lay-up, the laminates were vacuum bagged and cured in autoclave for 2 h at 130°C under 6 bar pressure, according to the prepreg supplier guidelines. The dimensions of the plates were 300 mm × 150 mm × 3 mm. Five mode I (DCB) samples were cut from both the reference and the modified plate. The incorporation of the SP film in the mid-plane of the modified laminate did not appear to have a significant effect on the thicknesses of the samples. The fiber volume fraction of all manufactured plates was calculated to be close to 60%.

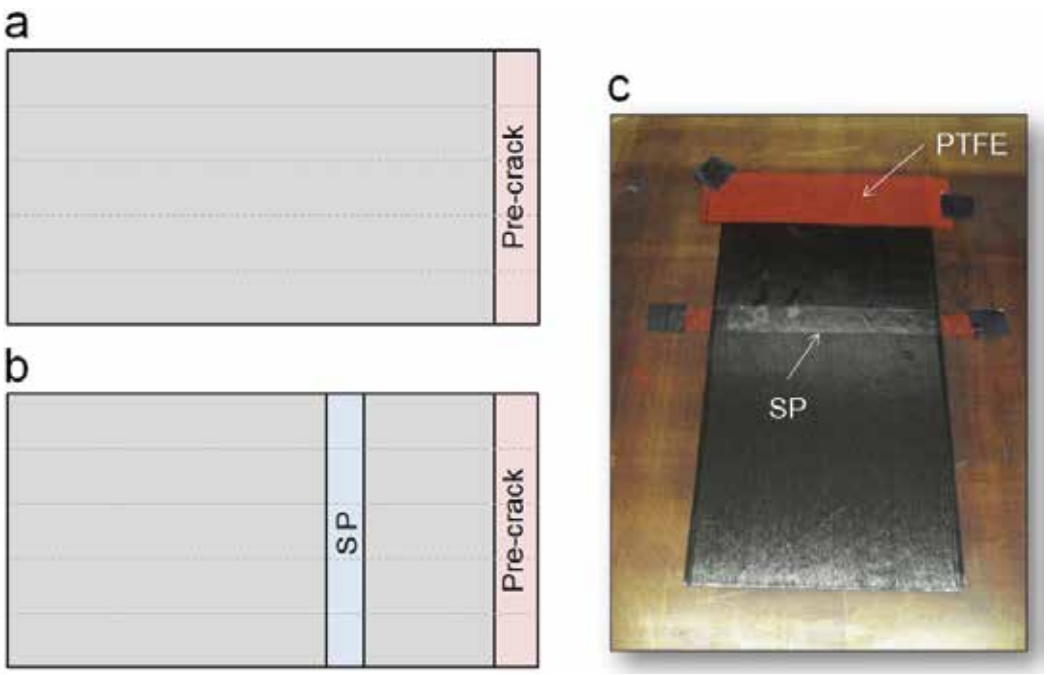

Figure 14. Schematic representation of the mid-plane of (a) the reference plate and (b) the SP containing modified plate. (c) Photograph of the mid-plane of the modified plate, where a SP strip was carefully positioned, together with the PTFE film.

4.2. Mode II interlaminar fracture toughness testing

The mode II experiments were performed according to specifications described in Section 2.1.4. Based on Eq. (2), the crack length (a) has to be known in order the G_{IIC} value to be calculated. For brittle materials, the moment of unstable crack growth can be clearly determined; P_{max} is attributed to the critical load at the onset of crack growth. On the other hand, for modified materials containing ductile interleaves in which the crack is growing through the ductile interleaved layer as described in Section 3, the crack initiation (P_{ini}) occurs long before P_{max}. In addition, in mode II loading of the pre-cracked specimen the crack tends to close which hinder a clear visualization of its tip. Thus, mode II fracture characterization of CFRPs with a ductile interlayer remains a major challenge including uncertainties on the results. **Figure 15**, depicts the modified ENF test specimen configuration as derived from DCB specimen.

Based on these, whereas in the case of reference CFRPs the G_{IIC} calculations were extracted directly from the P-d data without any concern, for the modified CFRPs the monitoring of the crack growth was carried out by using a high-resolution digital camera system **Figure 16**. It is suggested that the crack initiation point of the modified CFRPs corresponds to the onset of the visual deviation of linearity in P-d curves. In addition, a vertical line with pencil was marked at the end of the starter film, as shown in **Figure 16**. It is suggested that the separation of the line into two lines corresponds to the crack initiation.

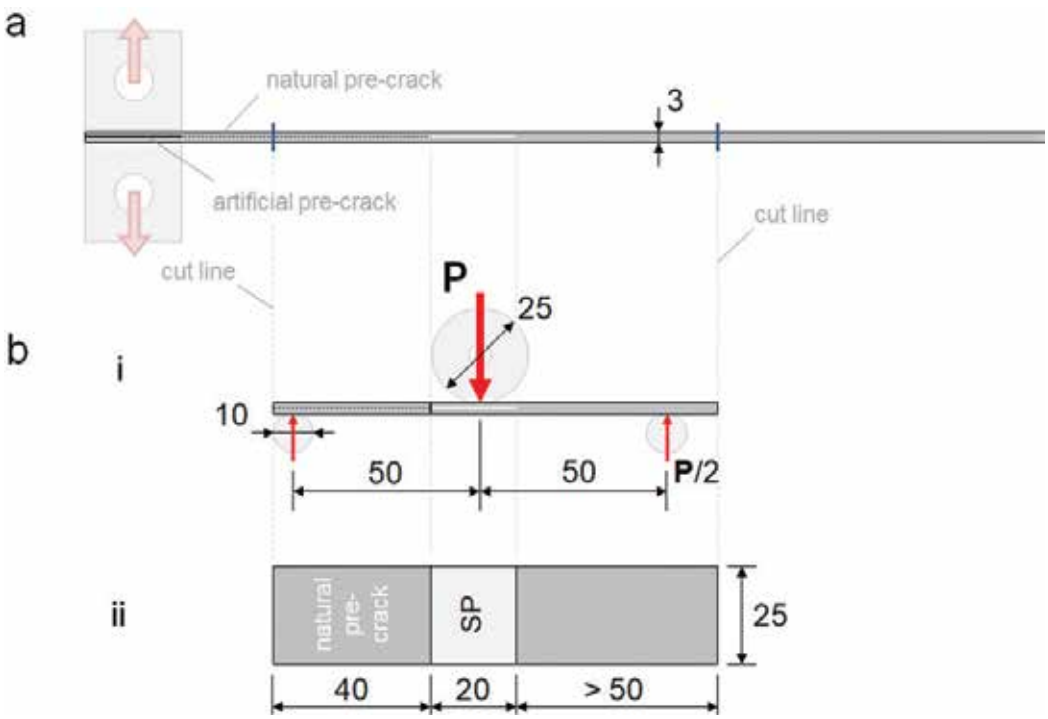

Figure 15. Schematic depiction of the modified ENF test specimen configuration as derived from DCB specimen. (a) DCB specimen, (b) ENF specimen, (i) side view, (ii) top view. Dimensions in mm.

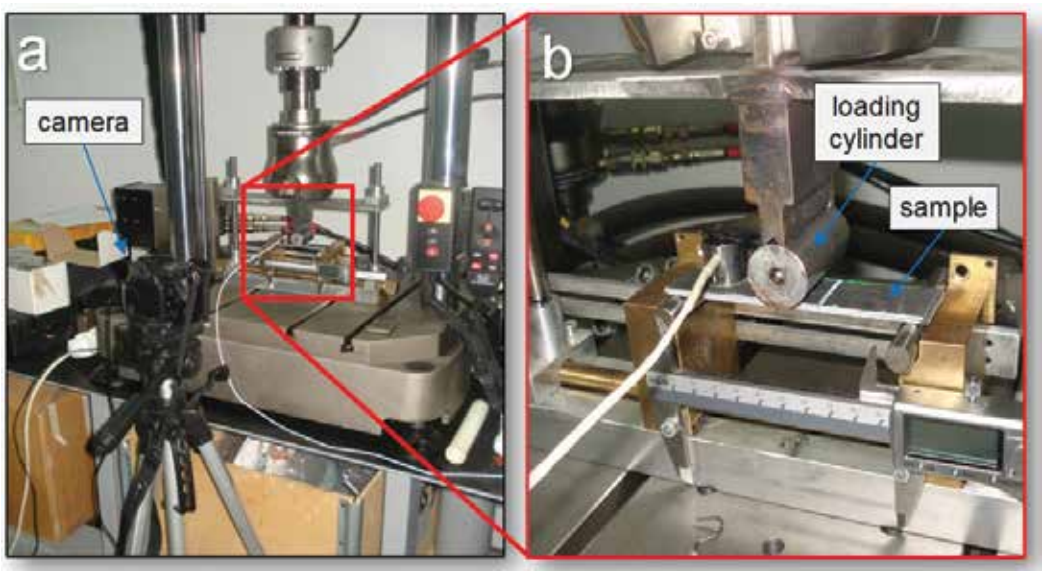

Figure 16. Experimental setup of the mode II interlaminar fracture toughness tests where the high-resolution camera monitoring of the crack evolution is seen.

4.3. Results and discussion

The study is deployed in two parts. The first part covers the assessment of the performance change due to the introduction of the SHA in the reference CFRP system. It is possible that the approach to introduce the healing functionality may jeopardize the load-bearing capacity of the composite. This change in performance is commonly referred to as the knock-down effect. The second part of this study deals with the healing functionality of the composite system and its performance. Essentially, once the SHA has been incorporated, the system is expected to have a healing functionality; meaning the capability to heal damage in the form of cracks (intrinsic or externally activated). The extent to which this functionality delivers its purposes is assessed in the second level of this work. Details on the procedure are given in the next paragraph.

4.3.1. Mode II fracture toughness: reference versus modified CFRP

The introduction of the SHA in the CFRP architecture is expected to have an impact on the material performance. At this part of the work the impact on mode II fracture toughness is assessed. The mechanical response of the reference and the modified CFRP to mode II fracture loading in combination with crack evolution camera recording was studied.

Typical load-displacement (P-d) curves for the reference and the modified plate are given in **Figure 17(a)**. All specimens within each set showed a similar behavior. The average values and standard deviation for the two material sets are shown in **Figure 17(b)**. As previously mentioned, the P-d behavior of the two material sets differs. For the reference material, the applied load increases linearly until the onset of the pre-crack propagation where the load drops abruptly. On

http://dx.doi.org/10.5772/intechopen.70884

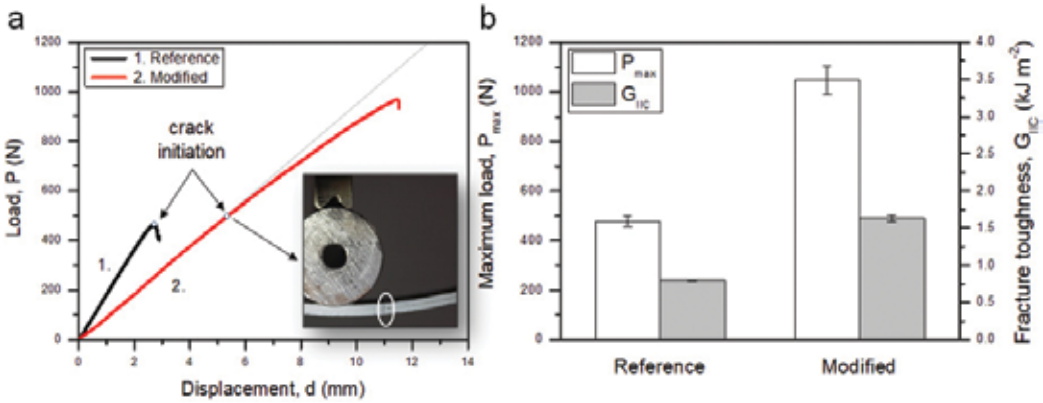

Figure 17. (a) Representative load (P) versus displacement (d) curves for the reference and modified CFRPs during the mode II interlaminar fracture toughness test. (b) Comparison between the reference and the modified CFRP, for the P_{max} and the G_{IIC} values, respectively.

the other hand, for the modified CFRP, the initially linear P-d relation is followed by a distinguishable deviation from linearity and much latter the load drop appears. Whereas the load drop for the reference case is attributed to the crack evolution onset, for the modified CFRP the P_{max} indicates the load-bearing capacity of the composite before undergoing major damages. Interestingly, the modified laminate exhibits a significantly higher P_{max} and respective displacement. As seen in the **Figure 17(a)**, P_{max} is more than double that of the reference CFRP (120% increase) while the displacement at failure is approximately four times larger than the reference.

From the recorded mechanical data, the mode II interlaminar fracture toughness (G_{IIC}) was calculated. For the calculation, the displacement (d) at crack propagation onset is needed to be known. The crack initiation points for the reference and the modified CFRP, determined as described in Section 4.2, are marked in **Figure 17(a)**. The snapshot of **Figure 17(a)** corresponds to the marked crack initiation point for the modified specimen. In this snapshot, a slight separation of the pencil line into two lines is observed. The G_{IIC} for both material sets were calculated using in Eq. (2) the (P, d) values that correspond to the indicated points of the curve. The average values and standard deviation are shown in **Figure 17(b)**. The G_{IIC} values for the modified CFRP exhibit an increase of 100%, which is related both to the slightly higher corresponding load (P) recorded and to the displacement (d) at that instance.

The post-tests inspection revealed the in-plane crack propagated through the SP interleaf rather than along the SP-epoxy interface. This observation indicates that the interface of the interleaf to the host matrix is stronger than the properties of the interleaf, thus guiding the crack to a lower energy path through the interleaf (see Section 3). This was also monitored in the case of mode I experiments. This behavior essentially maximizes the effectiveness of the interleaf and explains the higher resistance to crack propagation. In addition, high displacements are recorded while the load increased steadily. This can be related to the ductile behavior of SP polymer, in combination with its strength. Even when the crack initiated, the presence of the SP interleaf arrests the crack and prevents propagation due to the developed shear bridging (see Section 3) within the crack sides. These results to lower stress at the crack tip

and consequently to an increased mode II interlaminar fracture toughness. Based on these results, it is clearly shown that the presence of the SP interleave in the composite resulted in a considerable increase of the mode II interlaminar fracture toughness characteristics. On the other hand, the mechanisms delivering this increase of mode II fracture toughness are related both to the SP-epoxy interface (the diffusion of SP polymer into epoxy matrix), as well as the structural properties of the interleaf itself. Thus, it is obvious that the fracture toughness characteristics of the composite have been enhanced significantly by the introduction of the SP interleaf. It can be concluded that, regardless of the healing functionality performance, this finding is extremely positive and of great interest.

4.3.2. Assessment of healing functionality of composites

The healing functionality of these SP interleaves into CFRP composites was assessed by subjecting the samples to a healing cycle consisting of heating and compression as described in Section 2.1.7. Indeed, a large recovery of the interlaminar characteristics (P_{ini}, P_{max} and G_{IIC}) during the repeated mode II experiments was observed when the fractured samples had been subjected to multiply healing cycles.

In **Figure 18(a)**, the recorded load-displacement data are shown for a representative modified CFRP specimen. There are five curves; one for the initial test (before healing) and one after each consecutive healing cycle. In all curves, the general trend is the same; the initially linear P-d part of the curve is followed by a deviation from linearity. In subsequent healing cycles, the sample exhibits a drop in stiffness as well as a smaller P_{max} value. Nevertheless, the lowest P_{max} value remains well above that of the reference value (approximately 80% higher). In **Figure 18(a)**, a magnification of the curves at the crack initiation points is given and for each curve the crack initiation points are marked. In the histogram of **Figure 18(b)**, the effect of the number of healing cycles on the mode II fracture characteristics (P_{ini}, P_{max} and G_{IIC}) of the modified CFRP is presented. After the first healing activation, the P_{ini} and P_{max} values of the modified CFRP showed a decrease of approximately 5 and 16%, respectively. The same decreasing trend was observed also after the second healing cycle when the values are compared against the values concluded after the first healing cycle. Following the third healing cycle the decrease of the P_{ini} and P_{max} values were much lower, this was also the trend after the fourth healing cycle. On the other hand, the G_{IIC} values appear a slight increase with increasing the number of healing activation cycles; the G_{IIC} value after the fourth healing cycle is 14% higher than that achieved by the initial SP-modified CFRPs. This behavior is attributed to the fact that the displacement value at crack propagation onset increases as the healing cycles increase (see Eq. (2)). In **Figure 18(c)**, the actual HE values for the three quantities of interest (namely G_{IIC}, P_{ini} and P_{max}) calculated based on Eq. (3), are given as a function of the number of healing cycles. In subsequent healing cycles a drop for the HE_{Pini} and HE_{Pmax} is observed. Nevertheless, the lowest value remains over 70% of the reference values of pristine CFRPs. On the other hand, the bending stiffness of the modified laminate presents a gradual decrease with increasing the number of healing activations.

The partial recovery may is associated with the degradation of the SP properties, as well as the epoxy-SP interface after each loading/healing cycle. In addition, the interlaminar cracked area is only partially healed after the subsequent healing cycles. Snapshots of the sample during the mode II experiments at the crack initiation and fracture points before and after the healing

http://dx.doi.org/10.5772/intechopen.70884

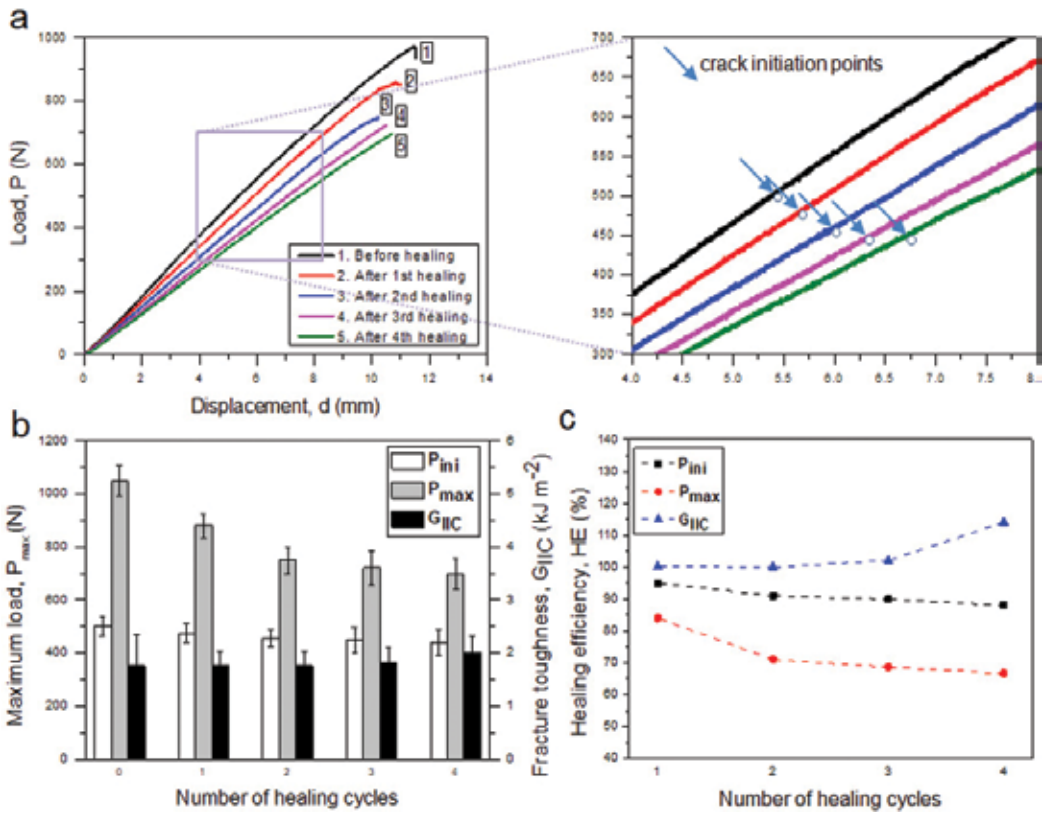

Figure 18. Results from the mode II interlaminar fracture toughness tests of the modified CFRPs before and after four healing cycles. (a) Representative load (P) versus displacement (d) curves for the modified CFRP before and after the healing cycles and determination of the crack initiation point. (b) Bar diagrams for the P_{ini}, P_{max} and G_{IIC} values of the modified CFRP, before and after the healing cycles. (c) The effect of the number of healing cycles on the HE of the modified CFRP, in terms of the P_{ini}, P_{max} and the G_{IIC}.

cycles are illustrated in **Figure 19(a)**. The high HE proportions and the ability of the SP interleaf to heal the cracks are attributed to the SP material's chains that can reconnect themselves after the mechanical rapture during the mode II experiments. Critical parameters are a good coverage of the fractured surfaces by the SP material and a sufficiently low viscosity of the reversible polymer at 100°C in order to be able to flow into the crack flanks and to reposition itself equally over the debonded surface. Therefore, the observed reduction in the P_{max} value with increasing number of healing cycles can be attributed further of the degradation of SP material, to an uneven spreading of the SP interleaf over the fracture surface during the healing cycle. An important point to note is the observation that the apparent flexural stiffness of the system decreases after multiple healing activations. Several reasons have been identified to answer to this observation. Firstly, the tests extended to very large deformation which can lead to the breakage of the fibers on the outer layers. As a matter of fact, **Figure 19(b)** shows evidence of broken fibers on the loading cross-head side. It is proposed that these excessive damages were reflected as portion reduction in the load versus displacement curve. Secondly, during the SHA activation it is possible that not all the interface surface of the crack is healed. Thus, the system

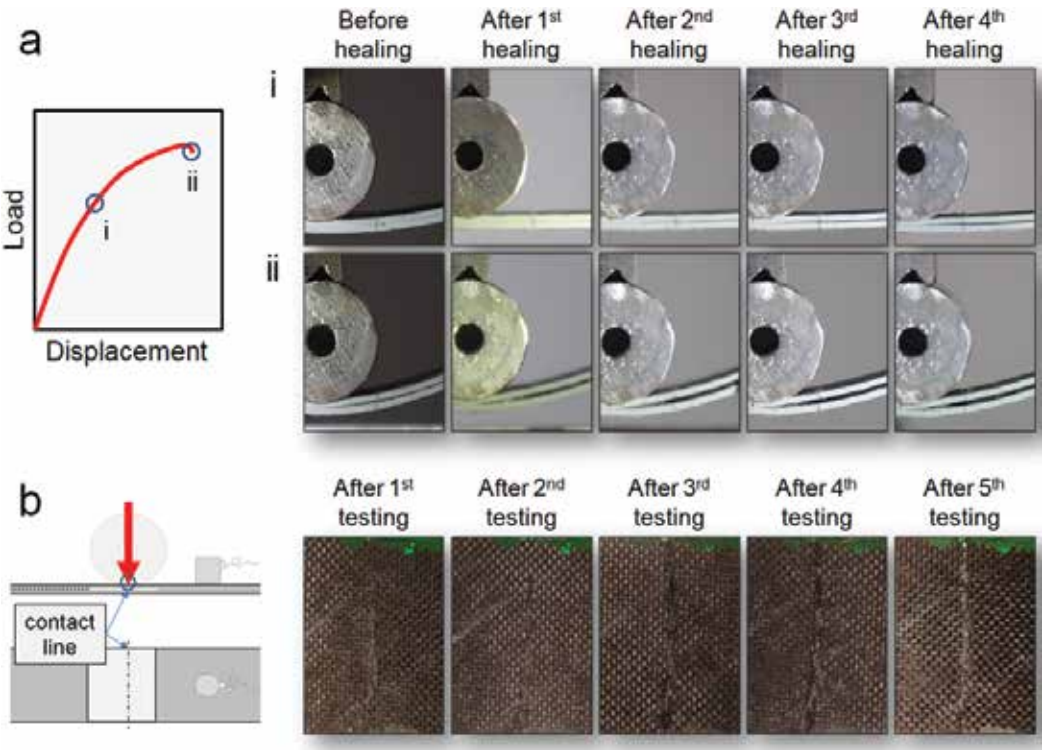

Figure 19. (a) Snapshot during the mode II interlaminar fracture toughness testing of the modified CFRP (i) just after crack propagation onset and (ii) just before failure (i.e. $P \sim P_{max}$), before and after healing. (b) Photographs showing the progressive damage accumulation on the upper layers of the modified CFRP during the mode II testing, with increasing the number of testing cycles. The damaged line is the contact line between the specimen and the loading cylinder.

cannot recover the initial stiffness since the extent of the delamination is larger. Finally, the healing functionality of the SP may degrade after multiple activations; an observation also noted in Section 3 with the same material. According to this work, the bulk SP material can withstand at least seven healing cycles with excellent healing recoveries (still higher toughness values compared to the reference one), but in the present case of mode II loading the experiments were stopped after the fourth loading/healing cycle. The post-testing examination of the fracture surface of the healed laminates revealed that the SHA was clearly separated between the two adjacent fracture surfaces. Thus, the healing effect of the SP material was fully utilized. More information can be found in Ref. [34].

5. Low-velocity impact response and compression after impact assessment of carbon fiber/epoxy composites containing hydrogen-bonded supramolecular prepregs as SHA

5.1. Composites manufacturing

Two types of quasi-isotropic laminated plates containing 16 plies, with $[45/0/-45/90]_{2S}$ stacking sequence each were manufactured for the needs of the current study; the reference laminate,

and the modified laminate, with two SP prepregs placed symmetrically into the composite. Both material groups (reference and modified) were tested under compression prior of impact, in order to identify possible knock down in compression strength. After exposed to LVI, CAI tests were performed for the pristine CFRP plates as well as for the SP prepreg modified ones, but in this case before and after the application of the healing activation cycle. **Figure 20**, shows schematically the configuration of the plates (**Figure 20(a)**) and the position where the two SP prepregs were placed (**Figure 20(b)**). The SP prepregs replaced the 6th and 11th UD 90° layers of the composite (**Figure 20(b)**). Following the lay-up, the laminates were vacuum bagged and cured in an autoclave for 2 h at 130°C under 6 bars applied pressure, according to the prepreg manufacturer guidelines. The dimensions of the final plates were 150 mm × 100 mm × 2.1 mm. Ten reference and 15 modified impact test samples were manufactured, respectively. Five samples of pristine CFRPs and 10 samples of SP prepreg-modified CFRPs were exposed to impact tests. All the samples were tested to CAI. In the case of SP prepreg-modified samples one group was tested to CAI just after initial impact, while a second group was passed through a healing cycle (following the earlier described cycle) and after this step they were also tested to CAI.

5.2. Results and discussion

5.2.1. Composites manufacturing

The handling of the CF/SP prepreg plies at RT and the incorporation of them into composite laminate did not create any concerns. SP prepreg seem to combine characteristics of both traditional thermoplastics (good processability, softening and flow at elevated temperatures). The modified prepreg UD plies had an average thickness of 180 μm each and thus they did not alarmingly thicken the entire CFRP laminate. The fiber volume fraction of both composite groups was calculated to be slightly lower for the modified plates (approximately 60% for the reference while approximately 59% for the modified ones, respectively). They also did not disrupt the fiber architecture. In **Figure 21**, optical microscopy cross-section photographs of reference and modified CFRPs with SHA based on SP are illustrated. Optical microscopy photograph of the modified CFRPs show the location where the SHA has been incorporated symmetrically.

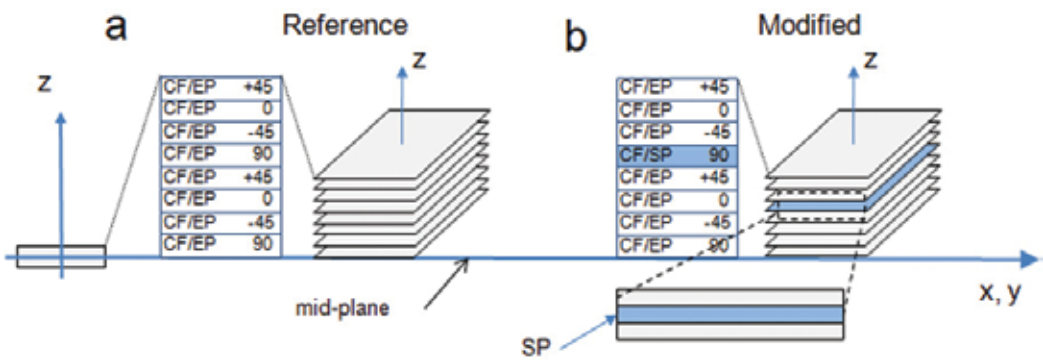

Figure 20. Design of (a) the reference CFRP, (b) the modified CFRP with SP prepregs.

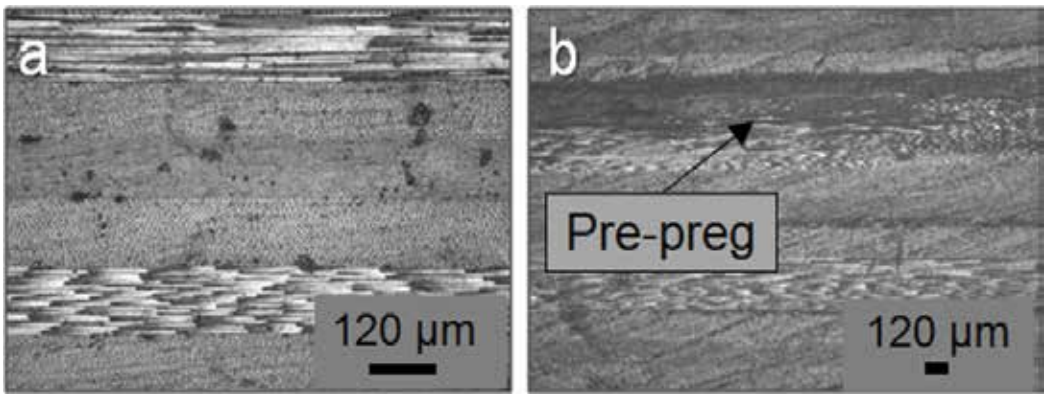

Figure 21. Optical microscopy photographs of (a) the cross-section area of reference CFRPs, (b) the cross-section area of modified CFRPs with SP prepregs in which the SHA area is also clearly illustrated.

5.2.2. Resistance to low-velocity impact

Reference and modified CFRPs were subjected to LVI as described in Section 2.1.5. After testing, C-scan inspection measurements were performed to evaluate the impact-induced damage. The typical C-scans for all material types in the before and after impact situations are shown in **Figure 22**(**a**, **b**). The white region in the center of the images in **Figure 22**(**a**, **b**) represents the damage area (mainly delamination) induced by the impact event. For the determination of the impact damage area, post-processing software was utilized. The software was able to quantify the white region area (damage area) of the recorded C-scan images after the LVI event for both material sets. These areas were calculated to be approximately 592 and 115 mm^2 for the reference and the modified plates, respectively. Thus, the modified composites exhibit higher resistance to delamination, compared against the reference ones. The incorporation of the SHA in prepreg form into composite laminate increases the LVI damage resistance of the final material. The SP prepreg provides higher energy absorption characteristics to the entire composite due its ductile nature, during LVI. In the present work impact energy of 25 J was used. It is considered a moderate amount of impact energy that does not occurs fiber breakage and the main damage mode that is promoted is delamination. In fact, no visible or detectable damage was shown on the top and bottom faces of the reference samples after LVI testing. On the contrary, optical inspection of SP-modified prepreg samples exhibited only indentation on the top face (**Figure 22(ci)**), while no ply splitting phenomena were observed on the bottom face of the CFRP plate (**Figure 22(cii)**).

In general, during an impact event with moderate impact energy, the impact energy introduced into the composite structure is mainly absorbed through elastic deformation and through different failure modes. In CFRPs, plastic deformation does not take place. Samples containing SHAs with a ductile nature such as SP, plastic deformation takes place. **Figure 23** illustrates cross-section photos at the center of reference and modified CFRPs (around the impact site) after LVI. According to **Figure 23(a)**, the formation of multiple delaminations sites in the reference sample is apparent. On the contrary modified CFRPs exhibited different

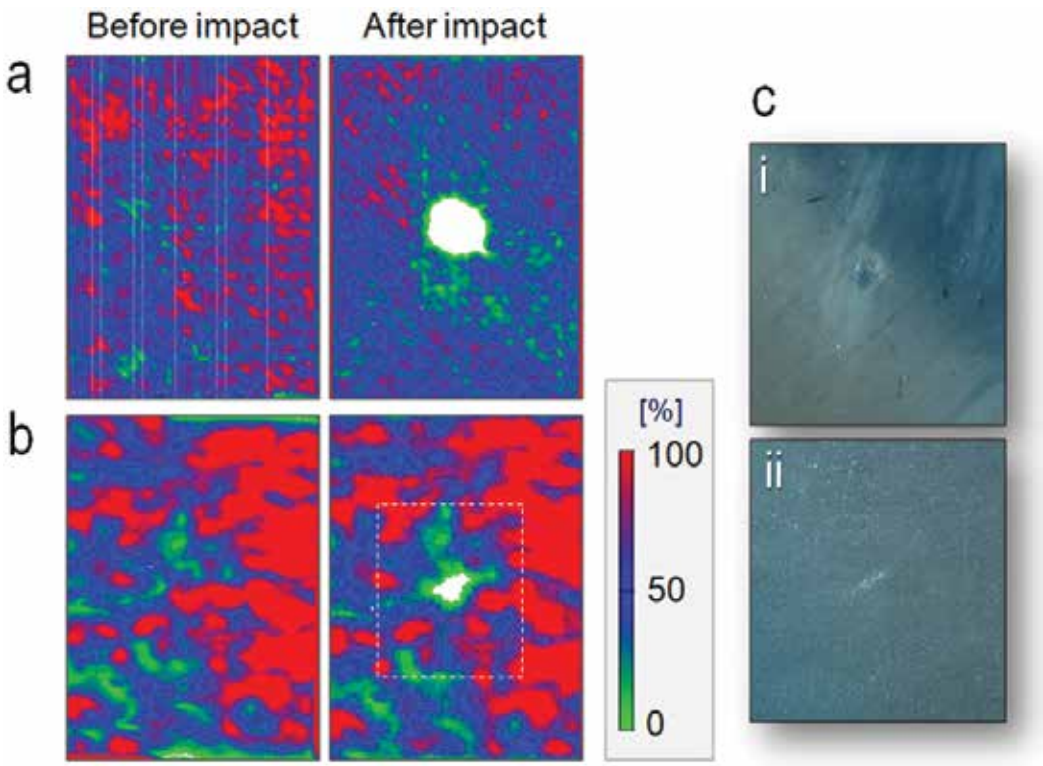

Figure 22. Representative C-scan inspection images of the (a) reference CFRP, (b) modified CFRP with SP prepregs in the before and after the LVI situation. (c) Indicative top- and bottom-face photographs after LVI for the SP prepreg-modified composites.

behavior after LVI. Extended damage has been occurred into the composite in the form of delaminations and significant transverse cracks that leads to off axis ply split.

5.2.3. Repair of the impact-induced damages via the healing treatment

After LVI tests, one group of the SP prepreg-modified samples were subjected to heating under controlled through-the-thickness compression as described in Section 2.1.7. After healing, C-scan was performed in order to evaluate the reduction of the impact damage in the areas where the SP prepregs have been placed. Interestingly, it was found that after healing the modified samples exhibited macroscopically a HE of about 40% (accounting by the measurement of the impact damage area before and after healing, as it demonstrated globally in the C-Scan plots (**Figure 24**(**a**, right)).

The HE value was calculated according to Eq. (4). Modified composites were not able to heal the entire damage after the healing process as **Figure 24** suggests. The SHA has the trend to follow the carbon fibers (90^{o} ply). This behavior was also validated by optical microscopy examination of the damaged samples after the healing process. Materials micro-structure examination under optical microscopy was used to validate the results from non-destructive

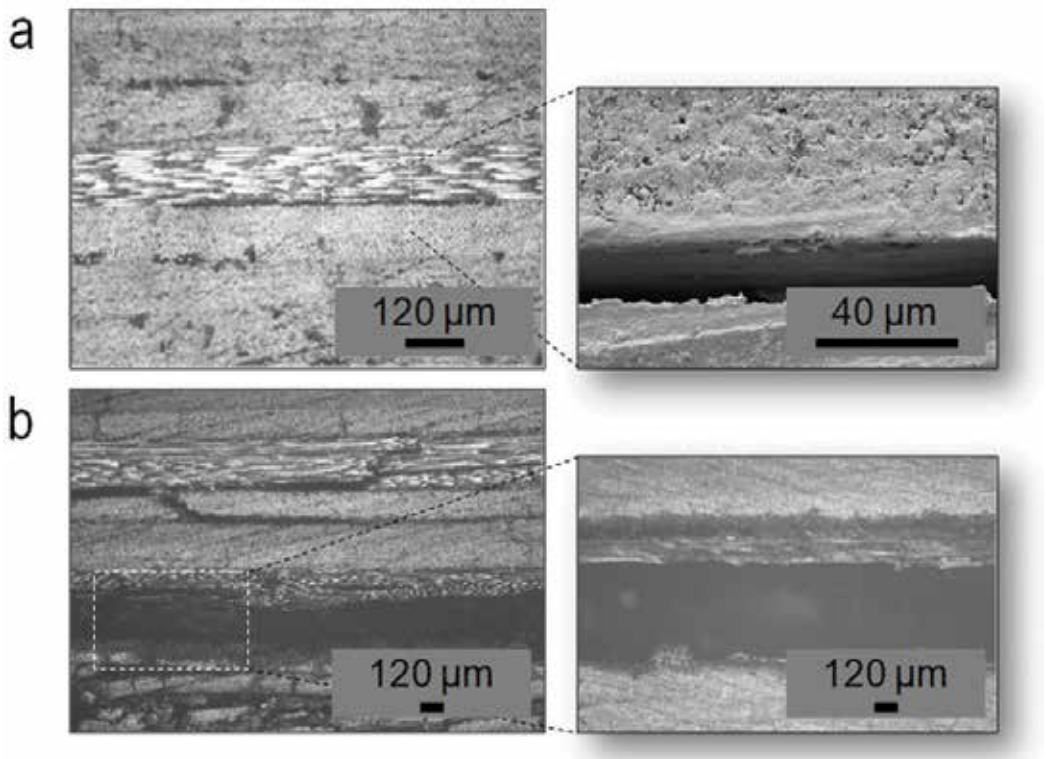

Figure 23. Optical microscopy photographs for reference and modified CFRPs cross sections after LVI situation (a) reference CFRP, (b) modified CFRP with SP prepregs.

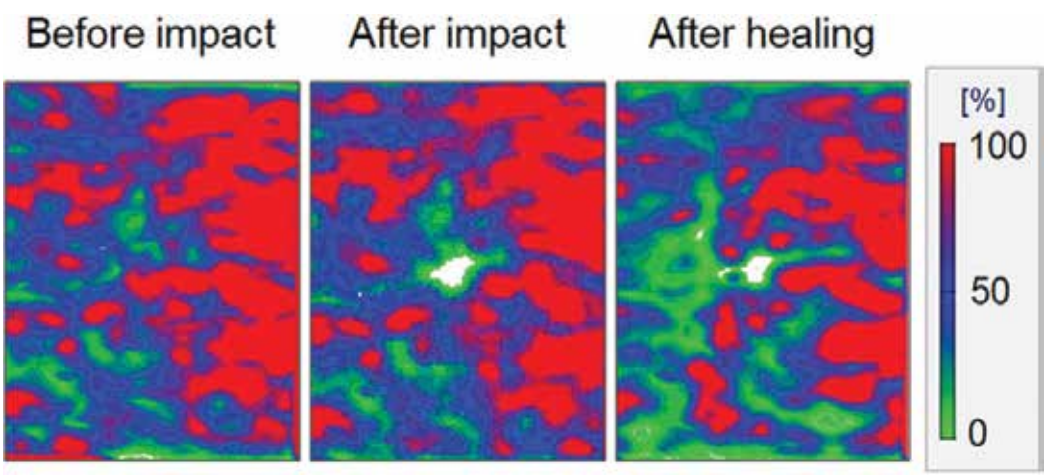

Figure 24. Representative C-scan inspection images of the modified CFRP plates with SP prepregs, in before, after impact situation and after healing process.

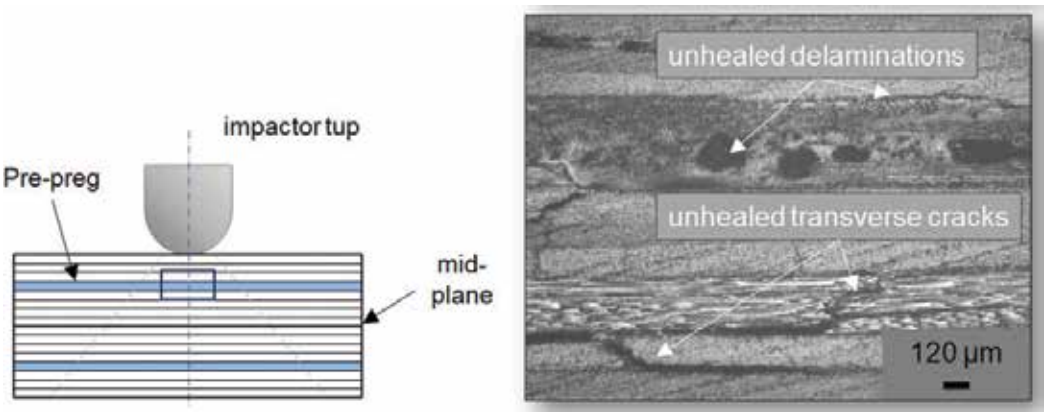

Figure 25. Optical microscopy photograph of the SP-modified CFRP cross section after the healing process.

C-scan inspections. In **Figure 25**, the optical microscopy photos of the cross sections of the repaired modified CFRPs are illustrated. **Figure 25** zooms in the SHA area (CF/SP prepreg layer) and the upper and lower adjacent layers of the laminate. For the modified samples (**Figure 25**) the presence of many delaminations after the healing process is still apparent, as it is expected in all the interfaces that do not contain SP material. Only areas adjacent to SP were healed and this is the reason why low HE value for the damaged area in modified samples was achieved.

5.2.4. Compressive behavior of CFRPs before impact

The incorporation of SP prepreg into composite laminate is expected to have an impact (i.e., knock-down effect) on final composites' mechanical performance. In the present subsection, the effect on the compressive properties is assessed. Typical stress versus strain curves under compression before impact (CBI) for the reference and modified CFRPs (unimpacted) are illustrated in **Figure 26(a)**. In all curves, the initially linear stress versus strain response is

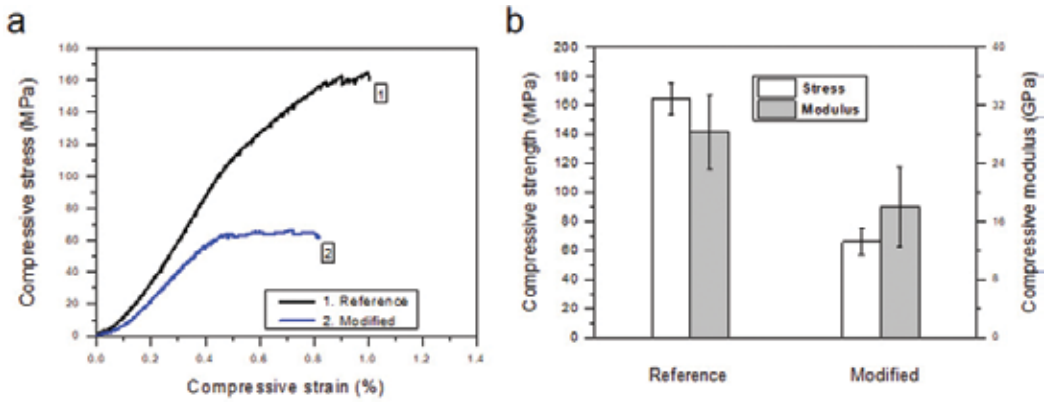

Figure 26. (a) Representative compressive stress versus compressive strain (%) curves from the CBI testing of the reference and modified CFRPs. (b) σ_{max} and E_{comp} the values of the two material types.

followed by a deviation from linearity and load drop just before the end of the test. The compressive strength (σ_{max}) and the effective compressive modulus (E_{comp}) values of the two material types are summarized in **Figure 26(b)**. Modified CFPRs exhibited lower compression characteristics than the reference ones. The σ_{max} was decreased by 60% whereas E_{comp} by 55% due to SP SHA introduction. Thus, even though SP prepreg promotes the energy absorption under out-of-plane impact loading, it adversely deteriorates the in-plane (compressive) properties of the final CFRP.

5.2.5. Residual compressive properties of the CFRPs after LVI

As already described, after LVI tests reference and SP-modified samples were loaded in compression to assess their CAI properties. Also, the introduced healing functionality of the SP-modified samples was quantified by subjecting these samples to a simple healing cycle as described in Section 2.1.7 and then, repeating the CAI tests in order to investigate the post-healing CAI performance of the modified plates.

Typical compressive stress versus compressive strain (%) curves after LVI for reference and SP-modified samples (prior and after healing) are illustrated in **Figure 27(a)**. In addition, σ_{max} and E_{comp} values of both the reference and modified CFRPs in prior impact, after impact and after healing situation are summarized in **Figure 27(b)**. According to these results, it is shown that after LVI, the σ_{max} of the reference samples was reduced by 16%. SP modified samples, exhibited also the same reduction (16%) for the σ_{max} value. The reduction of the apparent compressive modulus (E_{comp}) is 5% for the reference and 9% for the SP-modified CFRPs. Furthermore, the SP-modified samples passed through healing process as it is has been already described earlier, and after that they exposed to CAI tests in order the post-healing performance of the composite plates to be investigated. According to these tests, it was shown that healed samples presented higher σ_{max} and E_{comp} values approximately 6 and 42%, respectively compared against the unhealed SP-modified ones (impacted samples). Therefore, modified samples improved CAI properties via healing treatment.

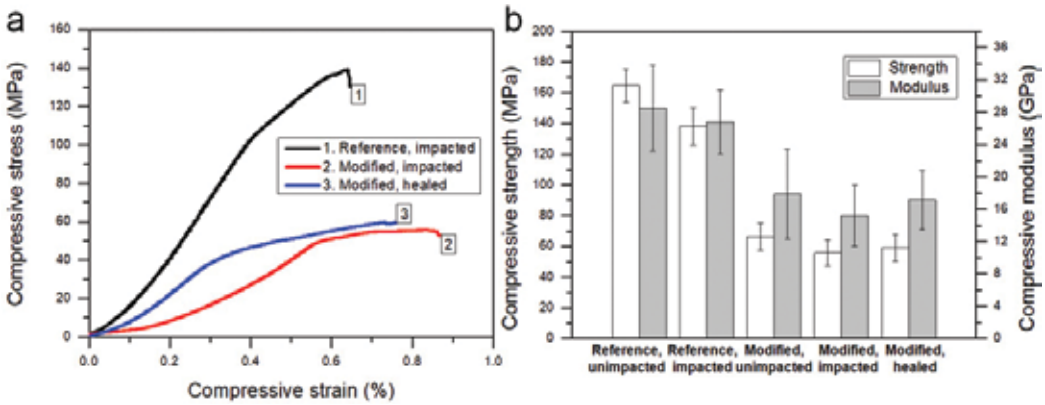

Figure 27. (a) Representative compressive stress versus compressive strain (%) curves from the CAI testing of both the reference and modified CFRPs (prior and after healing). (b) σ_{max} and E_{comp} values of both the reference and modified CFRPs prior impact, after impact and after healing.

As previously mentioned, the SP SHA was not able to heal all the cracks in the through-the-thickness direction. Only delaminations in the adjacent interfaces to the SP-modified ply were healed. After healing process, samples containing SP prepregs showed better load transfer characteristics. Finally, it is of note that whereas reference composites fail in a brittle manner, SP-modified CFRPs fail in a ductile or less brittle manner, both the virgin and healed ones. It is suggested that this result is a reflection of the ductile nature of the SP and of the softening effect induced by the presence of this type of plies as SHA into composites' architecture.

6. Outlook

The self-healing technology described in this chapter is envisioned to be incorporated locally in the early failure regions and other highly stressed areas of aeronautical CFRP structures. Also, this self-healing technology based on reversible polymers can be placed in known critical regions of structures where the damage predominately occurs, such as around drilled holes or on skin-stringer run-outs. These regions will take advantage of these repair mechanisms and do not represent the overall host matrix mechanical performance due to the knock-down effect of these polymers to the whole composite. It is obvious that the current tests do not represent the "real life service" conditions of these materials; however, this investigation demonstrates the self-healing capabilities of SP polymers. This preliminary "model study" proves the viability of the concept of incorporating the current SHAs into epoxy CFRPs.

7. Conclusions

In this chapter, the effect of the SP interleaf on the mode I and mode II interlaminar fracture toughness, as well as on LVI, CAI of CFRPs, and the provided healing capability was studied. SP polymer interlayers were locally incorporated into the area that the crack is expected to propagate. According to experimental results, it was shown that SP was able to considerably enhance the mode I and mode II interlaminar fracture toughness of the composites laminates through toughening and extended bridging. Characteristic example is G_{IC} value that was increased by more than one order of magnitude (1550%). These modified samples also exhibited high fracture performance recovery after first fracture for both mode I and II interlaminar fracture toughness. Potential knock-down effects on the in-plane properties of these modified samples were assessed. 3PB experiments revealed that by the incorporation of the SP interleaf into mid-thickness area, the ultimate stress (σ_{ult}) value was significantly decreased.

For the assessment of LVI behavior of CFRPs, SP prepregs were fabricated in order to the incorporation of the SHA into the composite to be simplified. Samples containing SP prepregs were examined under LVI and CAI tests and compared. Initially, it was shown that by the incorporation of the SP into composites laminate, the compression properties of the CFRPs were decreased. After LVI tests, samples containing SP prepregs exhibited higher resistance to damage, if compared against the reference ones. Healing process revealed that SP SHA was

not able to fully restore, even locally, the damage into the composite. Even though 100% healing was not achieved, SP prepreg-modified samples exhibited slightly improved compression characteristics after healing cycle.

Acknowledgements

The work described herein has been funded by: (a) the EU FP7 Transport (including Aeronautics) Programme within the frame of the project: Self-healing polymers for concepts on self-repaired aeronautical composites HIPOCRATES (ACP3-GA-2013-605412). Also, the authors thank Tony Bosman (Suprapolix BV) for the material supply.

Author details

Vassilis Kostopoulos* and Athanasios Kotrotsos

*Address all correspondence to: kostopoulos@mech.upatras.gr

Applied Mechanics Laboratory, Department of Mechanical Engineering and Aeronautics, University of Patras, Greece

References

[1] Ashby MF. Technology in the 1990s: Advanced materials and predictive design. Philosophical Transactions of the Royal Society of London. 1987;**332**:393-407. DOI: 10.1098/rsta.1987.0059

[2] O'Brian TK. Towards a damage tolerance philosophy for composite materials and structures. Composite Materials: Testing and Design, ASTM special technical publication. 1990; **1059**:7-33. DOI: 10.1520/STP24105S

[3] Wisnom MR. The role of delamination in failure of fibre-reinforced composites. Philosophical Transactions of the Royal Society A. 2012;**370**:1850-1870. DOI: 10.1098/rsta.2011.0441

[4] Blaiszik BJ, Kramer SLB, Olugebefola SC, Moore JS, Sottos NR, White SR. Self-healing polymers and composites. Annual Review of Materials Research. 2010;**40**:179-211. DOI: 10.1146/annurev-matsci-070909-104532

[5] Mezzenga R, Boogh L, Manson J. A review of dentritic hyperbranched polymer as modifiers in epoxy composites. Composites Science and Technology. 2001;**61**:787-795. DOI: 10.1016/S0266-3538(01)00022-7

[6] Masters JE. Improved impact and delamination resistance through interleaving. Key Engineering Materials. 1989;**37**:317-348. DOI: 10.4028/www.scientific.net/KEM.37.317

[7] Stevanovic MM, Stecenko TB. Mechanical behaviour of carbon and glass hybrid fibre reinforced polyester composites. Journal of Materials Science. 1992;**27**:941-946. DOI: 10.1007/BF01197646

[8] Dransfield KA, Jain LK, Mai YW. On the effects of stitching in CFRPs–I. Mode I delamination toughness. Composites Science and Technology. 1998;**58**:815-827. DOI: 10.1016/S0266-3538(97)00229-7

[9] Gilbert EN, Hayes BS, Seferis JC. Interlayer toughened unidirectional carbon pre-preg systems: Effect of preformed particle morphology. Composites Part A: Applied Science and Manufacturing. 2003;**34**:245-252. DOI: 10.1016/S1359-835X(02)00141-0

[10] Mouritz AP. Review of z-pinned composite laminates. Composites Part A: Applied Science and Manufacturing. 2007;**38**:2383-2397. DOI: 10.1016/j.compositesa.2007.08.016

[11] Chan WC. Design approaches for edge delamination resistance in laminated composites. Journal of Composites, Technology and Research. 1991;**13**:91-96. DOI: 10.1520/CTR10212J

[12] Chan WC, Ochoa OO. Edge delamination resistance by a critical ply termination. Key Engineering Materials. 1989;**37**:285-304. DOI: 10.4028/www.scientific.net/KEM.37.285

[13] Choi J, Yee AF, Laine RM. Toughening of cubic silsesquioxane epoxy nanocomposites using core-shell rubber particles: A three-component hybrid system. Macromolecules. 2004;**37**:3267-3327. DOI: 10.1021/ma0303723

[14] Howard WE, Gossard T Jr, Jones RM. Composite laminate free-edge reinforcement with U-shaped caps part II: Theoretical-experimental correlation. AIAA Journal. 1989;**27**:617-623. DOI: 10.2514/3.48818

[15] Whittingham B, Baker AA, Harman A, Bitton D. Micrographic studies on adhesively bonded scarf repairs to thick composite aircraft structure. Composites Part A: Applied Science and Manufacturing. 2009;**40**:1419-1432. DOI: 10.1016/j.compositesa.2008.12.011

[16] Baker A, Dutton S, Kelly D. Composites materials for aircraft structures. 2nd ed. American Institute of Aeronautics and Astronautics (AIAA) Publication Series; 2004. 601 p. DOI: 10.2514/4.861680

[17] Bekas DG, Tsirka K, Baltzis D, Paipetis AS. Self-healing materials: A review of advances in materials, evaluation, characterization and monitoring techniques. Composites Part B: Engineering. 2016;**87**:92-119. DOI: 10.1016/j.compositesb.2015.09.057

[18] Diesendruck CE, Sottos NR, Moore JS, White SR. Biomimetic self-healing. Angewandte Reviews. 2015;**127**:10572-10593. DOI: 10.1002/anie.201500484

[19] Williams G, Trask R, Bond I. A self-healing carbon fibre reinforced polymer for aerospace applications. Composites Part A: Applied Science and Manufacturing. 2007;**38**:1525-1532. DOI: 10.1016/j.compositesa.2007.01.013

[20] White SR, Moore JS, Sottos NR, Krull BP, Santa Cruz WA, Gergely RCR. Restoration of large damage volumes in polymers. Science. 2014;**344**:620-623. DOI: 10.1126/science.1251135

[21] Varley RJ, Craze DA, Mouritz AP, Wang CH. Thermoplastic healing in epoxy networks: Exploring performance and mechanism of alternative healing agents. Macromolecules Materials and Engineering. 2013;**298**:1232-1242. DOI: 10.1002/mame.201200394

[22] van Gemert GML, Peeters JW, Sontjens SHM, Janssen HM, Bosman AW. Self-healing supramolecular polymers in action. Macromolecules Chemistry and Physics. 2012;**213**: 234–242. DOI: 10.1002/macp.201100559

[23] Bai N, Saito K, Simon GP. Synthesis of a diamine cross-linker containing Diels-Alder adducts to produce self-healing thermosetting epoxy polymer from a widely used epoxy monomer. Polymer Chemistry. 2013;**4**:724-730. DOI: 10.1039/C2PY20611K

[24] Brunsveld L, Folmer BJB, Meijer EW, Sijbesma RP. Supramolecular polymers. Chemical Reviews. 2001;**101**:4071-4098. DOI: 10.1021/cr990125q

[25] Cordier P, Tournilhac F, Soulie-Ziakovic C, Leibler L. Self-healing and thermoreversible rubber from supramolecular assembly. Nature. 2008;**451**:977-980. DOI: 10.1038/nature06669

[26] Palmer LC, Velichko YS, de la Cruz MO, Stupp SI. Supramolecular self-assembly codes for functional structures. Philosophical Transactions of the Royal Society A. 2007;**365**: 1417-1433. DOI: 10.1098/rsta.2007.2024

[27] Brunsvel L, Folmer BJ, Meijer EW, Siblesma RP. Supramolecular polymers. Chemical Reviews. 2001;**101**:4071-4098. DOI: 10.1021/cr990125q

[28] Greenland BW, Hayes W, Colquhoun HM. Design, synthesis and computational modeling of aromatic tweezer-molecules as models for chain-folding polymer blends. Tetrahedron. 2008;**64**:8346-8354. DOI: 10.1016/j.tet.2008.05.077

[29] Iyer PK, Beck JB, Rowan SJ. Synthesis and optical properties of metallo-supramolecular polymers. Chemical Community. 2005;**41**:319-321. DOI: 10.1039/B410734A

[30] Kalista SJ, Ward TC. Thermal characteristics of the self-healing response in poly (ethylene-co-methacrylic acid) copolymers. Journal of Royal Society Interface. 2007;**4**:405-411. DOI: 10.1098/rsif.2006.0169

[31] Sijbesma RP, Beijer FH, Brunsveld L, Folmer BJB, Hirschberg JHKK, Lange RFM, Lowe JKL, Meijer EW. Reversible polymers formed from self-complementary monomers using quadruple hydrogen bonding. Science. 1997;**278**:1601-1604. DOI: 10.1126/science.278.5343.1601

[32] Söntjens SHM, Renken RAE, van Gemert GML, Engels TAP, Bosman AW, Janssen HM, Govaert LE, Baaijens FPT. Thermoplastic elastomers based on strong and well-defined hydrogen-bonding interactions. Macromolecules 2008;**41**:5703-5708. DOI:10.1021/ma800744c.

[33] Kostopoulos V, Kotrotsos A, Tsantzalis S, Tsokanas P, Loutas T, Bosman AW. Toughening and healing of continuous fibre reinforced composites by supramolecular polymers. Composites Science and Technology. 2016;**128**:84-93. DOI: 10.1016/j.compscitech.2016.03.021

[34] Kostopoulos V, Kotrotsos A, Baltopoulos A, Tsantzalis S, Tsokanas P, Loutas T, Bosman AW. Mode II fracture toughening and healing of composites using supramolecular polymer interlayers. eXPRESS Polymer Letters. 2016;**10**:914-926. DOI: 10.3144/expresspolymlett.2016.85

Section 4

Application of Dendrimers as Dopant Carriers

Chapter 7

Dendrimers as Dopant Atom Carriers

Haigang Wu and Yaping Dan

Additional information is available at the end of the chapter

http://dx.doi.org/10.5772/intechopen.71397

Abstract

Properties of modern semiconducting transistors and future electron or quantum devices are essentially determined by single dopant atoms. How to precisely control the individual dopant position is one of the key factors to advance these technologies. In this chapter, we first briefly introduce the research progress in single dopant devices. To fabricate single dopant devices at large scale, we then overview our previous propose to control the locations of single dopants by self-assembly of large molecules (polyglycerols) with each carrying one dopant atom. The synthesis process, doping properties, and challenges of the molecular doping technique will be thoroughly elaborated before we conclude this chapter.

Keywords: monolayer doping, dendrimer, dopant carriers, hyperbranched polyglycerols

1. Introduction

Dopants play an important role in electrical [1], optical [2], and other properties [3] of semiconductors. As the size of semiconducting devices scales down, the device functionality will be essentially determined by the property of a single dopant atom. In recent years, these single atom devices such as single atom transistors [4] and atomic memory devices [5] have been demonstrated. The technology that can place dopants precisely at arbitrary locations is the key to electronics based on single dopant atoms. Although single atom devices have not commercialized, the precise control of dopant locations is still important to today's integrated circuits. For example, an ordered array of dopants in the channel of metal-oxide-semiconductor field-effect transistors (MOSFET) will help suppress the fluctuation of threshold voltage [6–8].

In 2005, Shinada et al. [6] reported that transistors based on uniformly distributed dopants were successfully developed by single ion implantation (SII) technique in which individual

ions were controlled by chopping a focused ion beam through an aperture. With this technique, a broad range of single ions such as B, Si, and P can be controlled individually. Indeed, for transistors based on dopants that are spatially distributed at a uniform pattern, the fluctuation of threshold voltages is significantly suppressed, compared to those based on randomly distributed dopants by traditional ion implantation. In the meantime, an Australian research group developed a new "hydrogen lithography" technique to control single dopants. In 2012, this group first reported transistors based on a single P dopant atom. The "hydrogen-lithography" technique is based on the removal of single hydrogen atom on the Si-H surface by scanning tunneling microscopy (STM). A single phosphine molecule will be self-assembled onto the Si dangling bond after the hydrogen is removed. In the end, the P atoms will be diffused into the Si substrate by thermal annealing. Transistors based on single P atoms were fabricated and investigated. In addition, resistors based on a line of P dopants were also characterized, showing that the Ohm's law is still effective at atomic level [9].

However, these single dopant control techniques are time-consuming serial processes and will be inefficient for industry applications. How to control individual dopants at large scale is urgently needed for future electronics based on single dopant atoms. We previously proposed to control individual dopants at large scale by the self-assembly of molecules with each carrying one dopant atom [10]. The substrate surface is patterned chemically by advanced lithography so that the carrier molecules will be grafted onto the desired locations as designed. Due to the limitation of the today's advanced lithography, the surface patterns are on an order of 10 nm. Multiple molecules will be grafted onto each patterned area unless the molecule size is comparable to the surface pattern size. Clearly, large molecule carriers are required to control single dopants at large scale.

Dendrimers are a series of large molecules, the size of which can be controlled during synthesis. We previously synthesized dendrimers with a diameter of more than 10 nm [10]. Each dendrimer carries only one P dopant. These dendrimers as dopant carriers can be self-assembled on the substrate. The dopants will be driven into silicon to form electrically active dopants by thermal annealing. Although the dopants will diffuse in all directions during the annealing process, the rapid thermal annealing and other techniques, such as laser-based annealing process can limit the dopants in the ultra-shallow surface. In short, the dendrimer-based monolayer doping technique is potentially a promising approach to control individual dopants at large scale. This chapter is to review the potential application of dendrimers as single dopant carriers.

2. Atom control and devices design

As reported [6], deterministic dopants help suppress the fluctuation of threshold voltages in CMOS field-effect transistors. More importantly, individual dopant-related devices are also the frontier in the microelectronic field. For example, single atom transistor and single magnetic atom memory were demonstrated. In this section, we will briefly overview the single atom devices and related properties.

Xie *et al.* [11] firstly reported a single atom transistor (**Figure 1**) based on redox circles of the electrochemistry. To fabricate the device, a pair of Ag electrodes was etched to be in contact via a single Ag atom using $AgNO_3$ and HNO_3 mixture as the electrolyte. When the single Ag atom

contact was electrochemically oxidized, the circuitry would be in "off" state. As a reverse process, the circuitry can be in "on" state by reduction. Besides silver, Pb can be also made to single atom transistors by a similar method [12]. Moreover, Martin *et al.* [13] used the elastic properties of single atom relays and substrates to control single-atom switch in which the gate voltage can be performed to regulate the switch "on-off" state between the monatomic contact condition and the tunneling regime state. These works opened a new horizon to investigate atomic level switches, although the devices were made in electrolyte solution. However, one critical shortage of monatomic contact-based transistor is the poor stability and repeatability of single atom contact in the "on-off" circles, which is of significant impact on the development and application in industry.

In 1998, Kane proposed [14] a new architecture of spin transistors made of single P atoms in silicon substrate (**Figure 2**), based on the well-developed Si:^{31}P system in the past four decades. As known in semiconductor physics, phosphorus dopants as a donor-type of dopants in Si will provide free electrons with the wavefunction spreading out in the crystal lattice. The electron wave function of one P donor is also easily affected by the nuclear spin of another P donor. This nuclear-nuclear spin interaction mediated by electrons can be employed as an excellent approach to control the logical operation, because these hyperfine interactions can be controlled by gate voltages [15]. For the purified ^{28}Si isotope bulk with P-doping, the outer electron of ^{31}P at low temperature (1.5 K) is unionized, and it can be ionized by external electric field, for example, metallic gate voltage. When ^{31}P donor is under positive charge with 1/2 nuclear spin, the interaction range of electron wave function can extend tens of nanometers away from ionized phosphorus nucleus, and the electron-mediated nuclear spin coupling can be observed by using electron spin-resonance spectroscopy (ESR). To perform this type of quantum calculations, there are three necessary parameters: modulation of the hyperfine interaction length by gate voltage, control of "on-off" states for single donor, and the resonance flipping of nuclear spins by global magnetic field. Pla *et al.* [16] reported the readout and control of ^{31}P spin in Si with 99.8% fidelity. Vrijen *et al.* [17] presented in their work that Si/Ge epitaxial heterostructures were selected to control the single-phosphorus electron spin. Morton *et al.* [18] demonstrated a quantum memory by using ^{31}P nuclear spin. However, the most important obstacle of spin-based quantum computers is the short coherent time (less than 100 ms) at low temperature. It is caused by the ^{29}Si isotope and the environment effect. It still needs more work to explore and optimize the testing condition to achieve a long coherent and dephase time.

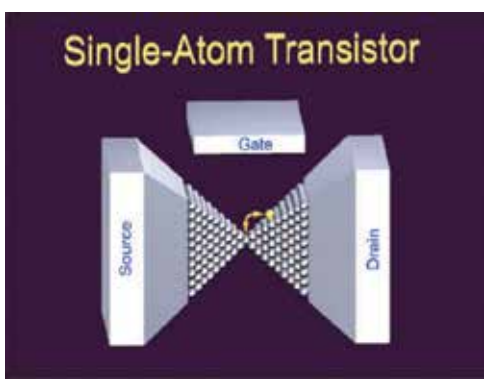

Figure 1. Single atom transistor to be as switch (Ref. 11).

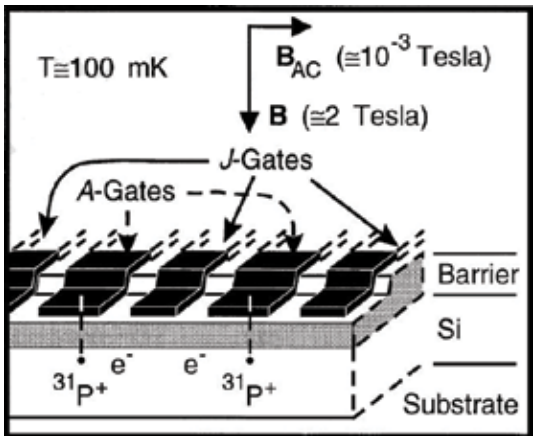

Figure 2. ^{31}P nuclear-spin-based single atom transistor (Ref. 14).

In the microelectronics industry, how to produce the large area density of bit information in memory devices is an important task [19]. Richard Feynman once said "all of the information that man has carefully accumulated in all the books in the world, can be written… in a cube of material one two-hundredth of an inch wide" [20]. He used the cubic array 125 atoms (5 × 5 × 5 array) to store the information (one bit) [21], which is comparable to the data storage in DNA (32 atoms for one bit). This sentence gives a glimpse into how to significantly improve the areal density of data storage down to atomic level. Afterward, using single molecules or nanotubes as basic unit to store information has been extensively explored, and the types of memory structures also have been extended to be more diversiform, for example, nanowire arrays [22]. However, the final goal of memory devices is to achieve the atomic level storage at room temperature [23]. To reach this goal, Feynman designed the atomic level memory bit structure [21], which is more efficient than classical CD-ROM storage as shown in **Figure 3**. These images were coded by Morse code, and this atomic level memory

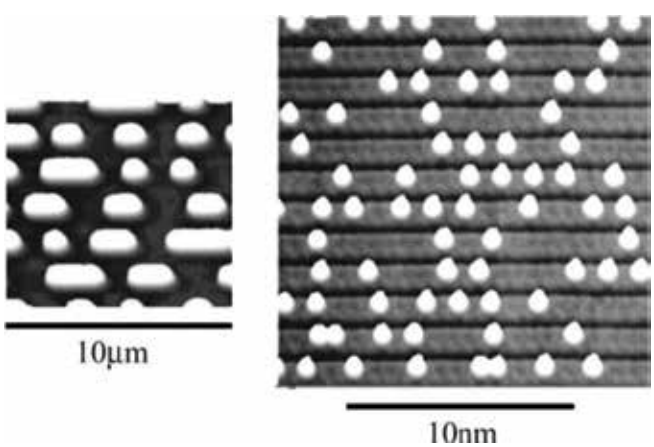

Figure 3. Comparison of atomic memory with CD-ROM (Ref. 21).

significantly improves the capacity for per area. To achieve this final goal, it is the key to develop a technology that can place individual dopants at specific sites at a large scale.

Recently, Kalff *et al.* [24] reported the kilobyte rewritten atomic memory devices. In their work, the chlorine self-assembled atomic layer was first prepared on the Cu(100) surface, and then scanning tunneling microscope (STM) was used to control the vacancy of chlorine on the copper surface. An array of 12 × 12 atoms as the basic memory unit was created, and the ASCII code was used to encode the characters on the copper surface. These memory units can operate at 77 K, and were used to write the Feynman's lecture "There's plenty of room at the bottom." The authors successfully used the vacancy of atoms to encode the byte information, and the memory volume is significantly improved to 1016 bytes, the area density of which achieved to 0.778 bits nm^{-1}. Moreover, Schirm *et al.* [23] reported the current-driven single atom memory by changing the "on-off" state to code the information. Maze *et al.* [25] demonstrated the individual electronic spin state in the diamond to code information. Clearly, the fabrication of atomic memory devices needs the precise control of the atom positions to code information bit by bit (**Figure 4**).

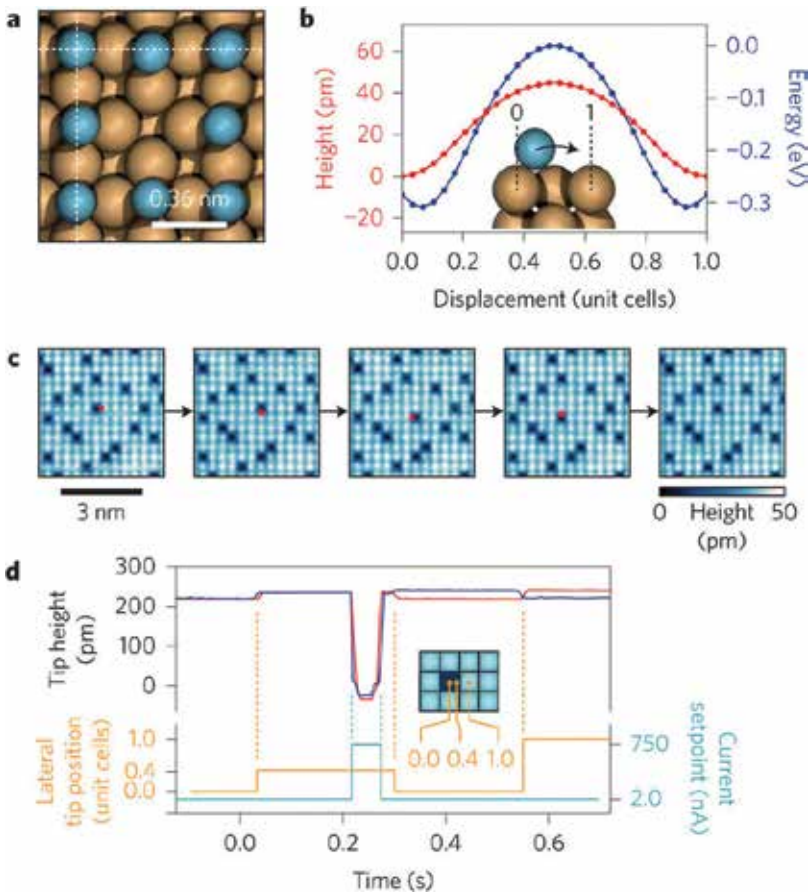

Figure 4. Hopping mechanism of chloride atom vacancy on the chlorinated copper surface (Cu < 100>) (Ref. 24). (a) Theoretical atomic structure near a vacancy by density function theory (DFT). Cl atom, Cu atom. (b) Theoretical height profile and potential energy of Cl atom in a switch circle. (c) STM images of consecutive process. (d) Measured tip height in a successful and unsuccessful manipulation.

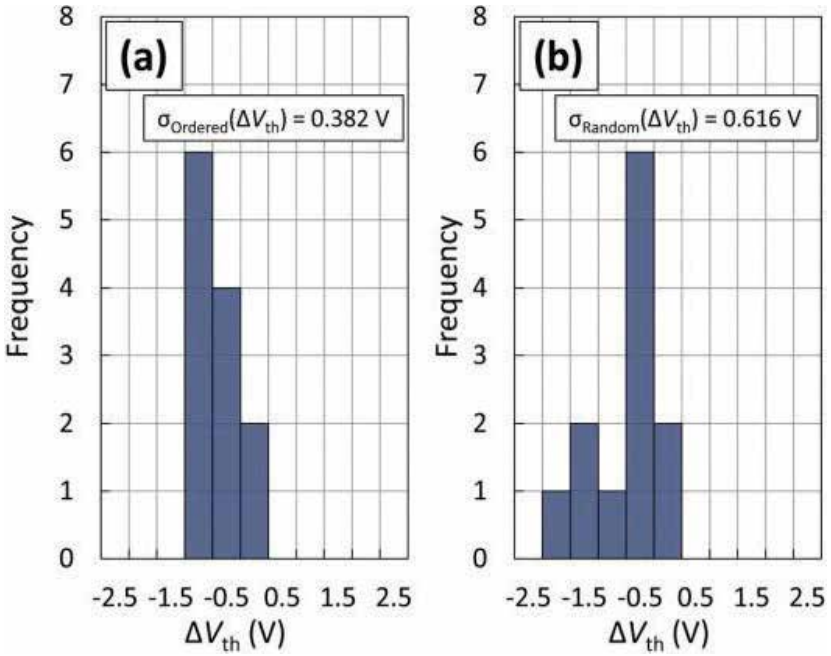

Figure 5. Histograms of voltage shift of (a) ordered array and (b) conventional random dopant distribution (Ref. 31).

The field-effect transistors (FETs) are the workhorse of the microelectronics industry [26]. A decade ago, the channel lengths of FETs were at micrometer level, and the fluctuation of dopants in the bulk device has nearly no impact on the threshold voltage [27, 28]. When the gate length of MOSFET is only ~10 nm, the active channel region of devices will only contain several dopants, and the fluctuation in dopant number will generate much stronger random telegraph noise than the average threshold voltage [29, 30]. Ohdomari group reported the phosphorus dopant array [6], As dopant array [31], and other dopants [32] in the silicon devices. It was found that the fluctuation of dopants increases the threshold voltage variation significantly (**Figure 5**), making the circuitry consisting of these transistors less reliable. This effect will be exacerbated as the transistor size continues to scale down [33]. Consequently, how to precisely control the positions of individual impurities is critical to the reproducibility and reliability of MOSFET circuits.

In conclusion, the individual dopant control is a key to quantum devices. The STM-based atom control and single ion implantation does not meet the industry demand for large-scale fabrication. From the engineering point of view, it is required to develop technologies that can precisely control individual dopants at a large scale.

3. Molecular monolayer doping

Thermal diffusion and ion implantation are the two main doping techniques that are widely used to introduce impurities into semiconductors [34]. By thermal diffusion, the concentration and profile of dopants follow the diffusion equation, which is determined by diffusion

time, temperature, and diffusivity of dopants [35]. The advantage of thermal diffusion is low cost, but it is difficult to obtain shallow junctions due to the fact that dopants are required to be activated at high temperature [36]. The high activation temperature in turn pushes the dopants further into the substrate. Ion implantation and rapid thermal annealing were created to decouple the dopant activation and thermal diffusion of dopants. The depth of dopants is controlled by acceleration voltage and the dopants are activated by rapid annealing temperature. The thermal annealing is accomplished in seconds so that the thermal diffusion of dopants is negligible. Unfortunately, the high-energy ion beam will create a lot of damages to the crystalline lattice [37], which not only amorphizes the silicon surface but also induces defects in bulk.

In 2008, Ho *et al.* [38] reported that the molecular monolayer doping is a potential method to resolve these issues. The monolayer doping protocol consists of two major steps: molecular monolayer formation by hydrosilylation process with dopant-carried precursor molecules (dopant carriers), and rapid thermal annealing (RTA) with a capping layer to block the out-diffusion of dopants. In the first step of self-assembled monolayer on the silicon surface, the density of dopant is determined by the coverage of dopant carrier and molecular size (or footprint). The monolayer is then capped by a thin SiO_2 layer. In the end, dopants are diffused into the silicon shallow surface by RTA process. Through analysis of monolayer doping results under different annealing conditions, the authors found that the depth of diffusion and amount of dopants are determined by both annealing time and temperature [39]. By carefully controlling these parameters, the ultra-shallow junctions were obtained [39].

Since the monolayer doping protocol had been reported, several critical dopants including As, N, Sb, and Bi were performed to control the electronic properties of semiconductor substrate. Here, we would like to discuss in detail the development of monolayer doping in the last decade by different aspects, for example, dopant elements, doping parameters control, and III-V group substrate doping.

a. Dopant elements in monolayer doping

The natural feature of monolayer doping is dopant thermal diffusion, which is originated from precursor molecules on the surface. Silicon is the primary semiconductor material for modern microelectronic industry. Silicon is doped to be n-type by Group V elements and p-type by Group III elements. In Ho's work [38], it was found that the area density of boron is lower than phosphorus, which is caused by significant out-diffusion of boron in SiO_2 capping layer.

Arsenic is also an important donor-type dopant for silicon semiconductor [40]. O'Connell *et al.* [41] reported that As dopants were introduced into silicon surface by using triallylarsine (TAA) molecules which contain three unsaturated C=C bond. As shown in **Figure 6**, the As-carrying molecules were first anchored on the silicon surface, and As elements were then diffused into the silicon surface with the protection of a capping layer by annealing process. The surface doping concentration reaches to ~2×10^{20} cm^{-3}, and the diffusing depth is ~120 nm after rapid thermal annealing at 1050°C for 5 s. To investigate the electronic properties after doping process, the authors used a "four point probe test structure" to measure I-V curves for nanowires with different width. The results show that the nanowire conductance is linearly dependent on the nanowire width, implying that the doping is uniform. Moreover, the

cross-sectional transmission electron microscopy (TEM) confirmed that this organic arsenic monolayer doping process will not introduce the lattice damages or crystal defects into the nanowire crystal structure. These results are consistent with other literature reports, such as Ang *et al.* reported [42] the 300 mm level monolayer doping on FIN structure without crystal damage-free.

Another Group V element, nitrogen, is not often used to dope silicon. As reported, nitrogen can decrease the defects and dislocation of silicon crystal, and increase the mechanical strengthen of silicon [43]. Nitrogen as n-type dopants in silicon has two energy levels at 0.28 and 0.19 eV [44]. However, there is no literature to report the role of nitrogen co-doping with phosphorus in silicon, in particular for the interaction between two dopants. Our group found that nitrogen dopants retard the electrical activity of phosphorus when co-doped with phosphorus via monolayer doping process [45]. As shown in **Figure 7**, nitrogen elements were introduced into the silicon surface by Boc-allylamine or P-N bond with phosphorus. 10-undecenoic molecules that contain the same length of carbon chain were used as a control. Van der Pauw measurements indicate that the sheet resistance of nitrogen-doped silicon is ~35.6 kΩ, close to the sheet resistance of the N and P co-doped samples. The profile of P and N dopants in the samples is retrieved by secondary ion mass spectroscopy (SIMS) [46]. However, the sheet resistances are not consistent with SIMS data on the assumption of full activation of P dopants, although high activation rates for P dopants in silicon introduced by monolayer doping were reported [39]. To further explore the mechanism of dopants interaction, low temperature Hall measurements were employed to obtain the concentration of dopants that are electrically active. It was found that nitrogen is the key factor to explain these

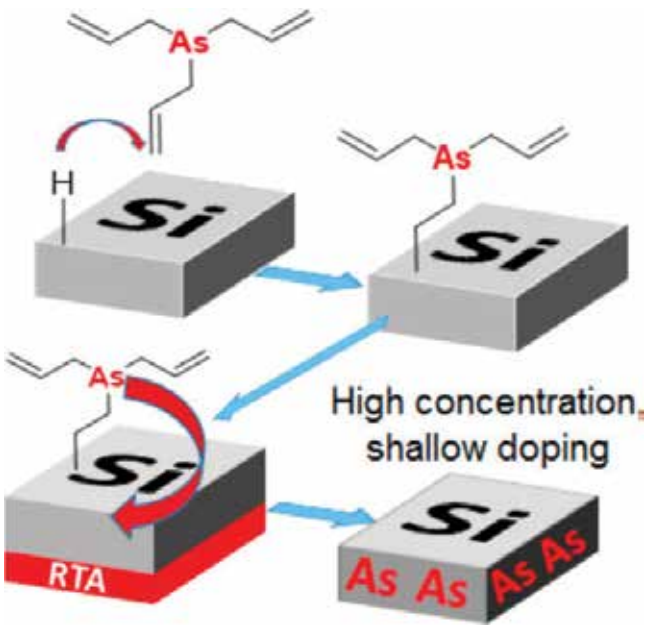

Figure 6. Schematic protocol of organic arsenic monolayer doping process (Ref. 45).

results. When nitrogen was co-doped with phosphorus into silicon, some kind of nitrogen-phosphorus complex entities will form, retarding the electrical activation of phosphorus to ~1%. These results indicate that nitrogen dopants should be avoided to achieve a high activation rate of phosphorus by monolayer doping, although the dopant-carrying molecules that contain nitrogen were used in micelles discrete doping process by Popere *et al.* [47] and anti-oxidation surface with "click" cycloaddition by O'Connell *et al.* [48].

Most monolayer doping processes were performed on the oxide-free Si-H surface. However, the hydrogen-passivated Si surface must be prepared in the glovebox or Schlenk line system, because of the low stability of Si-H in ambient environment and the resultant poor quality of self-assembled monolayer [49]. If the monolayer doping process can be performed on the thin oxide layer of silicon surface, it will simplify the monolayer doping process and find

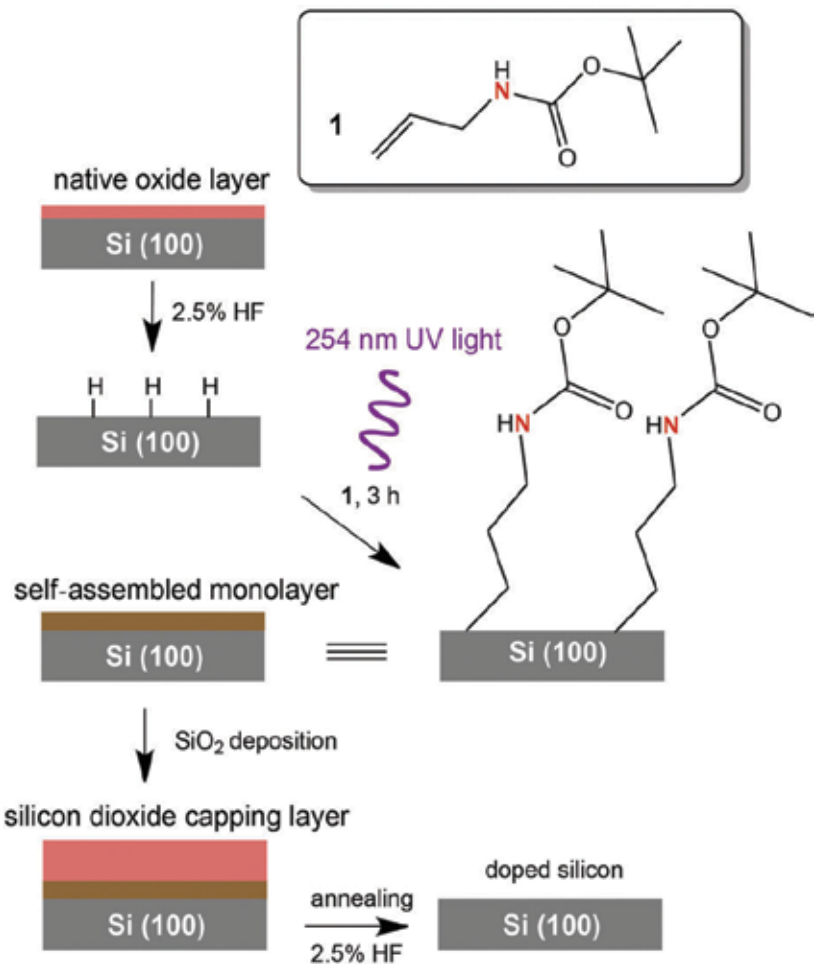

Figure 7. Nitrogen-containing molecule monolayer doping protocol. The small molecules containing nitrogen were anchored on the Si-H surface through the UV initiating method (Ref. 45).

more applications on the silicon devices. Hydrogen silsesquioxane, so-called HSQ as e-beam resist [50], is a series of inorganic Si-O framework compounds with a cubic cage structure. The cage rearrangement will be performed by reacting with phosphoric acid at the Si-O-Si bridge of cage structure [51]. Alphazan *et al.* reported that polyhedral oligomeric silsesquioxane (POSS) (**Figure 8**) carrying phosphorus was grafted onto the oxide-passivated silicon surface [52]. The POSS molecules were synthesized by substitution of phosphoric acid at one site of POSS cage. As shown in **Figure 8**, the POSS molecules were grafted onto the thin oxide layer through the new Si-O-Si bond formation, and POSS with Si-O framework also can be treated as the capping layer instead of coating with an extra SiO_2 layer in the aforementioned doping protocol. The dopants successfully diffused into the silicon surface, and the thin SiO_x layer (0.7 nm) has little impact on the doping process. In addition, this POSS-based monolayer doping on the oxide surface was also used to dope other elements such as antimony in the SiO_2 [53] and Ge substrates [54].

In addition to the applications in nanowire and Fin-structure doping, highly ordered nanopattern doping is another potential application for monolayer doping. In fact, the combination of monolayer doping and nanoimprint lithography is a powerful approach to obtain ordered doping patterns. Based on this technique, Voorthuijzen *et al.* [55] reported two different protocols to attain doped micro-belts by monolayer doping with or without pre-surface monolayer modification process, as shown in **Figure 9**. For the protocol with pre-surface modification, the extra monolayer will be completely removed by O_2 RIE process, while the residual monolayer is under the protection of lithography resist. After RTA process, TOF-SIMS clearly shows the large-scale doping region, indicating that nanoimprint-controlled monolayer doping with ordered patterns is efficient. Moreover, Taheri *et al.* [56] further improved the monolayer pattern doping method by gas-phase monolayer doping, which can achieve smaller doping belt (~2 μm) than nanoimprint-based monolayer pattern doping (~100 μm). The silicon sample with e-beam-lithographic pattern was put into the reactor with gas-phase molecules to obtain the monolayer absorption under a temperature of ~120°C. The gas-phase molecules with unsaturated bonds form stable covalent bonds as the molecules are grafted onto the Si substrate. The width of doping region (~2 μm) and electronic property of the doped micro-belts were confirmed by conductive AFM and I-V measurements, respectively.

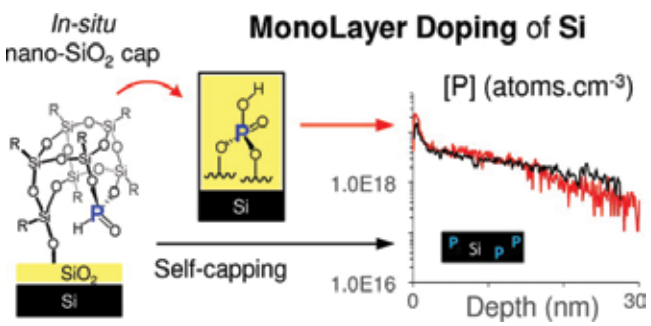

Figure 8. POSS-based monolayer doping process (Ref. 52).

http://dx.doi.org/10.5772/intechopen.71397

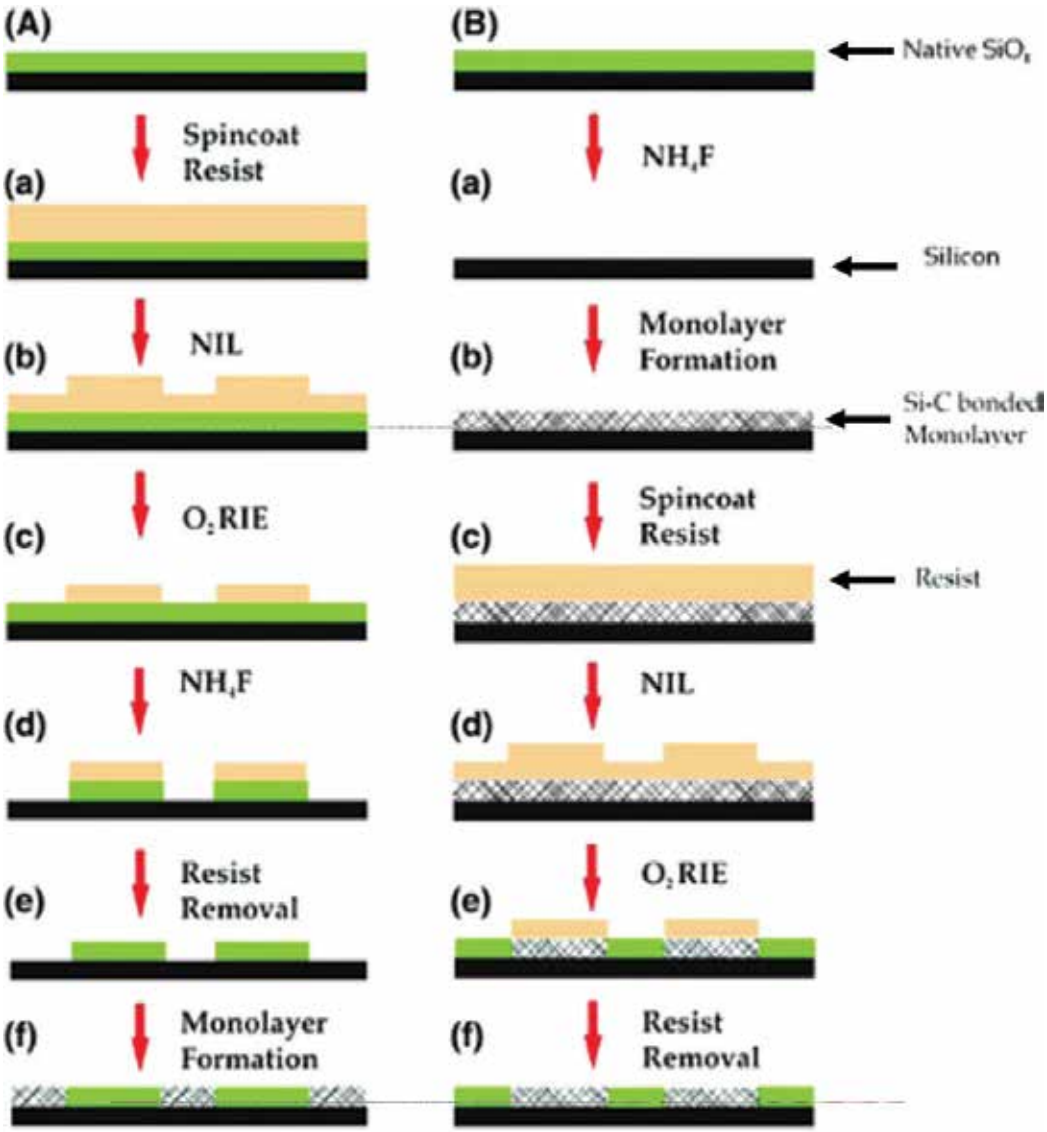

Figure 9. Nanoimprint monolayer doping protocol (Ref. 55). (A) Pattern formation of self-assembled monolayer after nanoimprint process. (B) Pattern formation using nanoimprint and RIE etching. NIL, nanoimprint lithography.

To sum up, we find that the monolayer doping is a potential doping technology for 3D nanodevices at low cost. Owing to the well-developed organic synthesis methods, many dopants can be introduced to different substrates. Nevertheless the monolayer doping process is still under development. More research work is needed on its application particularly in the COMS doping process. [57]

b. Doping concentration control by monolayer doping

Besides the kinds of dopants, the doping concentration is another important factor for the device performance. In Ref. [38], the authors explored the impact of thermal temperature and annealing time on the area doping dose. The control of doping concentration can be also achieved by tuning the molar ratio of dopant-containing molecules and the neutral molecules that do not carry any dopant atoms. The dopant-containing molecules and the neutral molecules are structurally similar, as a result of which similar chemical reactions will occur in the self-assembly process. After the same rapid thermal annealing (RTA) process, the dopant dose show the linear correlation between the rise in sheet resistance and the mixing molar ratio of the dopant-containing molecules to neutral molecules. For example, as the mixing ratio increases from 1:5 to 1:20, the sheet resistance increases from 5 to 20 folds.

Ye *et al.* [58] studied in detail how to control the area doping dose by tuning the mixing ratio of the dilution reagent (1-undecene) and dopant precursors (diethyl vinylphosphonate), as shown in **Figure 10**. After the molecules were grafted to the Si substrate surface, X-ray photoelectron spectroscopy (XPS) was employed to investigate the surface chemistry. The electron energy for different carbon component (C-O vs. C-C, for instance) is different as expected. For example, diethyl vinylphosphonate has two C-O bonds per molecule whereas only C-C bounds exist in the dilution reagent 1-undecene. The ratio of different carbon bonds from XPS allows the authors to derive the ratio of the dilution reagent and dopant precursors that are immobilized on the Si surfaces. As the mixing ratio of dopant precursors increases, the sheet resistance of doped silicon samples significantly decreases. Surprisingly, the surface doping dose is dependent on the mixing ratio in a monomial (instead of linear) correlation as shown in D-SIMS measurements. This phenomenon can be attributed to the difference in reaction efficiency between dopant precursor and diluting reagent.

As mentioned previously, one critical disadvantage of boron monolayer doping is the low doping efficiency (~33%) [38] due to the high diffusivity of boron in SiO_2. The SiO_2 capping layer can effectively block the out-diffusion of phosphorus but less efficiently for boron dopants. This results in a lower doping concentration of boron in silicon. To improve the B doping concentration, one possible solution is to increase the number of boron atoms that each molecule carries. For instance, organoboron or carborane compounds contain a larger amount of boron atoms than the ordinary precursors such as allylboronic acid, pinacol ester, and ABAPE [59]. Ye *et al.* [60] reported that 10-boron carborane (**Figure 11**) was used as the doping precursor to improve the boron doping concentration. The resultant area doping dose reaches ~3×10^{13} cm^{-2}, which is almost 20 times higher than the dose introduced by ABAPE although the number of boron atoms per molecule is only 10 times higher. This is because the footprint of the carborane is relatively smaller when compared to the latter. Clearly, dopant atoms for per footprint area are the critical parameter for doping dose control.

Besides the high area doping dose, the discrete doping also can be prepared by suitable dopant precursors. Micelles, which are micro- or nanoscale globular particles, are prepared by amphiphilic block co-polymers and can carry several guest molecules at the core region. The size selection of micelles is achieved by centrifuging the samples at different speed [61]. Popere *et al.* [62] reported that micelles, which were formed by copolymer polystyrene-block-poly(4-vinylpyridine)

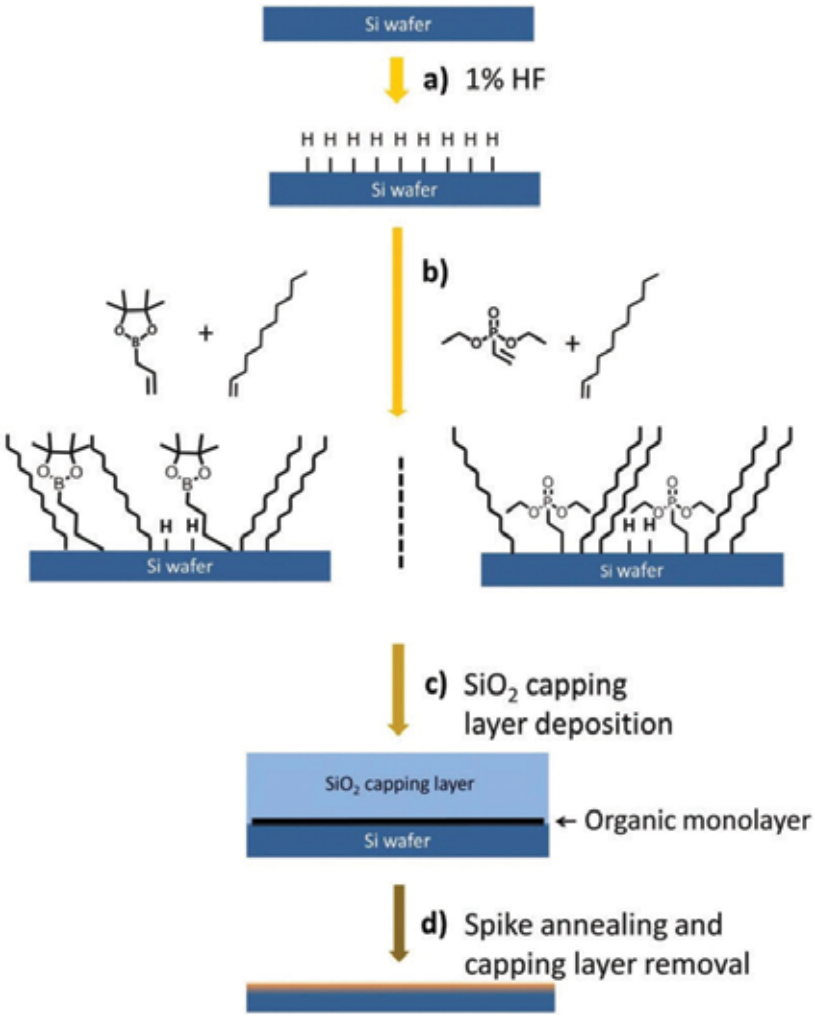

Figure 10. Mixing method to control doping concentration (Ref. 58).

(PS-b-P4VP), carried the dopant precursor molecules to prepare the discrete doping. Before the monolayer doping process, the surface morphology was characterized by AFM, confirming that a compact self-assembled film consists of the micelle particles. To check the dopants distribution, the core part of micelles was replaced by HSbF6 which can be directly observed by transmission electron microscopy (TEM). After the monolayer doping process, the discrete distribution of dopants was indirectly confirmed by TEM.

c. Monolayer doping on III-V semiconductors

Group III-V compounds are direct bandgap semiconductors and often have a much higher electron mobility than silicon [63]. These semiconductors are widely used as light emitting devices (LEDs), lasers, and high-speed transistors. Sulfur is often used as the n-type dopants. For the molecular monolayer doping on Group III-V semiconductors, most attention focuses

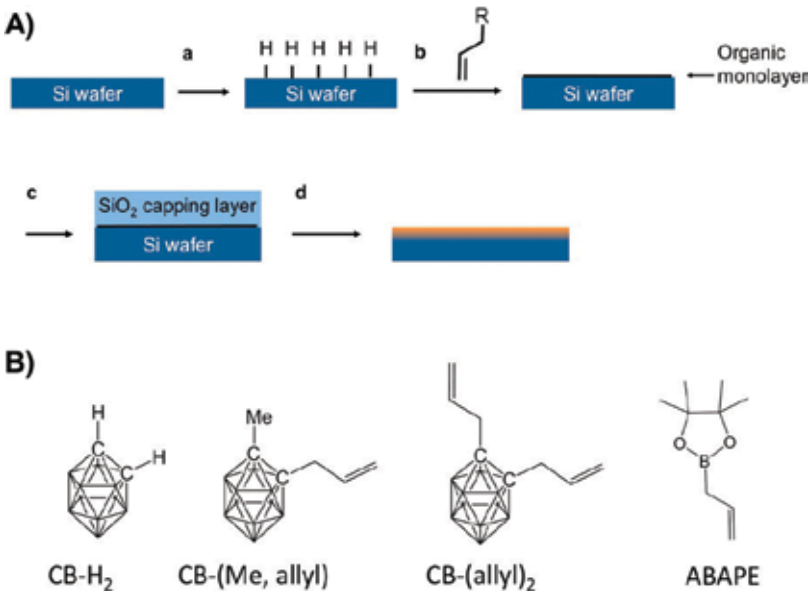

Figure 11. Carborane-based monolayer doping protocol (Ref. 60). (a) Schematic of monolayer doping process. (b) Molecular structure of related-carborane molecules.

on how to obtain high uniform vertical doping profile, for fin structure in particular [64]. The conformal nature of self-assembled monolayers provides the possibility to obtain a uniform doping profile for three dimension structures. Loh *et al.* [65] reported that sulfur-contained inorganic salts (for example, sulfate and sulfite) were applied to dope the InAsGa thin layer. It was found that oxygen atoms in the dopant carrier molecules are of great impact on the doping dose. Cho *et al.* [66] reported later that sulfur was introduced to dope InP. Ho *et al.* [67]

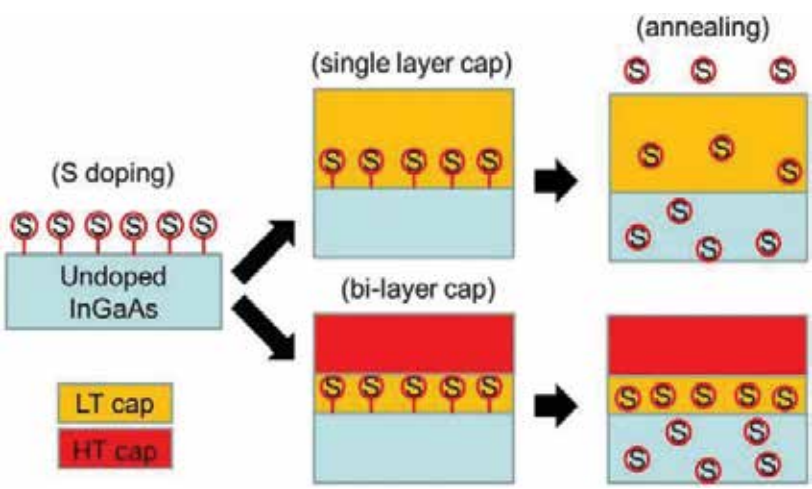

Figure 12. Monolayer doping protocol for group III-V semiconductors (Ref. 68).

reported that ammonium polysulfide was used to dope InAs. To improve the doping dose, Yum *et al.* [68] used a compact capping layer (**Figure 12**) to obtain the higher S doping dose (1.34×10^{13} cm^{-2}), which is 3 times higher than the previous reports [38]. The knowledge on the molecular monolayer doping on III-V semiconductors is still limited although quite some research works have been conducted on this topic.

d. Impact of other unwanted elements on monolayer doping process

In the self-assembled monolayer doping protocol, the precursors play the essential role to introduce the dopants. However, the dopant precursor molecules also contain other elements such as carbon, oxygen, and hydrogen. These elements other than the desired dopants may

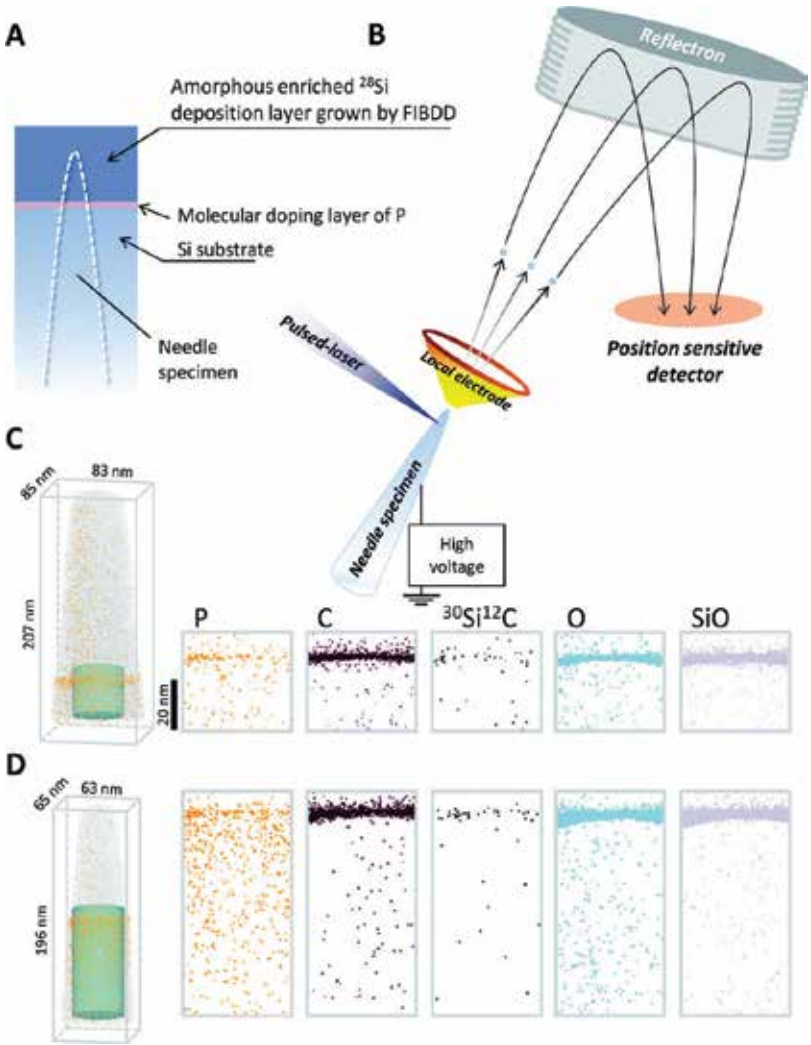

Figure 13. (A) Fabricated specimen by FIB technique. (B) Schematic of APT technique. (C) Elemental distribution of silicon sample annealed by 800 ℃ and 1025 ℃ (D), respectively.

have undesired impacts on the electrical properties of the doped devices. Shimizu *et al.* [69] studied the distribution of carbon and other inorganic moieties such as CO, SiO, and O. Laser-assisted atom probe tomography (ATP) was employed to measure the elemental distribution profile. The unwanted diffusion of C- and O-related molecules is revealed, showing that the diffusion of C and O is only limited to the first few atomic layers near the surface. Moreover, the Ar + ion etching results in a different work [70] also indicates the SiC moiety mostly located in the ultra-shallow depth underneath the surface.

However, the effect of unwanted impurities introduced by the monolayer doping process still remains largely unexplored, in particular for carbon and oxygen impurities. In 1960s and 1970s, carbon and oxygen impurities in silicon were the major challenge to develop high-performance integrated circuits. Only when the carbon and oxygen impurities in silicon reduced to a level of 10^{15} cm^{-3} or lower have an era of microelectronics opened. The molecular monolayer doping technique is a promising low-cost doping technique that may potentially replace the traditional ion implantation technology. But it would not happen unless the unwanted carbon and oxygen impurities are removed from the doping process (**Figure 13**).

4. Structural features of dendrimers and dendrimer monolayers

Dendrimers are a series of dendritic molecules containing a core and repeating units. In the past 30 years, the processes for dendrimer synthesis have been well developed. Various dendrimers with different chemical characteristics were synthesized including poly-(amidoamine) with multiple amine-terminated groups [71], polyglycerols with polyetheric chains and hydroxyl groups [72], and silane dendrimers with carboxyl groups [73]. It is relatively easy to synthesize the dendrimers that carry dopant atoms such as phosphorus, sulfur, nitrogen or even iron [74] in addition to carbon, oxygen, and hydrogen. Therefore, dendrimers can be potentially used as precursor molecules for monolayer doping.

Due to their symmetric structure, dendrimers are often in a globular form [75], as shown in **Figure 14**. Previously, we mentioned that periodic discrete doping was achieved by self-assembled micelles. Except for the difference in particle size, dendrimer and micelles are similar in several aspects. For instance, both have moderately rigid structures and their core is both designable. Logically, dendrimers can also be used as dopant precursors or carriers to create discrete doping. In the following, we will discuss in detail the dendrimer synthesis methods and immobilization of dendrimers on silicon surfaces for doping.

According to the literature reports [76], the synthesis strategy of dendrimers can be classified as divergent and convergent growth method as shown in **Figure 15**. In **Figure 15a**, the divergent growth method is initiated from the active sites of core part [77], which is synthesized step-by-step and can obtain the unique molecular weight, such as the highest reported generations (G10) of PAMAM [78]. Another approach is the convergent assembly of well-defined branches to the core [79]. The convergent approach is to generate dendrons which are catenated to the core structure, as shown in **Figure 15b**. It provides a way to control molecular structures and obtain a faster synthesis speed owing to fewer coupling steps and the ability of precisely functionalizing specific growing sites. However, the molecular weight

http://dx.doi.org/10.5772/intechopen.71397

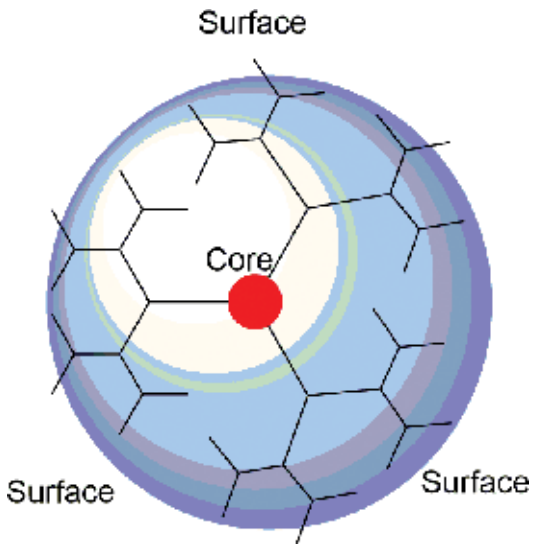

Figure 14. Dendrimer structure containing core and branched units.

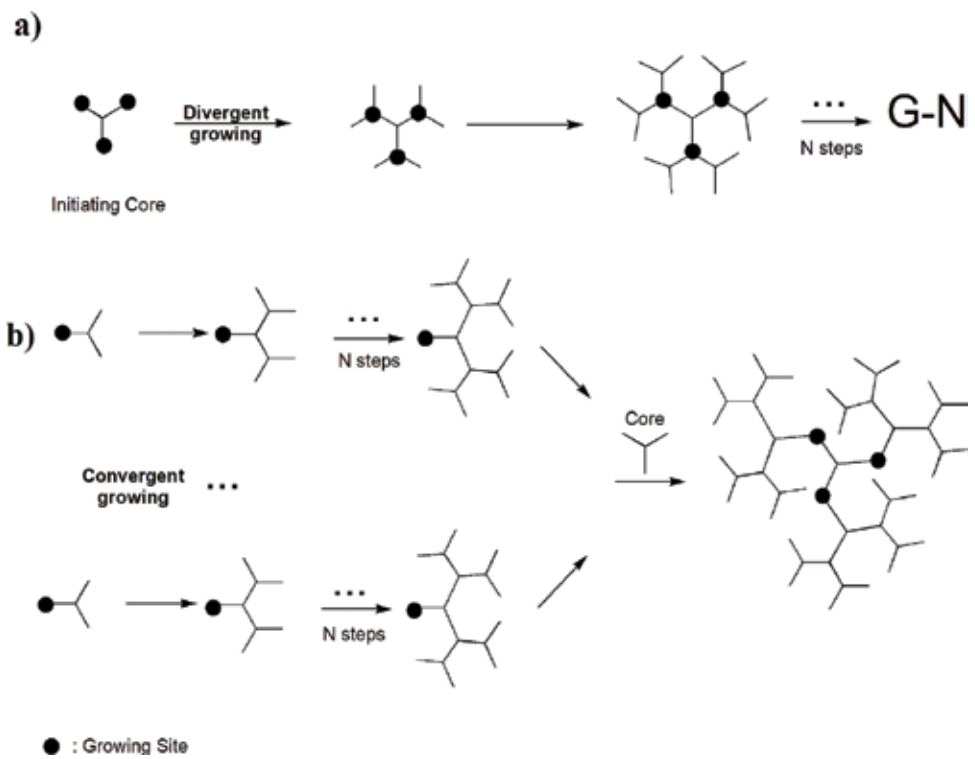

Figure 15. Divergent (a) and convergent growth (b) of dendrimers synthesis.

of dendrimers by convergent methods is smaller than by divergent growth, which is caused by the crowding environment around the core molecules [80]. By using dendrimers as single dopant carriers, it is necessary to ensure that each dendrimer carries only one dopant and the molecular weight is easily controlled from low to high by conventional approaches. Although the convergent method can provide a controlled parallel synthesis route with fewer steps, only the divergent growth can provide a broad range of molecular weight. As a result, we selected the divergent approach as the basic synthesis strategy to generate the dopant carriers.

Polyglycerols are dendrimers in the simplest form. The basic molecular skeleton of polyglycerols is polyetheric chains, and the monomers only contain carbon, oxygen, and hydrogen which are not electrically active in silicon. The excellent water solubility allows polyglycerol molecules to be purified to the CMOS grade using the conventional dialysis in deionized water. In our opinion, polyglycerols are potentially an ideal candidate as dopant carriers.

Depending on the molecular degree of branching, polyglycerols can be classified as dendritic and hyperbranched structures [81]. Dendritic polyglycerols is normally synthesized by the divergent method, as shown in **Figure 16** [72]. The main synthesis steps contain the substitution of 2-propenyl group and formation of vicinal diol moiety by oxidation process (i.e., oxidized by using K_2OsO_4). This synthesis strategy is time-consuming, but the dendritic structure of products is well-defined with unique molecular weight. However, the substitution efficiency decreases as the generation increases. The highest generation with fully dendritic is 5 [82], indicating that it is impossible to synthesize dendritic polyglycerols with very high molecular weight. Unlike time-consuming synthesis of dendritic polyglycerols, hyperbranched polyglycerols (hbPGs) are synthesized by self-polymerization of glycidol monomers at initiating sites. To overcome the drawbacks of the wide molecular weight distribution and the uncontrollable polymerization when using base reagents in earlier studies [83], Sunder *et al.* [84] performed the anionic ring-opening polymerization to obtain the controlled glycidol self-polymerization process, in which the slow addition strategy is adapted to attain a narrow molecular weight distribution. The reported hbPGs molecular weight is typically ranged from 1 to ~7 kDa. The particularly high molecular weight hbPGs can reach up to approximately 25 kDa via the two-step strategy based on the pre-synthesis low molecular weight hbPGs [85]. Meanwhile, Kainthan *et al.* [86] took a different strategy to obtain high molecular weight hbPGs in which dioxane was used as the emulsifying reagent with similar addition strategy. The SEC/MALLS results showed that the molecular weight of hbPGs can achieve to ~700 kDa with low polydispersities (PDI = 1.1–1.3). Besides the synthesis strategy, polyglycerols were synthesized with various initiating cores including tris(hydroxymethyl)-propane [84], graphene [87], and SiO_2 particles [88], implying that hbPGs molecules also can carry different dopants, such as phosphorus, nitrogen, boron, arsenic, iron or even rare earth elements.

Besides the synthesis of polyglycerols as dopant carriers, the graft of polyglycerols onto the substrate surface is another important step for monolayer doping process. Molecules or particles can be grafted onto the solid surface via physical absorption by Van de Waals force, electrostatic interaction or covalent bonds [89]. The physical absorption is weak and the electrostatic interaction is not specific, which, as a result, are not suitable for dopant control. The self-assembly via covalent bonds can generate a stable film for further modification, which

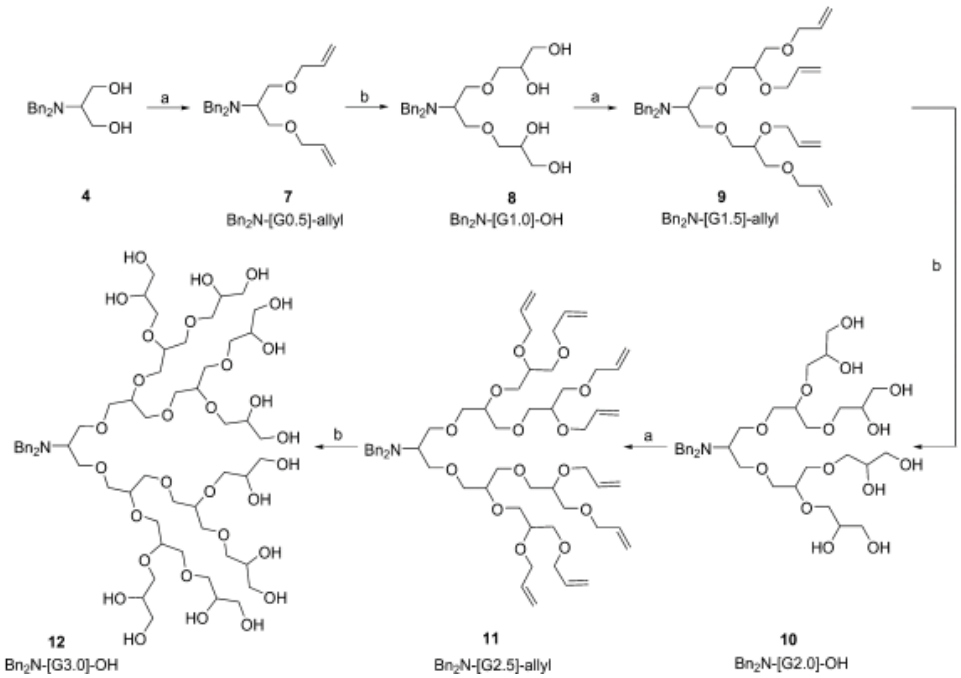

Figure 16. Synthesis flowchart of PG dendrons by substitution and oxidation process (Ref. 72).

is suitable for doping control. In particular, it has been demonstrated that the patterned self-assembled monolayer or ordered lithography patterns with monolayer films can provide ordered and discrete doping patterns [47, 55].

Depending on the order of polymerization and grafting, the graft of polymers can be classified "*grafting to*" and "*grafting from*" approaches [90]. As shown in **Figure 17**, the "*grafting to*" method is to immobilize pre-synthesized polymers or macromolecules onto solid surface. The "*grafting from*" method is to polymerize on functional surfaces [91]. Ordinary amino-terminated dendrimers are often anchored by covalent bonds with carboxyl groups. For example, Mark *et al.* [92] reported in **Figure 18** that the gold surface was firstly modified by AUT and bis-[sulfosuccinimidyl]suberate molecules through Au-S bonds. Then, through the activated carboxyl by NHS, the G4 dendrimer can be bonded to the carboxyl group by formation of amide bonds.

Polyglycerols contains a large amount of hydroxyl groups mostly located at the molecular surfaces. These hydroxyl groups in return can be modified by other functional groups such as disulfide to bind to gold surface [93]. Although there are few reports on applying the "grafting to" method on silicon surfaces, the well-developed silicon surface chemistry can provide some feasible resolutions to graft hbPGs molecules to, for example, carboxyl-functionalized or halogen-terminated silicon surfaces [49].

Briefly in this section, we discussed in detail the possibility of using molecules as the potential dopant carriers, and the grafting methods of these molecular dopant carriers.

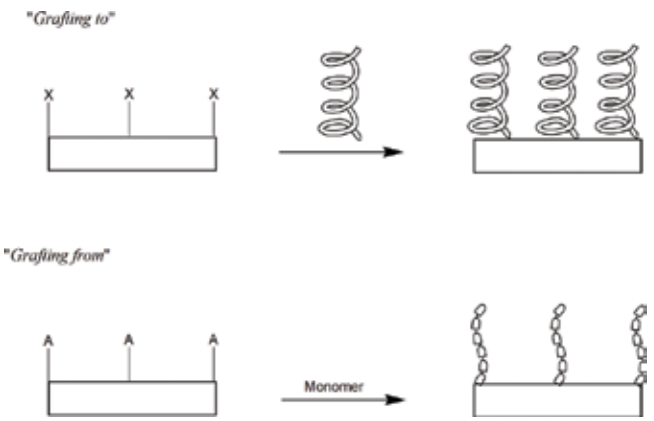

Figure 17. Flowchart of "*grafting to*" and "*grafting from*." In figure, X is functional group, and A is initiating site.

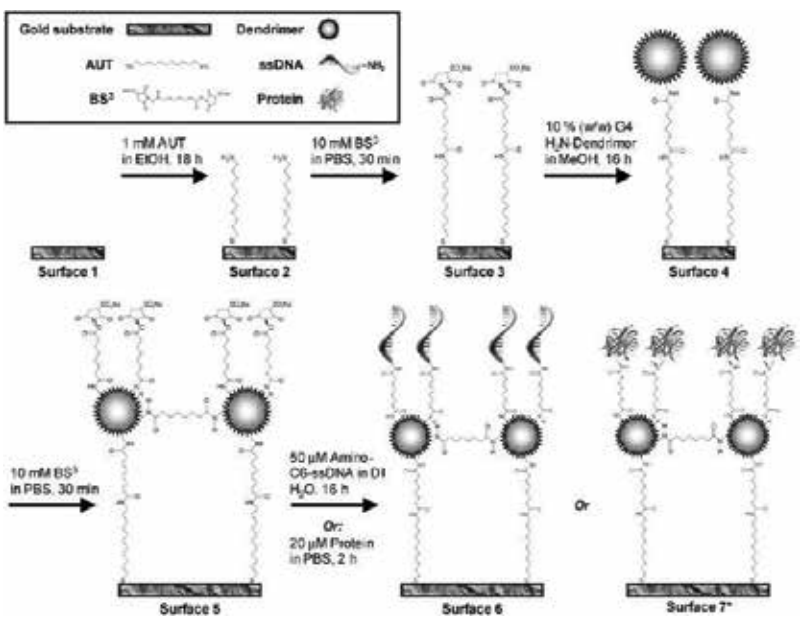

Figure 18. PAMAM G4 was anchored to the carboxyl-terminated gold surface (Ref. 92).

5. Dendrimer-based monolayer doping

hbPGs is an ideal potential candidate as dopant carriers. The molecular size can be readily controlled and the number of dopants that the molecule carries can be precisely tuned. In addition, the unique polymerization process allows the molecules to carry different kinds of dopants. Phosphorus is n-type dopants in silicon [4]. Several research groups have reported the atomic devices based on single phosphorus dopants [4].

Recently, we reported on using hyperbranched polyglycerols (hbPGs) as the phosphorus carriers [10]. The hbPGs were synthesized through the ring-open multibranching polymerization with (tri(4-hydroxylphenyl)phosphine oxide) which is the initiating core. To graft hbPGs onto silicon surfaces, the hydrogen-terminated silicon surfaces were modified with 10-undecenoic acid molecules. The hbPGs were anchored by a process shown in **Figure 19** during which ester bonds are formed. After the rapid annealing process, the phosphorus dopants were diffused into a shallow depth underneath the surface (~100 nm) and the areal dose of dopants is approximately 1.64×10^{11} cm^{-2} with a surface doping concentration of ~1017 cm^{-3}. According to the empirical equation [38], the experimental sheet resistance (Rs) would be close to the sheet resistance Rs predicated by SIMS results. However, the actual activation rate evaluated by low temperature Hall measurement is unexpectedly low (~7%) by comparing the electrically active phosphorus dopants with the total phosphorus elements. As our group previously reported [45], nitrogen is one of the factors to retard the activation of phosphorus by forming N-P complex. We believe that the observed low ionization rate is due to nitrogen contamination introduced by coupling reagents (DCC and DMAP) in the reaction process. The XPS full survey and narrow scan also confirmed the nitrogen contamination. Although the final doping efficient of phosphorus is lower than expectation, this protocol confirmed that it is feasible to use dendrimer-like hbPGs molecules as dopant carriers.

Clearly, a nitrogen-free doping process is a must to obtain the highly efficient doping protocol. In the following experiments, we will perform the nitrogen-free and one-step self-assembled monolayer process, which will help us to explore the impact of other elements on the doping efficiency.

Although oxygen and carbon do not electrically dope silicon, they form defects which lower the ionization rate of electrically active dopants by trapping electrons [94]. In the previous studies, different types of carbon-related defects were successfully observed by using deep level transient capacitance spectroscopy (DLTS), for example, interstitial carbon (C_i), interstitial-carbon-substitutional-carbon (C_i-C_s) pairs, and interstitial-carbon-substitutional-phosphorus (C_i-P_s) pairs. These carbon-related defects display different energy levels from 100 to 300 meV [95, 96]. Our group further explored the effect of carbon elements on the doping efficiency by

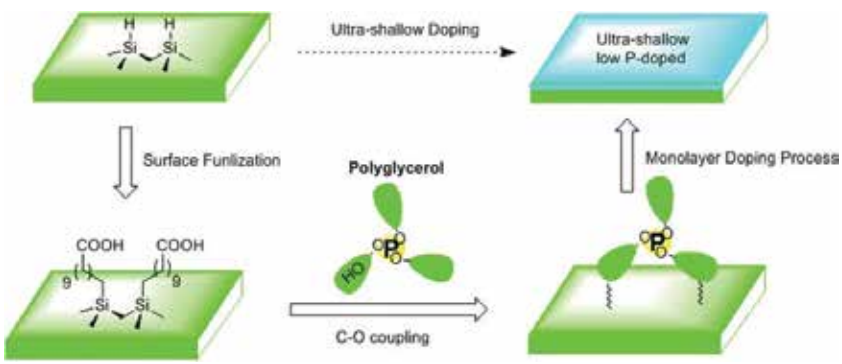

Figure 19. Dendrimer-like macromolecular monolayer doping protocol (Ref. 10).

using DLTS. With the assistance of low temperature Hall measurements, we found that the ionization rate of phosphorus dopants is ~64% when the P concentration is high. This ionization rate is lowered to 10% when the P concentration is low because phosphorus dopants are electrically retarded by the carbon defects by forming interstitial carbon-substitutional phosphorus (C_i-P_s) pairs [95, 97, 98]. Developing techniques to reduce the concentration of carbon impurities introduced by the molecular monolayers is the key to the control of single dopants by the self-assembly of macromolecule dopant carriers.

6. Conclusion

The precise control of individual dopants is critical for the development of single atom electronics and quantum devices. We propose to control single dopant atoms by the self-assembly of individual hbPGs molecules with each carrying one phosphorus atom. Unlike the single atom manipulation techniques by STM and single ion implantation, the dendrimer-based monolayer doping process is more feasible to achieve the controllable doping at large scale from the engineering point of view.

Acknowledgements

This work is supported by the National Science Foundation of China (No. 21503135).

Author details

Haigang Wu[1,2] and Yaping Dan[1]*

*Address all correspondence to: yaping.dan@sjtu.edu.cn

1 University of Michigan-Shanghai Jiao Tong University Joint Institute, Shanghai Jiao Tong University, Shanghai, China

2 School of Biomedical Engineering, Shanghai Jiao Tong University, Shanghai, China

References

[1] Sharma KC, Sharma R, Garg JC. Effect of silver dopant on optical and electrical properties of solution-grown cadmium selenide thin films. Japanese Journal of Applied Physics. 1992;**31**(3R):742

[2] Etemad S, Aspnes D, Kelly M, Thompson R, Tarascon J-M, Hull G. Correlation of dopant-induced optical transitions with superconductivity in $La_{2-x}Sr_xCuO_{4-\delta}$. Physical Review B. 1988;**37**(7):3396

[3] Nakano T, Momono N, Matsuzaki T, Nagata T, Yokoyama M, Oda M, et al. Effects of Zn substitution on magnetic properties and superconductivity in $La_{2-x}Sr_xCuO_4$. Physica C Superconductivity. 1999;**s 317-318**(1):575-578

[4] Fuechsle M, Miwa JA, Mahapatra S, Ryu H, Lee S, Warschkow O, et al. A single-atom transistor. Nature Nanotechnology. 2012;**7**(4):242-246

[5] Maruyama T, Shiota Y, Nozaki T, Ohta K, Toda N, Mizuguchi M, et al. Large voltage-induced magnetic anisotropy change in a few atomic layers of iron. Nature Nanotechnology. 2009;**4**(3):158

[6] Shinada T, Okamoto S, Kobayashi T, Ohdomari I. Enhancing semiconductor device performance using ordered dopant arrays. Nature. 2005;**437**(7062):1128-1131

[7] Tucker JR, Shen TC. Prospects for atomically ordered device structures based on STM lithography. Solid-State Electronics. 1998;**42**(7-8):1061-1067

[8] Hori M, Shinada T, Ono Y, Komatsubara A, Kumagai K, Tanii T, et al. Impact of a few dopant positions controlled by deterministic single-ion doping on the transconductance of field-effect transistors. Applied Physics Letters. 2011;**99**(6):223

[9] Weber B, Mahapatra S, Ryu H, Lee S, Fuhrer A, Reusch T, et al. Ohm's law survives to the atomic scale. Science. 2012;**335**(6064):64-67

[10] HG W, Guan B, Sun YR, Zhu YP, Dan YP. Controlled doping by self-assembled dendrimer-like macromolecules. Scientific Reports. 2017;**7**:41299

[11] Xie F-Q, Nittler L, Obermair C, Schimmel T. Gate-controlled atomic quantum switch. Physical Review Letters. 2004;**93**(12):128303

[12] Xie FQ, Hüser F, Pauly F, Obermair C, Schön G, Schimmel T. Conductance of atomic-scale Pb contacts in an electrochemical environment. Physical Review B. 2010;**82**(7):2283-2288

[13] Martin CA, Smit RH, van der Zant HS, van Ruitenbeek JM. A nanoelectromechanical single-atom switch. Nano Letters. 2009;**9**(8):2940-2945

[14] Kane BE. A silicon-based nuclear spin quantum computer. Nature. 1998;**393**(6681):133-137

[15] Slichter CP. Principles of Magnetic Resonance. New York, USA: Springer Science & Business Media; 2013

[16] Pla JJ, Tan KY, Dehollain JP, Lim WH, Morton JJ, Zwanenburg FA, et al. High-fidelity readout and control of a nuclear spin qubit in silicon. Nature. 2013;**496**(7445):334-338

[17] Vrijen R, Yablonovitch E, Wang K, Jiang HW, Balandin A, Roychowdhury V, et al. Electron-spin-resonance transistors for quantum computing in silicon-germanium heterostructures. Physical Review A. 2000;**62**(1):012306

[18] Morton JJ, Tyryshkin AM, Brown RM, Shankar S, Lovett BW, Ardavan A, et al. Solid-state quantum memory using the 31P nuclear spin. Nature. 2008;**455**(7216):1085-1088

[19] Tseng GY, Ellenbogen JC. Toward nanocomputers. Science. 2001;**294**(5545):1293-1294

[20] Feynman RP. There's plenty of room at the bottom. Engineering and science. 1960;**23**(5):22-36

[21] Bennewitz R, Crain JN, Kirakosian A, Lin J, McChesney J, Petrovykh D, et al. Atomic scale memory at a silicon surface. Nanotechnology. 2002;**13**(4):499

[22] Kou X, Fan X, Dumas RK, Lu Q, Zhang Y, Zhu H, et al. Memory effect in magnetic nanowire arrays. Advanced Materials. 2011;**23**(11):1393-1397

[23] Schirm C, Matt M, Pauly F, Cuevas JC, Nielaba P, Scheer E. A current-driven single-atom memory. Nature Nanotechnology. 2013;**8**(9):645-648

[24] Kalff F, Rebergen MP, Fahrenfort E, Girovsky J, Toskovic R, Lado JL, et al. A kilobyte rewritable atomic memory. Nature Nanotechnology. 2016;**11**(11):926-929

[25] Maze J, Stanwix P, Hodges J, Hong S, Taylor J, Cappellaro P, et al. Nanoscale magnetic sensing with an individual electronic spin in diamond. Nature. 2008;**455**(7213):644-647

[26] Ferain I, Colinge CA, Colinge J-P. Multigate transistors as the future of classical metal-oxide-semiconductor field-effect transistors. Nature. 2011;**479**(7373):310

[27] Mizuno T, Okamura J-i, Toriumi A, editors. Experimental study of threshold voltage fluctuations using an 8k MOSFET's array. Symposium on VLSI Technology. IEEE Institute of Electrical and Electronics; 1993

[28] Mizuno T, Okumtura J, Toriumi A. Experimental study of threshold voltage fluctuation due to statistical variation of channel dopant number in MOSFET's. IEEE Transactions on Electron Devices. 1994;**41**(11):2216-2221

[29] Wong H-SP, Taur Y, Frank DJ. Discrete random dopant distribution effects in nanometer-scale MOSFETs. Microelectronics Reliability. 1998;**38**(9):1447-1456

[30] Koenraad PM, Flatté ME. Single dopants in semiconductors. Nature Materials. 2011;**10**(2):91

[31] Hori M, Taira K, Komatsubara A, Kumagai K, Ono Y, Tanii T, et al. Reduction of threshold voltage fluctuation in field-effect transistors by controlling individual dopant position. Applied Physics Letters. 2012;**101**(1):013503

[32] Ohdomari I, Kamioka T. Surface modification of silicon with single ion irradiation. Applied Surface Science. 2007;**254**(1):242-246

[33] Huang W-T, Li Y. Electrical characteristic fluctuation of 16-nm-gate trapezoidal bulk FinFET devices with fixed top-fin width induced by random discrete dopants. Nanoscale Research Letters. 2015;**10**(1):116

[34] Ziegler JF. Ion Implantation Science and Technology. Amsterdam, Netherlands: Elsevier; 2012

[35] Fahey PM, Griffin P, Plummer J. Point defects and dopant diffusion in silicon. Reviews of Modern Physics. 1989;**61**(2):289

[36] Kim K-S, Song Y-H, Park K-T, Kurino H, Matsuura T, Hane K, et al. A novel doping technology for ultra-shallow junction fabrication: Boron diffusion from boron-adsorbed layer by rapid thermal annealing. Thin Solid Films. 2000;**369**(1):207-212

[37] EerNisse E. Sensitive technique for studying ion-implantation damage. Applied Physics Letters. 1971;**18**(12):581-583

[38] Ho JC, Yerushalmi R, Jacobson ZA, Fan Z, Alley RL, Javey A. Controlled nanoscale doping of semiconductors via molecular monolayers. Nature Materials. 2008;**7**(1):62

[39] Ho JC, Yerushalmi R, Smith G, Majhi P, Bennett J, Halim J, et al. Wafer-scale, sub-5nm junction formation by monolayer doping and conventional spike annealing. Nano Letters. 2009;**9**(2): 725-730

[40] Pandey K, Erbil A, Cargill G III, Boehme R, Vanderbilt D. Annealing of heavily arsenic-doped silicon: Electrical deactivation and a new defect complex. Physical Review Letters. 1988;**61**(11):1282

[41] O'Connell J, Verni GA, Gangnaik A, Shayesteh M, Long B, Georgiev YM, et al. Organo-arsenic molecular layers on silicon for high-density doping. ACS Applied Materials & Interfaces. 2015;**7**(28):15514-15521

[42] Ang KW, Barnett J, Loh WY, Huang J, Min BG, Hung PY, et al. 300mm FinFET results utilizing conformal, damage free, ultra shallow junctions (X-j similar to 5nm) formed with molecular monolayer doping technique. 2011 Ieee International Electron Devices Meeting (Iedm). 2011

[43] Imai M, Sumino K. In situ X-ray topographic study of the dislocation mobility in high-purity and impurity-doped silicon crystals. Philosophical Magazine A. 1983;**47**(4):599-621

[44] Tokumaru Y, Okushi H, Masui T, Abe T. Deep levels associated with nitrogen in silicon. Japanese Journal of Applied Physicspt Letters. 1982;**21**(7):L443-L4L4

[45] Guan B, Siampour H, Fan Z, Wang S, Kong XY, Mesli A, et al. Nanoscale nitrogen doping in silicon by self-assembled monolayers. Scientific Reports. 2015;**5**(12641)

[46] Sze SM. Semiconductor Devices: Physics and Technology. Hoboken, New Jersey, USA: John Wiley & Sons; 2008

[47] Popere BC, Russ B, Heitsch AT, Trefonas P, Segalman RA. Large-area, Nanometer-scale discrete doping of semiconductors via block copolymer self-assembly. Advanced Materials Interfaces. 2016;**2**(18)

[48] O'Connell J, Collins G, Mcglacken GP, Duffy R, Holmes JD. Monolayer doping of Si with improved oxidation resistance. ACS Applied Materials & Interfaces. 2016;**8**(6):4101

[49] Ciampi S, Harper JB, Gooding JJ. Wet chemical routes to the assembly of organic monolayers on silicon surfaces via the formation of Si-C bonds: Surface preparation, passivation and functionalization. Chemical Society Reviews. 2010;**39**(6):2158

[50] Kupper D, Kupper D, Wahlbrink T, Henschel W, Bolten J, Lemme MC, et al. Impact of supercritical CO2 drying on roughness of hydrogen silsesquioxane e-beam resist. Journal of Vacuum Science & Technology B Microelectronics & Nanometer Structures. 2006;**24**(2):570-574

[51] Janeta M, John L, Ejfler J, Szafert S. Novel organic-inorganic hybrids based on T8 and T10 silsesquioxanes: Synthesis, cage-rearrangement and properties. RSC Advances. 2015;**5**(88): 72340-72351

[52] Alphazan T, Mathey L, Schwarzwalder M, Lin T-H, Rossini AJ, Wischert R, et al. Monolayer doping of silicon through grafting a tailored molecular phosphorus precursor onto oxide-Passivated silicon surfaces. Chemistry of Materials. 2016;**28**(11):3634-3640

[53] Alphazan T, Florian P, Thieuleux C. Ethoxy and silsesquioxane derivatives of antimony as dopant precursors: Unravelling the structure and thermal stability of surface species on SiO 2. Physical Chemistry Chemical Physics. 2017;**19**(12):8595-8601

[54] Alphazan T, Diaz Alvarez A, Martin F, Grampeix H, Enyedi V, Martinez E, et al. Shallow heavily-doped n++ germanium by organo-antimony monolayer doping. ACS Applied Materials & Interfaces. 2017

[55] Voorthuijzen W, Yilmaz MD, Naber WJ, Huskens J, van der Wiel WG. Local doping of silicon using nanoimprint lithography and molecular monolayers. Advanced Materials 2011;**23**(11):1346-1350

[56] Taheri P, Fahad HM, Tosun M, Hettick M, Kiriya D, Chen K, et al. Nanoscale junction formation by gas-phase monolayer doping. ACS Applied Materials & Interfaces. 2017

[57] O'Connell J, Biswas S, Duffy R, Holmes JD. Chemical approaches for doping nanodevice architectures. Nanotechnology. 2016;**27**(34):342002

[58] Ye L, Pujari SP, Zuilhof H, Kudernac T, de Jong MP, van der Wiel WG, et al. Controlling the dopant dose in silicon by mixed-monolayer doping. ACS Applied Materials & iInterfaces. 2015;**7**(5):3231-3236

[59] Williams RE. The polyborane, carborane, carbocation continuum: Architectural patterns. Chemical Reviews. 1992;**92**(2):177-207

[60] Ye L, González-Campo A, Núñez R, de Jong MP, Kudernac T, van der Wiel WG, et al. Boosting the boron dopant level in monolayer doping by Carboranes. ACS Applied Materials & Interfaces. 2015;**7**(49):27357-27361

[61] Sun JT, Hong CY, Pan CY. Formation of the block copolymer aggregates via polymerization-induced self-assembly and reorganization. Soft Matter. 2012;**8**(30):7753-7767

[62] Popere BC, Russ B, Heitsch AT, Trefonas P, Segalman RA. Large-area, Nanometer-scale discrete doping of semiconductors via block copolymer self-assembly. Advanced Materials Interfaces. 2015;**2**(18):1500421

[63] Del Alamo JA. Nanometre-scale electronics with III-V compound semiconductors. Nature. 2011;**479**(7373):317

[64] Yum JH, Shin HS, Hill R, Oh J, Lee HD, Mushinski RM, et al. A study of capping layers for sulfur monolayer doping on III-V junctions. Applied Physics Letters. 2012;**101**(25):072108-072105

[65] Loh W-Y, Lee R, Tieckelmann R, Orzali T, Sapp B, Hobbs C, et al., editors. 300mm wafer level sulfur monolayer doping for III–V materials. Advanced Semiconductor Manufacturing Conference (ASMC), 2015 26th Annual SEMI; 2015: IEEE

[66] Cho K, Ruebusch DJ, Lee MH, Moon JH, Ford AC, Kapadia R, et al. Molecular monolayers for conformal, nanoscale doping of InP nanopillar photovoltaics. Applied Physics Letters. 2011;**98**(20):203101

[67] Ho JC, Ford AC, Chueh YL, Leu PW, Ergen O, Takei K, et al. Nanoscale doping of InAs via sulfur monolayers. Applied Physics Letters. 2009;**95**(7):072108-072103

[68] Yum J, Shin H, Hill R, Oh J, Lee H, Mushinski RM, et al. A study of capping layers for sulfur monolayer doping on III-V junctions. Applied Physics Letters. 2012;**101**(25):253514

[69] Shimizu Y, Takamizawa H, Inoue K, Yano F, Nagai Y, Lamagna L, et al. Behavior of phosphorous and contaminants from molecular doping combined with a conventional spike annealing method. Nanoscale. 2014;**6**(2):706-710

[70] Pillers MA, Lieberman M. Embedded silicon carbide "replicas" patterned by rapid thermal processing of DNA origami on silicon. Journal of Vacuum Science & Technology B, Nanotechnology and Microelectronics: Materials, Processing, Measurement, and Phenomena. 2016;**34**(6):060602

[71] Ferruti P, Marchisio MA, Duncan R. Poly (amido-amine) s: Biomedical applications. Macromolecular Rapid Communications. 2002;**23**(5-6):332-355

[72] Wyszogrodzka M, Möws K, Kamlage S, Wodzińska J, Plietker B, Haag R. New approaches towards monoamino polyglycerol dendrons and dendritic triblock amphiphiles. European Journal of Organic Chemistry. 2008;**2008**(1):53-63

[73] Boisselier E, Ornelas C, Pianet I, Aranzaes JR, Astruc D. Four generations of water-soluble Dendrimers with 9 to 243 benzoate tethers: Synthesis and dendritic effects on their ion pairing with acetylcholine, Benzyltriethylammonium, and dopamine in water. Chemistry-A European Journal. 2008;**14**(18):5577-5587

[74] Kim C, Park E, Song CK, Koo BW. Ferrocene end-capped dendrimer: Synthesis and application to CO gas sensor. Synthetic metals. 2001;**123**(3):493-496

[75] Tokuhisa H, Kubo T, Koyama E, Hiratani K, Kanesato M. A new method to fabricate single-molecule Nanoarrays using Dendrimer-based templates. Advanced Materials. 2003;**15**(18):1534-1538

[76] Ooya T, Lee J, Park K. Hydrotropic dendrimers of generations 4 and 5: Synthesis, characterization, and hydrotropic solubilization of paclitaxel. Bioconjugate Chemistry. 2004; **15**(6):1221-1229

[77] Brauge L, Magro G, Caminade A-M, Majoral J-P. First divergent strategy using two AB2 unprotected monomers for the rapid synthesis of dendrimers. Journal of the American Chemical Society. 2001;**123**(27):6698-6699

[78] Hedden RC, Bauer BJ, Smith AP, Gröhn F, Amis E. Templating of inorganic nanoparticles by PAMAM/PEG dendrimer–star polymers. Polymer. 2002;**43**(20):5473-5481

[79] Miller TM, Neenan TX. Convergent synthesis of monodisperse dendrimers based upon 1, 3, 5-trisubstituted benzenes. Chemistry of Materials. 1990;**2**(4):346-349

[80] Holister P, Vas CR, Harper T. Dendrimers. Technology white papers. 2003;**6**:1-15

[81] Calderón M, Quadir MA, Sharma SK, Haag R. Dendritic polyglycerols for biomedical applications. Advanced Materials. 2010;**22**(2):190-218

[82] Haag R, Sunder A, Stumbé J-F. An approach to glycerol dendrimers and pseudo-dendritic polyglycerols. Journal of the American Chemical Society. 2000;**122**(12):2954-2955

[83] Sandler SR, Berg FR. Room temperature polymerization of glycidol. Journal of Polymer Science Part A: Polymer Chemistry. 1966;**4**(5):1253-1259

[84] Sunder A, Hanselmann R, Frey H, Mülhaupt R. Controlled synthesis of hyperbranched polyglycerols by ring-opening multibranching polymerization. Macromolecules. 1999;**32**(13): 4240-4246

[85] Wilms D, Wurm F, Jr N, Böhm P, Kemmer-Jonas U, Frey H. Hyperbranched polyglycerols with elevated molecular weights: A facile two-step synthesis protocol based on polyglycerol macroinitiators. Macromolecules. 2009;**42**(9):3230-3236

[86] Kainthan RK, Muliawan EB, Hatzikiriakos SG, Brooks DE. Synthesis, characterization, and viscoelastic properties of high molecular weight hyperbranched polyglycerols. Macromolecules. 2006;**39**(22):7708-7717

[87] Sui K, Zhang Q, Liu Y, Tan L, Liu L. Improved interfacial and impact properties of carbon fiber/epoxy composites through grafting hyperbranched polyglycerols on a carbon fiber surface. E-Polymers. 2014;**14**(2):145-150

[88] Khan M, Huck WT. Hyperbranched polyglycidol on Si/SiO2 surfaces via surface-initiated polymerization. Macromolecules. 2003;**36**(14):5088-5093

[89] Rajca A. An introduction to ultrathin organic films: From Langmuir-Blodgett to self-assembly. Advanced Materials. 2010;**4**(4):309

[90] Minko S. Grafting on solid surfaces:"grafting to" and "grafting from" methods. Polymer surfaces and interfaces: Springer. 2008:215-234

[91] Stamm M. Polymer surfaces and interfaces. Polymer Surfaces and Interfaces: Characterization, Modification and Applications. Berlin, Germany: Springer Berlin Heidelberg; 2008;1. ISBN 978-3-540-73864-0

[92] Mark SS, Sandhyarani N, Zhu C, Campagnolo C, Batt CA. Dendrimer-functionalized self-assembled monolayers as a surface plasmon resonance sensor surface. Langmuir. 2004;**20**(16):6808-6817

[93] CS D-C, Biesalski M, Dr RH. Self-assembled monolayers of dendritic Polyglycerol derivatives on gold that resist the adsorption of proteins. Chemistry-A European Journal. 2004;**10**(11):2831-2838

[94] Stavola M, Pearton SJ, Davies G. Defects in Electronic Materials. Pittsburgh, PA: Materials Research Society; 1988

[95] Zhan XD, Watkins GD. Electron paramagnetic resonance of multistable interstitial-carbon–substitutional-group-V-atom pairs in silicon. Physical Review B Condensed Matter. 1993;**47**(11):6363

[96] Song LW, Benson BW, Watkins GD. Identification of a bistable defect in silicon: The carbon interstitial-carbon substitutional pair. Applied Physics Letters. 1987;**51**(15):1155-1157

[97] Song L, Watkins G. EPR identification of the single-acceptor state of interstitial carbon in silicon. Physical Review B. 1990;**42**(9):5759

[98] Gao XJ, Guan B, Mesli A, Chen KX and Dan YP. Deep level transient spectroscopic investigation of phosphorus-doped silicon by self-assembled molecular monolayers. Under review in Nature Communications

Edited by Claudia Maria Simonescu

Dendrimers are defined as nanoscale macromolecules having a particular architecture consisting of treelike arms or branches. They are characterized by special properties that make them promising candidates in medicine, biology, materials science, synthetic organic chemistry, biotechnology, environmental engineering, optics, electronics, catalysis, electrochemistry, photochemistry, and sensors and even for production of cosmetics and personal care products. The dendrimers research field is growing day by day, and scientists are exploring new synthesis and functionalization methods in order to improve and to determine new properties and thus new applications. The main purpose of this book is to highlight the issues regarding properties and applications of dendrimers in the field of biology, medicine, liquid crystal devices, electronics, quantum devices, and self-healing technology.

Published in London, UK

IntechOpen

ISBN 978-1-83881-351-2